

INAUGURAL-DISSERTATION

ZUR
ERLANGUNG DER DOKTORWÜRDE
DER
NATURWISSENSCHAFTLICH-MATHEMATISCHEN GESAMTFAKULTÄT
DER
RUPRECHT-KARLS-UNIVERSITÄT HEIDELBERG

VORGELEGT VON
MAXIMILIAN MENCHE
AUS
GROß-GERAU

TAG DER MÜNDLICHEN PRÜFUNG: 28. OKTOBER 2021

QUANTUM CHEMICAL INVESTIGATIONS IN
HOMOGENEOUS CATALYSIS:
DEHYDROGENATION, CARBONYLATION AND
VINYLATION

QUANTENCHEMISCHE UNTERSUCHUNGEN IN DER HOMOGENEN KATALYSE: DEHYDRIERUNG,
CARBONYLIERUNG UND VINYLIERUNG

VORGELEGT VON

MAXIMILIAN MENCHE

ERSTER GUTACHTER: PROF. DR. PETER COMBA
ZWEITER GUTACHTER: PROF. DR. ANDREAS DREUW

“An oft-overlooked additional benefit is that neither the environment nor any researcher has yet been accidentally poisoned by computational substrates.”

C. J. Cramer, G. R. Famini in *J. Am. Chem. Soc.* **1990**, *112*, 5460 – 5464.

On the other hand, no computational substrate has ever been used to build a physical object or to cure a patient!

Indeed, computational methods are powerful and versatile and can nowadays take on tasks that have traditionally been carried out in chemical laboratories and therefore reduce risks. However, the goal of computational chemists should not be to substitute as many of these tasks as possible, but to find those specific aspects where computational methods can unfold their greatest benefit in a shared project and to find the most effective ways to work alongside experiments.

While carrying out my research in the past three years, I have been in the fortunate situation to be surrounded by colleagues who shared this mindset and carefully assessed if it might be helpful for them to ask for computational support and if a single experiment could help avoid weeks of computing elaborate, but irrelevant reaction mechanisms.

Acknowledgements

Due to the complex framework, in which my PhD was carried out, a short introduction of the three involved parties might be necessary: the group of Peter Comba at Heidelberg University, the Catalysis Research Laboratory (CaRLa) managed by Thomas Schaub and the Quantum Chemistry group of BASF lead by Ansgar Schäfer. While this situation might sound complicated, it also enabled me to meet, work with, and learn from many different individuals across the three institutions (and beyond). Firstly, let me thank the heads of these groups for the opportunity to perform my PhD studies in their groups – without their continuous support, mentorship, and their experience this would not have been possible.

Peter, thank you for supervising me during these past three years! Even though I was an external PhD student and was not working on one of the common topics in your group, you have always supported me to the fullest. Thank you for the helpful discussions, your time, and your great job in building a supportive, positive, and helpful group! Also let me thank you for your long-time support of the CaRLa framework. I truly believe that this is a fantastic opportunity for postdocs and PhD students alike and I am glad that your support enabled me to perform research and my PhD here.

Thomas, thank you for being my mentor when it came to homogeneous catalysis, organometallic chemistry, and industrial chemistry! Not many computational chemists get the opportunity to learn so much about applications and considerations in chemical industry and this fact constantly reassured me that I made a fantastic choice in coming to CaRLa. Also, I want to thank you for your support of computational chemistry! It is not often that computational results are accepted as an equal partner next to experimental results and have such a high impact on the projects. Moreover, you were not just open towards applying and integrating established computational methods, but also gave me the time and freedom to learn about and explore new methods. Your willingness to continue to do so and your own interest in these new approaches makes me certain that computational chemistry will continuously be employing state-of-the-art methods to support experiments at CaRLa. Last but not least let me thank you for your support towards presenting our research at conferences (whether in-person or digital). If you would not have pushed and supported me in this direction right from the beginning of my PhD, I most likely would have missed in-person conferences altogether as the COVID pandemic prohibited this in the second half of my time at CaRLa and I would have missed out on a lot of practice, experience and networking opportunities.

Ansgar, thank you for being my mentor especially when it came to computational chemistry topics in the past three years! As a (more or less) new TURBOMOLE user, your in-depth knowledge and our discussions helped me very much. You were equally supportive when it came to any other topics like machine learning, scripting, or any other new approaches we wanted to discuss or try. Thank you also for providing me with the possibility to visit multiple conferences in Germany, France, and the United Kingdom in the first 1.5 years of my PhD. Only due to this early support I was not completely missing

out on this aspect of my PhD. I also want to thank you for the fantastic job you have done in building a diverse group within BASF. Since the group investigates and supports such a high range of different topics enabled me to get glimpses into many aspects of industrial quantum-chemistry. While this also means that you are extremely busy with keeping up on all these different projects, you've always found time for our biweekly meeting, which served as a platform for lots of help and advice. Thank you!

CaRLa is additionally managed by Stephen Hashmi, who co-leads the laboratory from the university's side. Thank you for your many contributions to the discussions and the helpful advice during my group meeting presentations or the publication process!

Moreover, I want to thank all four of you for working so well as a team. Being part of a construct with so many supervisors and scientific heads can lead to difficult situations if tricky compromises between individual wishes must be found. However, this was never the case during my time at CaRLa and we could always be focused on working towards advancing our common goals.

I would also like to extend my thanks to Prof. Andreas Dreuw for preparing the second review for this thesis.

Daniel, thank you for being a great colleague and supporting me on our way to our first CaRLa paper. I thoroughly enjoyed our fun and educational (although at times tedious) discussions about ester hydrogenation mechanisms. Apart from that, I will surely remember the entertaining lunch meetings (at a pre-COVID time where these were still possible ...) and conversations. I am sure you were not expecting to get through this acknowledgment section without me mentioning our interesting trip to Bristol, but maybe we can postpone this discussion until we can meet for a decent size portion of fish 'n' chips.

Sara, I have to thank you for two things: First, obviously, thank you for working together on the carbonylation of the phenyl ethanol system, which can also be found in this thesis. But maybe more importantly than anything else, thank you for getting me to CaRLa in the first place! If we would not have met in Constance, I most likely would have missed this fantastic opportunity!

Niels, it was great to work with you on the second part of the carbonylation project. I am sure that I have bothered you (at least at times) with the many reaction ideas I had to support the mechanistic investigations and that it became very tricky to maintain an overview over the high number of reactions you had carried out. Thank you! I wish we would have met in a time where more personal interactions would have been possible and one could have decided to go on some nice photography adventures, but we will have to leave this for the future.

Nikolai, thank you for your amazing work on the vinylation of pyrrolidone! This project really was a prime example of why CaRLa is such a great place to perform research (at least as computational chemist, which I can vouch for): constant feedback, productive discussions and computational investigations being truly integrated into the whole process.

Robert, even if our work on the reductive amination did not make it into this thesis, it was an interesting rollercoaster ride to work with you on it. Similarly, interesting was to be part of your personal CaRLa journey from meeting and discussing in Bristol to seeing you move on to BASF. I am sure one day the desired $\epsilon\epsilon$ will be achieved! What was the number again ...?

Tamal, thank you for also working on and supporting the carbonylation and reductive amination!

Thank you also to my predecessor as CaRLa theoretician, Marko, for helping me with information about CaRLa and providing me with the foundation and advice for the reductive amination project.

Imke, thank you for guiding me through my first steps at BASF (and in general through the forest of bureaucracy that exists in a large company) as well as being there for any questions I had no matter whether they were of technical or scientific nature.

Nedko, thank you for being a fantastic office colleague and for regularly informing me about new automation techniques that you were testing or that I should keep an eye on.

Obviously, I want to extend my gratitude not just to the individuals that worked on these larger projects with me but to the whole of the highly dynamic CaRLa team that has kindly accepted me three years ago. Even though a new generation of postdocs joined throughout the years, the acceptance for me as somewhat of an outsider (as a computational PhD student amongst a group of experimental postdocs) has never changed. I only wish that this would not have happened in a time where a pandemic managed to keep us apart for such a significant portion of my time at CaRLa. In any case, our discussions, lunch meetings and work (whether digital or in-person) have brought me a lot of fun, inspiration and insights that will accompany me for years to come. Thank you, Alban, Chloe, Elena, Francesca, Frank, Juri, Patrizio, Philippe, Pilar, Saumya, Somnath, Viktoriia, and Wei!

As previously introduced, this is far from the only group that accepted me into their midst. I also want to thank the whole Comba group that has always made me feel welcome even though I could join them less than usual due to the many workplaces. The group activities, ski seminars and discussions were always interesting and fun. A special thank you to Dieter for helping me with the initial bureaucracy, Bodo for helping with information about the university IT systems, Saskia for doing the EPR measurements of the carbonylation project, and Patrick for starting to make the CaRLa theoretician chili a tradition.

Moreover, I want to thank the Quantum Chemistry group at BASF for their constant support and for showing me the high variety of projects that are carried out with quantum chemistry in an industrial context. The international nature of the group being in Ludwigshafen, Tarrytown, and Mumbai meant that the IT infrastructure was existing, that everyone was familiar with online (or at least hybrid) meetings and made the required transition to home office significantly easier. Even during this difficult time, the group has remained motivated to staying connected via digital meetings.

Furthermore, I am very grateful to BASF and Heidelberg University for setting up the Catalysis Research Laboratory in the first place. Without their funding and continued support, I would never have gotten the chance to experience the benefits of close collaboration between industrial and academic research.

Last but not least, I want to thank my family and friends that supported me not just while pursuing my PhD studies in the last three years, but also in getting to this point in the first place. Thank you!

QUANTENCHEMISCHE UNTERSUCHUNGEN IN DER HOMOGENEN KATALYSE: DEHYDRIERUNG, CARBONYLIERUNG UND VINYLIERUNG

Zusammenfassung

Diese Arbeit beschreibt detaillierte mechanistische Untersuchungen zu homogen-katalysierten Reaktionen mit engem Bezug zu industriellen Prozessen. Drei unterschiedliche Reaktionsklassen wurden mittels Dichtefunktionaltheorie untersucht: Dehydrierung, Carbonylierung und Vinylierung. Hierbei wurden alle Projekte in einer Umgebung durchgeführt, in welcher die Experimente und Berechnungen im kontinuierlichen Austausch standen, um die Qualität, Genauigkeit und Effizienz der Forschungsarbeit zu gewährleisten.

Zuerst werden die Untersuchungen zu der dehydrierenden Kupplung von Alkoholen zu Estern beschrieben. Die aktive Form des häufig verwendeten Ru-MACHO Katalysator, für welchen in vorherigen Arbeiten die Zersetzung bei katalytischen Bedingungen gezeigt wurde, konnte stabilisiert werden und führte, basierend auf der Wahl des eingesetzten Phosphans, zu zwei unterschiedlichen Strukturmotiven. Beide gebildeten Komplexe sind ebenfalls Katalysatoren für basenfreie (De-)Hydrierungsreaktionen. Die quantenchemischen Berechnungen konnten hierbei tiefgehende Informationen zum Reaktionsmechanismus und Erklärungen für die unterschiedlichen Struktur motive aufzeigen.

Die Arbeiten über die Carbonylierung von Alkoholen zu Carbonsäuren wurden in zwei Projektabschnitten durchgeführt. Anfangs wurde ein Ni-basiertes Katalysatorsystem für Phenylethanol entwickelt, welches als Modell für die Ibuprofen-Synthese dient. Nachdem die computergestützten Untersuchungen Einblicke in zwei parallel ablaufende Reaktionsmechanismen und in die Rolle des LiI-Additivs ermöglichte, wurde der Anwendungsbereich der Reaktion auf Produkte der Koch-Carbonylierung erweitert. Obwohl auch diese Reaktion erfolgreich durchgeführt werden konnte, deuteten die experimentell beobachteten Selektivitäten und verschiedene Kontrollexperimente auf einen anders gearteten Reaktionsmechanismus hin. Mit Hilfe der zweiten ausführlichen mechanistischen Untersuchung konnte erneut ein tiefgehendes Verständnis der zu Grunde liegenden Prozesse erreicht werden.

Abschließend werden die Untersuchungen zur Vinylierung von Pyrrolidon zu *N*-Vinylpyrrolidon berichtet, welche unter Verwendung von einfachen Phosphanen als Organokatalysatoren und direkter Verwendung von Acetylen gas bei niedrigem Druck erreicht werden konnte. Die durchgeführten DFT-Rechnungen wurden dazu genutzt den Reaktionsmechanismus sowie eine Vielzahl an Neben- und Zersetzungsreaktionen besser zu verstehen. Mit Hilfe der experimentellen und theoretischen Ansätze konnte außerdem eine Wittig-artige Modifikation der Reaktion erarbeitet werden, in welcher Carbonylverbindungen mit dem intermediär gebildeten Ylid reagieren.

QUANTUM CHEMICAL INVESTIGATIONS IN HOMOGENEOUS CATALYSIS: DEHYDROGENATION, CARBONYLATION AND VINYLATION

Abstract

This thesis describes in-depth mechanistic investigations of homogeneously catalyzed reactions with industrial relevance. Three different reaction classes were studied with the means of density functional theory: dehydrogenation, carbonylation and vinylation. All projects were carried out in a highly integrated framework with continuous exchange between experimental and computational efforts to achieve a high level of accuracy and efficiency.

Firstly, the investigations on the dehydrogenative coupling of alcohols to esters are described. The frequently used Ru-MACHO catalyst was shown to undergo degradation after base-induced activation of the pre-catalyst. Attempts to stabilize the highly active species were successful and were shown to lead to two different structural motifs based on the employed phosphine, both of which are active catalysts in base-free (de-)hydrogenation reactions. Quantum-chemical calculations were employed to gain insights into the phosphine-dependent behavior as well as the reaction mechanism.

Secondly, the carbonylation of alcohols to carboxylic acids was explored in two project phases. The initial investigation focused on employing Ni complexes and simple phosphine ligands for the transformation of phenyl ethanol as a model compound for ibuprofen. After the computational studies had provided insights into a combination of two reaction mechanisms, which explain the experimental observations and the crucial role of LiI as an additive, the scope was expanded to tertiary Koch-type carbonylation targets. While the desired conversion for these systems was achieved, the observed selectivities and control experiments clearly indicated that different reaction pathways are responsible for the observed conversion. A second set of quantum-chemical investigations was able to provide relevant information about this adapted reaction mechanism and helped to evaluate the catalytic system.

Finally, the vinylation of pyrrolidone to *N*-vinylpyrrolidone was investigated, which was achieved by phosphine organocatalysis and direct employment of acetylene gas at low pressure. The DFT calculations were used to explain the mechanistic details of the reaction as well as to evaluate several side reactions and degradation pathways. The methods were also able to support a modification of the reaction that employs suitable carbonyl compounds to perform Wittig-type reaction steps after the initial formation of an ylide intermediate.

Previous Publications and Patents

Several projects covered in this thesis have been published in or submitted to peer-reviewed academic journals over the past three years. Additionally, a patent application was filed for the phosphine-catalyzed vinylation methodology.

DEHYDROGENATIVE COUPLING OF ALCOHOLS TO ESTERS

Daniel J. Tindall,[#] Maximilian Menche,[#] Mathias Schelwies, Rocco Paciello, Ansgar Schäfer, Peter Comba, Frank Rominger, A. Stephen K. Hashmi, and Thomas Schaub, Ru⁰ or Ru^{II}: A Study on Stabilizing the “Activated” Form of Ru-PNP Complexes with Additional Phosphine Ligands in Alcohol Dehydrogenation and Ester Hydrogenation, *Inorganic Chemistry* **2020**, 59(7), 5099 – 5115. DOI: [10.1021/acs.inorgchem.0c00337](https://doi.org/10.1021/acs.inorgchem.0c00337)

CARBONYLATION OF ALCOHOLS TO CARBOXYLIC ACIDS

Sara Sabater,[#] Maximilian Menche,[#] Tamal Ghosh, Saskia Krieg, Katharina S. L. Rück, Rocco Paciello, Ansgar Schäfer, Peter Comba, A. Stephen K. Hashmi, and Thomas Schaub, Mechanistic Investigation of the Nickel-Catalyzed Carbonylation of Alcohols. *Organometallics* **2020**, 39(6), 870-880. DOI: [10.1021/acs.organomet.0c00082](https://doi.org/10.1021/acs.organomet.0c00082)

Niels Lichtenberger,[#] Maximilian Menche,[#] Katharina S. L. Rück, Rocco Paciello, Ansgar Schäfer, Peter Comba, A. Stephen K. Hashmi, and Thomas Schaub, Revisiting Nickel-Catalyzed Carbonylations: Unexpected Observation of Substrate-dependent Mechanistic Differences. *manuscript in preparation* **2021**.

VINYLATION OF PYRROLIDONE TO N-VINYLPYRROLIDONE

Nikolai Sitte,[#] Maximilian Menche,[#] Pavel Tužina, Frank Bienewald, Ansgar Schäfer, Peter Comba, Frank Rominger, A. Stephen K. Hashmi, and Thomas Schaub, Phosphine-catalyzed Vinylation at Low Acetylene Pressure. *The Journal of Organic Chemistry* **2021**, *manuscript accepted*.

Thomas Schaub, Pavel Tužina, Nikolai Sitte, Maximilian Menche, Frank Bienewald, A. Stephen K. Hashmi, Synthesis of N-vinyl compounds by reacting NH-compounds with acetylene in presence of homogeneous phosphine catalyst. EP21174651, **2021** (Priority Date: 19.05.2021).

[#] these authors contributed equally.

Table of Contents

1 Introduction	1
2 Theoretical Background	7
2.1 The Electronic Problem	7
2.1.1 The Born-Oppenheimer Approximation.....	8
2.1.2 The Variational Principle and Hartree Product.....	9
2.1.3 The Hartree-Fock Theory	11
2.1.4 Linear Combination of Atomic Orbitals and Basis Sets.....	12
2.2 Density Functional Theory.....	16
2.2.1 The Hohenberg-Kohn Theorems	16
2.2.2 The Kohn-Sham Approach.....	18
2.2.3 Development of Density Functionals	19
2.2.4 Resolution of Identity Approximation	21
2.2.5 Dispersion Corrections	22
2.2.6 Thermodynamic Corrections.....	24
2.2.7 Solvent Corrections	25
2.2.8 Relativistic Effects.....	27
2.3 Methodology.....	29
2.3.1 Geometry Optimization.....	30
2.3.2 Single Point Energies	31
2.3.3 Investigation of Reaction Pathways	32
3 Dehydrogenative Coupling of Alcohols	37
3.1 Motivation	37
3.2 Computational Details	43
3.3 Results and Discussion	44
3.3.1 Rationalization of the Observed Chemoselectivities.....	44
3.3.2 Noyori-type Dehydrogenation Pathway.....	53
3.3.3 Dub-type Dehydrogenation Pathway.....	56
3.3.4 Other Investigated Dehydrogenation Pathways.....	63
3.3.5 Investigation of Ligand Dissociation to Enable Further Reactivity	69
3.3.6 Catalytic Cycle for Alcohol-Aldehyde Coupling.....	73

3.4 Summary and Outlook	79
4 Carbonylation of Alcohols	83
4.1 Motivation	83
4.2 Computational Details	89
4.3 Carbonylation of Phenyl Ethyl Alcohol.....	90
4.3.1 Neutral Reaction Pathways.....	90
4.3.2 Anionic Reaction Pathways	100
4.3.3 Catalytic Pathways with other Phosphine Ligands	105
4.3.4 Investigation of Potentially Interfering Side Reactions.....	111
4.3.5 Summary and Outlook	117
4.4 Carbonylation of <i>tert</i> -Butyl Alcohol.....	120
4.4.1 Investigation of Previously Established Catalytic Cycles.....	122
4.4.2 Isobutene-based Reaction Pathways.....	128
4.4.3 Summary and Outlook	153
4.5 Summary and Outlook	156
5 Vinylation of Pyrrolidone	157
5.1 Motivation	157
5.2 Computational Details	162
5.3 Results and Discussion	163
5.3.1 Investigation of a Nucleophilic Reaction Mechanism.....	163
5.3.2 Investigation of the Reppe-type Mechanism.....	181
5.3.3 Wittig-type Extended Schweizer Reaction	184
5.4 Summary and Outlook	193
6 Summary and Outlook	195
7 Appendix.....	201
7.1 Dehydrogenative Coupling of Alcohols.....	201
7.2 Carbonylation of Alcohols.....	205
7.3 Vinylation of Pyrrolidone.....	212
8 References.....	217

List of Abbreviations

API	Active Pharmaceutical Ingredient
B3LYP	Exchange-Correlation GGA Functional Developed by Becke, Lee, Yang, and Parr
BDE	Bond Dissociation Energy
BP86	Exchange-Correlation Hybrid Functional Developed by Becke and Perdew
CaRLa	Catalysis Research Laboratory
CASPT2	Multireference Complete Active Space Perturbation Theory
CCDC	Cambridge Crystallographic Data Centre
CNN (ligand)	Tridentate Ligand with Bridged Carbon-Nitrogen-Nitrogen Donor Atoms
COD (ligand)	Cyclooctadiene
COSMO	Conductor-Like Screening Model
COSMO-RS	Conductor-Like Screening Model for Real Solvents
Cy	Cyclohexyl (Group)
def2-QZVPP	Quadruple-Zeta Basis Set Developed by Ahlrichs and Co-workers
def2-SV(P)	Double-Zeta Basis Set Developed by Ahlrichs and Co-workers
DFT	Density Functional Theory
DMAA	Dimethylacetamide
DMF	Dimethylformamide
DZ	Double-Zeta Basis Set
ECP	Effective Core Potential
EPR	Electron Paramagnetic Resonance (Spectroscopy)
<i>fac</i>	<i>facial</i>
GEA	Gradient Expansion Approximation
GGA	Generalized Gradient Approximation
GTO	Gaussian Type Orbital
HF	Hartree-Fock
<i>i</i> Bu	<i>iso</i> -Butyl (Group)
<i>i</i> Pr	<i>iso</i> -Propyl (Group)
IR	Infrared (Spectroscopy)
IRC	Intrinsic Reaction Coordinate
LCAO	Linear Combination of Atomic Orbitals
LDA	Local Density Approximation
MACHO (ligand)	Bis[2-(diphenylphosphino)ethyl]amine (PNP Ligand)
MD	Molecular Dynamics

Me	Methyl (Group)
MEK	Methyl Ethyl Ketone
<i>mer</i>	<i>meridional</i>
MLA	Metal-Ligand Assisted
MLC	Metal-Ligand Cooperation
MRCI	Multireference Configuration Interaction
<i>n</i> Bu	<i>n</i> -Butyl (Group)
NHC (ligand)	N-Heterocyclic Carbene
NMR	Nuclear Magnetic Resonance (Spectroscopy)
NVP	N-Vinylpyrrolidone
PBE0	Exchange-Correlation Hybrid Functional Developed by Purdue, Burke, and Enzerhof
PES	Potential Energy Surface
Ph	Phenyl (Group)
PNN (ligand)	Tridentate Ligand with Bridged Phosphorous-Nitrogen-Nitrogen Donor Atoms
PNP (ligand)	Tridentate Ligand with Bridged Phosphorous-Nitrogen-Phosphorous Donor Atoms
PVP	Polyvinylpyrrolidone
QZ	Quadruple-Zeta Basis Set
RI	Resolution of Identity Approximation
Ru-MACHO	Commercially Available Ru-PNP Complex Developed by Takasago (see MACHO)
SNS (ligand)	Tridentate Ligand with Bridged Sulfur-Nitrogen-Sulfur Donor Atoms
STO	Slater Type Orbital
SV	Split-Valence (Basis Set)
SZ	Single-Zeta Basis Set
TBP	Tri- <i>n</i> -butylphosphine
<i>t</i> Bu	<i>tert</i> -Butyl (Group)
TEP	Tolman Electronic Parameter
TP	Triple-Zeta Basis Set
TS	Transition State
TZV	Triple-Zeta Split-valence Basis Set

1

Introduction

The key concept of catalysis is enabling a desired chemical transformation by addition of one or more components called catalyst to a reaction system, which could not or only slowly achieve the transformation without this catalyst at the given conditions. These additional components allow the access to alternative and more feasible reaction pathways with lower activation barriers that provide an easier, faster, more selective or even the sole access to the desired reaction product while the catalyst is regenerated after use (see Figure 1.1). This allows for small amounts of the catalyst being able to drive a reaction to full conversion and multiple time use of the catalytic components called recycling. While many facets of catalysis play a role in various aspects of our lives – from enzyme-catalyzed processes in all living organisms to the large-scale production of chemicals with heterogeneous catalysts – this thesis is directed towards the use of homogeneous catalysis. In homogeneous catalysis, molecular species are employed, which can often be more precisely defined and adapted to the own requirements than the erratic structure of surfaces in heterogeneous catalysis. Thus, this approach is often chosen to develop chemo- or stereoselective systems. In this field, highly versatile species like transition metal complexes are commonly used, which enable many different modes of coordination and therefore have the potential to provide access to complex reaction pathways that afford the sought-after transformations at low activation energies. While this versatility can lead to the targeted reactivity, it can also lead to a variety

of undesired side reactions, that lower the applicability of the developed experimental procedure. Thus, it can significantly improve the development of catalysts to identify and understand the underlying key steps of the desired chemical transformation and of any competing reaction pathways. The general knowledge of reaction mechanisms and the capabilities of different reactive species cannot just lead to direct improvements in the investigated reaction but can also significantly improve the identification of suitable catalyst systems in the first place. This understanding can lead to more economical and sustainable processes with improvements such as understanding and avoiding side product formation, removing reactants from the catalytic system altogether, or the use of more efficient catalysts. Similarly, some of the green chemistry principles focus on the same aspects of chemical processes and are aiming (amongst others) to use catalytic instead of stoichiometric reactions to prevent waste via a high atom-economy.¹⁻²

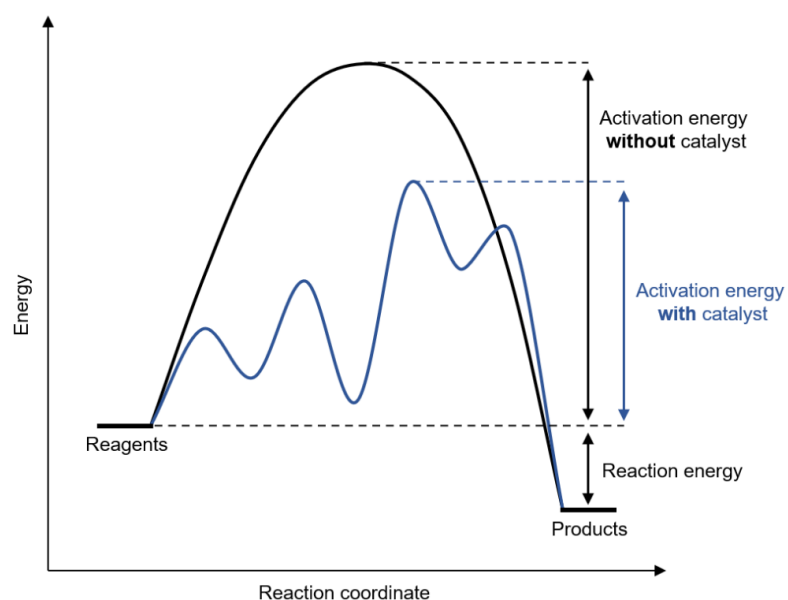


Figure 1.1: Generic potential energy surface for a reaction without catalyst (black) and with catalyst (blue) that lowers the activation energy by providing access to alternative reaction pathways.

However, this investigation of the reaction mechanism is far from being trivial. Due to the high reactivity of the intermediates involved in the reaction and the inherent instability of all transition states along the reaction pathway, experimental methods are usually limited to observing secondary properties and effects of the catalytic cycle. Similarly, the small sizes of chemical bonds of just a few ångströms and the short timescales of femto- or picoseconds of these molecular reaction steps makes it extremely difficult to gather experimental evidence or data, which help to identify the steps themselves, e.g., by spectroscopy. The experiments, that are most often carried out to gain insights into the reaction, are kinetic studies, where the rate of substrate depletion and product formation can be observed in dependence of several

variables like temperature, concentration, solvent, or pressure. Other methods include careful evaluation of the observed selectivities (e.g., radical clocks), by-products, trapped intermediates, and isotope labelling experiments or varying the employed substrates and components to indicate and identify key factors and pathways leading to the observed reactivity. In recent decades, a plethora of experimental methods has been developed to further increase the capabilities of mechanistic studies. However, even elaborate and time-consuming combinations of these experimental methods can often only give scarce indications on how the elementary steps of the reaction take place on an atomistic scale.

This is where quantum chemistry can provide an additional approach to mechanistic investigations. These studies enable the specific characterization of every single intermediate and transition state along the reaction coordinate and therefore are not limited to secondary properties of these steps, but can directly provide detailed information about the structures, energies and effects predominant in each of the atomistic transformations. Due to these capabilities, the field of computational chemistry has steadily strengthened its role in mechanistic investigations and has become a regularly deployed and valued tool especially in organometallic chemistry and catalysis. This growth can be explained by a combination of several factors: Firstly, computational methods have just been developed in recent decades, even though the theoretical foundation has been described significantly earlier in the seminal works by Erwin Schrödinger in 1926,³ by Douglas R. Hartree in 1928,⁴ and by Wladimir A. Fock in 1930.⁵ Further breakthroughs were only made decades later in the form of molecular orbital theory (linear combination of atomic orbitals) by Clemens C. J. Roothaan⁶ and George G. Hall⁷ in 1951 as well as the development of the foundation of density functional theory by Pierre Hohenberg, Walter Kohn and Lu Jeu Sham in 1964 and 1965. For his contributions, Walter Kohn was awarded the 1998 Nobel prize in chemistry together with John A. Pople, who has also made major contributions to the usability of quantum chemistry on computer systems. Pople is additionally well-known for starting the development of the Gaussian program suite,⁸ which has become one of the most popular quantum chemistry packages to date. In the last decades, the development of more efficient algorithms for the calculation of energies and gradients as well as for geometry optimizations and analytical second derivatives have significantly advanced the field. The implementation of the hybrid exchange-correlation functional B3LYP,⁹⁻¹¹ which at the time enabled achieving chemical accuracy for systems of relevant sizes, is a very prominent example for these developments. Since then, many more functionals and methods have been developed to further increase the accuracy and efficiency of density functional theory and computational chemistry in general. The second aspect, that has supported the continuous rise of computational chemistry, is the drastic increase in computational resources over the past decades. This is caused by the significant improvements in semiconductor technology and due to the higher priority of digitalization and computational approaches in chemical industry and in academic

institutions. The improvements in the performance of microchips, by an increase in the number of transistors on the microchip, are commonly described as Moore's law and state that the number of transistors doubles every two years.¹² The first commercially available Intel processor "Intel 4004" included 2,250 transistors in 1971. Just above ten years later in 1982, the new "Intel 80286" chip included 134,000 transistors representing a nearly 60-fold increase. Another decade later, in 1992, the transistor count of the "Intel i960CF" had already increased to 900,000 (400-fold increase compared to 1971) and Intel's newest processors with information available, the "Intel Xeon Platinum 8180" from 2017, includes 8 billion transistors on each chip. The newest AMD microprocessor from 2019, the "AMD Epyc Rome", raises this count to 39.5 billion transistors and shows an over seventeen-million-fold increase in transistor count relative to the original "Intel 4004". While this trend has been accurate for the past 50 years, Gordon E. Moore and other industry experts are currently debating on how long this increase can hold true. In any case, the field of quantum computing has already risen on the horizon and is being investigated as a potential breakthrough to further increase the available computing power.¹³ The rising importance of digitalization in the chemical industry can, in addition to personal experiences, press releases and scientific publications, be measured in the industry's investment into powerful supercomputers to drive these efforts. In 2017, BASF set up its supercomputer "Curiosity" with a performance of 1.75 quadrillion floating point operations per second, which joined the Top500 list of the most powerful supercomputers in the world on place 66 and currently represents the most powerful system in chemical industry.¹⁴ The capabilities of this new machine lay the foundation for the wide variety of different digitalization projects performed at BASF as well as for the calculations carried out as part of this PhD thesis.

These developments have led to a growing involvement of computational methods in various fields of chemistry. In the field of organometallic chemistry and its application directed toward homogeneous catalysis, quantum-chemical calculations have become a vital aspect of most mechanistic investigations over the last decades and are nowadays regularly employed either alone or in combination with experimental studies. The latter, where experimental and computational investigations are carried out in combination, is also the approach that is taken at the Catalysis Research Laboratory (CaRLa) in Heidelberg, a joint laboratory of Heidelberg University and the industrial partner, BASF, which mainly focuses on applying homogeneous catalysis in an industrial context. The computational work at CaRLa splits into multiple key tasks. Firstly, brief thermodynamic studies are employed to help with project evaluation. Even a few calculations can sometimes identify whether a project might be feasible or not and prevent the synthetic chemists from wasting valuable resources. Secondly, and this represents the most time-consuming aspect, detailed quantum-chemical mechanistic investigations are carried out in collaboration with the experimental chemists in order to gain insights into the concepts behind the reactions that are being developed. Lastly,

it is important to keep an eye on the latest developments in the scientific literature and new approaches in computational chemistry to keep the colleagues at CaRLa informed and identify methods that could significantly improve the day-to-day procedures in the framework of an academic-industrial collaboration such as CaRLa. In all three aspects, the close collaboration with the experimental colleagues is crucial to make sure that these different approaches can significantly benefit from each other. Therefore, computations suggesting further experiments as well as experiments guiding and validating calculations was part of the regular exchange and discussions.

In this thesis, three industrially relevant reactions and the corresponding approaches developed at CaRLa were studied computationally and are presented here: Firstly, the dehydrogenative coupling of alcohols to esters is discussed. While this is a well-established reaction, which can be performed with a variety of catalytic systems, the most prominent examples like the commercially available Ru-MACHO catalyst require a strong base for the activation of the system and tend to degrade under these harsh conditions. A method for the stabilization of the metal complex was supported by the calculations and the possibilities for alternative reaction pathways of the stabilized motifs were investigated. The second reaction studied is the carbonylation of alcohols to carboxylic acids, for which a catalytic system based on nickel iodide, simple phosphine ligands and lithium iodide (LiI) was developed. Density functional theory calculations were employed to provide understanding of the observed reactivity and to explain the drastic effect of LiI addition on reaction yields. The adaption of the catalytic system to further substrates revealed new substrate-dependent reaction pathways, which were subsequently investigated in another set of quantum-chemical calculations. Thirdly, the organocatalytic vinylation of pyrrolidone to *N*-vinylpyrrolidone was studied. Due to the simple phosphine catalysis in combination with the direct employment of acetylene gas at low-pressure conditions, this represents a highly interesting approach rivalling the currently industrially employed Reppe carbonylation process. The in-depth computational investigation was able to provide insights into the mechanistic pathways of the reaction as well as to help to understand side reactions that had lowered the feasibility of the reaction. Moreover, a Wittig-type reaction modification could be developed, which provides a further application for the methodology.

The research that was performed as part of this PhD thesis is computational but was – in line with the scientific concept of CaRLa and its partners – developed in close collaboration with my postdoctoral colleagues carrying out the experiments in the laboratory: Daniel J. Tindall for the dehydrogenative coupling of alcohols to esters, Sara Sabater, Niels Lichtenberger, and Tamal Ghosh for the carbonylation of alcohols to carboxylic acids, and Nikolai Sitte for the vinylation of pyrrolidone. Furthermore, these projects were also regularly discussed with the industrial collaborators to ensure the industrial applicability of the catalytic systems throughout the projects.

2

Theoretical Background

This chapter provides a brief introduction to the theoretical background and the methodologies, which lay the foundation for this work. Due to the high complexity of the applied methods, it can only provide a short overview of the most important concepts and approaches. For detailed information, please refer to the available literature¹⁵⁻¹⁸ and the publications cited within this chapter.

2.1 The Electronic Problem

In order to accurately and *ab-initio* calculate the properties of any given molecular system, the electronic structure of this system in terms of its wavefunction has to be fully known. This can be achieved by solving the non-relativistic, time-independent Schrödinger equation (Equation 2.1).

$$\hat{H}\Psi = E\Psi \quad (2.1)$$

Herein, Ψ is the non-observable wavefunction, which contains all information regarding the system. While Ψ itself is not observable, its squared modulus $|\Psi|^2$ describes the probability density of its particles. The Hamiltonian \hat{H} is a differential operator, which returns the energy

eigenvalue when used on the system. For a system containing N electrons and M nuclei, the Hamiltonian (in atomic units) can be written as:

$$\hat{H} = \underbrace{-\frac{1}{2} \sum_{i=1}^N \nabla_i^2}_{\hat{T}_e} - \underbrace{\frac{1}{2} \sum_{A=1}^M \frac{1}{M_A} \nabla_A^2}_{\hat{T}_N} - \underbrace{\sum_{i=1}^N \sum_{A=1}^M \frac{Z_A}{r_{iA}}}_{\hat{V}_{eN}} + \underbrace{\sum_{i=1}^N \sum_{j>i}^N \frac{1}{r_{ij}}}_{\hat{V}_{ee}} + \underbrace{\sum_{A=1}^M \sum_{B>A}^M \frac{Z_A Z_B}{R_{AB}}}_{\hat{V}_{NN}} \quad (2.2)$$

Hereby, the parameters r_{iA} , r_{ij} and R_{AB} are the electron-nucleus, electron-electron, and the interatomic nucleus-nucleus distances, respectively. M_A describes the mass of the nucleus A (due to atomic units in multiples of the mass of an electron) and Z_A and Z_B describe the nuclei charges. The terms \hat{T} describe the kinetic energy operators for the electrons (\hat{T}_e) and the nuclei (\hat{T}_N) and the Laplacian operators ∇_i^2 (in \hat{T}_e) and ∇_A^2 (in \hat{T}_N) are defined as the second derivatives with respect to the coordinates. Furthermore, the terms \hat{V} describe the potential energy operators. These are further split into electrostatic electron-nucleus attraction (\hat{V}_{eN}) and Coulomb repulsion between electrons (\hat{V}_{ee}) and nuclei (\hat{V}_{NN}).

2.1.1 The Born-Oppenheimer Approximation

The Born-Oppenheimer approximation significantly simplifies solving the Schrödinger equation.¹⁹ At its core, the Born-Oppenheimer approximation is based on the high mass difference of electrons and nuclei (1:1836) and assumes that the treatment of the nuclei as stationary will only result in a minor and negligible energy change due to the significant difference in electron and nuclei movements. This approach leads to the fact that the electronic and nuclear parts of the Hamiltonian can be separated. In the electronic part, the term for the kinetic energy of the nuclei (\hat{T}_N) can be omitted and the nucleus-nucleus repulsion term (\hat{V}_{NN}) remains constant. The electronic part of the separation is also described as the electronic Hamiltonian \hat{H}_{elec} , which is used in the electronic Schrödinger equation (see Equations 2.3 and 2.4).

$$\hat{H}_{elec} = \hat{T}_e + \hat{V}_{eN} + \hat{V}_{ee} \quad (2.3)$$

$$\hat{H}_{elec} \Psi_{el} = (\hat{T}_e + \hat{V}_{eN} + \hat{V}_{ee}) \Psi_{el} \quad (2.4)$$

The total energy of the system (E_{total}) results as the sum of the electronic energy E_{el} and the constant nuclei potential \hat{V}_{NN} (Equation 2.5). The following chapters focus on the electronic problem at hand; therefore Ψ_{elec} will be abbreviated as Ψ for easier readability.

$$E_{total} = E_{el} + \sum_{A=1}^M \sum_{B>A}^M \frac{Z_A Z_B}{R_{AB}} = E_{el} + \hat{V}_{NN} = E_{el} + E_{nuc} \quad (2.5)$$

To determine the eigenvalues E_i and the corresponding eigenfunctions Ψ_i , the eigenvalue problem of the electronic Schrödinger equation has to be solved. The exact solution of this problem is only possible for very small (one-electron) systems, e.g., the hydrogen atom, while all bigger systems lead to many-body problems of the electron-electron Coulomb interactions and thus must be solved with approximative methods, which are based on the optimization of the ground state wavefunction in a mean-field approach. This says that every electron is moving in a mean field of all other electrons of the system. The approaches discussed in this thesis are, in principle, so-called *ab-initio* methods because they solely rely on fundamental physical constants as opposed to semi-empirical methods or most of molecular dynamics, which are also commonly used in computational chemistry. However, it should be noted that many density functional theory functionals or corrections include empirical components.

2.1.2 The Variational Principle and Hartree Product

The variational principle describes a method to optimize a ground state wavefunction. It postulates that an energy expectation value E_{test} of the Hamiltonian, for any guessed wavefunction Ψ_{test} , sets an upper limit for the real ground state energy E_0 , which is connected to the real ground state wavefunction Ψ_0 (see Equation 2.6). Consequently, E_{test} and E_0 can only match if Ψ_{test} and Ψ_0 are identical as well.

$$\langle \Psi_{test} | \hat{H} | \Psi_{test} \rangle = E_{test} \geq E_0 = \langle \Psi_0 | \hat{H} | \Psi_0 \rangle \quad (2.6)$$

Therefore, the ground state wavefunction could be attained if every N -electron wavefunction was investigated (see Equation 2.7).

$$E_0 = \min_{\Psi \rightarrow N} E[\Psi] = \min_{\Psi \rightarrow N} \langle \Psi | \hat{T}_e + \hat{V}_{eN} + \hat{V}_{ee} | \Psi \rangle \quad (2.7)$$

Due to the infinite possibilities for incremental steps, the investigation of every function is clearly not possible, but has to be limited to a subgroup of functions, which subsequently limits the result to an approximation of the real ground state energy as well (apart from the highly unlikely case that the real wavefunction is part of the investigated subgroup). Multiple approaches exist to further simplify solving such a multiple electron system. The following is based on the separation of the N -electron wavefunction into N one-electron wavefunctions $\chi_i(\vec{x}_1)$, which are called spin orbitals.

$$\chi_i(\vec{x}_1) = \phi_i(\vec{r}) \cdot \sigma_i(s) \quad (2.8)$$

Herein, every one-electron wavefunction is made up by the spatial part $\phi_i(\vec{r})$ and the spin part $\sigma_i(s)$ (see Equation 2.8). The simplest way to combine such a set of one-electron wavefunctions to one N -electron wavefunction is the Hartree product (Equation 2.9).

$$\Psi_{Hartree-Product}(x_1, x_2, \dots, x_N) = \chi_i(\vec{x}_1) \cdot \chi_j(\vec{x}_2) \cdot \dots \cdot \chi_k(\vec{x}_N) \quad (2.9)$$

This method comes with the major flaws that neither the indistinguishability of electrons (see Equation 2.10) nor the Pauli exclusion principle²⁰ (sometimes called antisymmetry principle, see Equation 2.11) are considered. The Pauli exclusion principle states that the sign of the wavefunction must change upon exchange of two electrons (x_1, x_2).

$$\Psi_{12}^{HP}(x_1, x_2) = \chi_i(\vec{x}_1) \cdot \chi_j(\vec{x}_2) \neq \chi_i(\vec{x}_2) \cdot \chi_j(\vec{x}_1) = \Psi_{21}^{HP}(x_1, x_2) \quad (2.10)$$

$$\Psi^{HP}(x_1, x_2) \neq -\Psi^{HP}(x_2, x_1) \quad (2.11)$$

The solution to this problem is the use of an antisymmetric product in the form of a so-called Slater determinant Φ_{SD} .²¹ The Slater determinant that represents an N -electron wavefunction as N electrons in N spin orbitals reads as follows:

$$\Phi_{SD} = \frac{1}{\sqrt{N!}} \begin{vmatrix} \chi_1(\vec{x}_1) & \chi_2(\vec{x}_1) & \cdots & \chi_N(\vec{x}_1) \\ \chi_1(\vec{x}_2) & \chi_2(\vec{x}_2) & \cdots & \chi_N(\vec{x}_2) \\ \vdots & \vdots & \ddots & \vdots \\ \chi_1(\vec{x}_N) & \chi_2(\vec{x}_N) & \chi_i(\vec{x}_N) & \chi_N(\vec{x}_N) \end{vmatrix} \quad (2.12)$$

In contrast to the preceding Hartree product, this Slater determinant takes the Pauli exclusion principle as well as the indistinguishability of electrons into account and establishes a suitable approximation for further use.

2.1.3 The Hartree-Fock Theory

The Hartree-Fock approximation is one of the central concepts of modern quantum chemistry and is used as a starting point for many high-level *ab-initio* methods.^{4,5} The initial approach of the Hartree-Fock approximation is the separation of the Hamiltonian into one-electron operators \hat{h} for each electron (depending on the mean field generated by all other $N - 1$ electrons). After the separation of the Hamiltonian \hat{H} into the one-electron operator \hat{h} , the latter is applied to the previously described Slater determinant to yield the Hartree-Fock energy (see Equation 2.13).

$$E_{HF} = \langle \Phi_{SD} | \hat{H} | \Phi_{SD} \rangle = \sum_i^N \langle i | \hat{h} | i \rangle + \frac{1}{2} \sum_i^N \sum_j^N \langle ii | jj \rangle - \langle ij | ji \rangle \quad (2.13)$$

This equation is comprised of the terms for the kinetic energy of the electrons in combination with the electron-nucleus interaction ($\langle i | \hat{h} | i \rangle$), the Coulomb integral ($\langle ii | jj \rangle$) and the exchange integral ($\langle ij | ji \rangle$; see Equations 2.14, 2.15 and 2.16, respectively).

$$\langle i | \hat{h} | i \rangle = \int \chi_i^*(\vec{x}_1) \left\{ -\frac{1}{2} \nabla^2 - \sum_A^M \frac{Z_A}{r_{1A}} \right\} \chi_i(\vec{x}_1) d\vec{x}_1 \quad (2.14)$$

$$\langle ii | jj \rangle = \int \int |\chi_i(\vec{x}_1)|^2 \frac{1}{r_{12}} |\chi_j(\vec{x}_2)|^2 d\vec{x}_1 d\vec{x}_2 \quad (2.15)$$

$$\langle ij | ji \rangle = \int \int \chi_i(\vec{x}_1) \chi_j^*(\vec{x}_1) \frac{1}{r_{12}} \chi_j(\vec{x}_2) \chi_i^*(\vec{x}_2) d\vec{x}_1 d\vec{x}_2 \quad (2.16)$$

Further consideration of these equations shows that correlation is only considered for electrons with the same spin quantum number, while the exchange integral ($\langle ij | ji \rangle$) is cancelling out for electrons with unequal spin. Because of the mean-field approach (*vide supra*), the resulting energy can only be an approximate solution. In accordance with the

variational principle, the resulting energy is higher than the real energy. The energy difference between this real energy and the approximate result is called correlation energy.

Typically, the Hamiltonian is rewritten in terms of the definition of effective one-electron operators, which are called Fock operators \hat{f} (see Equation 2.17).

$$\hat{H} = \sum_{i=1}^N \hat{f}(i) \quad \text{with } \hat{f}|X_i\rangle = \varepsilon_i|X_i\rangle \quad (2.17)$$

Furthermore, this leads to the definition of the Fock matrix \hat{F} that combines the one-electron operators in matrix form, and this nomenclature will be used in the following equations. For further information on the Fock matrix and the mathematical derivation, please refer to the theoretical chemistry literature and especially the detailed mathematical descriptions in “Modern Quantum Chemistry” by Attila Szabo and Neil S. Ostlund.¹⁵

While standalone Hartree-Fock theory is rarely applied in modern quantum chemistry, it has played an important role in the development of the currently applied methods. Moreover, it is commonly used to factor in amounts of exact Hartree-Fock exchange into functionals in density functional theory (see Section 2.2.3) or to generate initial guesses for more sophisticated calculations.

2.1.4 Linear Combination of Atomic Orbitals and Basis Sets

Despite all the previously discussed approximations, solving these equations is far from easy and represents a complex non-linear eigenvalue problem. Therefore, Clemens C. J. Roothaan and George G. Hall introduced the linear combination of atomic orbitals (LCAO), in which each molecular orbital is represented by such a linear combination (see Equation 2.18).⁶⁻⁷

$$\Psi_i = \sum_{\mu=1}^L c_{\mu i} \Phi_{\mu} \quad (2.18)$$

After several mathematical transformations, this enables the formulation of the Roothaan-Hall matrix equation:

$$\hat{F}C = \hat{S}Ce \quad (2.19)$$

with Fock matrix \hat{F} (see Equation 2.20) and overlap matrix \hat{S} (see Equation 2.21):

$$\hat{F}_{\mu\nu} = \langle \Phi_\mu | \hat{f}(i) | \Phi_\nu \rangle \quad (2.20)$$

$$\hat{S}_{\mu\nu} = \langle \Phi_\mu | \Phi_\nu \rangle \quad (2.21)$$

Matrix C represents the wavefunction and contains the linear combination coefficients $c_{\mu i}$ as matrix elements with each column vector representing one of the molecular orbitals. The solved diagonal matrix e contains the corresponding orbital energies. As the Roothaan-Hall equations depend on the orbitals themselves, the problem can only be solved iteratively: (1) Guessing initial coefficients C , (2) constructing of the Fock matrix \hat{F} , (3) solving the Roothaan-Hall equation through diagonalization and (4) variation of coefficients C and repeating from step 2 until convergence is reached.

The atomic orbitals/functions, that are combined in the LCAO approach, are also named basis functions, and a set of basis functions is consequently named a basis set. The choice of basis set is an important factor when carrying out quantum-chemical calculations. Regardless of whether this is a HF, DFT or even more computationally expensive post-Hartree-Fock calculation involving e.g., perturbation theory or coupled cluster theory, it can heavily influence the required computation time and accuracy. In theory, to perfectly reproduce the desired molecular orbital, a linear combination of an infinite number of atomic basis functions would be required. In reality, this needs to be trimmed to a finite number of basis functions that accurately enough represent the molecular orbital for the desired application and must find the balance between the high computational cost of many basis functions and the exactness of the approximation. While many types of functions could be used for these basis functions, they should ideally fulfill certain requirements. Firstly, it is preferred if these functions are chosen in a physically rational manner. Secondly, in line with the reasons given above, as few functions as possible should be used to replicate the molecular orbital. Thirdly, the quadratic integration should be as easy as possible as this mathematical operation represents a major part of the computational effort in the equations presented above. Finally, a systematic extension for larger basis sets and towards the basis set limit should be possible. Obviously, it is again extremely difficult to fulfill all these requirements in reality, and a balance between the various aspects needs to be found. In modern molecular quantum chemistry, two types of functions called Slater Type Orbitals (STOs)²² and Gaussian Type Orbitals (GTOs)²³ have become the most popular approaches. For periodic systems (in solid-state chemistry), plane wave basis sets are far more common as they inherently reproduce the periodicity of the chemical system.

Slater Type Orbitals (Φ_{STO}) are described by the following mathematical expression (in polar coordinates):

$$\Phi_{STO} = Nr^{n-1}e^{-\zeta r}Y_{l,m}(\vartheta, \varphi) \quad (2.22)$$

The orbitals are dependent on the quantum numbers (principal quantum number n ; azimuthal quantum numbers l and m), the normalization factor (N), spherical harmonic functions ($Y_{l,m}(\vartheta, \varphi)$) and Slater's orbital exponent (ζ). This exponent is dependent on the nuclear charge and can be calculated following Slater's rules.²² STOs fulfill the first requirement of suitable basis functions, which means that they represent physically plausible conditions. Due to the predominant $e^{-\zeta r}$ term (see Equation 2.21), the function approximately resembles the exponential decay of hydrogen-like atoms, and the basis function also satisfies the cusp conditions formulated by Kato, which state that at the core ($r = 0$) the electron density has a finite value.²⁴⁻²⁵ However, the integration of STOs (especially considering the complex three- and four-center integrals) is computationally difficult and thus, is expensive. This has led to the fact that STOs are mostly used for very small systems or for approximations, in which these multi-center integrals are not considered.

Gaussian Type Orbitals are a concept that was introduced for basis functions by Samuel Francis Boys in 1950 (see Equation 2.23).²³

$$\Phi_{GTO} = Nr^{2n-2-l}e^{-ar^2}Y_{l,m}(\vartheta, \varphi) \quad (2.23)$$

The stand-out difference of GTOs compared to STOs is the r^2 term in the exponential function. This consequently leads to a less rational description of the physical foundations. Firstly, the exponential decay is too steep for an accurate description and secondly, the cusp condition is no longer satisfied because the derivative of a Gaussian function is not a maximum, but zero at $r = 0$. These disadvantages can be counteracted by combining multiple Gaussian functions that overall depict the underlying physics more accurately and despite these problems, GTOs have managed to become the most widely used type of basis functions today. This is due to the original idea of Boys, which was to use this type of function because of their easier calculation of multi-center integrals based on the Gaussian product theorem, even when multiple Gaussian functions are used to reproduce the same physical robustness of STOs. The combination of Gaussian functions also coins one of the most prominent terms in basis set selection and modern quantum chemistry. In the smallest possible case, a single-zeta basis set (also single- ζ or SZ; referring to the Slater orbital exponent ζ), only one function is used for each atomic orbital (i.e., 1s, 2s, 2p, and so on

depending on the treated atom). In the other cases, where multiple functions are combined to provide a more accurate representation of the STO by GTOs, the terms double-zeta (two functions), triple-zeta (three functions), quadruple-zeta (four functions) or higher are used. As using multiple functions for every orbital in each atom of a large molecule can quickly lead to an explosion of the number of functions and therefore of the computational cost, the split-valence approach has been developed. In split-valence basis sets, denoted by a “V” in the name, e.g., TZV for triple-zeta split-valence basis set, only the valence electrons, which are crucial for chemical bonding, are described by multiple Gaussian functions, while all inner electrons are deemed less important and limited to a single-zeta basis set leading to a significant reduction in the required calculation time. Other often used additions to basis sets are the use of polarization functions and diffuse functions. Polarization functions are functions with a higher orbital angular momentum quantum number l (i.e., p-function for an s-orbital, d-function for a p-orbital, and so forth), which are added to the atoms to enable a higher angular flexibility with the goal of enabling a better description of bonding situations. Diffuse functions serve the same purpose but are, as the name suggests, more diffuse versions of the function with the same orbital angular momentum quantum number. These, in addition to the angular flexibility of polarization functions, increase the radial flexibility. In the past decades, a wide variety of GTO basis sets have been developed. Some of the best known are the 3-21G/6-31G/6-311G basis sets by Pople and co-workers,²⁶⁻³³ the correlation consistent basis sets by Dunning and co-workers (cc-pVXZ, where X denotes the number of basis functions per orbital, i.e., D for double, T for triple, ...),³⁴⁻³⁵ or the basis sets developed by Ahlrichs and co-workers in Karlsruhe.³⁶⁻⁴⁰ The modern Karlsruhe basis sets can usually be recognized by their naming starting with “def-“ or “def2-“ for the revised form and were used for the calculations performed as part of this thesis. The indication of polarization functions and diffuse functions varies significantly between each group of basis sets. In Pople basis sets, these are named with “+” for diffuse and “*” for polarization functions, while Dunning basis sets always include polarization functions and add diffuse functions with the prefix “aug-“ for “augmented with diffuse functions”. Karlsruhe basis sets indicate polarization functions with the letter “P”. Moreover, it should be noted that for the smallest Karlsruhe basis set, def2-SV(P), which was also used for the geometry optimizations in this thesis, “SV”, contrary to the naming introduced above, does not stand for a single-zeta split-valence basis set, but for a double-zeta split-valence basis set, where “SV” abbreviates “split-valence”. This is changed for the larger triple-zeta basis sets, which are denoted as def2-TZVP and so on. In accordance with the concept of split-valence basis sets described above, a single-zeta split-valence basis set would be nonsensical as it would not lead to a different description of inner and valence electrons but would simply correspond to a single-zeta basis set. Lastly, the indication of polarization function with “P” in brackets in the def2-SV(P) basis set expresses that these functions are only added to non-hydrogen atoms. The basis set def2-SVP that includes polarization functions on all atoms is equally available but was not used in this work.

2.2 Density Functional Theory

Apart from wavefunction-based methods for solving the Schrödinger equation, e.g., the previously discussed Hartree-Fock theory, density functional theory (DFT) provides a significantly different approach to solving the electronic structure of a given system. In accordance with its name, density functional theory, the energy is described as a functional of the system's electron density, which represents the key difference between DFT and wavefunction-based methods. Due to this approach, the N -electron wavefunction is replaced by the electron density $\rho(\vec{r}_1)$ (see Equation 2.24) leading to a reduced dimensionality of three (in opposite to $3N$ for Hartree-Fock theory). This leads to significantly faster calculations, especially when investigating larger systems and enables the full-size treatment of complex chemical systems in homogeneous catalysis (or other fields of research).

$$\rho(\vec{r}_1) = N \int \dots \int |\Psi(\vec{r}_1, \vec{r}_2, \dots, \vec{r}_N)|^2 d\vec{r}_2 \dots d\vec{r}_N \quad (2.24)$$

The spatial integral of the electron density $\rho(\vec{r}_1)$ results in the number of electrons N . The electron density can only have positive values at any given point in space and is zero for an unlimited distance to the nucleus (see Equation 2.25).

$$\int \rho(\vec{r}_1) d\vec{r}_1 = N \quad \text{and} \quad \rho(\vec{r} \rightarrow \infty) = 0 \quad (2.25)$$

2.2.1 The Hohenberg-Kohn Theorems

The two Hohenberg-Kohn theorems set the theoretical foundation for applied density functional theory.⁴¹ They describe the relationship between the ground-state energy and the electron density (first theorem) and provide a proof of concept for its optimization (second theorem).

Hohenberg-Kohn Theorem 1:

The external potential $V_{ext}(\vec{r})$ is an unambiguous functional of $\rho(\vec{r}_1)$; since $V_{ext}(\vec{r})$ determines the Hamiltonian \hat{H} , the ground-state of a multiple-electron system has to be an unambiguous functional of the electron density $\rho(\vec{r}_1)$.

In their first theorem, Pierre Hohenberg and Walter Kohn introduce the term ρ_0 , which incorporates the information about the number of electrons N , the nuclear charge Z_A and the nucleus-nucleus distance R_A (see Equation 2.26).

$$\rho_0 \Rightarrow \{N, Z_A, R_A\} \Rightarrow \hat{H} \Rightarrow \Psi_0 \Rightarrow E_0 \quad (2.26)$$

It follows:

$$E_0[\rho_0] = E_{eN}[\rho_0] + T[\rho_0] + E_{ee}[\rho_0] \quad (2.27)$$

$$E_0[\rho_0] = \underbrace{\int \rho_0(\vec{r}) V_{eN} d\vec{r}}_{\text{system dependent}} + \underbrace{T[\rho_0] + E_{ee}[\rho_0]}_{\text{universally valid}} \quad (2.28)$$

If one summarizes the universally valid components, which in their form are independent of N , R_A and Z_A , in the so-called Hohenberg-Kohn functional $F_{HK}[\rho_0]$, it follows:

$$E_0[\rho_0] = \int \rho_0(\vec{r}) V_{eN} d\vec{r} + F_{HK}[\rho_0] \quad (2.29)$$

However, the description of the kinetic energy $T[\rho_0]$ and the non-classical contributions of $E_{ee}[\rho_0]$ is not possible in an exact form and remains subject to approximations, which researchers around the globe are continuously trying to improve further to extend the applicability of DFT. Due to this, the development of various functionals for the correlation and exchange parts has led to major improvements in density functional theory and remains one of the main goals in DFT to date.

Hohenberg-Kohn Theorem 2:

The second Hohenberg-Kohn theorem states that to determine the ground-state energy the functional $F_{HK}[\rho_0]$ gives back the lowest possible energy precisely in the case, in which the density $\tilde{\rho}$ is equal to the real ground-state density ρ_0 (see Equation 2.30).

Thus, this Hohenberg-Kohn theorem is in accordance with the variational principle described above (see Equation 2.6) with the exception that it is not based on wavefunction methods but on the electron density.

$$E_0[\rho_0] \leq E[\tilde{\rho}] = T[\tilde{\rho}] + E_{ee}[\tilde{\rho}] + E_{eN}[\tilde{\rho}] \quad (2.30)$$

2.2.2 The Kohn-Sham Approach

One year after the Hohenberg-Kohn theorems, Walter Kohn and Lu Jeu Sham provided the method to apply these theorems.⁴² The two scientists provided a way to significantly simplify the description of the kinetic energy term, which was one of the main problems in DFT. This was achieved by their re-introduction of orbitals into density functional theory. Nonetheless, the non-classical portion of the electron-electron interactions $E_{nkl}[\rho(\vec{r})]$ remains described in a non-exact way, leading to an ongoing need for more accurate approximations. Together with the non-described parts of the kinetic energy $T_c[\rho(\vec{r})]$ and by taking the Coulomb repulsion $J[\rho(\vec{r})]$ into account, this results in the following general functional $F[\rho(\vec{r})]$:

$$F[\rho(\vec{r})] = T[\rho(\vec{r})] + E_{ee}[\rho(\vec{r})] = T_S[\rho(\vec{r})] + J[\rho(\vec{r})] + E_{XC}[\rho(\vec{r})] \quad (2.31)$$

$$E_{XC}[\rho(\vec{r})] = T_c[\rho(\vec{r})] + E_{nkl}[\rho(\vec{r})] \quad (2.32)$$

Similar to the previous equations for the Hartree-Fock approximation it is possible to establish these terms for the Kohn-Sham orbitals, which in the following are, for easier distinguishability, described as φ . The kinetic energy operator results as follows:

$$\hat{T}_S = -\frac{1}{2} \sum_i^N \langle \varphi_i | \nabla^2 | \varphi_i \rangle \quad (2.33)$$

The resulting total energy $E[\rho(\vec{r})]$ (see Equation 2.34) is, apart from the exchange-correlation energy $E_{XC}[\rho(\vec{r})]$, precisely determinable. Therefore, the exchange-correlation energy $E_{XC}[\rho(\vec{r})]$ is the collection of all non-exactly solvable terms (see Equation 2.32), and it has been and still is a major goal to find new methods and functionals to approximately solve this exchange-correlation energy.

$$E[\rho(\vec{r})] = T_S[\rho(\vec{r})] + J[\rho(\vec{r})] + E_{XC}[\rho(\vec{r})] + E_{eN}[\rho(\vec{r})] \quad (2.34)$$

One should note that the correlation effects are sometimes divided into dynamic and static correlation. Dynamic correlation describes the correlated movement of electrons, while the term static correlation is used for interactions between different electronic states. Electronic systems, in which capturing static correlation is crucial to obtain accurate results, usually cannot be appropriately described by DFT methods and will require multireference methods

like a multireference configuration interaction (MRCI) or a multireference complete active space perturbation theory (CASPT2).

2.2.3 Development of Density Functionals

Although density functional theory is a very concise and theoretically well described theory, it has a major flaw: In contrast to Hartree-Fock or other high-level *ab-initio* methods (e.g., Coupled-Cluster or perturbation theory) there is no systematic way to improve DFT functionals. Although there are different approaches or steps if one chooses to climb Jacob's ladder of density functional theory⁴³⁻⁴⁴, which are generally regarded as more capable, different approaches and functionals remain in use to date as each has its strengths and weaknesses. Therefore, it is often necessary to perform detailed benchmark studies to choose an appropriate computational method, which fits the specific field and questions that are being addressed in the project. Such a study was also performed in our group, in which Marko Hermesen has benchmarked various computational methods for the use in transition metal-based homogeneous catalysis.⁴⁵ Jacob's ladder of DFT comprises a steadily increasing number of steps with increasing computational cost and, possibly, accuracy. Generally, the approaches towards method development in DFT are split into two communities, systematic or empirical improvement of functionals. The former is keen to stick to the underlying physical principles and try to improve the approximations for said physical foundation, while the latter are willing to miss out on physical interpretability for better energetical performance, producing more accurate geometries or accurately representing the underlying wavefunction (e.g., for predicting and validating spectroscopic data).

Local Density Approximation (LDA):

The most basic approach is the Local Density Approximation (LDA). In this case the inhomogeneous electron density of the molecules is described by a collection of homogeneous density areas, which only represents a very rough approximation for a real chemical system. While the exchange energy for a homogeneous electron gas is analytically known and can be applied to these areas, this is not the case for the correlation energy, and various correlation functionals have been developed. Prominent examples of this group are the VWN functional by Vosko, Wilk and Nusair⁴⁶ and the PW92 functional by Perdew and Wang.⁴⁷ LDA calculations typically result in structures in moderately good agreement with experimentally observed structural data but entail a significant error in energy (especially considering the exchange term).

Generalized Gradient Approximation (GGA):

The next significant step was the introduction of the Generalized Gradient Approximation (GGA)⁴⁸⁻⁵⁰ which followed the low success of the Gradient Expansion Approximation (GEA).⁴¹ The concept of GEA is the logical expansion of LDA theory, which treats the

systems exclusively as a collection of homogeneous areas and adds density gradients to the collection of these homogeneous density spots. This approach has significant problems with the description of the exchange-correlation hole function, which was improved in the subsequently developed GGA functionals. At this point the split into systematic, at this time mostly represented by Perdew,⁵¹ and empirical method development, e.g., by Becke,⁹ occurred. The systematic method development community has approached these problems with the description of the exchange-correlation hole function by trimming the badly described parts to achieve physically rational conditions. On the other hand, the teams of the empirical method development community took a different approach and did not strictly adhere to physical rationale as long as the resulting functional provides more accurate results. Instead of developing completely new functionals that replace the previous LDA methods, the GGA approaches are achieving their improvements by applying corrections or scaling to the LDA energies. Well-known examples for this step of Jacob's ladder were developed by Becke,⁹ by Lee, Yang and Parr (BLYP)¹⁰ or by Perdew, Burke and Ernzerhof (PBE).⁵² While details are clearly functional-dependent, the group of GGA functionals generally tends to slightly overestimate bond lengths.

meta-GGA:

The GGA approach can be further extended by including the second derivative of the electron density (“curvature”). This is known as meta-Generalized Gradient Approximation (meta-GGA) and is achieved either with the Laplacian of the electron density ($\Delta\rho(r)$) or more-commonly with the kinetic energy density τ (see Equation 2.35).

$$\tau(r) = \frac{1}{2} \sum_i |\nabla X_i(r)|^2 \quad (2.35)$$

A prominent example of this group is the functional developed by Tao, Perdew, Staroverov and Scuseria, which in the common fashion of DFT is more known for its abbreviation (comprised of the initials of the developers): TPSS.⁵³ Furthermore, there are meta-hybrid functionals that combine the approaches of meta-GGA and hybrid functional methods (see the following section). Most prominently, this includes the set of Minnesota functionals developed by Donald G. Truhlar and co-workers, also known by their abbreviations M06(-2X)⁵⁴⁻⁵⁵ or M11 (further including range separation).⁵⁶

Hybrid Functionals:

In the next step, Becke was a major contributor to one of the most important developments in density functional theory: the introduction of Hartree-Fock/DFT hybrid functionals. The

foundation of these functionals is the treatment of the exchange part with the exact equations of Hartree-Fock theory (see Equation 2.36).

$$E_{XC}^{Hybrid} = (1 - a_x)E_X^{GGA} + a_x E_X^{HF} + E_C^{GGA} \quad (2.36)$$

However, while full treatment of the exchange with HF led to worse results (i.e., $a_x = 1$), Becke continued by empirically fitting the percentage of exact HF exchange against sets of molecules to determine the best set of parameters.¹¹ This subsequently led to the best-known and probably most applied density functional to date, the combination of Becke's exchange functional and the correlation functional by Lee, Yang and Parr, best known by its abbreviation B3LYP.⁹⁻¹¹ It was the first functional, which achieved chemical accuracy, meaning that the accuracy of the method is high enough in order to differentiate between reaction pathways and their respective relative energies in closed-shell systems. This is usually regarded as an accuracy of 1 kcal mol⁻¹ (= 4.2 kJ mol⁻¹). Even though other functionals in the wide range of available methods have caught up (or significantly surpassed this functional) in respect to energetical accuracy, B3LYP remains one of the most used density functionals to date due to its well tested performance in thousands of studies that paint a clear picture of its strengths and flaws.⁵⁷⁻⁵⁸

Double Hybrid Functionals:

More recently, the introduction of double hybrid functionals has further extended on the concept of combining multiple methods to achieve the most accurate results. For example, the double hybrid functionals by Stefan Grimme and co-workers combine the previously used mix of HF and DFT terms with an additional portion of Møller-Plesset perturbation theory correlation, which provided a significant improvement in accuracy over other hybrid functionals.⁵⁹

2.2.4 Resolution of Identity Approximation

Despite these continuous developments for more efficient and accurate density functionals, the increasing computing power (see Chapter 1) and the two-step approach usually applied in quantum-chemical investigations (see Chapter 2.3), the calculations of full-size transition metal complexes, especially when hundreds of calculations are needed for an in-depth mechanistic investigation, is still costly. A significant part of the computational effort is attributed to solving the two-electron four-center integrals (see Equation 2.37), which are part of the Coulomb ($\langle\langle ii|jj \rangle\rangle$; see Equation 2.15) and exchange ($\langle\langle ij|ji \rangle\rangle$; see Equation 2.16) parts of the Hartree-Fock energy equation.

$$\langle \alpha\beta | \mu\nu \rangle \quad (2.37)$$

An approach to reduce the time required for this step is the so-called resolution of identity approximation (RI), which is relying on auxiliary basis sets (see Equation 2.38).^{40,60-63}

$$|\mu\nu\rangle \approx \sum_i c_i |\varphi_i\rangle \quad (2.38)$$

These auxiliary basis sets are specifically chosen so that they fulfill the identity operator in the limit of a complete basis (also leading to the choice of name: “resolution of identity”).

$$\sum_i |\varphi_i\rangle \langle \varphi_i| \approx 1 \quad (2.39)$$

Based on these requirements, the RI method as an approximation for $\langle \alpha\beta | \mu\nu \rangle$ can be written as:

$$\langle \alpha\beta | \mu\nu \rangle \approx \sum_i \sum_j c_i c_j \langle \alpha\beta | \varphi_i \rangle \langle \varphi_i | \varphi_j \rangle^{-1} \langle \varphi_j | \mu\nu \rangle \quad (2.40)$$

Therefore, the original two-electron four-center integral $\langle \alpha\beta | \mu\nu \rangle$ is effectively reduced to multiple three-center integrals $\langle \alpha\beta | \varphi_i \rangle$ and $\langle \varphi_j | \mu\nu \rangle$, which overall are significantly faster to solve. The coefficients included in the auxiliary basis sets (c_i, c_j) must be defined during method development and are optimized to reduce the resulting error. For the above-mentioned complete basis, the RI approximation would be exact, however, this is not possible, and the use of the method usually entails an error of around 0.1 kJ mol⁻¹. This deviation is significantly lower than the accuracy of most DFT methods (especially considering various correction terms) and can therefore be neglected, while the calculation speed-up obtained from the approximation is far more significant.⁶⁴

2.2.5 Dispersion Corrections

One of the main problems of DFT is its insufficient description of dispersion. Dispersion is a major part of the van der Waals interactions that are caused by temporary fluctuations of the electron density. These fluctuations cause a temporary dipole moment within the molecules,

which consequently can induce a similar dipole in a second interacting molecule. Although these interactions are generally weak and significantly weaker than any covalent bonds within the molecules itself, there are many van der Waals interactions and the sum of these small values can add up to a significant error. Neglect of these interactions introduces an additional error into the calculations, which adds to other errors caused by previous approximations. In some cases, this error can lead to a qualitatively wrong description of the chemical system, e.g., in the case of long-chain alkanes, which due to the dispersion interactions exhibit a folded instead of a linear configuration that is only predicted to be more stable by DFT if dispersion is taken into account. Mathematically, dispersion interactions are generally described as an attractive potential with an $\frac{1}{r^6}$ term (see Equation 2.41).⁶⁵⁻⁶⁷

$$U \sim \frac{1}{r^6} \quad (2.41)$$

In many cases, empiric corrections are used to correct for the effects of dispersion that are not included in Kohn-Sham DFT. These energy corrections are added to the original DFT energy (see Equation 2.42). This is also the approach used in the widely applied D2⁶⁸ and D3⁶⁹⁻⁷¹ dispersion correction methods as well as in the more recent D4 model⁷²⁻⁷³ developed by Stefan Grimme and co-workers in Bonn. The D3 correction was used as part of this thesis.

$$E = E_{DFT} + E_{Dispersion} \quad (2.42)$$

Other approaches exist that directly include dispersion terms into the functionals instead of applying a correction term, but these methods are not further discussed here. The dispersion energy in Grimme's approach is given as the sum of atom-pairwise interaction energies (see Equation 2.43).

$$E_{Dispersion} = -s_6 \sum_{i=1}^{N-1} \sum_{j=i+1}^N \frac{C_6^{ij}}{R_{ij}^6} f_{damp}(R_{ij}) \quad (2.43)$$

In this equation, i and j are two atoms that build an interacting pair, which has an interatomic distance of R_{ij} . The dispersion energy is additionally affected by the scaling factor s_6 , the pair dependent dispersion coefficient C_6^{ij} and the damping function $f_{damp}(R_{ij})$ that is also dependent on R_{ij} . A commonly used damping function, which was also used in this thesis, is the Becke-Johnson damping function.⁷⁴

2.2.6 Thermodynamic Corrections

All the previously discussed energies are electronic energies obtained directly from the *ab-initio* calculation and the discussed correction terms. However, the desired thermodynamic quantity in computational chemistry is often the Gibbs free energy (G), which is comprised of additional thermal contributions (see Equation 2.44).

$$G = H - T \cdot S = E_{elec} + \Delta H_{therm} - T \cdot S \quad (2.44)$$

One should note that another correction for the solvation is usually also applied. However, this is a free energy term and can therefore directly be added to the Gibbs free energy given above. The use of solvation corrections is discussed in Section 2.2.7. ΔH_{therm} itself is a combination of four parts: the zero-point vibrational energy ($E_{zero-point}$) and the translational (E_t), rotational (E_r) and vibrational (E_v) contributions to the enthalpy (see Equation 2.45).

$$\Delta H_{therm} = E_{zero-point} + E_t + E_r + E_v \quad (2.45)$$

The contribution E_t , E_r and E_v can be derived from the respective partition functions q and the translational, rotational, and vibrational degrees of freedom (see Table 2.1 and Equations 2.46, 2.47 and 2.48).

Table 2.1: Translational, rotational, and vibrational degrees of freedom for atoms, linear molecules, and non-linear molecules. N is the number of atoms in the molecule.

Degrees of Freedom	Atom	Linear molecule	Non-linear molecule
Translational	3	3	3
Rotational	0	2	3
Vibrational	0	$3N - 5$	$3N - 6$
Total	3	$3N$	$3N$

$$E_t = \frac{3RT}{2} \quad (2.46)$$

$$E_r = \frac{3RT}{2} \text{ for non-linear molecules} \quad (2.47)$$

$$E_v = R \sum_i \frac{1}{e^{\frac{hv_i}{k_B T}} - 1} \frac{hv_i}{k_B} \quad (2.48)$$

As the three translational degrees of freedom are always accessible in the molecular systems, which are treated here, E_t is a temperature-dependent constant. Similarly, all three rotational degrees of freedom are relevant for all non-linear molecules, which leads to the same mathematical expression for E_r for most relevant molecules. This term is different for linear molecules (e.g., acetylene, H₂, CO, ...), for which the expression needs to be adapted to RT . Atoms do not have any rotational degrees of freedom, which leads to $E_r = 0$. The vibrational contributions to ΔH_{therm} , E_v , can be calculated in dependence of the vibrational degrees of freedom, i.e., in dependence of the size of the molecular system (see Equation 2.48). The zero-point vibrational energy, as the name suggests, is calculated from the same equation with the occupation of the lowest level of each vibrational mode (see Equation 2.49).

$$E_{zero-point} = R \sum_i \frac{1}{2} \frac{hv_i}{k_B} \quad (2.49)$$

Detailed information on the determination of these values in the TURBOMOLE program, which has been used in thesis, can be found in the output of the *freeh* module and the corresponding documentation.

2.2.7 Solvent Corrections

The solvent of a reaction can play a major role in chemistry and homogeneous catalysis. However, the energies resulting from uncorrected quantum-chemical calculations do not take any solvents into account and are only providing the gas-phase results (i.e., the geometry and energy for an isolated molecule without any further molecules in its surrounding). There are two different approaches for treating solvent effects: Firstly, explicit solvation, meaning that solvent molecules are directly included in the calculation, theoretically represents the ideal approach as all characteristics of the solvent interactions could be captured. However, for this to be an accurate representation of the real chemical system, an incredibly high number of solvent molecules would need to be included, which cannot be treated with DFT considering today's approaches and computational resources. This approach is commonly used in molecular dynamics (MD), where significantly larger system can be investigated in combination with a wide set of advantages and disadvantages of MD compared to DFT (see the computational chemistry textbooks for details).¹⁷⁻¹⁸ The second approach is implicit solvation, which has become common practice in DFT investigations. Within the field of

implicit solvent corrections, multiple approaches have been developed, but this section is limited to a description of the conductor-like screening model for real solvents (COSMO-RS),⁷⁵⁻⁷⁷ which is the approach that was used for the calculations in this thesis. For a detailed description of other approaches (e.g., the Polarizable Continuum Model; PCM), please refer to the available literature.⁷⁸⁻⁷⁹

The COSMO-RS theory was initially developed by Andreas Klamt in 1995⁷⁵ and further refined by Klamt and co-workers in 1998.⁷⁶ The model uses screening charge density profiles $p(\sigma)$ on the molecular surfaces of the chemical species as well as of the solvent to compute the chemical potential $\mu(\sigma)$ in solution (see Equation 2.50). To be able to do this, the screening charge surface density profile is calculated with the conductor-like screening model (COSMO), which was also developed by Klamt and co-workers⁸⁰ and led to the development of various databases of these profiles.⁸¹ The generation of these screening charge density profiles (also known as σ -profiles) with the COSMO methodology will not be further discussed here.

$$\mu(\sigma) = -kT \ln \int p(\sigma') e^{-\frac{E_{interaction}(\sigma, \sigma') - \mu(\sigma')}{kT}} d\sigma' \quad (2.50)$$

In this equation, $p(\sigma')$ describes the screening charge density profile of the solvent, $E_{int}(\sigma, \sigma_{solv})$ is the interaction energy between the screening charges σ and σ' on the molecular surfaces, and $\mu(\sigma')$ represents the chemical potential of a surface section with a certain screening charge. As the calculation of $\mu(\sigma)$ depends on the chemical potential $\mu(\sigma')$ itself, this equation, as many other equations described in this chapter, can only be solved iteratively. The term for the interaction energy contains various interactions like electrostatic interactions, hydrogen bond energies and van der Waals interactions and has been parameterized based on available thermochemical data. While these chemical potentials can also be used to calculate activity coefficients, solubility, or vapor pressures, in this thesis, it was solely used to calculate the free energy of solvation (ΔG_{solv}). For each chemical species, this can be achieved based on its chemical potential at infinite dilution (μ_s) and its chemical potential in the ideal gas state (μ_{ig} ; see Equation 2.51).

$$\Delta G_{solv} = \mu_s - \mu_{ig} - RT \ln \left(\frac{\rho_s V_{ig}}{M_s} \right) \quad (2.51)$$

Here, M_s is the molecular weight of the solvent, V_{ig} is the calculated molar volume in the boundaries of an ideal gas and ρ_s describes the solvent density. Subsequently, this correction term is added to the equation presented above (see Equation 2.52; cf. Equation 2.44).

$$G = E_{elec} + \Delta G_{therm} + \Delta G_{solv} \quad (2.52)$$

2.2.8 Relativistic Effects

Particles moving at very high speeds are affected by relativistic effects. For electrons, the particle speed is strongly dependent on the orbital, which they are occupying (or more specifically: the electron shell, in which the electron is positioned, defined by the principal quantum number n) and the atomic number. As a simple illustration, the classical formula for the kinetic energy (Equation 2.53) can be rearranged to give the electron velocity v_e based on the kinetic energy and the mass (see Equation 2.54).

$$E_{kin} = \frac{1}{2} m_e v_e^2 \quad (2.53)$$

$$v_e = \sqrt{\frac{2E_{kin}}{m_e}} \quad (2.54)$$

With an approximated term for the kinetic energy of an electron with $n = 1$, it follows:

$$v_e = cZ\alpha \quad (2.55)$$

where c denotes the speed of light, Z denotes the atomic number and with:

$$\alpha = \frac{e^2}{4\pi c \epsilon_0 \hbar} \quad (2.56)$$

Consequently, the velocity of the inner electrons significantly increases with the atomic number (see Equation 2.55). While the electron velocity for hydrogen ($Z = 1$) is $0.007c$, the electron velocity obtained for ruthenium ($Z = 44$), which was used in the dehydrogenative coupling of alcohols and, in general, is a frequently used transition metal in

catalysis, is $0.32c$. Due to this, the inner electrons in heavier atoms are subject to relativistic effects. One of these effects is the increase of the mass of the moving particle. This leads to a contraction of the inner atomic orbitals and propagates to the other shells, meaning that when the $1s$ orbital in an atom with a large atomic number contracts, all s -orbitals in higher electron shells are also affected.⁸² While there are various approaches to dealing with these relativistic effects in quantum chemistry, the use of effective core potentials (ECPs; also commonly referred to as pseudopotentials) is widely spread in DFT investigations.⁸³ These potentials replace the inner electrons of the molecular system in the calculation and lead to a reduction of computational cost as well as to the inclusion of relativistic effects. In the development of ECPs, the parametrization of the effective potentials as well as the selection of the replaced electrons needs to be carefully tested and validated against experimental data or data from all-electron calculations, which specifically include relativistic effects. In this thesis, the ECPs developed by Andrea *et al.* in Stuttgart were used for the description of ruthenium in the hydrogenative coupling of alcohols and iodine in the carbonylation of alcohols.⁸⁴

2.3 Methodology

Apart from the theoretical foundations of DFT, which have been outlined before, an introduction into the application of these methods to carry out mechanistic investigations in homogeneous catalysis is given in this section.

When applying quantum-chemical methods to mechanistic investigations in homogeneous catalysis, a two-step approach is commonly used to appropriately describe the given chemical system. The first step is performing a geometry optimization, which leads from a guess structure defined by the user to an optimized geometry of the given molecule. Due to the high amount of optimization steps that can be involved in this process, a computationally less expensive method is commonly chosen to enable the application of this time-intensive procedure to relevant systems in homogeneous catalysis, which can easily feature up to 100 atoms when employing large ligands without applying any truncations. Once the geometry optimization is completed, a more expensive high-level method is applied for a single energy calculation of the optimized structure to provide a more accurate energy value for the given system. This energy is combined with various system- and method-dependent correction terms to yield the final absolute energy. However, the absolute energies do not carry much meaning when studying reaction mechanisms as these describe the energy required for formation of the chemical species from infinitely separated atoms, which does not represent a relevant process in chemical reactions. Therefore, only the relative energies of the calculated species are considered and often referenced to a highly stable experimentally observed compound. These relative energies then offer the possibility to assess the far more relevant relative stabilities of intermediates, transition states and products and thus, allow prediction and evaluation of accessible pathways, formed compounds and reaction conditions.

While this section presents an overview of the general procedures, each of the following chapters includes a detailed explanation of the underlying computational methods that have been used for the geometry optimization and single point calculations as well as the applied energy corrections for each project (see Chapters 3.2, 4.2 and 5.2). Unless otherwise noted, all energies given are Gibbs free energies in kJ mol^{-1} .

All quantum-chemical calculations were carried out using the TURBOMOLE program⁸⁵⁻⁸⁸ (Version 7.3) distributed by TURBOMOLE GmbH. The free energies of solvation in this thesis were calculated using the COSMOtherm program developed by COSMOlogic GmbH & Co KG (recently acquired by BIOVIA),⁸⁹ however, implementations of the COSMO-RS methodology are also available in other program suites.

2.3.1 Geometry Optimization

Geometry optimizations represent the initial step of any calculation performed in this thesis as only these optimized or ‘relaxed’ structures, which represent a stationary point on the potential energy surface, carry a relevant meaning in the description of the reaction mechanisms shown here. As dozens to hundreds of intermediary structures, and thus energy calculations, are part of every geometry optimization only a less expensive low-level method was chosen to be able to perform these calculations at reasonable timescales. In this work, the GGA-type BP86 functional in combination with the def2-SV(P) basis set³⁹ was used for all geometry optimizations. This functional is a combination of Becke’s exchange functional,⁹ developed in 1988, and Perdew’s correlation functional,⁵¹ developed in 1986, which in part also contains the previously developed LDA-type functional from Vosko, Wilk and Nusair.⁴⁶

The BP86 functional has previously been successfully used for the geometry optimization of a wide variety of chemical systems. It exhibits a very good value-to-cost ratio, which can be crucial when investigating homogeneously catalyzed reactions with complex chemical systems. For example, some of the Ni diphosphine complexes, which have been calculated for the carbonylation of alcohols (see Chapter 4), easily reach a size of more than 100 atoms and therefore, require fast and cost-effective methods to be included in full-size in a thorough mechanistic investigation. For this reason, the previously described two-step approach was taken. An effective and fast low-level method was chosen for geometry optimization, which can include hundreds of individual energy calculations and a high-level, more accurate and expensive method was employed for subsequent single point calculations.

The accuracy of BP86 has also been tested and reported in the literature: Firstly, reports by Koch, Schaefer, and Jensen independently showed a good agreement for a wide set of structures, including carbonyl-coordinated transition metal complexes, with a slight overestimation of bond lengths by a few picometers.^{16, 90-91} Furthermore, BP86 geometry optimizations have been tested and successfully applied by the previous computational chemists at CaRLa, Philipp Plessow⁹² and Marko Hermsen,⁴⁵ which similarly found small bond length deviations. Lastly, in this work, it was possible to characterize some of the ruthenium complexes by X-ray diffraction measurements, which served as ideal comparison to validate the computed structures for this project specifically as well as for transition metal complexes in general.

The structural optimization of transition state (TS) species generally proves to be more difficult than the optimization of reaction intermediates. This is due to their instable position located on a saddle point of the potential energy surface (PES) and their basic physical property to be higher in energy than the two intermediates, which the TS is connecting on this PES. Therefore, if the chosen starting structure for the geometry optimization is not very close to the final optimized structure, the optimization will usually fail to locate the correct

TS. Although the vibrational mode can give an indication of the chemical transformation that is facilitated by the TS, only an intrinsic reaction coordinate (IRC) calculation can appropriately support the claim that the desired TS has been located. This further increases the computational effort needed to locate and characterize each structure.

2.3.2 Single Point Energies

After a stationary point, either a reaction intermediate or a transition state, has been located, the second part of the commonly employed two-step procedure is performed, a single-point energy calculation. It should be noted that due to the change in method, the structure, which resulted from the previous geometry optimization, does not represent a stationary point/minimum on the potential energy surface of the single-point method. However, due to this affecting all optimized structures in the same way, error cancellation and the small nature of this difference leads to this being neglected and a more accurate energy being observed.⁴⁵ While it would obviously be desirable to reoptimize this structure with the higher-level method, this can be extremely costly for large systems, which is the reason why a two-step approach was applied in the first place. In this thesis, the hybrid functional PBE0 developed by John P. Perdew, Kieron Burke, Matthias Ernzerhof, and Gustavo E. Scuseria was used for the single-point energies.^{52,93} In PBE0, a certain percentage of the DFT exchange in the underlying GGA exchange-correlation function (PBE)⁵² is replaced by exact Hartree-Fock exchange as described in section 2.2.3 (see Equation 2.57).

$$E_{exchange}^{PBE0} = \frac{3}{4} E_{exchange}^{PBE} + \frac{1}{4} E_{exchange}^{HF} \quad (2.57)$$

For PBE0, the Hartree-Fock exchange contribution was set to 25% based on a comparison with Møller-Plesset perturbation theory calculations⁹⁴ instead of fitting against experimental data, which is regularly done to determine a suitable percentage of Hartree-Fock exchange. In the past decades, the PBE0 functional has become one of the most popular hybrid functionals in use.⁵⁸ The functional is combined with the Karlsruhe-type quadruple-zeta def2-QZVPP basis set,³⁸⁻³⁹ the RI approximation for faster integration of multi-center integrals (*vide supra*),^{40, 60, 62-63} and Grimme's empirical D3 correction⁶⁹ with Becke-Johnson damping⁷⁴ to account for dispersion. The thermodynamic corrections as well as the Gibbs free energy of solvation were added following the methodology described above to obtain the desired Gibbs free energies in solution. In the two decades after its initial introduction, PBE0 has been used in many mechanistic investigations showing its capability of achieving the required tasks. Similarly, it has been benchmarked and applied by Marko Hermsen at CaRLa.⁴⁵ Furthermore, the investigations carried out for his PhD thesis included phosphine-coordinated ruthenium complexes, which is also an important aspect of the investigation of

the dehydrogenative coupling of alcohols reported in this thesis (see Chapter 3). Nonetheless, a regular comparison of calculations with experimentally observables (e.g., solid-state structures, reaction rates, and spectroscopy) whenever possible should be highly desired to ensure that an accurate representation of the chemical system is achieved.

2.3.3 Investigation of Reaction Pathways

The main concept behind mechanistic investigations with quantum chemistry is identifying the individual intermediates and transition states, which connect the reactants (substrate, catalyst, additives, ...) with the corresponding products. Understanding these fundamental processes that take place over the course of the reaction can provide important insights into how the reaction can be improved further or serve as basis for experimental or computational screening of alternative reactants.

In such an investigation, one cannot limit oneself to just calculating the expected route of transformations but must also carefully and thoroughly investigate all possible alternative reaction pathways connecting the species. Furthermore, the formation of side products, especially when full conversion is not observed experimentally, must be investigated to fully understand the reactions taking place in the chemical system. This is especially critical in homogeneous transition metal catalysis, where the organometallic complexes can access a wide variety of coordination modes and reactions and several species (as reaction partners) are present in solution at the same time. For this reason, the bias of the chemist or research group must be carefully considered. Researchers generally tend to investigate reaction pathways that have been commonly suggested in previous publications and that are prominent in their field of research (confirmation bias). Furthermore, when the expected/desired pathway has already been found, pressure towards publishing in academic journals, cost of available resources or the desire to avoid any unexpected complications due to additional pathways, can lead to prematurely stopping the investigation before all pathways have been explored. In the worst cases, due to the wide variety of available computational methods, corrections, and parameters, the computational details can be adjusted until the results fit the expectations instead of further exploring the chemical landscape of the potential energy surface. Many of these effects can, at least in part, be counteracted: Firstly, a large and diverse team with many different research backgrounds can significantly reduce confirmation bias. Secondly, a supportive research environment that prioritizes scientific rigor over publication speed and is open for a close collaboration between experiments and computations further reduces the chances for mistakes to happen. Moreover, unjustified, meaning without any physical/methodological reasoning, changes of the employed methods simply to better fit the own expectations should be avoided. Reasons for such a change can be inaccurate representations of chemical structures or important interactions that have not been properly treated before. Some of these and other points have

also been summarized in the recent publication from Mu-Hyun Baik and co-workers.⁹⁵ Another approach that can significantly reduce some of these problems is the automated generation of reaction networks,⁹⁶⁻¹⁰⁰ which are often combined with methods for the automated generation of transition state guesses from reactant and product structures (e.g., the molecular growing string method by Paul Zimmerman).¹⁰¹⁻¹⁰² While these tools that automatically generate all possible combinations of reaction steps are currently gaining traction especially in organic chemistry, their use in organometallic chemistry is still limited by their ability to deal with the flexible reactivity of transition metal complexes. However, even when following all these steps, one is not guaranteed to avoid any problems. Due to the tricky nature of transition state optimization (see Section 2.3.1), computational chemists can never be sure whether a transition state that was not characterizable does truly not exist or the initial guesses were not good enough. As a proof of non-existence is impossible, the non-existence of a transition state or the existence of a barrierless reaction pathway must be assumed when a multitude of attempts to localize the structure have failed. In any case, as already emphasized, a close collaboration between experimental and computational work, where both aspects are treated as equal partners, can significantly improve the overall process of mechanistic investigations. In such an environment, experimentalists can suggest fitting calculations and computational chemists can equally suggest helpful experiments as well as help to avoid false conclusions.

To further provide insights into the characterization of reaction pathways, a brief explanation of intermediates and transition states is also necessary. Both, intermediates and transition states, represent stationary points on the potential energy surface i.e., the gradient, which is the first derivative of the energy with respect to the atom coordinates, has to be zero. For further differentiation between intermediates and transition states, an eigenvalue analysis of the second derivative of the energy term, the so-called Hesse matrix, is required. While for an intermediate (i.e., a minimum on the potential energy surface) all eigenvalues must be non-negative (rotation/translation = 0; all others > 0), a transition state will be indicated by exactly one eigenvalue being negative. Therefore, a transition state represents a first order saddle point on the potential energy surface, which is a maximum along the reaction coordinate while being a minimum on all other coordinates. This negative eigenvalue is commonly referred to as negative vibrational frequency or imaginary vibrational frequency due to being caused by an imaginary number. Stationary points with n negative vibrational frequencies represent n^{th} order saddle points and are chemically irrelevant as a more feasible pathway on the potential energy surface can always be found. This can regularly happen over the course of a mechanistic investigation and reoptimization of the obtained chemical structure is required until the appropriate amount of negative vibrational frequencies is observed for intermediates (0) and transition states (1). Once a transition state was found, an intrinsic reaction coordinate (IRC) calculation should be performed to validate that the

vibrational mode does actually induce the postulated structural changes and does not connect two different minima on the potential energy surface.¹⁰³

After the characterization of various stationary points is completed and a reaction network of multiple pathways has been built, the Gibbs free energies of activation (ΔG^\ddagger) of these pathways are usually evaluated and compared. Unless ΔG^\ddagger is very close for multiple calculated reaction pathways, it is usually assumed that one pathway is responsible for the majority of product formation, which is the pathway that is associated with the lowest overall reaction barrier. Based on this pathway's Gibbs free energy of activation and the reaction temperature T , the rate constant k can be calculated from the Eyring equation (see Equation 2.58),¹⁰⁴ which enables comparison to experimentally observed kinetics.

$$k = \frac{k_B T}{h} e^{-\frac{\Delta G^\ddagger}{RT}} \quad (2.58)$$

For this equation, pseudo-first order kinetics and a transmission coefficient of $\kappa = 1$ have been assumed, so that the rate constant is only dependent on ΔG^\ddagger and the reaction temperature. However, kinetic studies are far from trivial and can be a time-consuming phase of the project that is only carried out in a later stage of the investigation. Therefore, trying to connect the activation barriers with direct experimental observables is highly preferred, which can be achieved by calculating the half-life λ from the reaction rate (Equation 2.59) and the conversion x from λ and the time t (Equation 2.60).

$$\lambda = \frac{\ln(2)}{k} \quad (2.59)$$

$$x = 1 - \frac{1}{2^{\frac{t}{\lambda}}} \quad (2.60)$$

In his PhD thesis, Marko Hermesen presented a plot of the reaction time against the activation barrier height at different reaction temperatures (amongst other plots combining these variables).⁴⁵ This has been extremely helpful on countless occasions and led me to provide a similar plot for the readers of this thesis, that can be directly used to compare the activation barriers presented in the following chapters with the experimental conversions. For this, the given formulas need to be rewritten to give the reaction time t in dependence of the conversion, temperature, and the activation barrier (see Equation 2.61).

$$t = \frac{h \ln\left(\frac{1}{1-x}\right)}{k_B T} e^{\frac{\Delta G^\ddagger}{RT}} \quad (2.61)$$

This results in the plots shown in Figure 2.1 with a conversion of 99%, an activation energy range of 90 to 140 kcal mol⁻¹, and the temperatures used in the projects presented in this thesis (110 °C: dehydrogenative coupling of alcohols; 120 °C: carbonylation of phenyl ethyl alcohol; 140 °C: vinylation of pyrrolidone; 180 °C: carbonylation of *t*-butyl alcohol). It should be noted that these plots can only provide a rough estimate of which reaction barriers might be accessible in certain timespans. Due to the various approximations (e.g., $\kappa = 1$, not accounting for any alternative reaction pathways, equilibria of reactive species, etc.), this cannot be used for detailed comparison with experimental results. For this purpose, time-intensive approaches towards microkinetic modelling are available, which take more of these difficulties into account, and might serve as a significantly better basis for such comparisons.¹⁰⁵⁻¹⁰⁷

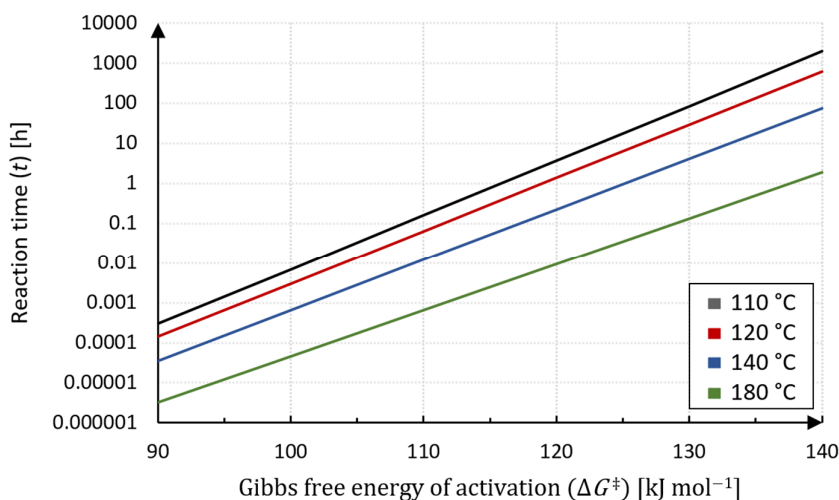


Figure 2.1: Calculated reaction times in hours to achieve a conversion of 99% for reaction barriers from 90 to 140 kJ mol⁻¹ at the temperatures of the dehydrogenative coupling of alcohols (110 °C, top, black), of the carbonylation of phenyl ethyl alcohol (120 °C, second from top, red), of the vinylation of pyrrolidone (140 °C, second from bottom, blue), and of the carbonylation of *t*-butyl alcohol (180 °C, bottom, green).

In a second plot, the most relevant section that covers reaction times from a few minutes (0.1 h) up to reaction times of multiple days (e.g., 96 h for a four-day reaction; see Figure 2.2) is magnified and allows for better comparison of the activation energies with the corresponding reaction times.

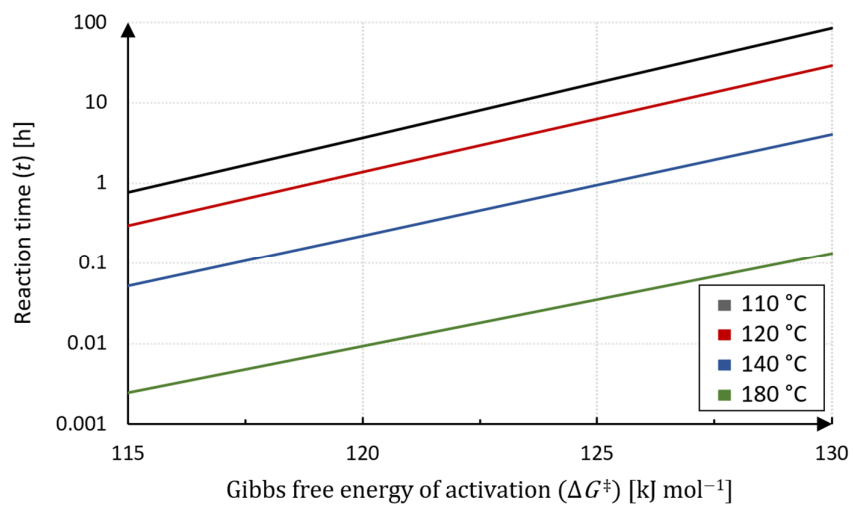


Figure 2.2: Calculated reaction times in hours to achieve a conversion of 99% for reaction barriers from 115 to 130 kJ mol⁻¹ at the temperatures of the dehydrogenative coupling of alcohols (110 °C, top, black), of the carbonylation of phenyl ethyl alcohol (120 °C, second from top, red), of the vinylation of pyrrolidone (140 °C, second from bottom, blue), and of the carbonylation of *t*-butyl alcohol (180 °C, bottom, green).

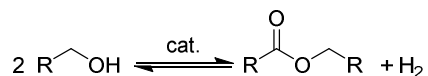
3

Dehydrogenative Coupling of Alcohols

Reproduced in part with permission from Daniel J. Tindall, Maximilian Menche, Mathias Schelwies, Rocco Paciello, Ansgar Schäfer, Peter Comba, Frank Rominger, A. Stephen K. Hashmi and Thomas Schaub, Ru⁰ or Ru^{II}: A Study on Stabilizing the “Activated” Form of Ru-PNP Complexes with Additional Phosphine Ligands in Alcohol Dehydrogenation and Ester Hydrogenation, *Inorganic Chemistry* **2020**, 59(7), 5099 – 5115. Copyright 2020 American Chemical Society.

3.1 Motivation

The acceptorless dehydrogenative coupling of alcohols leading to the formation of esters as well as the reverse reaction, the hydrogenation of esters with H₂, are highly interesting for the industrial synthesis of bulk chemicals (see Scheme 3.1).

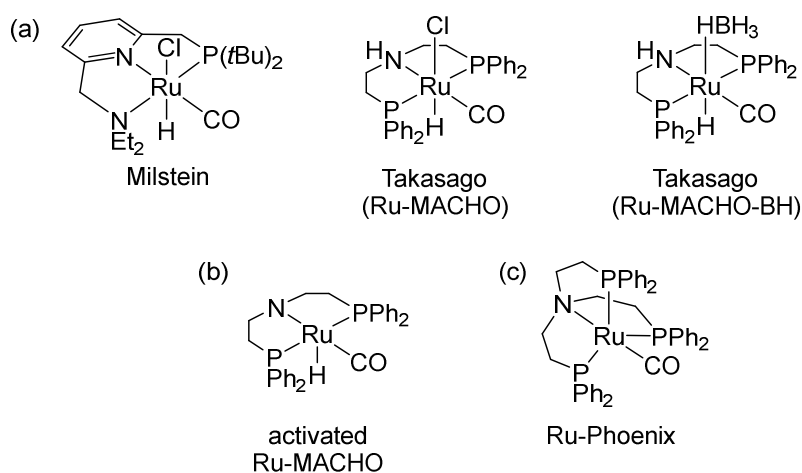


Scheme 3.1: Acceptorless dehydrogenative coupling of alcohols to esters and reverse hydrogenation with H₂.

More specifically, catalytic dehydrogenative couplings are mild reactions, which employ easily accessible alcohols and form H₂ as sole side product. In some regards, the use of homogeneous catalysts for this transformation also is superior to the use of heterogeneously

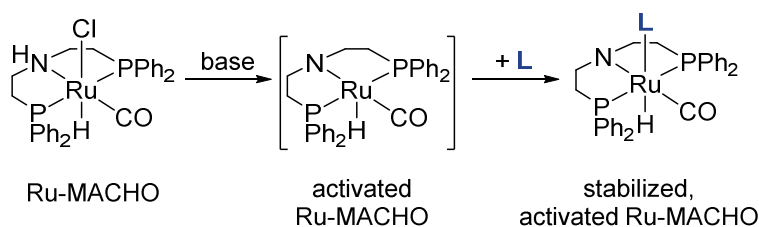
catalyzed processes. For example, homogeneous catalysts are typically used at milder reaction conditions, which can reduce side product formation and energy cost.¹⁰⁸⁻¹¹⁰ This can have wide ranging consequences for work-up procedures and the amount of waste that is generated throughout the reaction, which are key factors in achieving more economic and sustainable processes.¹⁻² In 2005 and 2006, Milstein and co-workers have pioneered the use of highly active ruthenium pincer complexes for the dehydrogenative coupling of alcohols¹¹¹ and the hydrogenation of esters¹¹² with a Ru-PNN complex (see Scheme 3.2a). In the following years, many research groups have made their contributions,¹¹³⁻¹¹⁶ which have been highly successful for the dehydrogenation of alcohols¹¹⁷⁻¹¹⁹ and amines,¹²⁰ for the hydrogenation of esters¹²¹⁻¹²² and imines,¹²³ and for CO₂ reduction.¹²⁴⁻¹²⁵ This has also led to the development of the Ru-MACHO complex by the Japanese chemical company Takasago^{121, 126} (Scheme 3.2a) as well as the subsequent development of the derivatives with *i*Pr¹²⁷ and *t*Bu^{124, 128} substituents on the phosphine atoms of this PNP ligand. However, all of these catalysts require at least one equivalent of base for activation through dehydrochlorination, which forms the activated 16-electron Ru^{II} complexes (see Scheme 3.2b). Moreover, many regularly employed procedures even use a large excess of base for this activation. While attempts to isolate and characterize the activated species have been successful for the *i*Pr¹²⁹⁻¹³⁰ and *t*Bu^{117, 131-132} substituted complexes, the activated Ru-MACHO complex (Scheme 3.2b) remains elusive to date and only a mass spectrum has been reported by Krishnakuma *et al.*¹³³ In previous work at CaRLa, Aviel Anaby *et al.* were able to show that the activated Ru-MACHO species exhibits a low stability and immediately degrades in the absence of substrate.¹³⁴ During their detailed study of the mixture of formed species, the team was able to characterize three fragmentation products, of which the Ru⁰ system “Ru-Phoenix” (see Scheme 3.2c) was selected for further investigation and proved to be an excellent system for the base-free dehydrogenations. Similarly, it exhibited high catalytic activity for base-free hydrogenations after activation with an alcohol. By not requiring the harsh activation conditions, such a catalyst could for example be used with base-sensitive substrates and therefore extend the scope of this methodology. This application potential for base-free catalysts¹³⁵⁻¹³⁷ was also recognized by Takasago, who have developed the commercially available Ru-MACHO-BH system (see Scheme 3.2a),¹²⁶ however this complex has been shown to decompose over time.¹³⁸⁻¹³⁹ Moreover, the Ru-Phoenix complex also represents a rather rare example in (de-)hydrogenations: a Ru⁰ catalyst. In 2019, Anthony Chianese and co-workers reported that various of their own Ru^{II}-CNN complexes and Milstein’s Ru^{II}-PNN complex can undergo base-induced dehydroalkylation, which leads to similar Ru⁰ complexes in the presence of PCy₃.¹⁴⁰ While these complexes are also catalytically active, it is not yet understood whether Ru⁰ species are also involved as on-cycle intermediates or are limited to a role as precatalyst. One example of Ru⁰ being actively involved in the catalytic cycle was presented by Hansjörg Grützmacher and co-workers.¹⁴¹ In their work, they have

demonstrated the conversion of methanol and water into H_2 and CO_2 based on a $\text{Ru}^0/\text{Ru}^{\text{II}}$ catalytic cycle.



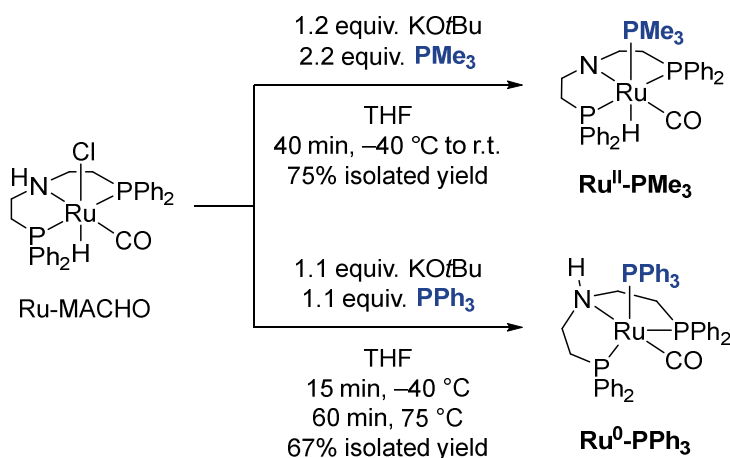
Scheme 3.2: (a) Previously developed ruthenium PNP pincer complexes by the groups of Milstein¹¹¹ and Takasago,^{121,126} (b) postulated structure of Ru-MACHO after dehydrochlorination, which has eluded isolation until now, and (c) Ru^0 complex “Ru-Phoenix” isolated from the degradation mixture of Ru-MACHO.¹³⁴

Because the shown degradation of the activated Ru-MACHO complex can be accompanied by multiple problems such as loss of catalytic activity or uncontrolled side product formation, an investigation into stabilizing this intermediate was carried out. For this, it was envisioned that the activated, unsaturated Ru-MACHO intermediate could be stabilized by apical coordination of a phosphine ligand (**L**; see Scheme 3.3), which, similar to the Ru-MACHO-BH complex, might represent a base-free catalyst for (de-)hydrogenation reactions. Ideally, the complex would be able to dissociate the phosphine ligand during the reaction to free up the coordination site allowing the (de-)hydrogenation to take place and reassociate the stabilizing ligand to the Ru center once full conversion is achieved. This could help increase the overall stability of the Ru-MACHO system and lower the negative effects caused by degradation of the complex. The only reported system employing an equivalent ligand coordination strategy with the Ru-MACHO system replaced the CO ligand with an *N*-heterocyclic carbene (NHC),¹⁴² but still required a large excess of base to achieve the catalysis.



Scheme 3.3: Envisioned route for the synthesis of a base-free (de-)hydrogenation catalyst by stabilization of the activated Ru-MACHO species.

Attempts to synthesize the desired complex with PMe_3 were successful (see Scheme 3.4) and enabled a detailed characterization of $\text{Ru}^{\text{II}}\text{-PMe}_3$ by ^1H - and $^{31}\text{P}\{^1\text{H}\}$ NMR spectroscopy, IR spectroscopy and X-ray diffraction analysis. The solid-state structure of $\text{Ru}^{\text{II}}\text{-PMe}_3$ is shown in Figure 3.1a and [CCDC 1958133](#). Interestingly, when attempting to stabilize the activated Ru -MACHO species with PPh_3 , no hydride signal was observed in the ^1H NMR spectrum. While $^{31}\text{P}\{^1\text{H}\}$ NMR spectroscopy and the presence of a CO ligand (by IR spectroscopy) gave some indications, the structure could only be fully evaluated after suitable crystals for X-ray diffraction analysis had been grown (see Figure 3.1b and [CCDC 1958130](#)). This revealed, in strong contrast to $\text{Ru}^{\text{II}}\text{-PMe}_3$, a five-coordinate ruthenium complex with a formal oxidation state of the metal of 0, which strongly resembles the previously reported Ru -Phoenix complex (cf. Scheme 3.2c). Contrary to the octahedral Ru^{II} complex, in which the PNP ligand is occupying three equatorial positions, the PNP ligand is placed at two equatorial (P donors) and one axial position (N donor) in the trigonal bipyramidal Ru^0 system. This also moves the CO ligand from an equatorial position in $\text{Ru}^{\text{II}}\text{-PMe}_3$ to an axial position in the Ru^0 complex. Interestingly, the two complexes also exhibit different phosphine conformations: In $\text{Ru}^{\text{II}}\text{-PMe}_3$, one of the three P-C bonds of the phosphine is adopting a syn-periplanar conformation to the carbonyl group, which seems intuitive as it should reduce steric pressure. On the other hand, the PPh_3 ligand in the Ru^0 complex adopts an anti-periplanar conformation to CO, which is accompanied by a Ru-P-C bond angle distortion that places the phenyl group closely over the NH functionality in the ligand backbone (see atom C71 in Figure 3.1b). A comparison to computed structures and explanation for this behavior is provided in Section 3.3.1.



Scheme 3.4: Synthesis of $\text{Ru}^{\text{II}}\text{-PMe}_3$ and $\text{Ru}^0\text{-PPh}_3$ from Ru -MACHO via dehydrochlorination and subsequent stabilization of the activated species with PMe_3 or PPh_3 . All experiments were carried out by Daniel J. Tindall at CaRLa.

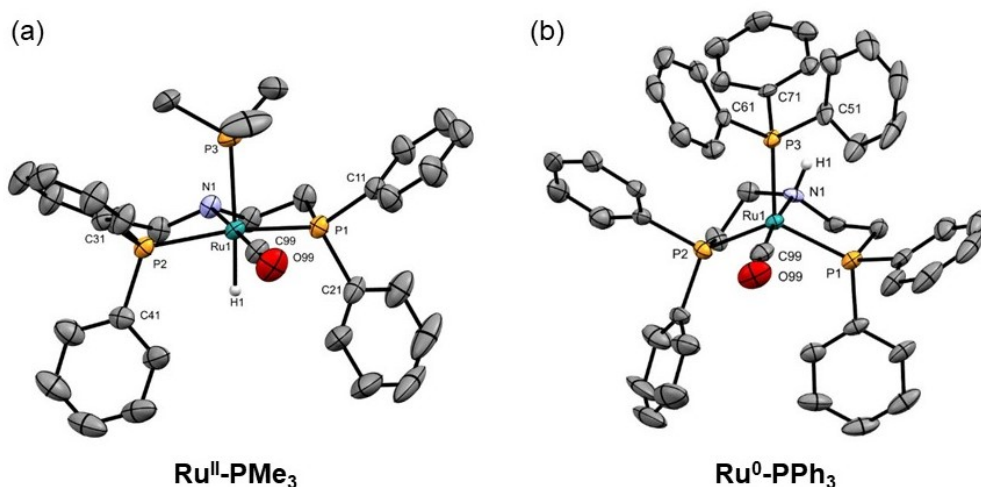
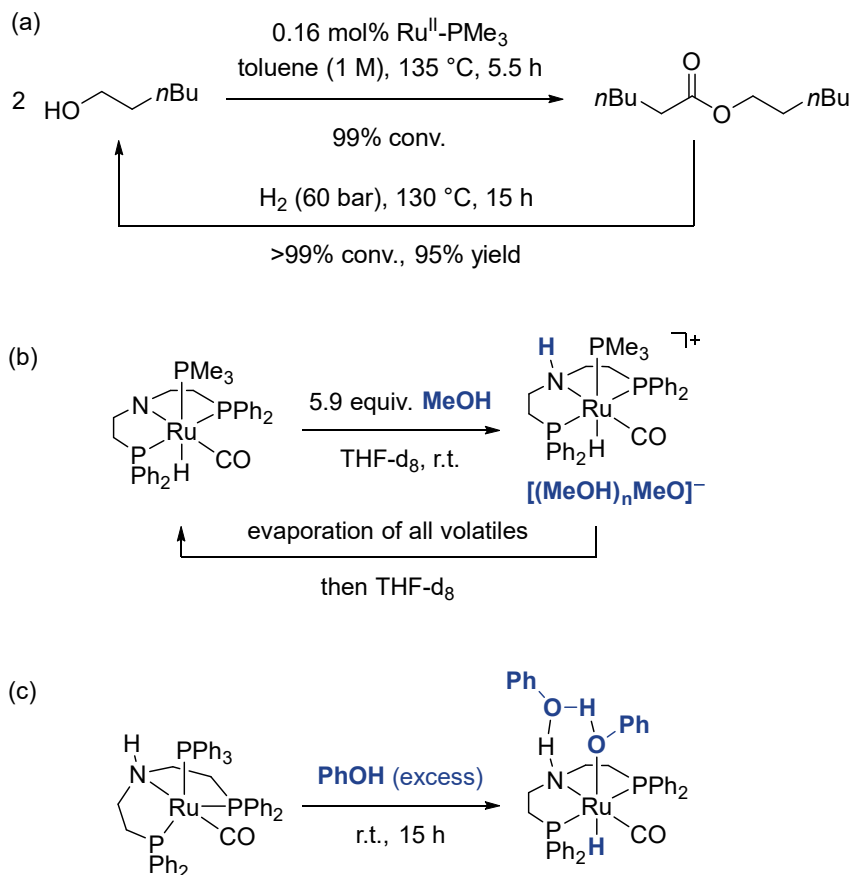


Figure 3.1: (a) Solid-state structure of Ru^{II}-PMe₃ (CCDC 1958133) and (b) solid-state structure of Ru⁰-PPh₃ (CCDC 1958130). C–H hydrogen atoms and co-crystallized benzene were omitted for clarity. Experiments and characterization were carried out by Daniel J. Tindall and Frank Rominger.

After the characterization of these two species, their ability to catalyze (de-)hydrogenation reactions was tested while simultaneously probing whether the results indicate any mechanistic differences between the Ru^{II} and Ru⁰ complexes. Employing Ru^{II}-PMe₃ as catalyst for the dehydrogenative coupling of hexanol to hexyl hexanoate provided full conversion after a few hours in toluene at 135 °C (see Scheme 3.5a). Similarly, the reverse hydrogenation reaction from hexyl hexanoate to hexanol was facilitated by the same catalyst at 60 bar of H₂ and achieved yields above 95% in an overnight reaction at 130 °C. Both hydrogenation and dehydrogenative coupling were equally feasible when employing the structurally different Ru⁰-PPh₃ complex. To further analyze similarities and differences in the reactive behavior of the two species, experiments with stoichiometric amounts of alcohols were carried out. The reaction of Ru^{II}-PMe₃ towards MeOH resulted in the fast protonation of the complex at room temperature leading to formation of a cationic octahedral complex (see Scheme 3.5b), which could be reversed by removal of all volatiles and addition of THF. Protonation was equally possible with phenol leading to the equivalent onium complex, which could be characterized by X-ray diffraction analysis (see CCDC 1958131). Interestingly, the two highly similar onium complexes behave differently when being employed as catalysts for the dehydrogenative coupling of hexanol, which was only successful for the phenol-based complex. Heating the two complexes revealed that only the PhOH system is stable, which could indicate carbonylation/formylation of the MeOH complex. Similar species were previously observed by Kar *et al.* in their work on MeOH dehydrogenation.¹⁴³ In contrast to Ru^{II}-PMe₃, Ru⁰-PPh₃ did not react with MeOH at room temperature. Slow reaction with PhOH could be observed and lead to the identification as Ru^{II} hydride alcoholato complex (see Scheme 3.5c and CCDC 1958136), which has been

previously observed for similar PNP ligands by the groups of Gusev¹²⁷ and Gauvin.¹⁴⁴ The alcoholato complex was also shown to be a competent catalyst for the base-free dehydrogenative coupling of hexanol to hexyl hexanoate.



Scheme 3.5: (a) Dehydrogenative coupling of hexanol to hexyl hexanoate and reverse hydrogenation reaction with Ru^{II}-PMe₃, (b) stoichiometric reaction of Ru^{II}-PMe₃ with MeOH and (c) stoichiometric reaction of Ru⁰-PPh₃ with PhOH. All experiments were carried out by Daniel J. Tindall at CaRLa.

After these drastic differences in molecular structure and reactivity towards alcohols in stoichiometric reactions had been observed, an in-depth quantum-chemical investigation was employed to understand the reason(s) for the observed selectivities as well as to gain insights into the elementary steps of the dehydrogenation reaction, for which both complexes were competent catalysts. In the case of an alternating reaction mechanism for Ru⁰ complexes, the structural motif could provide access to new approaches and improvements, while Ru^{II} complexes have been thoroughly studied in the literature (*vide supra*) and offer a lower potential to find a novel easily synthesizable, economically feasible and highly active catalyst.

3.2 Computational Details

All geometry optimizations were carried out at the BP86/def2-SV(P)^{9, 39, 51} level of theory with effective core potentials⁸⁴ (ECP) for ruthenium. Stationary points were verified via analysis of the vibrational frequencies at the level of geometry optimization. Final electronic energies were obtained by single-point calculations at the PBE0-D3(BJ)/def2-QZVPP^{38-39, 93} level of theory employing Grimme's D3 dispersion correction⁶⁹ incorporating Becke-Johnson damping.⁷⁴ All quantum-chemical calculations were carried out using the TURBOMOLE program⁸⁵⁻⁸⁸ (Version 7.3) with the resolution-of-identity (RI) approximation^{40, 60, 62-63} and the corresponding auxiliary basis sets¹⁴⁵⁻¹⁴⁶ implemented in the program. Zero-point vibrational energies and thermodynamic corrections were obtained at the level of geometry optimization ($T = 298.15$ K and $p = 1$ bar) and scaled to the given reaction temperatures (25 °C for stoichiometric experiments or 110 °C for catalytic pathways). For all species, the thermodynamic reference concentration was set to $x = 0.01$, except for the substrate when investigating catalytic cycles (ethanol; $x = 2.5$) because a constant reaction rate was observed above this 250-fold excess. Solvent corrections to Gibbs free energies in toluene were calculated for all species, except CO and H₂, with the conductor-like screening model for real solvents (COSMO-RS)⁷⁵⁻⁷⁶ carried out with the COSMOtherm program^{77, 89} (Version 18.0.0; Revision 4360; Parameters BP_TZVP_18.ctd). All energies discussed are Gibbs free energies (G) in kJ mol⁻¹. Connectivities between minima and transition states implied in figures and schemes were validated by intrinsic-reaction-coordinate (IRC) calculations.¹⁰³ Pictures of molecular structures were generated with the CYLview¹⁴⁷ program.

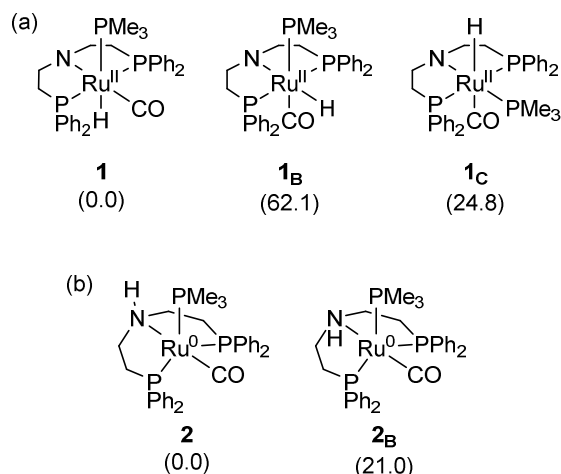
In the whole investigation, the full catalytic system was employed in the calculations without any truncations to the ligands. Mass balance for additional stabilizing substrate equivalents is ensured in all catalytic reaction schemes. All relevant intermediates and transition states were calculated without as well as with one and two explicit substrate molecules. Furthermore, a multitude of geometrical isomers was analyzed for all complexes. Due to the vast number of structures, the herein reported structures are limited to the isomer lowest in energy for each species.

Please note that the numbering of the calculated and experimental structures is reset for every chapter.

3.3 Results and Discussion

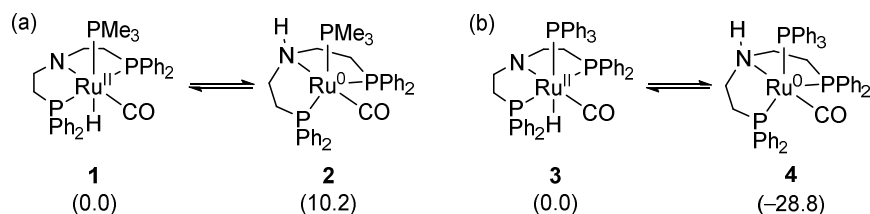
3.3.1 Rationalization of the Observed Chemoselectivities

As initial step in the computational investigation of the experimentally observed phenomena, the formation of the two different underlying structural types was studied. At the time when these DFT calculations started, the structural characterization by X-ray crystallography had not yet been achieved and only the ligands that were most likely coordinated to the Ru center had been identified by NMR spectroscopy. Therefore, all possible combinations of coordination for these ligands had to be computationally tested to ensure that the lowest energy structures would be found, which was of special importance as these complexes would serve as reference points for the calculated energies in subsequent investigations. However, it should also be mentioned, that the DFT calculations aimed at describing the most stable configuration in solution. While this can significantly differ from the solid-state structure obtained from X-ray crystallography, the structures in solution are the ones, which are present in the catalytic pathways. In the case of Ru^{II}-PMe₃ complex **1**, various different structures could be obtained and indicated that the isomer corresponding to the desired apical stabilization of the activated Ru-MACHO system is most stable (see Scheme 3.6). The two metallacycles in **1** and **1_C** adopt an *envelope* conformation, in which four atoms are placed in one plane. The fifth atom of the five-membered ring, which does not lay in this plane, is called the *endo* atom. Although this conformation was also tested for **1_B**, it could not be located, and a *twist* conformation was observed for one of the two five-membered rings. In the *twist* conformation, three adjacent atoms are placed in one plane and of the other two atoms one is positioned above and one below this plane. The investigation of **2** required the consideration of another parameter: the position of the NH proton, which can be positioned towards the PMe₃ ligand (**2**; *syn* to the apical ligand) or between the two phosphine moieties of the PNP ligand (**2_B**; *anti* to the apical ligand). Other isomers (similar to **1_B** or **1_C**) could not be located, which can be explained by the higher flexibility in this system due to the lower coordination number of the complex. This led to the fact that the more stable configuration **2** was obtained from the geometry optimizations of the other attempts. The complexes **2** and **2_B** exhibit one *envelope*- and one *twist*-configured metallacycle, which enables the PNP ligand to adapt to the trigonal bipyramidal structure. Considering the PPh₃-coordinated complexes, the formation of a N–H... π -phenyl interaction, leading to an anti-periplanar arrangement and bend of the PPh₃ group is only possible in the structural motif equivalent to **2**, in which the NH proton is positioned *syn* to the apical phosphine. Similarly, the investigation of the different isomers and the metallacycle configurations was done for all other complexes that are shown in this chapter. However, due to the number of calculated species only the lowest energy isomers are presented in the reaction schemes.



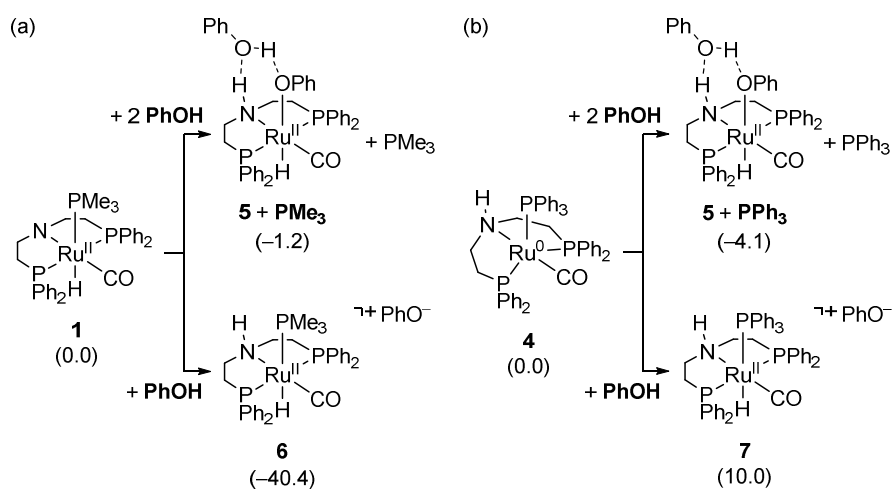
Scheme 3.6: Located isomers for the (a) $\text{Ru}^{\text{II}}\text{-PMe}_3$ and (b) $\text{Ru}^0\text{-PMe}_3$ system.

For these most stable isomers, the reaction from $\text{Ru}^{\text{II}}\text{-PMe}_3$ complex **1** to $\text{Ru}^0\text{-PMe}_3$ complex **2** was found to be slightly endergonic ($\Delta G^{298} = 10.2 \text{ kJ mol}^{-1}$; see Scheme 3.7a), which is in line with the experimental observation of the $\text{Ru}^{\text{II}}\text{-PMe}_3$ species. The analogous $\text{Ru}^{\text{II}}/\text{Ru}^0$ reaction step for **PPh**₃ is strongly exergonic and therefore predicts a contrasting result for that system, which is again in good agreement with the experimental observations (**4**: $\Delta G^{298} = -28.8 \text{ kJ mol}^{-1}$; see Scheme 3.7b). The causes for this behavior are mainly attributed to the steric properties of the two phosphines. The change in coordination environment from an octahedral system to a five-coordinate trigonal bipyramidal configuration in **2** and **4** affords significantly more space for the monodentate phosphine ligand. Due to the higher steric demand of **PPh**₃, which leads to significant repulsion in the octahedral Ru^{II} system, the pentagonal Ru^0 motif is favored in this case. Although the Tolman electronic parameters (TEP) of the two groups (TEP(PMe_3): 2064 cm^{-1} ; TEP(PPh_3): 2069 cm^{-1}) are very similar,¹⁴⁸ the more electron-rich Ru^0 motif should be slightly favored by the electron-poorer **PPh**₃, which provides an additional reason for the observation of the $\text{Ru}^0\text{-PPh}_3$ complex. Lastly, the N–H $\cdots\pi$ -phenyl interaction, which was identified in the crystal- and computational structures, also provides additional stabilization of the trigonal-bipyramidal geometry when **PPh**₃ is used.



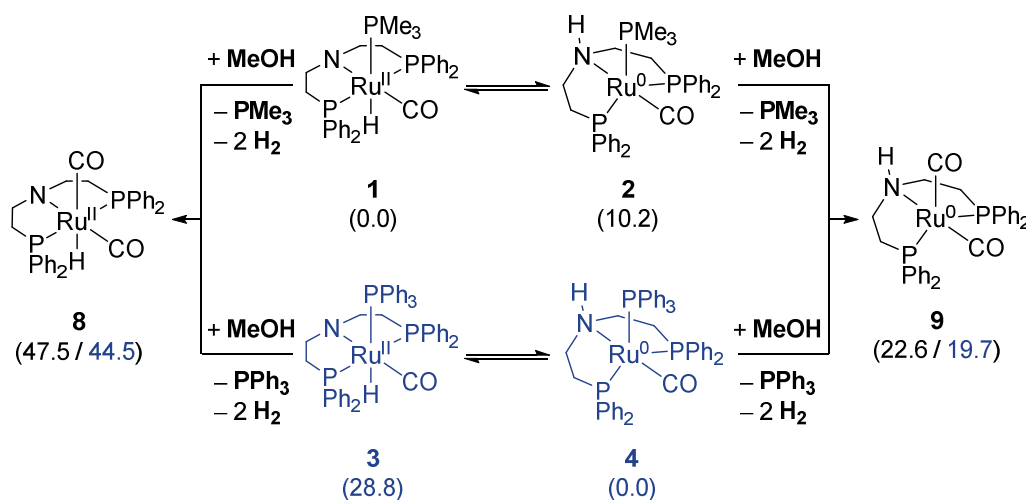
Scheme 3.7: (a) Comparison of the stabilities of the Ru^0 and Ru^{II} complexes for **PMe**₃ (**1** and **2**). (b) Comparison of the stabilities of the Ru^0 and Ru^{II} complexes for **PPh**₃ (**3** and **4**). ΔG^{298} in kJ mol^{-1} ; RI-PBE0-D3(BJ)/def2-QZVPP//BP86/def2-SV(P); COSMO-RS (toluene).

Based on the calculated and experimentally observed structures of **1** and **4**, calculations for the equimolar reaction of the ruthenium complexes with phenol were undertaken to compare the stability of a possible phenolate complex with the stability of an onium complex that is formed by protonation of the nitrogen atom (see Scheme 3.8). From **1**, formation of the phenolato complex **5** (i.e., the exchange of phosphine with the phenolate unit and simultaneous introduction of the NH proton) is slightly exergonic ($\Delta G^{298} = -1.2 \text{ kJ mol}^{-1}$). The complex exhibits stabilizing hydrogen-bond interactions of the protonated backbone and the phenolate ligand with a second molecule of phenol. The formation of the onium complex **6**, in which **PMe₃** remains coordinated to the Ru atom, is significantly more feasible and should lead to the strongly exergonic formation of **6** ($\Delta G^{298} = -40.4 \text{ kJ mol}^{-1}$). On the other hand, formation of **5** and **PPh₃** from Ru⁰-PPh₃ complex **4** is favored ($\Delta G^{298} = -4.1 \text{ kJ mol}^{-1}$) over the formation of **7** by protonation ($\Delta G^{298} = 10.0 \text{ kJ mol}^{-1}$). Once more, this observation is attributed to the high steric pressure that would be caused by **PPh₃** in an octahedral coordination environment (complex **7**). Comparing the stability of **7** with the stability of Ru^{II}-PPh₃ species **3** (see Scheme 3.7), reveals that for **PPh₃**, like **PMe₃**, the onium complex **7** is more stable than the corresponding non-protonated complex **3**. The experimental observation and computational preference of the phenolato complex show that if a different ligand replaces **PPh₃** the formation of octahedral species from the Ru⁰-PPh₃ precursor is possible. It should also be noted that the combination of multiple molecules into one for the **PhOH**-stabilized **5** ($4 + 2 \text{ PhOH} \rightarrow 5 + \text{PPh}_3$; 3 equiv. \rightarrow 2 equiv.) results in a negative entropic contribution, which will get more significant with increasing temperatures. Therefore, at higher temperatures (e.g., 110 °C, which is employed under catalytic conditions) the energetic gain from substrate stabilization should get less relevant, which might lead to phosphine-dependent differences in the reaction mechanism.



Scheme 3.8: (a) Comparison of the stabilities of the phenolato complex **5** and the onium complex **6** formed from **1**. (b) Comparison of the stabilities of the phenolato complex **7** and the onium complex **8** formed from **4**. ΔG^{298} in kJ mol^{-1} ; RI-PBE0-D3(BJ)/def2-QZVPP//BP86/def2-SV(P); COSMO-RS (toluene).

Apart from the reactions with phenol, **MeOH** was successfully employed in the experimental investigations to protonate the $\text{Ru}^{\text{II}}\text{-PMe}_3$ complex. However, subsequent heating has led to the observation of thermal instability and, presumably, to the formation of dicarbonyl complexes. Therefore, the stability of these species was compared with the stability of the known complexes **1** and **4** (see Scheme 3.9). The formation of Ru^{II} dicarbonyl complex **8** from $\text{Ru}^{\text{II}}\text{-PMe}_3$ complex **1** or from $\text{Ru}^0\text{-PPh}_3$ complex **4** (most likely via the corresponding Ru^{II} species **3**) is moderately endergonic ($\Delta G^{298} = 47.5$ and 44.5 kJ mol^{-1} for **1** and **4**, respectively). In addition to **8**, a Ru^0 dicarbonyl complex was investigated and found to be slightly more stable than **8** (**9**: $\Delta G^{298} = 22.6$ and 19.7 kJ mol^{-1} for **1** and **4**, respectively). Although these two complexes represent endergonic reaction pathways that by themselves should not lead to major amounts of degradation, the possible removal of gaseous H_2 or low-boiling PMe_3 from the system could lead to irreversibility and to slow build-up of the dicarbonyl complexes **8** and **9**.

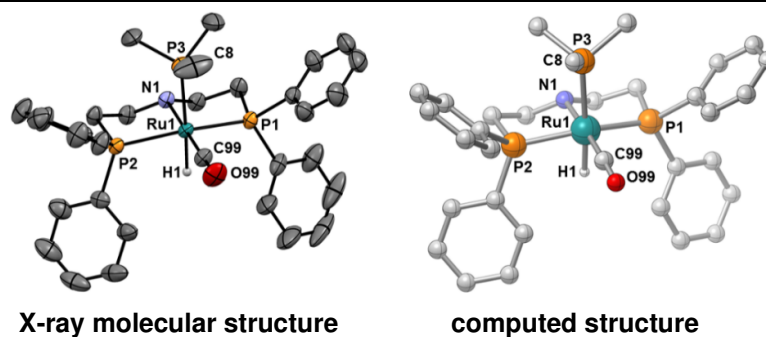


Scheme 3.9: Evaluation of key intermediates in the formation of the presumed dicarbonyl complexes (**9** and **10**) as a potential pathway for the deactivation of **1** and **4** in the presence of MeOH. The Gibbs free energies ΔG^{298} (in kJ mol^{-1}) are given relative to $\text{Ru}^{\text{II}}\text{-PMe}_3$ complex **1** (black) and $\text{Ru}^0\text{-PPh}_3$ complex **4** (blue); RI-PBE0-D3(BJ)/def2-QZVPP//BP86/def2-SV(P); COSMO-RS (toluene).

Throughout the experimental investigations and after these thermodynamic calculations to understand the observed selectivities, crystal structures of various calculated motifs became available and presented an ideal basis for the evaluation of the geometry optimization methodology (BP86/def2-SV(P)). Furthermore, this allows for assessing the accuracy of predicting ligand isomers as well as PNP metallacycle conformations. As discussed above, significant differences between DFT structures in solution and solid-state structures can exist, however, in many cases the differences are rather small.

A selection of distances, bond angles and dihedral angles of the solid-state structure and the computed geometry of the Ru^{II}-PMe₃ complex **1** is listed in Table 3.1. The bond lengths for the Ru–H, Ru–C, Ru–N and Ru–P bonds differ by only 0.01 – 0.05 Å, which is well-in-line with BP86’s general tendency to overestimate bond lengths. The bond angles for important key structural characteristics such as the P–Ru–P or the N–Ru–P angles are very accurately reproduced by the calculations with deviations between 0 and 3°. The dihedral angle C–Ru–P–C shows the largest deviation, which is not surprising as it corresponds to the rotation of the relatively small **PMe**₃ ligand. However, with a difference of 22° between experimental and computed structure, both exhibit the syn-periplanar configuration that would be expected to avoid steric pressure. Overall, the calculation, which was carried out before the crystal structure had been obtained, manages to reproduce the observed conformational isomer of the Ru^{II}-PMe₃ complex **1** with a good accuracy in bond lengths, bond angles, and dihedral angles.

Table 3.1: Selected distances, angles, and dihedral angles of the X-ray molecular structure (CCDC 1958133) and the computed structure of **1**. C-H hydrogen atoms are omitted for clarity. Experiments and characterization were carried out by Daniel J. Tindall and Frank Rominger.



	X-ray molecular structure	computed structure
Ru1–H1	1.62(2) Å	1.63 Å
Ru1–C99	1.8476(18) Å	1.87 Å
Ru1–N1	2.1574(14) Å	2.20 Å
Ru1–P1	2.3037(5) Å	2.34 Å
Ru1–P2	2.3109(5) Å	2.34 Å
Ru1–P3	2.4007(5) Å	2.45 Å
C99–O99	1.157(2) Å	1.18 Å
P1–Ru1–P2	158.523(17)°	158°
N1–Ru1–P3	88.52(4)°	89°
C99–Ru1–N1	178.24(7)°	175°
C99–Ru1–P3	93.03(6)°	95°
O99–C99–Ru1	179.23(19)°	176°
C99–Ru1–P3–C8	–2°	–24°

A similar comparison was carried out for Ru⁰-PPh₃ complex **4** obtained instead of the Ru^{II} species (see Table 3.2). The bond lengths again exhibit a consistent overestimation of up to 0.04 Å for the Ru–C, Ru–N and the three Ru–P bond lengths. The C–O bond length in the carbonyl ligand is slightly underestimated by 0.01 Å. Significantly larger deviations are found for the N–H bond lengths and the H–C(PPh₃) distance, which was included to compare the previously mentioned contact between NH functionality and π system of the triarylphosphine. One should note that experimental hydrogen positions determined by X-ray diffraction analysis usually tend to be too short due to the underlying physics of the method.¹⁴⁹ Therefore, the calculated NH bond lengths are most likely more accurate than the experimental value, although a small overestimation in the calculation might still be expected. The large difference between the C \cdots H distance (between the PNP backbone and the phenyl group of the monodentate phosphine unit) is partly caused by the just discussed deviation in NH bond length and a rotation of the **PPh**₃ group (*vide infra*). The various studied bond angles are well reproduced with a maximum difference of 1° for the P–Ru–P, N–Ru–P, C–Ru–N, C–Ru–P and O–C–Ru angles. Like **1**, the C–Ru–P–C dihedral angle showed a larger deviation than the bond angles. The 10° different angle places the phenyl group, which in both systems assumes an anti-periplanar conformation, more directly over the NH proton. This could also contribute to the significantly shorter C–H distance, which had been mentioned above. Overall, complex **4** is also well-described by density functional theory and the chosen methodological details.

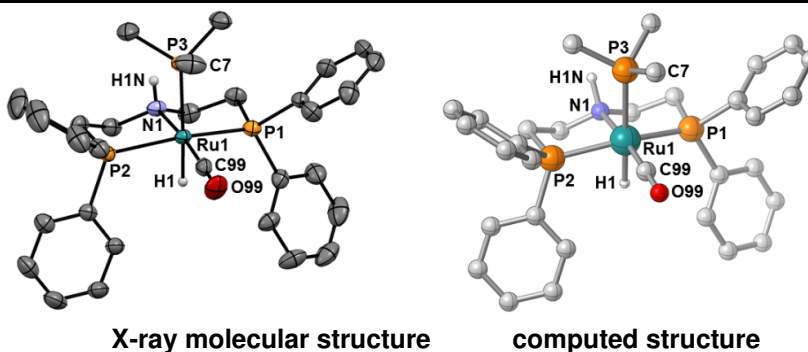
Table 3.2: Selected distances, angles, and dihedral angles of the X-ray molecular structure (CCDC 1958130) and the computed structure of **4**. C-H hydrogen atoms are omitted for clarity. Experiments and characterization were carried out by Daniel J. Tindall and Frank Rominger.

	X-ray molecular structure	computed structure
Ru1–C99	1.809(9) Å	1.84 Å
Ru1–N1	2.246(6) Å	2.29 Å
Ru1–P1	2.296(2) Å	2.33 Å
Ru1–P2	2.307(2) Å	2.33 Å
Ru1–P3	2.3303(15) Å	2.37 Å
N1–H1	0.89(6) Å	1.03 Å
C99–O99	1.193(9) Å	1.18 Å
H1–C71	2.60 Å	2.33 Å
P1–Ru1–P2	122.67(7)°	122°
N1–Ru1–P3	91.68(16)°	92°
C99–Ru1–N1	171.5(3)°	172°
C99–Ru1–P3	96.6(2)°	96°
O99–C99–Ru1	177.1(7)°	178°
C99–Ru1–P3–C71	–166°	–178°

After the two fundamental Ru^{II}/Ru⁰ structures have been observed by NMR spectroscopy, which had led to the start of the detailed DFT study and have also been energetically compared for **PMe**₃ and **PPh**₃ above (see Scheme 3.7), the onium complex **6** was structurally investigated (see Table 3.3). This species represents complex **1** after protonation at the ligand's nitrogen atom by phenol and therefore resembles it in many structural characteristics. Most of the bond lengths exhibit the same trend that was observed in the two previous analyses: a slight overestimation. For **6**, this reaches up to 0.06 Å when looking at Ru–C, Ru–N, C–O and the three Ru–P bonds. Again, more significant differences are obtained for bonds involving hydrogen atoms (Ru–H and N–H), which is expected due to typical underestimations in the experimental determination. The Ru–H bond length is measured to be significantly shorter in this crystal structure compared to **1**, where

experimental and computational lengths only deviated slightly with 1.62 and 1.63 Å. This might be partly caused by a higher polarization of the Ru–H bond in the positively charged complex. This underestimation for bonds with hydrogen originates from the fact that X-ray diffraction analysis is based on the electron density and the only electron of hydrogen is placed in the shared bond. All bond angles are again well described (P–Ru–P, N–Ru–P, C–Ru–N, C–Ru–P, O–C–Ru, and Ru–N–H) and the dihedral angles are similarly to the previous **PMe**₃-coordinated system in slightly lower agreement due to the high torsional flexibility of the **PMe**₃ group.

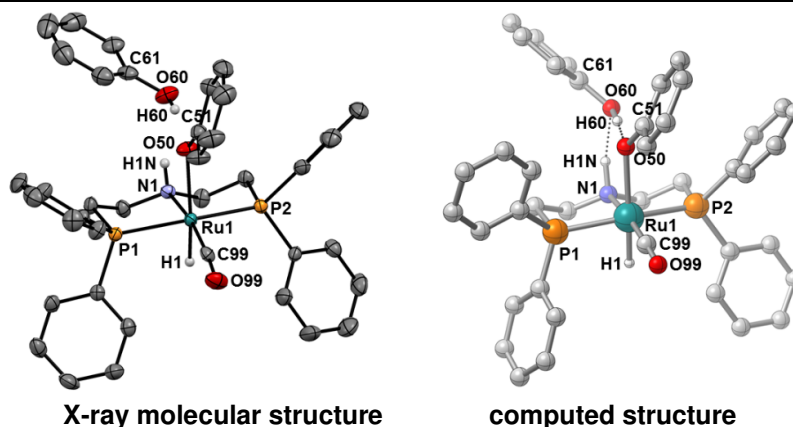
Table 3.3: Selected distances, angles, and dihedral angles of the X-ray molecular structure (CCDC 1958131) and the computed structure of **6**. C-H hydrogen atoms were omitted for clarity. Experiments and characterization were carried out by Daniel J. Tindall and Frank Rominger.



	X-ray molecular structure	computed structure
Ru1–H1	1.55(2) Å	1.64 Å
Ru1–C99	1.833(3) Å	1.85 Å
Ru1–N1	2.194(2) Å	2.24 Å
Ru1–P1	2.3152(8) Å	2.35 Å
Ru1–P2	2.3233(8) Å	2.35 Å
Ru1–P3	2.4170(7) Å	2.48 Å
C99–O99	1.161(3) Å	1.18 Å
N1–H1N	0.82(3) Å	1.10 Å
P1–Ru1–P2	160.59(3)°	159°
N1–Ru1–P3	91.46(6)°	94°
C99–Ru1–N1	173.22(10)°	173°
C99–Ru1–P3	95.17(9)°	93°
O99–C99–Ru1	177.6(3)°	178°
Ru1–N1–H1N	112(2)°	109°
H1N–N1–Ru1–C7	4°	–7°
C99–Ru1–P3–C7	–8°	12°

Lastly, the solid-state structure of the investigated phenolato complex is compared to the corresponding DFT structure (**5**; see Table 3.4). This comparison further supports the evaluation that the theoretical methods are capable of accurately describing the geometries of the investigated ruthenium PNP complexes. Bond lengths apart from hydrogen-containing bond lengths only show small deviations. Similar to above, the bond angles and dihedral angles also fit reasonably well.

Table 3.4: Selected distances, angles, and dihedral angles of the X-ray molecular structure (CCDC 1958136) and the computed structure of **5**. C-H hydrogen atoms were omitted for clarity. Experiments and characterization were carried out by Daniel J. Tindall and Frank Rominger.



	X-ray molecular structure	computed structure
Ru1–H1	1.50(4) Å	1.61 Å
Ru1–C99	1.811(4) Å	1.84 Å
Ru1–N1	2.200(3) Å	2.25 Å
Ru1–P1	2.3102(12) Å	2.35 Å
Ru1–P2	2.3280(12) Å	2.34 Å
Ru1–O50	2.234(3) Å	2.29 Å
C99–O99	1.173(5) Å	1.18 Å
N1–H1N	0.86(4) Å	1.05 Å
H1N–O60	2.17 Å	1.77 Å
O60–H60	0.73(6) Å	1.10 Å
H60–O50	1.80 Å	1.39 Å
P1–Ru1–P2	163.24(4)°	163°
N1–Ru1–O50	84.49(12)°	86°
C99–Ru1–N1	167.39(16)°	171°
C99–Ru1–O50	107.99(15)°	102°
O99–C99–Ru1	172.4(4)°	176°
Ru1–N1–H1N	111(3)°	104°
H1N–N1–Ru1–O50	1°	0°
C99–Ru1–O50–C51	6°	18°

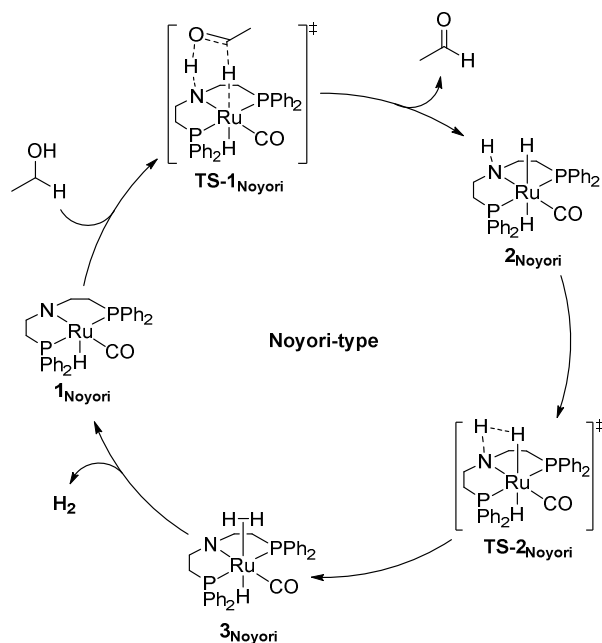
All in all, the initial calculations helped to provide understanding for the observed formation of two significantly different species when trying to stabilize the activated Ru-MACHO species, Ru^{II}-PMe₃ and Ru⁰-PPh₃. They are also able to explain the different reactivity towards alcohols and support the formation of dicarbonyl complexes after the reaction with methanol, which could not be unambiguously identified experimentally. An in-depth comparison of computed structures and measurements by X-ray diffraction analysis verified the good ability of density functional theory to reproduce experimental structures, which serves as the basis for the assumption that the computational method is well suited to accurately predict reactive intermediates, which cannot be probed by experimental means.

3.3.2 Noyori-type Dehydrogenation Pathway

After the formation of the Ru^{II}-PMe₃ and Ru⁰-PPh₃ complexes **1** and **4** have been rationalized and the capabilities of DFT to accurately model the ruthenium complexes have been shown, the efforts shifted towards calculating possible reaction pathways for the dehydrogenative coupling of alcohols to esters. Similar to the various groups that have been working towards developing the multitude of available catalytic systems (*vide supra*), a number of mechanistic investigations – mainly employing DFT calculations – have been reported for (de-)hydrogenation with pincer-type catalysts. In 2016, Matthias Beller and co-workers have published a detailed investigation for a Ru-MACHO-type complex, in which the PNP ligand carries *tert*-butyl groups.¹²⁹ Chen *et al.* have reported investigations into ruthenium complexes employing sulfur-nitrogen-sulfur pincer ligands, which have been popularized by Gusev and co-workers.¹⁵⁰ Similarly, Milstein's Ru-PNN system, which is proposed to work via aromatization/dearomatization pathways,¹⁵¹⁻¹⁵² and other related systems¹⁵³⁻¹⁵⁴ have been computationally studied. At the time, our team was only aware of two other computational investigations that had employed the Ru-MACHO system without any simplifications in the structural complexity to reduce computational cost: Firstly, Jiang *et al.* investigated the reaction mechanism for the MeOH-to-carbonate dehydrogenation.¹⁵⁵ However, methanol with its small size can significantly differ from other larger substrates such as ethanol or hexanol, which were used in this work and might interact differently with the Ru-PNP complex.¹⁵⁶⁻¹⁵⁹ This was also exemplified by the reactivity towards MeOH observed in this work (*vide supra*). Secondly, a recent report on the β methylation by Kaithal *et al.* included several reaction steps, which also played a major role in our investigation (see Section 3.3.3).¹⁶⁰ However, this investigation did not include any alternative mechanistic scenarios or a discussion of the relevant resting states. Several points were therefore identified that were specifically of interest in the context of this investigation: (a) the resting state of the catalyst especially with respect to the two experimentally observed species, the Ru^{II}-PMe₃ complex **1** and the Ru⁰-PPh₃ complex **4**, (b) the specific role of the NH function of the PNP backbone in the reaction mechanism, (c) an investigation of all possible reaction pathways and (d)

identifying whether the ruthenium oxidation state (Ru^{II} vs. Ru^0) leads to significant differences in the accessible pathways.

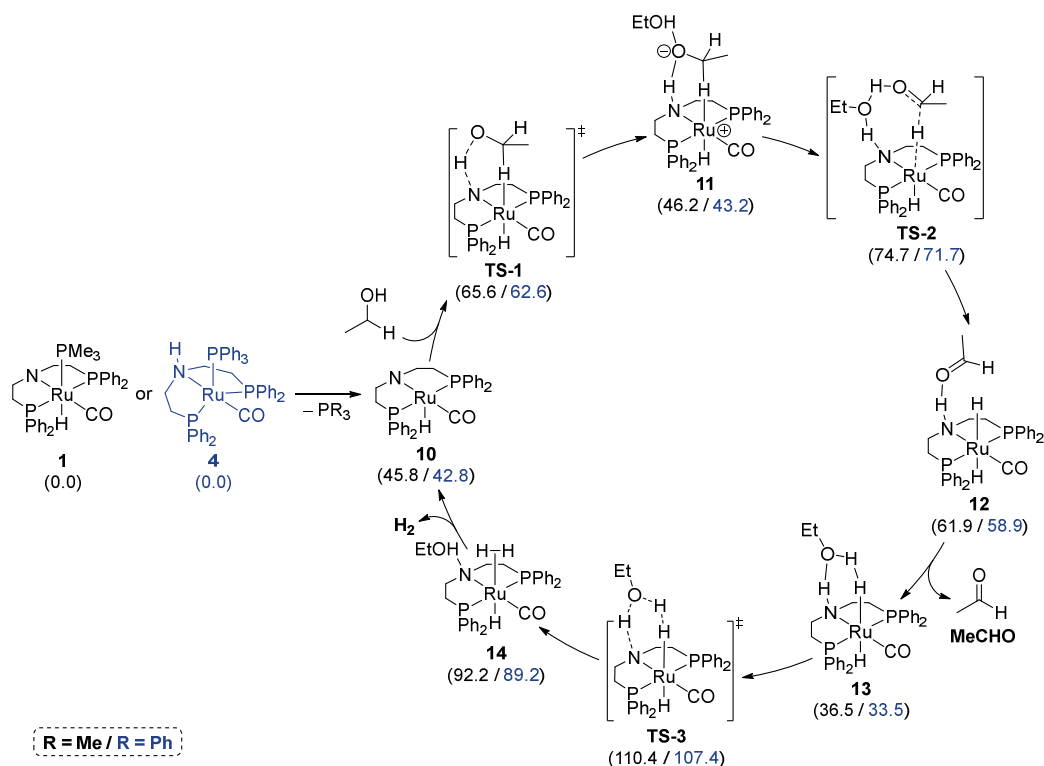
Most publications suggests that the (de-)hydrogenation takes place via a Noyori-type mechanism that employs metal-ligand cooperation (MLC) to achieve the required chemical transformations. The mechanism is named after Ryōji Noyori, who was awarded the 2001 Nobel prize in Chemistry for his work on asymmetric hydrogenations with ruthenium complexes employing chiral bidentate BINAP ligands, for which these mechanisms were first suggested.^{151, 161-164} The regularly proposed steps of the Noyori-type mechanism adapted to the herein investigated Ru-MACHO system are shown in Scheme 3.10. The catalytic cycle starts from the activated Ru-MACHO species ($\mathbf{1}_{\text{Noyori}}$), from which the concerted transfer of OH and CH protons of ethanol to NH proton and Ru hydride takes place ($\text{TS-1}_{\text{Noyori}}$). This directly leads to formation of the dehydrogenated product (acetaldehyde) and the formation of the Ru dihydride complex $\mathbf{2}_{\text{Noyori}}$. Subsequent intramolecular proton transfer $\text{TS-2}_{\text{Noyori}}$ to ruthenium leads to formation of the dihydrogen complex $\mathbf{3}_{\text{Noyori}}$, which can liberate H_2 to regenerate the activated Ru-MACHO species and close the catalytic cycle. For the hydrogenation of acetaldehyde, the catalytic cycle will proceed in reverse order with addition of H_2 . Very recently, it has been shown that alcohol-assisted transition states for the generation of H_2 might be preferred,^{150, 165-167} but unassisted species are still commonly proposed.



Scheme 3.10: Proposed catalytic cycle for the dehydrogenation of ethanol to acetaldehyde catalyzed by a Ru-PNP complex analogously to the proposed mechanisms by Noyori *et al.*¹⁶¹

The calculations on the Noyori-type dehydrogenation of ethanol to acetaldehyde (**MeCHO**) with the phosphine-stabilized Ru-MACHO species **1** and **4** begin with the formation of activated Ru-MACHO species **10** (see Scheme 3.11). For Ru^{II}-PMe₃ complex **1**, species **10** can simply be generated by dissociation of PMe₃ (**1**→**10**: $\Delta G^{383} = 45.8 \text{ kJ mol}^{-1}$). On the other hand, the generation of **10** from Ru⁰-PPh₃ species **4** requires prior isomerization to the respective Ru^{II}-PPh₃ species **3** (*vide supra*). While this has not been thoroughly investigated, the initial generation of this species, which takes place from **10**, already strongly suggests the availability of this reaction pathway (**4**→**10**: $\Delta G^{383} = 42.8 \text{ kJ mol}^{-1}$). From here, the reaction with ethanol was found to proceed differently as usually proposed and no concerted transfer step for both protons could be located (cf. **TS-1**_{Noyori}). Stepwise transfer can take place via **TS-1**, which describes the proton transfer from the oxygen to the nitrogen atom of the PNP ligand ($\Delta G^\ddagger = 65.6$ and 62.6 kJ mol^{-1} for **1** and **4**, respectively), and **TS-2**, which introduces the Ru hydride moiety by transferring the second hydrogen atom from the carbon center ($\Delta G^\ddagger = 74.7$ and 71.7 kJ mol^{-1} for **1** and **4**, respectively). **TS-1** and **TS-2** are connected by intermediate **11** ($\Delta G^{383} = 46.2$ and 43.2 kJ mol^{-1} for **1** and **4**, respectively), in which the anionic ethanolate fragment is exhibiting stabilizing Ru–H and O–H interactions as well as being stabilized by a second equivalent of ethanol (**EtOH**). This substrate-stabilization is also observed in the molecular transformation step via **TS-2**, where an **EtOH** molecule interacting with the substrate and the PNP ligand allows for more structural flexibility. An unassisted TS (i.e., without additional **EtOH**) for this step was found to be slightly less stable (**TS-2**_{unassisted}: $\Delta G^\ddagger = 72.6$ and 69.6 kJ mol^{-1} for **1** and **4**, respectively). After **TS-2**, **MeCHO** initially remains attached to the Ru dihydride complex forming an O–H interaction with the NH functionality (**12**: $\Delta G^{383} = 61.9$ and 58.9 kJ mol^{-1} for **1** and **4**, respectively), which will subsequently be replaced by **EtOH**, which provides significantly better stabilization (**13**: $\Delta G^{383} = 36.5$ and 33.5 kJ mol^{-1} for **1** and **4**, respectively) and leads to liberation of the desired **MeCHO** product. From **13**, a hydrogen shuffle step leads to the formation of dihydrogen η^2 -coordinated to ruthenium (**TS-3**: $\Delta G^\ddagger = 110.4$ and $107.4 \text{ kJ mol}^{-1}$ for **1** and **4**, respectively). The transition state, which corresponds to the unassisted proton transfer (cf. **TS-2**_{Noyori}) and is usually proposed to take place, was found to be over 40 kJ mol^{-1} less feasible than **TS-3** (**TS-3**_{unassisted}: $\Delta G^\ddagger = 151.7$ and $148.7 \text{ kJ mol}^{-1}$ for **1** and **4**, respectively) and should not play a role in the Ru-MACHO system. **TS-3** leads to **14**, which corresponds to **3**_{Noyori} with additional **EtOH** stabilization (**14**: $\Delta G^{383} = 92.2$ and 89.2 kJ mol^{-1} for **1** and **4**, respectively) and is ca. 15 kJ mol^{-1} more stable than the stabilized dihydrogen complex (**14**_{unstabilized}: $\Delta G^{383} = 107.4$ and $104.4 \text{ kJ mol}^{-1}$ for **1** and **4**, respectively). Finally, regeneration of the activated Ru-MACHO species takes place via liberation of H₂. The proton shuffle transition state **TS-3** represents the rate-determining barrier for the dehydrogenation of ethanol to acetaldehyde with the Ru-MACHO catalyst following the Noyori-type reaction pathways. With barriers of 110.4 and $107.4 \text{ kJ mol}^{-1}$ for the Ru⁰-PMe₃

and Ru⁰-PPh₃ systems, respectively, similar experimental observations (e.g., in terms of activity) are expected for both catalysts.

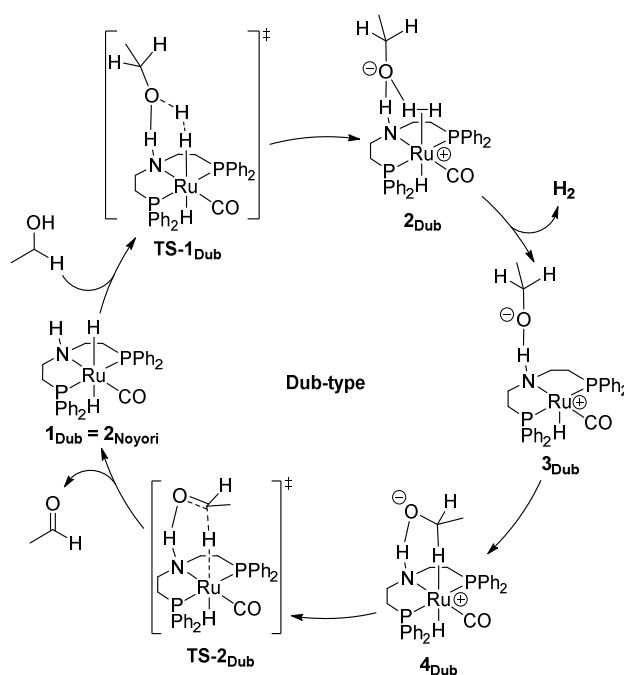


Scheme 3.11: Catalytic cycle for the Noyori-type dehydrogenation of ethanol to acetaldehyde. The Gibbs free energies ΔG^{383} (in kJ mol⁻¹) are given relative to Ru^{II}-PMe₃ complex **1** (black) and Ru⁰-PPh₃ complex **4** (blue). Mass balance for additional stabilizing substrate equivalents is ensured in the entire scheme; RI-PBE0-D3(BJ)/def2-QZVPP//BP86/def2-SV(P); COSMO-RS (toluene).

3.3.3 Dub-type Dehydrogenation Pathway

More recently, Pavel A. Dub, John C. Gordon and co-workers from Los Alamos National Laboratory have thoroughly investigated the reaction mechanism for (de-)hydrogenations with Noyori's bidentate^{154, 165, 168-169} and Milstein's tridentate PNN ligand.¹⁵¹ The team has provided extensive evidence that not only reaction pathways involving metal-ligand cooperation are accessible (*vide supra*) but non-cooperative pathways (i.e., not requiring the cleavage of the N-H bond in the ligand backbone) are competing with the pathways that were originally proposed by Noyori and suggested by many other groups for their (de-)hydrogenation catalysts carrying pincer-type ligands. Dub *et al.* have used the term metal-ligand assisted (MLA) catalysis for this as the N-H bond in the ligand backbone is not cleaved, but the NH group is still involved in the transformations via a hydrogen-bonding network. Adapting their suggested key reaction to the Ru-MACHO catalyst system led to Scheme 3.12, which starts from Ru dihydride complex **1**_{Dub}, which corresponds to **2**_{Noyori} (or

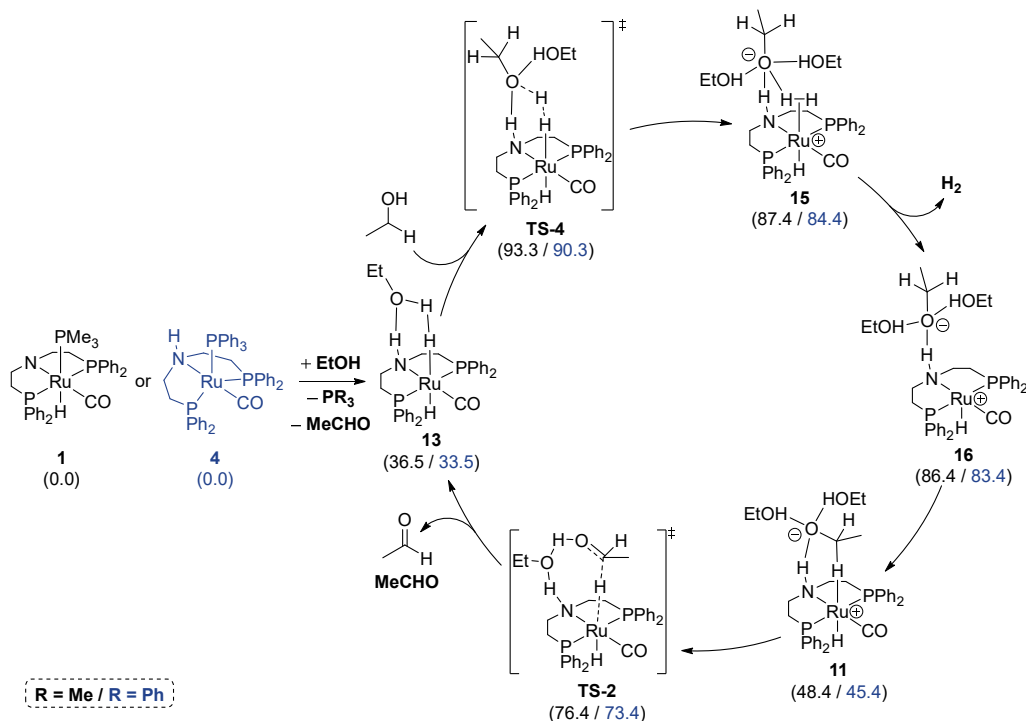
calculated complexes **12/13** without acetaldehyde/ethanol stabilization). The reaction proceeds via **TS-1_{Dub}**, which is closely related to the **EtOH**-assisted proton shuffle transition state **TS-3** in the Noyori-type cycle. However, instead of a proton shuffle, **TS-1_{Dub}** is characterized by a proton transfer forming a cationic dihydrogen complex and an ethanolate anion, which forms H-bond interactions with the NH functionality and one of the dihydrogen atoms. Subsequently, H₂ elimination leads to formation of **3_{Dub}**, which represents a backbone-protonated equivalent of the activated Ru-MACHO species (**1_{Noyori}**). The ethanolate anion can rearrange within the ion pair to form a Ru–H interaction (**4_{Dub}**), which sets the stage for hydrogen transfer to ruthenium, forming acetaldehyde and the Ru dihydride starting complex **1_{Dub}** via **TS-2_{Dub}**.



Scheme 3.12: Proposed catalytic cycle for the dehydrogenation of ethanol to acetaldehyde catalyzed by a Ru-PNP complex analogously to the proposed mechanisms by Dub *et al.*^{151, 165, 168-169}

From the calculated Ru dihydride complex **13** ($\Delta G^{383} = 36.5$ and 33.5 kJ mol⁻¹ for **1** and **4**, respectively), the Dub-type catalytic cycle proceeds via the previously discussed proton transfer transition state **TS-4**, which is associated with barriers of 93.3 and 90.3 kJ mol⁻¹ for Ru^{II}-PMe₃ catalyst **1** and Ru⁰-PPh₃ catalyst **4**, respectively (see Scheme 3.13). In this transition state, the ethanol molecule is stabilized by a second equivalent of ethanol. The corresponding non- and twice-stabilized transition states were attempted to be located. However, the non-stabilized transition state could not be located, and the twice-stabilized TS was found to be less feasible than **TS-4** (**TS-4_{twice-stabilized}**: $\Delta G^\ddagger = 103.6$ and 100.6 kJ mol⁻¹ for **1** and **4**, respectively; see Scheme 3.14). This leads to formation of the cationic dihydride complex **15**, which was found to be most stable with two stabilizing **EtOH** molecules (ΔG^{383}

= 87.4 and 84.4 kJ mol⁻¹ for **1** and **4**, respectively). Liberation of H₂ from **15** leads to the equally cationic **16** ($\Delta G^{383} = 87.4$ and 84.4 kJ mol⁻¹ for **1** and **4**, respectively), which leaves the Ru center with a significant electron-deficiency. This deficiency can be satisfied by intramolecular rearrangement of the anionic ethanolate fragment to form intermediate **11**, which exhibits a stabilizing Ru–H interaction and has been previously computed as the intermediate in the stepwise proton transfer of the adapted Noyori-type cycle ($\Delta G^{383} = 48.4$ and 45.4 kJ mol⁻¹ for **1** and **4**, respectively; cf. Scheme 3.11). Similarly, the subsequent **TS-2** represents the second step of the Noyori-type proton transfer and leads to the final formation of acetaldehyde in both catalytic cycles. However, **TS-2** is not the rate-determining transition state along the two reaction pathways, which are **TS-3** in the Noyori-type mechanism and **TS-4** in the Dub-type mechanism. **TS-4** of the Dub-type mechanism, which is discussed in this section, is associated with activation barriers of 93.3 and 90.3 kJ mol⁻¹ for Ru^{II}-PMe₃ complex **1** and Ru⁰-PPh₃ complex **4**, respectively.



Scheme 3.13: Catalytic cycle for the Dub-type dehydrogenation of ethanol to acetaldehyde. The Gibbs free energies ΔG^{383} (in kJ mol⁻¹) are given relative to Ru^{II}-PMe₃ complex **1** (black) and Ru⁰-PPh₃ complex **4** (blue). Mass balance for additional stabilizing substrate equivalents is ensured in the entire scheme; RI-PBE0-D3(BJ)/def2-QZVPP//BP86/def2-SV(P); COSMO-RS (toluene).

The initial generation of an on-cycle species for the Dub-type catalytic cycle can be envisioned to take place via two reaction pathways. Firstly, formation of the dihydride complex **13** can take place via the early reaction steps of the Noyori-type catalytic cycle (**1**→**10**→**TS-1**→**11**→**TS-2**→**12**→**13**; see Figure 3.2), which are all lower in energy than the rate-

determining barrier of the Dub-type pathways (**TS-4**). Secondly, direct protonation of **10** to **16** by ethanol could also enable access to the Dub-type cycle. However, both pathways are based on the formation of the activated Ru-MACHO species **10**, which requires cleavage of the NH functionality and therefore does not seem to offer the possibility for replacement of this functionality. On the other hand, this knowledge significantly helps with the rational design of new and improved catalysts. A further pathway, which provides access to the desired dihydride complex without cleavage of the NH bond is presented in Section 3.3.4.

For better comparison of the two presented reaction pathways, the Noyori- and Dub-type mechanisms are shown in Figure 3.2 for the Ru^{II}-PMe₃ catalyst. The potential energy surface based on Ru⁰-PPh₃ complex **4** is not shown here as it only differs from the Ru^{II}-PMe₃ by 3.0 kJ mol⁻¹. In Figure 3.2, the pathway for the generation of Dub-type on-cycle species **13** can be easily identified, which is readily available next to the significantly higher reaction barriers of **TS-3** and **TS-4** ($\Delta G^\ddagger = 110.4$ and 93.3 kJ mol⁻¹ for **TS-3** and **TS-4**, respectively). The potential energy surface is also well suited to show the drastic difference in the rate-determining reaction barrier between the two different pathways and highlights that the Dub-type pathway is also significantly favored in the case of the employed Ru-MACHO catalyst, which has not been quantum-chemically investigated before.

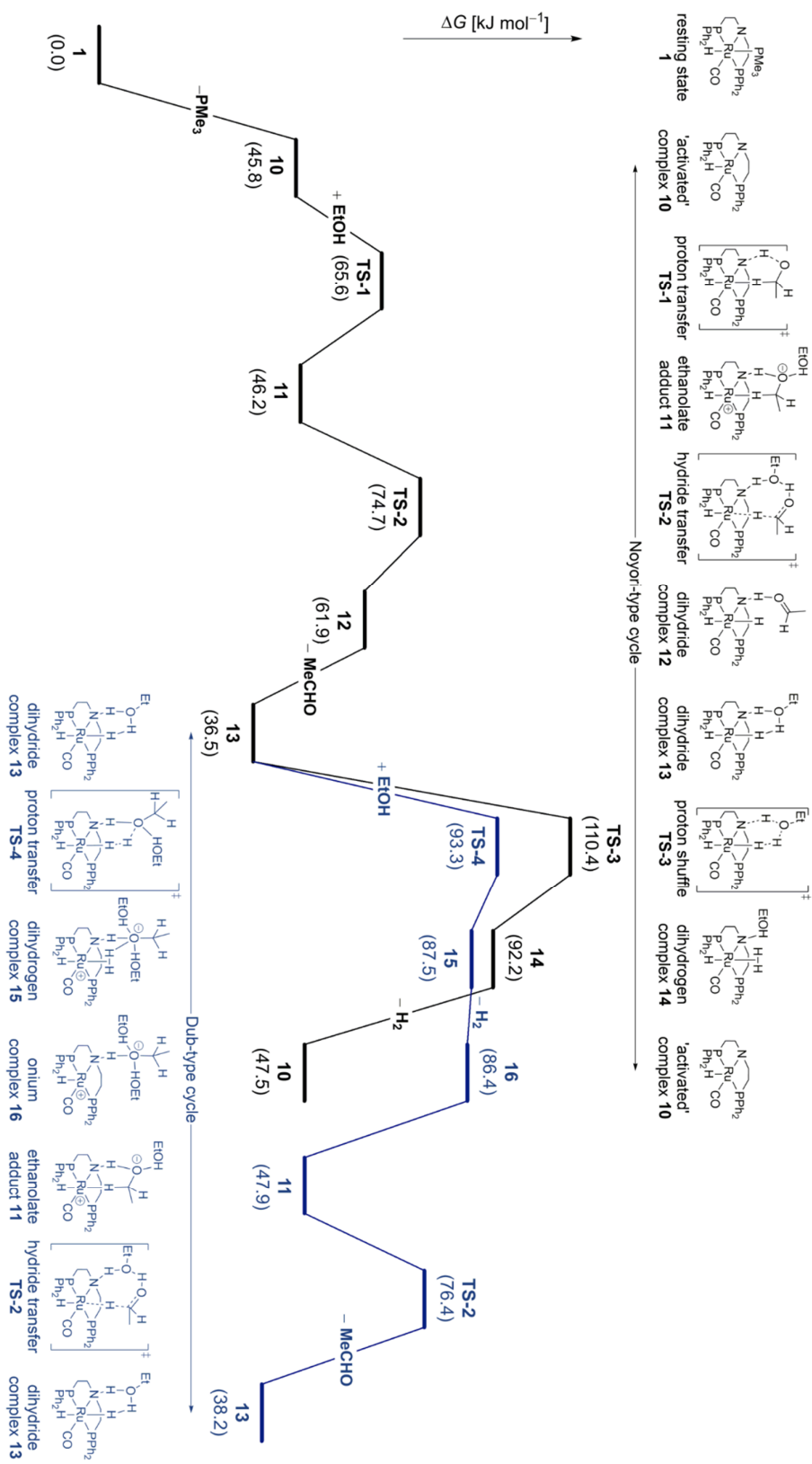
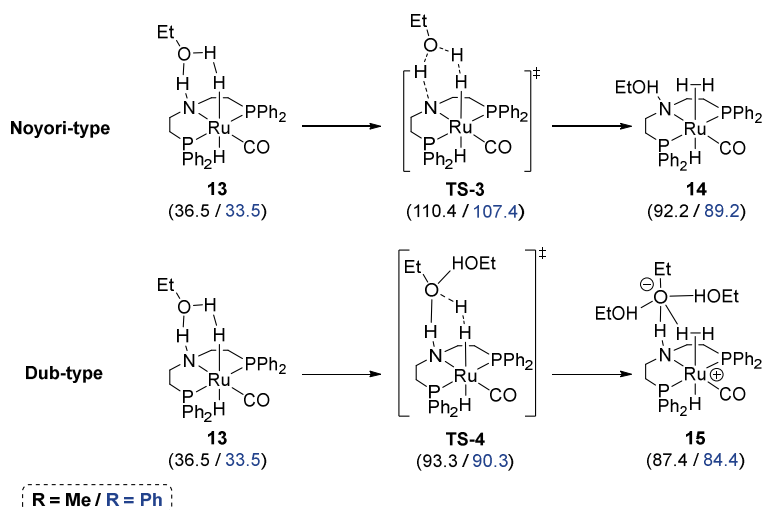
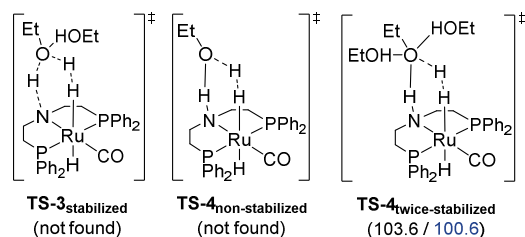


Figure 3-2: Noyori- (black) and Dub-type (blue) lowest energy pathways for the dehydrogenation of ethanol to acetaldehyde with $\text{Ru}^{\text{II}}\text{-PMe}_5$ complex **1**. Mass balance for additional stabilizing substrate equivalents is ensured in the entire scheme. ΔG^{383} in kJ mol^{-1} ; Ru -PBE0-D3(BJ)/def2-QZVPP//BP86/def2-SV(P); COSMO-RS (toluene).

Lastly, to enable a better comparison of the rate-determining steps and discuss the important influence of additional stabilizing substrate molecules, Scheme 3.14 summarizes the stabilized and non-stabilized structures of **TS-3** (in the Noyori-type reaction pathway) and **TS-4** (in the Dub-type reaction pathway). **TS-3** and **TS-4** both start from the ethanol-stabilized ruthenium dihydride complex **13** and represent a dividing point in the complex network of chemical transformations. While **TS-3** is a proton shuffle transition state, in which the assisting **EtOH** molecule will transfer its OH proton and will receive the NH proton of the ligand backbone, **TS-4** represents a ‘simple’ proton transfer. The substrate will transfer its OH proton without accepting another proton, which leads to the NH functionality remaining intact in the subsequent intermediate **15**. With these two transition states being structurally very close, the result from a geometry optimization attempt will be mainly determined by the electronic properties of the system. Stabilization of the **EtOH** oxygen atom will favor the formation of an anionic species, which forms strong interactions with the stabilizing substrate equivalents (e.g., in **TS-4**, **TS-4_{twice-stabilized}**, and **15**). On the other hand, the stabilization will disfavor the shuffle mechanism, which is built on the concept that the oxygen atom is ready to accept the proton of the NH group. This trend is also observed when looking at the structures that could be characterized. The ‘unstabilized’ proton shuffle transition state **TS-3** (not counting the **EtOH** molecule directly involved in the proton shuffle) could be located, while the stabilized version evaded characterization. On the contrary, attempts to locate **TS-4_{non-stabilized}** failed and the characterization of both, **TS-4** (once stabilized) and **TS-4_{twice-stabilized}**, were successful.



Further less feasible transition states:



Scheme 3.14: Formation of the dihydrogen complexes **14** and **15** from complex **13** in the Noyori- and Dub-type mechanisms, respectively. The Gibbs free energies ΔG^{383} (in kJ mol^{-1}) are given relative to $\text{Ru}^{\text{II}}\text{-PMe}_3$ complex **1** (black) and $\text{Ru}^{\text{0}}\text{-PPh}_3$ complex **4** (blue). Mass balance for additional stabilizing substrate equivalents is ensured in the entire scheme; RI-PBE0-D3(BJ)/def2-QZVPP//BP86/def2-SV(P); COSMO-RS (toluene).

To further illustrate the structural overlap of these two transition states that makes the characterization of the two species so difficult, the computed molecular structures of **TS-3** and **TS-4** are compared (see Figure 3.3). **TS-3** exhibits an N–H distance of 1.26 Å, an (N)H–O distance of 1.28 Å, an O–H(H) distance of 1.84 Å and a dihydrogen H–H bond length of 0.86 Å. In **TS-4**, the N–H bond length is 0.1 Å shorter than in **TS-3**, which is in line with expectations that this would be shorter as the hydrogen atom remains bound to nitrogen, however, the difference is extremely small. The associated O–H distance is extended by slightly more than 0.1 Å (1.40 Å) which is mainly caused by the change in hydrogen position, meaning that the spacial positioning of the ethanol molecule is nearly identical. The main difference between the two structures, **TS-3** and **TS-4**, is the O–H(H) distance of the two compounds with the distance being 0.59 Å longer in **TS-4** (2.43 Å). This also leads to a small rotation of the dihydrogen fragment in **TS-4**, for which the H–H bond length with 0.85 Å is nearly identical to the 0.86 Å found in **TS-3**. However, these structural changes are very small and have made the characterization of the different species highly difficult.

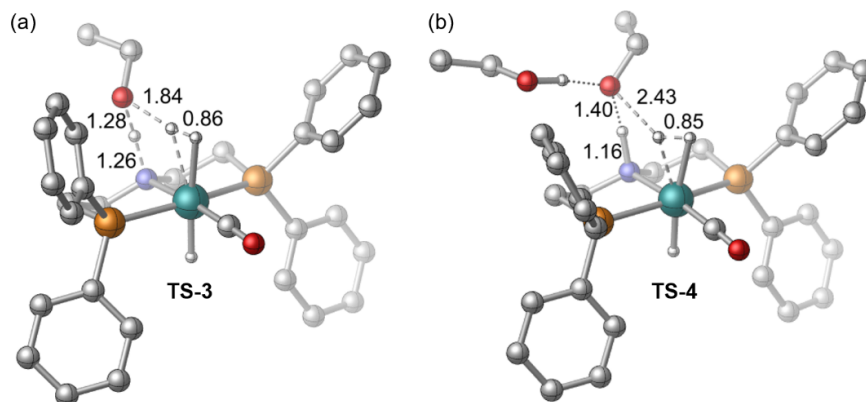


Figure 3.3: Computed molecular structures with selected bond lengths around the active center for (a) **TS-3** and (b) **TS-4**. ΔG^{383} in kJ mol^{-1} ; RI-PBE0-D3(BJ)/def2-QZVPP//BP86/def2-SV(P); COSMO-RS (toluene).

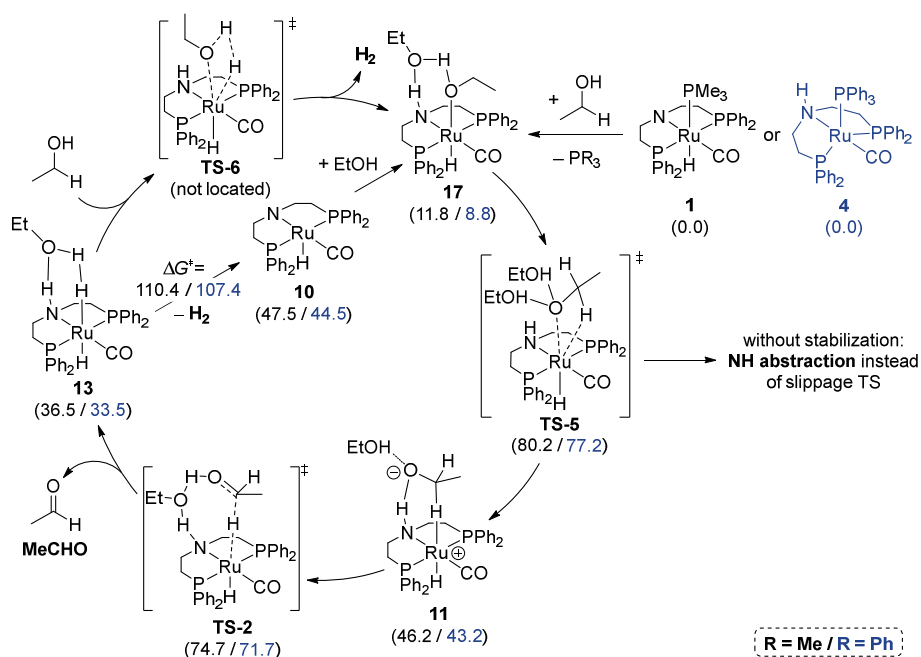
Overall, the investigations into the Dub-type pathway revealed a complex set of reaction steps that is closely interwoven with the Noyori-type pathway. It exhibits a lower activation barrier for the generation of acetaldehyde than the Noyori-type mechanism and shows that the metal-ligand assisted pathway (without NH cleavage) is favored over the classically proposed metal-ligand cooperative transformation (with NH cleavage). However, both mechanisms are feasible at reaction conditions and a combination of the two pathways might be responsible for the high activity that is observed. Once more, this also exemplifies the importance of a thorough DFT investigation considering all possible pathways.

3.3.4 Other Investigated Dehydrogenation Pathways

The Noyori- and Dub-type catalytic cycles both require the dissociation of the respective phosphine from the $\text{Ru}^{\text{II}}\text{-PMe}_3$ and $\text{Ru}^0\text{-PPh}_3$ pre-catalysts to form an on-cycle species. Although pathways are available for the formation of the activated Ru-MACHO species (**10**), the Ru dihydride complex **13** and the cationic Dub intermediate **16** (*vide supra*), these pathways all require reversible N–H deprotonation. Substitution of the proton of the NH functionality could help to increase catalyst stability as alkylation of this position is a relevant factor in the degradation of the Ru-MACHO complex at reaction conditions,¹³⁴ which leads to the tetradentate Ru-Phoenix complex (see Scheme 3.2). Moreover, reaction mechanisms, in which the additional phosphine fragment remains coordinated to the Ru center were of high interest as this would allow for further tunability of the catalyst system by employing different phosphines.

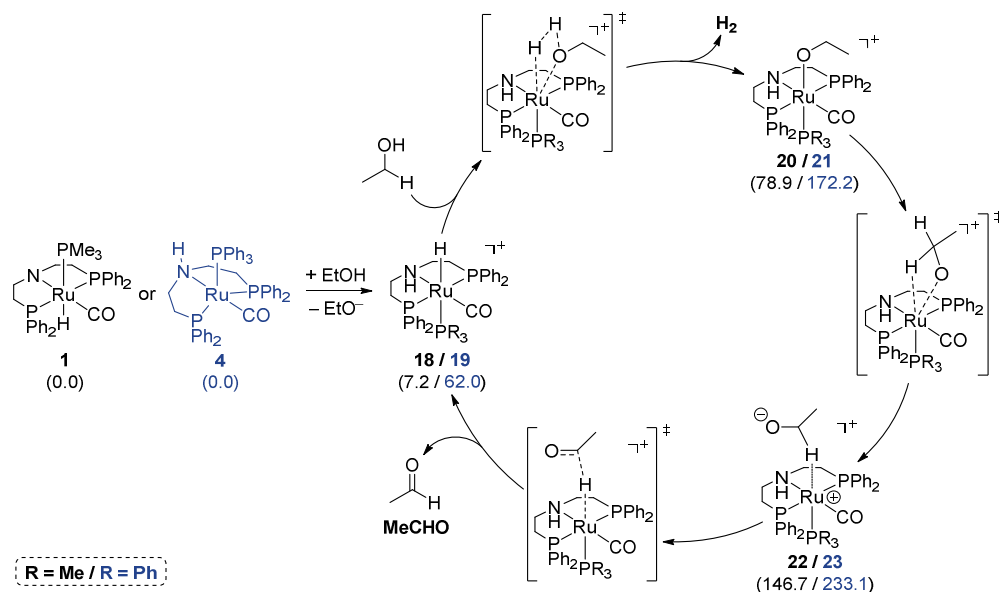
A reaction pathway based on ‘slippage’ of an alkoxy fragment was investigated (see Scheme 3.15). Similar pathways had been proposed and calculated by Goldman and co-workers in their work on the hydrogenation of dimethyl carbonate with Milstein’s PNN catalyst system.¹⁷⁰ This pathway starts with the formation of the stabilized Ru^{II} ethoxy complex **17**, which is analogous to the **PhOH**-stabilized phenoxy system **5** that has been

previously discussed as part of the rationalization of chemoselectivities (see Scheme 3.8 and Table 3.4). From **17** ($\Delta G^{383} = 11.8$ and 8.8 kJ mol⁻¹ for **1** and **4**, respectively), ‘slippage’ takes place via **TS-5** with moderate barriers of 80.2 and 77.2 kJ mol⁻¹ with respect to Ru^{II}-PMe₃ complex **1** and Ru⁰-PPh₃ complex **4**. In this transition state, the oxygen center is stabilized by two substrate molecules to support the formation of the anionic ethanolate fragment (**11**: $\Delta G^{383} = 46.2$ and 43.2 kJ mol⁻¹ for **1** and **4**, respectively). Attempts to locate unstabilized versions of **TS-5** remained unsuccessful and led to H abstraction at the NH position instead of the desired transition states. The activation barrier of **TS-5** is 14.6 kJ mol⁻¹ higher in energy than the barrier associated with **TS-1**, which leads to formation of **11** along the Noyori-type reaction pathway. To further investigate potential catalytic pathways that preserve the NH functionality a concerted formation of the alkoxy ligand and H₂ was tested (**TS-6**) but could not be located. In any case, conversion of ethanol to acetaldehyde can take place via the Dub-type cycle, which was reached via **TS-5** and is based on metal-ligand assistance without NH cleavage (as opposed to non-innocent metal-ligand cooperativity in the Noyori-type cycle). However, innocent regeneration of the pre-catalysts **1** or **4** can only take place via reverse reaction over **TS-5**, which is only accessible when the formed acetaldehyde has not reacted to the desired ester product. Alternatively, regeneration of **17** (and subsequently **1** and **4**) can take place via the activated Ru-MACHO species **10** as part of the Noyori-type mechanism. However, this is associated with NH cleavage and a significantly higher activation barrier (**TS-3**: $\Delta G^\ddagger = 110.4$ and 107.4 kJ mol⁻¹ for **1** and **4**, respectively). Overall, the alkoxy ‘slippage’ presents a highly interesting pathway that can lead to generation of Dub-type intermediates without cleavage of the NH bond in the PNP ligand with only a slightly higher barrier than NH cleavage.



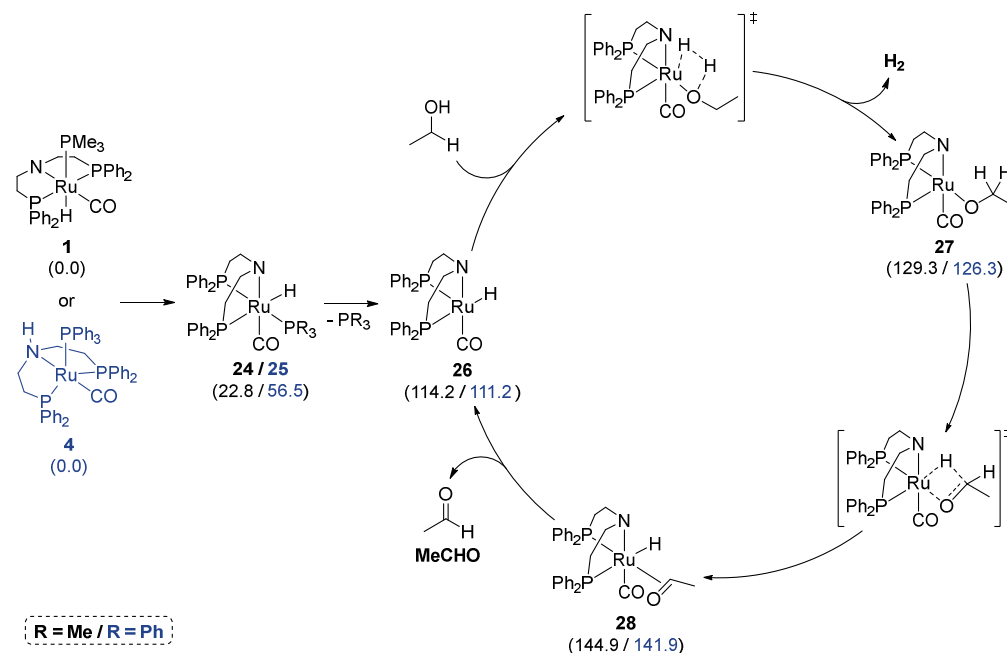
Scheme 3.15: Catalytic cycle for the dehydrogenation of ethanol via a ‘slippage’ pathway (**TS-5**) to avoid reversible N–H deprotonation. The Gibbs free energies ΔG^{383} (in kJ mol^{-1}) are given relative to Ru^{II}-PMe₃ complex **1** (black) and Ru⁰-PPh₃ complex **4** (blue). Mass balance for additional stabilizing substrate equivalents is ensured in the entire scheme; RI-PBE0-D3(BJ)/def2-QZVPP//BP86/def2-SV(P); COSMO-RS (toluene).

Due to this relatively low energy barrier of the ‘slippage’ transition state, another similar pathway was investigated. Herein, the ‘slippage’ was envisioned to take place in *trans* position to the phosphine ligand that remains coordinated to the Ru center (see Scheme 3.16). Initially, only the cationic intermediates along the reaction pathway were calculated to evaluate whether further investigations into this pathway are justified. The catalytic cycle starts with the generation of experimentally observed ion pairs **18** or **19** for the **PMe₃** and **PPh₃** complexes, respectively. Note that the cations in **18** and **19** are identical to the cations in **6** and **7** (see Scheme 3.8 and Table 3.3) but are separately listed due to being calculated with the ethanolate anion instead of the phenolate anion. A dihydrogen elimination transition state was envisioned that would lead to the cationic ethoxy complexes **20** and **21** ($\Delta G^{383} = 78.9$ and $172.2 \text{ kJ mol}^{-1}$ for **PMe₃** and **PPh₃**, respectively), which is significantly less feasible for the bulky **PPh₃** ligand and in line with the previously discussed steric hinderance in octahedral **PPh₃** systems. The cationic ‘slippage’ transition state would lead to complexes **22** and **23**, which exhibit the already observed Ru–H contacts. However, these species are very high in energy (**22**: $\Delta G^{383} = 146.7 \text{ kJ mol}^{-1}$; **23**: $\Delta G^{383} = 233.1 \text{ kJ mol}^{-1}$), rendering this pathway unfeasible. Due to the instable nature of the investigated intermediates along the envisioned pathway, an investigation into the transitions states was not carried out.



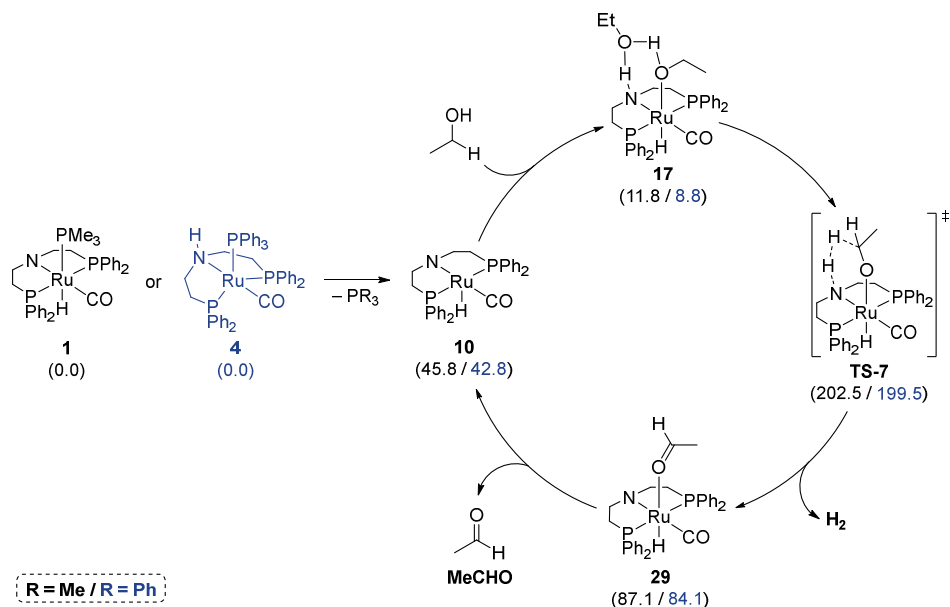
Scheme 3.16: Catalytic cycle for the dehydrogenation of ethanol via a cationic ‘slippage’ mechanism, in which the phosphine ligand remains coordinated to the metal complex. The Gibbs free energies ΔG^{298} (in kJ mol^{-1}) are given relative to $\text{Ru}^{\text{II}}\text{-PMe}_3$ complex **1** (black) and $\text{Ru}^0\text{-PPh}_3$ complex **4** (blue); RI-PBE0-D3(BJ)/def2-QZVPP//BP86/def2-SV(P); COSMO-RS (toluene).

As part of the thorough investigation of the various possible complex isomers, some *facial* (*fac*) isomers were found to be close in energy to the previously shown *meridional* (*mer*) intermediates (see Scheme 3.17). The isomerization of $\text{Ru}^{\text{II}}\text{-PMe}_3$ complex **1** and $\text{Ru}^0\text{-PPh}_3$ complex **4** to *fac*- Ru^{II} complexes **24** and **25** is moderately endergonic, but accessible at the given reaction conditions (**24**: $\Delta G^{383} = 22.8 \text{ kJ mol}^{-1}$; **25**: $\Delta G^{383} = 56.5 \text{ kJ mol}^{-1}$). Dissociation of the respective phosphine, PMe_3 or PPh_3 , generates the *fac*-type equivalent of the activated Ru-MACHO species **10**. The resulting five-coordinate complex **26** is significantly less stable than the rate-determining barriers of the Noyori- and Dub-type catalytic cycles (**26**: $\Delta G^{383} = 114.2$ and $111.2 \text{ kJ mol}^{-1}$ for **1** and **4**, respectively). Along the envisioned pathway, the Ru ethoxy complex **27** ($\Delta G^{383} = 129.3$ and $126.3 \text{ kJ mol}^{-1}$ for **1** and **4**, respectively) and the η^2 -coordinated aldehyde complex **28** ($\Delta G^{383} = 144.9$ and $141.9 \text{ kJ mol}^{-1}$ for **1** and **4**, respectively) were calculated and also found to be too unstable to represent relevant reaction intermediates.



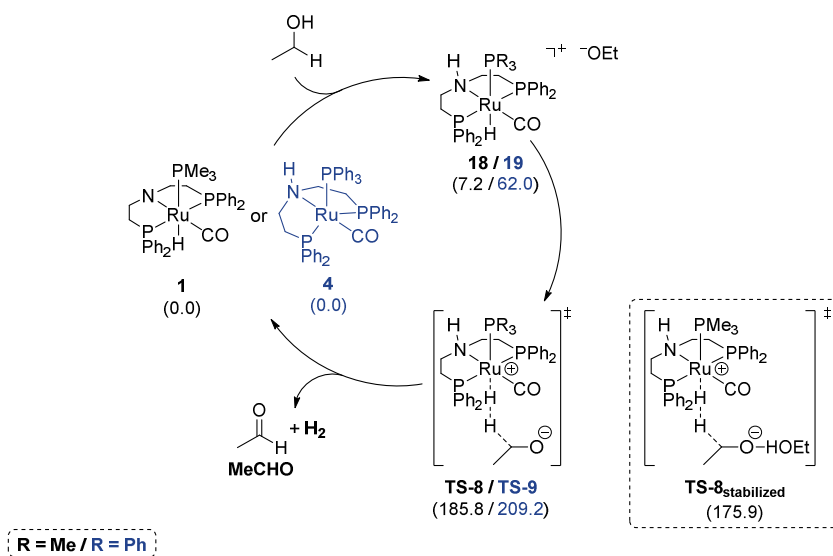
Scheme 3.17: Catalytic cycle for the dehydrogenation of ethanol considering *fac*-isomers derived from **1** and **4**. The Gibbs free energies ΔG^{298} (in kJ mol^{-1}) are given relative to $\text{Ru}^{\text{II}}\text{-PMe}_3$ complex **1** (black) and $\text{Ru}^0\text{-PPh}_3$ complex **4** (blue); RI-PBE0-D3(BJ)/def2-QZVPP//BP86/def2-SV(P); COSMO-RS (toluene).

Although the direct generation of H_2 and acetaldehyde (**MeCHO**) as shown in Scheme 3.18 is neither non-innocent nor includes the phosphine ligand on the complex and therefore could not encompass the desired changes, a complete exploration of the potential energy surface is required to gain insights and ensure accurate results. The reaction pathway starts with the previously discussed generation of activated Ru-MACHO species **10** ($\Delta G^{383} = 45.8$ and 42.8 kJ mol^{-1} for **1** and **4**, respectively) and addition of **EtOH** to form the stabilized ethoxy complex **17** ($\Delta G^{383} = 11.8$ and 8.8 kJ mol^{-1} for **1** and **4**, respectively). Formation of aldehyde and H_2 as well as direct elimination of H_2 takes place via **TS-7** with barriers of 202.5 and $199.5 \text{ kJ mol}^{-1}$ for the $\text{Ru}^{\text{II}}\text{-PMe}_3$ and $\text{Ru}^0\text{-PPh}_3$ pathways, respectively, and is thus not feasible at the employed reaction conditions. The resulting aldehyde-coordinated complex **29** ($\Delta G^{383} = 87.1$ and 84.1 kJ mol^{-1} for **1** and **4**, respectively) can liberate the desired acetaldehyde to regenerate intermediate **10**.



Scheme 3.18: Catalytic cycle for the dehydrogenation of ethanol via a direct H_2 elimination from complex **17**. The Gibbs free energies ΔG^{383} (in kJ mol^{-1}) are given relative to $\text{Ru}^{\text{II}}\text{-PMe}_3$ complex **1** (black) and $\text{Ru}^0\text{-PPh}_3$ complex **4** (blue); RI-PBE0-D3(BJ)/def2-QZVPP//BP86/def2-SV(P); COSMO-RS (toluene).

Lastly, a transition state that leads to concerted generation of acetaldehyde (**MeCHO**) and H_2 was investigated (see Scheme 3.19). This is based on directly employing the hydride that is present in almost all investigated intermediates (except the Ru^0 complexes **2** and **4**). Initially, the onium complex **18** or **19** is formed (**18**: $\Delta G^{383} = 7.2 \text{ kJ mol}^{-1}$; **19**: $\Delta G^{383} = 62.0 \text{ kJ mol}^{-1}$), from which the product formation takes place directly via **TS-8** or **TS-9**. This is associated with significantly larger reaction barriers of 185.8 and 209.2 kJ mol^{-1} than feasible for the employed reaction conditions. Stabilization of the **PMe**₃-based transition state **TS-8** was found to have only a minor effect on the reaction barrier (**TS-8**_{stabilized}: $\Delta G^\ddagger = 175.9 \text{ kJ mol}^{-1}$) and does not render this reaction pathway feasible.



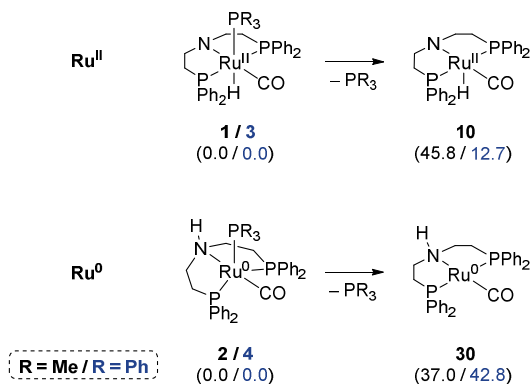
Scheme 3.19: Catalytic cycle for the dehydrogenation of ethanol via the concerted H₂ formation from **18** or **19**. The Gibbs free energies ΔG^{383} (in kJ mol⁻¹) are given relative to Ru^{II}-PMe₃ complex **1** (black) and Ru⁰-PPh₃ complex **4** (blue); RI-PBE0-D3(BJ)/def2-QZVPP//BP86/def2-SV(P); COSMO-RS (toluene).

All in all, the alternative reaction pathways that were investigated in addition to the Noyori- and Dub-type mechanisms are less feasible than these pathways. However, the ‘slippage’-type generation of Dub-type on-cycle species presents an interesting alternative to the non-innocent metal-ligand cooperative generation of these species, which might enable alternative approaches to ligand design. These might replace the cleavable NH functionality for a different polarized function, which forms similar stabilizing interactions required for metal-ligand assistance.

3.3.5 Investigation of Ligand Dissociation to Enable Further Reactivity

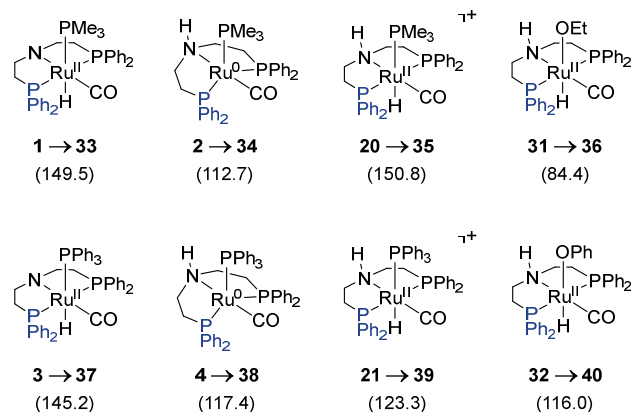
To exhaustively explore the chemical reaction network, the dissociation of various ligands from the experimentally employed pre-catalysts **1** (Ru^{II}-PMe₃) and **4** (Ru⁰-PPh₃) as well as from other relevant, low-energetic intermediates has been investigated. Note that the energies given in this section are bond dissociation energies (BDEs) relative to the preceding intermediate and are not necessarily referenced to **1** and **4**, which represent the most stable species in the **PMe**₃ and **PPh**₃ systems. Initially, the phosphine dissociation from the Ru^{II} complexes **1** and **3** was investigated, which leads to the known activated Ru-MACHO species **10**. The dissociation of **PMe**₃ from **1** is associated with an energy of 45.8 kJ mol⁻¹. For **PPh**₃, the dissociation of the phosphine group is significantly easier ($\Delta G^{383} = 12.7$ kJ mol⁻¹), which is reasonable due to the bulkier ligand. Additionally, as described above **3** is significantly less stable than Ru⁰-PPh₃ complex **4** (*vide supra*), which is observed experimentally and was attributed to the same steric pressure of **PPh**₃ in octahedral coordination environments. On

the other hand, the dissociation of the two phosphines from the Ru⁰ complexes **2** and **4** is equally feasible, which could indicate that in this trigonal bipyramidal geometry the steric pressure has mostly disappeared (**2**→**30**: $\Delta G^{383} = 37.0 \text{ kJ mol}^{-1}$; **4**→**30**: $\Delta G^{383} = 42.8 \text{ kJ mol}^{-1}$).



Scheme 3.20: PR₃ dissociation energies for the Ru^{II} and Ru⁰ complexes bearing PMe₃ or PPh₃ ligands. The Gibbs free energies ΔG^{383} (in kJ mol⁻¹) are given in the upper equation relative to the Ru^{II} complexes **1** (black) and **3** (blue) and in the lower equation relative to the Ru⁰ complexes **2** (black) and **4** (blue); RI-PBE0-D3(BJ)/def2-QZVPP//BP86/def2-SV(P); COSMO-RS (toluene).

In the next step, the dissociation of one of the phosphine arms of the tridentate PNP ligand is evaluated (see Scheme 3.21). The complex remained in the pseudo-octahedral coordination environment with a free coordination site and the dissociated phosphine unit is turned away from the metal center (see Figure 3.4). The dissociation of the phosphine arm in Ru^{II} complexes **1** and **3** is highly endergonic with BDEs of 149.5 kJ mol⁻¹ (**1**→**33**) and 145.2 kJ mol⁻¹ (**3**→**37**). The similar values for the **PMe**₃ and **PPh**₃ complexes indicate that the dissociation of the phosphine arm does not resolve the steric pressure, which is present in the octahedral **PPh**₃ system. In that case, a significantly lower BDE for **3** would be expected than for **1**. For the other investigated complexes, Ru⁰ systems **2** and **4** (**2**→**34**: $\Delta G^{383} = 112.7 \text{ kJ mol}^{-1}$; **4**→**38**: $\Delta G^{383} = 117.4 \text{ kJ mol}^{-1}$), the onium complexes **20** and **21** (**20**→**35**: $\Delta G^{383} = 150.8 \text{ kJ mol}^{-1}$; **21**→**39**: $\Delta G^{383} = 123.3 \text{ kJ mol}^{-1}$), and the Ru^{II} ethoxy and phenoxy intermediates **31** and **32** (**31**→**36**: $\Delta G^{383} = 84.4 \text{ kJ mol}^{-1}$; **32**→**40**: $\Delta G^{383} = 116.0 \text{ kJ mol}^{-1}$) similarly high endergonic bond dissociations are observed. It should be noted that with the additional conformational flexibility of the dissociated phosphine arm a small inaccuracy might be introduced as no exhaustive screening of rotational conformers was performed. The lowest obtained BDE from **31** to the bidentate phosphorus-nitrogen system **36** is 84.4 kJ mol⁻¹. However, even in the case of **EtOH**-stabilized intermediate of **31** (cf. **17**), the formation of this intermediate is endergonic by an additional 11.8 or 8.8 kJ mol⁻¹ (relative to **1** or **4**, respectively). Therefore, all phosphine arm dissociations of the PNP ligand are less feasible than the Dub-type reaction mechanism and do not play a role in the investigated Ru-MACHO system.



Scheme 3.21: Dissociation energies for one of the PNP ligands' phosphine arms (marked in blue) for pre-catalysts **1** and **4** as well as key intermediates **2**, **3**, **20**, **21**, **31**, and **32** of the catalytic cycles discussed in this work. ΔG^{383} in kJ mol^{-1} ; RI-PBE0-D3(BJ)/def2-QZVPP//BP86/def2-SV(P); COSMO-RS (toluene).

The molecular structure of one of these phosphine arm dissociation intermediates, **33**, is shown in Figure 3.4. The general structure of the other ligands remains intact with only a small displacement of the **PMe₃** ligand towards the free space being observed. The dissociated phosphine arm requires a significant amount of space around the free coordination site and will most likely block the coordination of larger potential ligands.

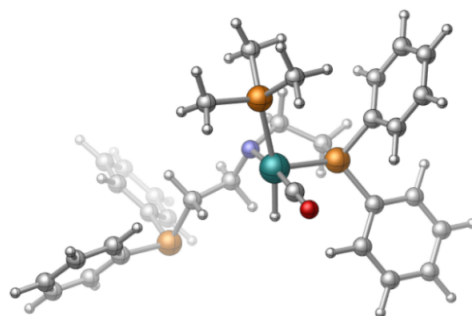
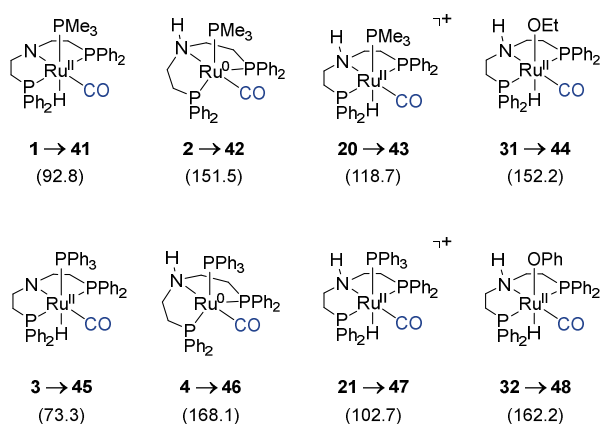


Figure 3.4: Molecular structure of **33**, in which one of the two phosphine arms of the PNP ligand was dissociated from the metal center. ΔG^{383} in kJ mol^{-1} ; RI-PBE0-D3(BJ)/def2-QZVPP//BP86/def2-SV(P); COSMO-RS (toluene).

Apart from PNP ligand dissociation, the dissociation of the CO ligand was also investigated for these species (see Scheme 3.22). Bond dissociation energies for the two $\text{Ru}^{\text{II}}\text{-PR}_3$ complexes **1** and **3** is the smallest of the investigated CO dissociation BDEs, but still significantly endergonic (**1**→**41**: $\Delta G^{383} = 92.8 \text{ kJ mol}^{-1}$; **3**→**45**: $\Delta G^{383} = 73.3 \text{ kJ mol}^{-1}$). **3** requires prior isomerization from **4**, which leads to a further increase in Gibbs free energy by 28.8 kJ mol^{-1} . BDEs for **2**, **4**, **31** and **32** are all above 150 kJ mol^{-1} (**2**→**42**: $\Delta G^{383} = 151.5 \text{ kJ mol}^{-1}$; **4**→**46**: $\Delta G^{383} = 168.1 \text{ kJ mol}^{-1}$; **31**→**44**: $\Delta G^{383} = 152.2 \text{ kJ mol}^{-1}$; **32**→**48**: $\Delta G^{383} = 162.2 \text{ kJ mol}^{-1}$) and although CO dissociation from the onium complexes **20** and **21** is more feasible (**20**→**43**: $\Delta G^{383} = 118.7 \text{ kJ mol}^{-1}$; **21**→**47**: $\Delta G^{383} = 102.7 \text{ kJ mol}^{-1}$), these bond

dissociations are still disfavored to the Dub-type reaction mechanism and will not be relevant for the (de-)hydrogenation.



Scheme 3.22: CO dissociation energies (marked in blue) for pre-catalysts **1** and **4** as well as key intermediates **2**, **3**, **20**, **21**, **31**, and **32** of the catalytic cycles discussed in this work. ΔG^{383} in kJ mol^{-1} ; RI-PBE0-D3(BJ)/def2-QZVPP//BP86/def2-SV(P); COSMO-RS (toluene).

Again, the structure of one of the CO dissociation intermediates is shown to illustrate the structural change that is induced by the CO dissociation (see Figure 3.5). The structure assumes a trigonal-bipyramidal geometry, in which the two PNP phosphine donors are placed at the axial positions. The apical phosphine ligand and hydride fragment move from a *trans* arrangement, which was assumed by the two axial ligands, into the free space generated by the free coordination site.

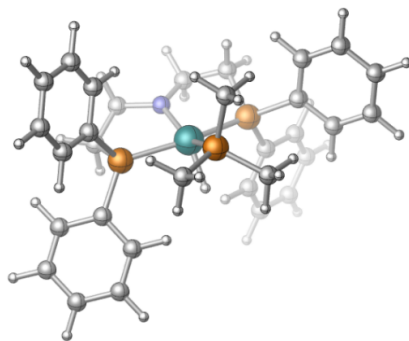


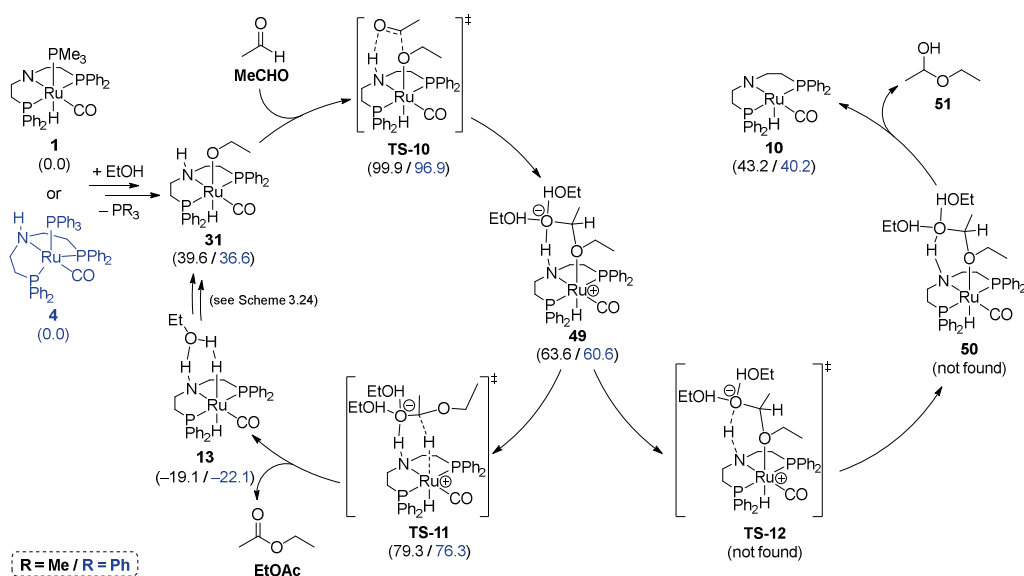
Figure 3.5: Molecular structure of **41**, in which the CO ligand was dissociated from the metal center. ΔG^{383} in kJ mol^{-1} ; RI-PBE0-D3(BJ)/def2-QZVPP//BP86/def2-SV(P); COSMO-RS (toluene).

The dissociation of the phosphine arm of the PNP ligand and of the CO ligand do not provide any possibilities for feasible reaction pathways as the ligand dissociations are strongly endergonic and are thus significantly disfavored to the previously calculated reaction mechanisms. Attempts to find structures corresponding to amine dissociation of the PNP ligand leading to a bidentate phosphorus-phosphorus system were unsuccessful and these motifs were subsequently ruled out.

3.3.6 Catalytic Cycle for Alcohol-Aldehyde Coupling

After the acetaldehyde (**MeCHO**) has been formed via the dehydrogenation of ethanol (**EtOH**), formation of the desired ester product can take place via two pathways: Firstly, the ester, ethyl acetate (**EtOAc**), can be directly formed from alcohol-aldehyde coupling. Secondly, alcohol-aldehyde coupling can lead to formation of the corresponding hemiacetal 1-ethoxyethanol (**51**), which can subsequently be dehydrogenated to equally yield **EtOAc**. As both pathways have been suggested in the past,^{111, 144, 153} a quantum-chemical evaluation for this step in the Ru-MACHO system was carried out (see Scheme 3.23). Both alternatives start with the formation of the Ru^{II} ethoxy complex **31** from Ru^{II}-PMe₃ **1** or Ru⁰-PPh₃ **4** ($\Delta G^{383} = 39.6$ and 36.6 kJ mol⁻¹ for **1** and **4**, respectively). Since the proposed reaction steps begin with the dissociation of the phosphine group, the energies for the Ru^{II}-PMe₃ and Ru⁰-PPh₃ system again only differ by 3.0 kJ mol⁻¹. The structure of the unstabilized ethoxy complex **31** is used instead of the **EtOH**-stabilized complex (cf. **17** in Scheme 3.18) as the space around the ethoxy group is needed for the subsequent addition of the aldehyde via **TS-10** ($\Delta G^\ddagger = 99.9$ and 96.9 kJ mol⁻¹ for **1** and **4**, respectively). **TS-10** represents the C–O bond formation step and the resulting anionic charge on the carbonyl oxygen is stabilized by additional substrate equivalents. From **49** ($\Delta G^{383} = 63.6$ and 60.6 kJ mol⁻¹ for **1** and **4**, respectively), which is formed via **TS-10**, the reaction can continue via **TS-11** (leading to ethyl acetate formation). Alternatively, **TS-12** leads to the formation of the hemiacetal intermediate **51** for subsequent dehydrogenation. **TS-11** represents the transfer of the C–H proton to the Ru center and is analogous to **TS-2**, which is part of the Noyori- und Dub-type pathways and equally represents the transfer of a proton from a carbonyl carbon atom to the metal (**TS-11**: $\Delta G^\ddagger = 79.3$ and 76.3 kJ mol⁻¹ for **1** and **4**, respectively). It leads to liberation of the **EtOAc** product and generation of the stabilized dihydride complex **13** ($\Delta G^{383} = -19.1$ and -22.1 kJ mol⁻¹ for **1** and **4**, respectively). The rate-determining barrier **TS-10** in this so-called Tishchenko-like pathway^{144, 153} is slightly higher than the activation barrier for the dehydrogenation of ethanol ($\Delta G^\ddagger = 93.3$ kJ mol⁻¹ for Ru^{II}-PMe₃ complex **1**; cf. Figure 3.2). Therefore, a small build-up of the aldehyde intermediate would be expected, which was observed by Gauvin and co-workers in their experimental mechanistic investigation of the Ru-MACHO system.¹⁴⁴ The alternative transition state **TS-12** (diverging from the Tishchenko-like pathway) represents the opposite approach, which leads to hemiacetal formation. Instead of transferring a proton to the metal center (**TS-11**), the anionic fragment abstracts the NH proton leading to the hemiacetal 1-ethoxyethanol, which would subsequently need to be dehydrogenated again via the Dub-type catalytic cycle. Despite all attempts, neither **TS-12** nor the subsequent intermediate **50** could be located and geometry optimization regularly led back to species **49**. Further efforts to characterize a concerted

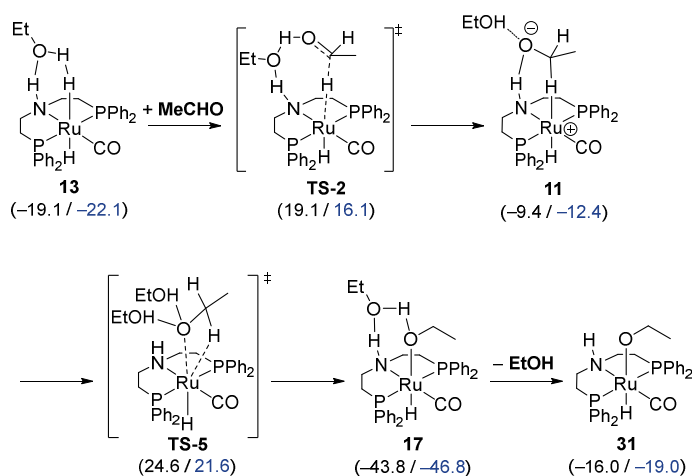
pathway from **49** to the activated Ru-MACHO species **10** and hemiacetal (**51**) also remained unsuccessful.



Scheme 3.23: Tishchenko-like pathway for generation of ethyl acetate from ethanol and acetaldehyde (left) and formation of hemiacetal for subsequent dehydrogenation (right). The Gibbs free energies ΔG^{383} (in kJ mol^{-1}) are given relative to $\text{Ru}^{\text{II}}\text{-PMe}_3$ complex **1** (black) and $\text{Ru}^0\text{-PPh}_3$ complex **4** (blue). Mass balance for additional stabilizing substrate equivalents is ensured in the entire scheme; RI-PBE0-D3(BJ)/def2-QZVPP//BP86/def2-SV(P); COSMO-RS (toluene).

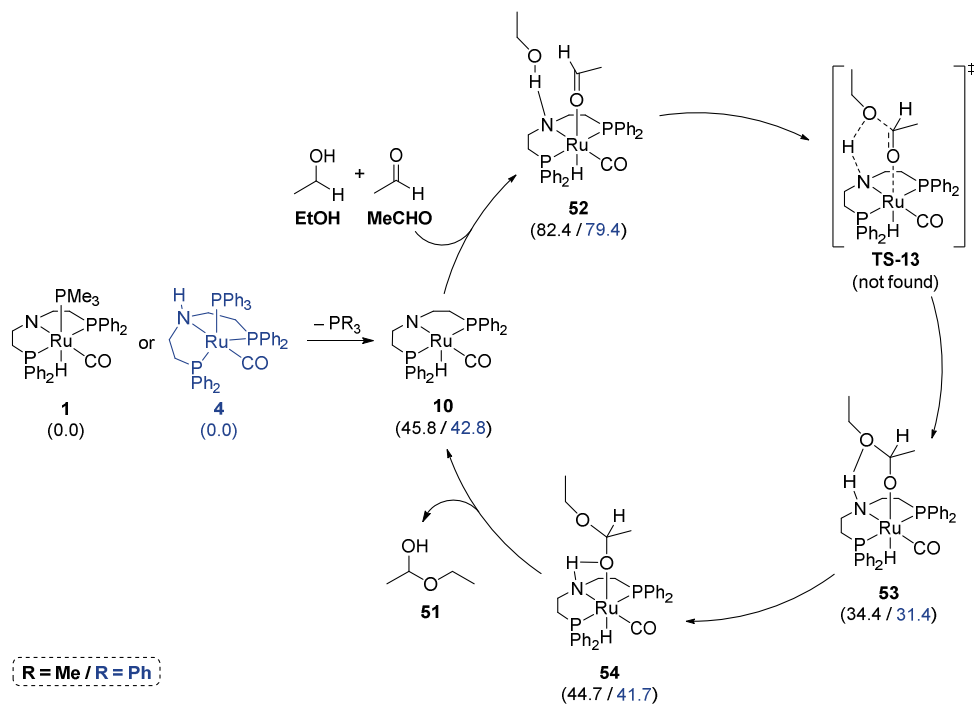
The network of accessible reaction pathways is highly complex. Various steps of the Noyori-type pathway or of an alternative ‘slippage’ pathway are feasible and are required for initial formation of Dub-type on-cycle species. Furthermore, the different catalytic steps share common intermediates and transition states, which makes distinguishing between the pathways difficult. This is further elevated by the fact that the presented Tishchenko-like reaction pathway transforms the Ru^{II} ethoxy complex **31**, which is assumed to be formed directly from the catalyst resting state (**1** or **4**), into the dihydride complex **13** and could lead to each active catalyst species alternating between the Dub-type and Tishchenko-like catalytic cycles. Furthermore, ethoxy complex **31** could most likely also be formed by a simple low-barrier rearrangement from Dub-type intermediate **16** (see Scheme 3.13). Nonetheless, a reaction pathway was investigated that would allow for conversion of **13** to **31** without cleavage of the NH functionality in the PNP ligand (metal-ligand assistance; see Scheme 3.24). From dihydride complex **13** that is formed in the last step of the Tishchenko-like pathway, hydride transfer from ruthenium to **MeCHO** via **TS-2** ($\Delta G^\ddagger = 19.1$ and 16.1 kJ mol^{-1} for **1** and **4**, respectively) leads to intermediate **11**, which still exhibits a Ru–H contact reminiscent of the transition state (**11**: $\Delta G^{383} = -9.4$ and $-12.4 \text{ kJ mol}^{-1}$ for **1** and **4**, respectively). ‘Slippage’-type transition state **TS-5** leads to rearrangement of the Ru–H

contact to form the Ru–O bond of the desired ethoxy ligand with an effective activation barrier of 43.7 kJ mol⁻¹ ($\Delta G^\ddagger = 24.6$ and 21.6 kJ mol⁻¹ for **1** and **4**, respectively). The EtOH-assisted transition state leads to equally stabilized Ru^{II} ethoxy complex **17** ($\Delta G^{383} = -43.8$ and -46.8 kJ mol⁻¹ for **1** and **4**, respectively), which needs to liberate the stabilizing substrate to enable addition of the next equivalent of aldehyde in the aldehyde-alcohol coupling (see Scheme 3.23).



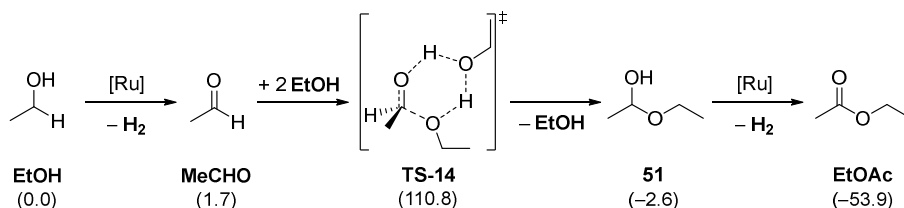
Scheme 3.24: A potential pathway for the regeneration of dihydride **31** from complex **13** closing the catalytic cycle for alcohol-aldehyde coupling (see Scheme 3.23). The Gibbs free energies ΔG^{383} (in kJ mol⁻¹) are given relative to Ru^{II}-PMe₃ complex **1** (black) or Ru⁰-PPh₃ **4** (blue), EtOH and MeCHO; RI-PBE0-D3(BJ)/def2-QZVPP//BP86/def2-SV(P); COSMO-RS (toluene).

Moreover, an alternative reaction pathway, which is based on coordination of the aldehyde fragment to the metal instead of the Ru^{II} ethoxy complex **31**, was investigated (see Scheme 3.25). The envisioned catalytic cycle starts by generation of the activated Ru-MACHO species **10** from Ru^{II}-PMe₃ complex **1** or Ru⁰-PPh₃ pre-catalyst **4** (**10**: $\Delta G^{383} = 45.8$ and 42.8 kJ mol⁻¹ for **1** and **4**, respectively). This sets the stage for many of the presented pathways. Coordination of the carbonyl oxygen atom of acetaldehyde to Ru leads to formation of Ru^{II} intermediate **52** ($\Delta G^{383} = 82.4$ and 79.4 kJ mol⁻¹ for **1** and **4**, respectively), which is stabilized by substrate coordination to the PNP nitrogen atom. The coordinated EtOH molecule was expected to undergo the equivalent outer-sphere bond formation step to the aldehyde as in the Tishchenko-like pathway via **TS-13** (cf. **TS-10**), however, the transition state search was not successful. Formation of **53** ($\Delta G^{383} = 34.4$ and 31.4 kJ mol⁻¹ for **1** and **4**, respectively) and rearrangement to **54** ($\Delta G^{383} = 44.7$ and 41.7 kJ mol⁻¹ for **1** and **4**, respectively) is thus not expected to take place. It should be noted that the intermediate preceding the transition state, **52**, is significantly less stable than the intermediate **31** in the catalytic cycle presented above. Therefore, even if locatable, the activation barrier for **TS-13** would not necessarily be expected to be competitive to **TS-10**.



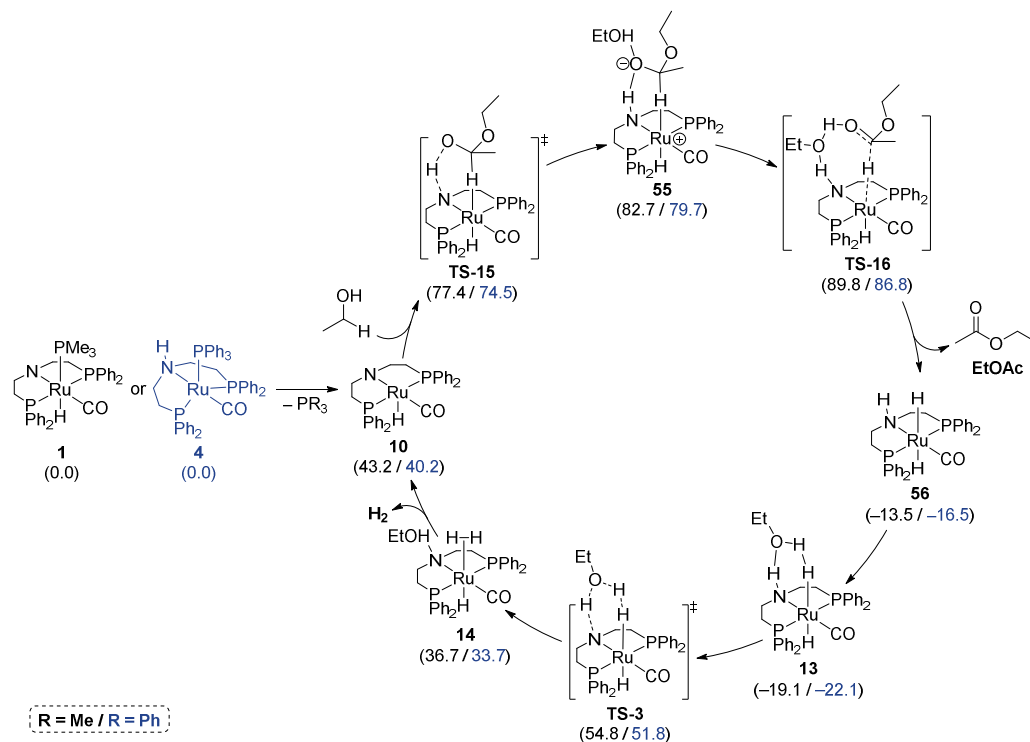
Scheme 3.25: Catalytic cycle for the alternative alcohol-aldehyde coupling, in which ethanol is added to the coordinated aldehyde. The Gibbs free energies ΔG^{383} (in kJ mol^{-1}) are given relative to $\text{Ru}^{\text{II}}\text{-PMe}_3$ complex **1** (black) and $\text{Ru}^0\text{-PPh}_3$ complex **4** (blue); RI-PBE0-D3(BJ)/def2-QZVPP//BP86/def2-SV(P); COSMO-RS (toluene).

To ensure that hemiacetal formation does not take place on an alternative metal-free pathway, the **EtOH**-assisted transition state **TS-14** was also calculated (see Scheme 3.26). Hydrogenation of **EtOH** to **MeCHO** is slightly endergonic ($\Delta G^{383} = 1.7 \text{ kJ mol}^{-1}$). Subsequent metal-free alcohol-aldehyde coupling via **TS-14** is associated with a higher barrier than the direct formation of **EtOAc** following a Tishchenko-like pathway ($110.8 \text{ kJ mol}^{-1}$ vs. 99.9 kJ mol^{-1}). The resulting hemiacetal **51** is slightly exergonic ($\Delta G^{383} = -2.6 \text{ kJ mol}^{-1}$), but the main driving force of the reaction is the formation of ethyl acetate (**EtOAc**: $\Delta G^{383} = -53.9 \text{ kJ mol}^{-1}$), which is also why the pathway directly forming **EtOAc** is preferred over all other investigated alternatives (*vide supra*).

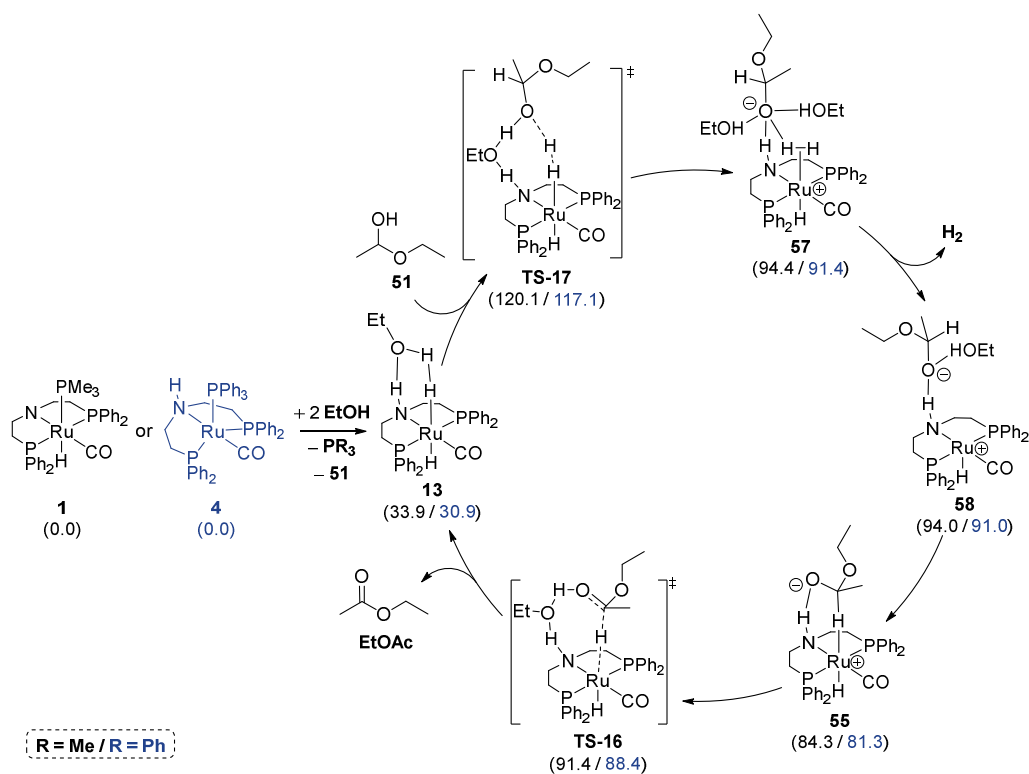


Scheme 3.26: Reaction scheme for the metal-free alcohol-aldehyde coupling to the corresponding hemiacetal. ΔG^{383} in kJ mol^{-1} ; RI-PBE0-D3(BJ)/def2-QZVPP//BP86/def2-SV(P); COSMO-RS (toluene).

Lastly, the Noyori- (Scheme 3.27) and Dub-type (Scheme 3.28) catalytic cycles for the dehydrogenation of hemiacetal **51** to **EtOAc** were briefly investigated. One of these two catalytic cycles would need to be accessible in the hemiacetal-based pathway to lead to **EtOAc** formation (as opposed to the direct formation of **EtOAc** via **TS-10** and **TS-11**). As the two mechanisms only differ in minor details, the individual reaction steps are not discussed here. Please refer to Sections 3.3.2 and 3.3.3 for an in-depth analysis of these pathways. Interestingly, the Noyori-type cycle is preferred over the Dub-type cycle for the dehydrogenation of **51** ($\Delta G^\ddagger = 89.8$ and 86.8 kJ mol⁻¹ (**TS-16**) vs. 120.1 and 117.1 kJ mol⁻¹ (**TS-17**) for **1** and **4**, respectively). This might be caused by the highly exergonic elimination of **EtOAc** shortly before the proton shuffle transition state **TS-3**, which represented the rate-determining step in the Noyori-type cycle for **EtOH**. In any case, this serves as a proof of concept for the fact that hemiacetal dehydrogenation would be a feasible pathway for ester hydrogenation if hemiacetal **51** is formed.



Scheme 3.27: Catalytic cycle for the Noyori-type dehydrogenation of hemiacetal **51** to ethyl acetate (**EtOAc**). The Gibbs free energies ΔG^{383} (in kJ mol⁻¹) are given relative to Ru^{II}-PMe₃ complex **1** (black) and Ru⁰-PPh₃ complex **4** (blue). Mass balance for additional stabilizing substrate equivalents is ensured in the entire scheme; RI-PBE0-D3(BJ)/def2-QZVPP//BP86/def2-SV(P); COSMO-RS (toluene).

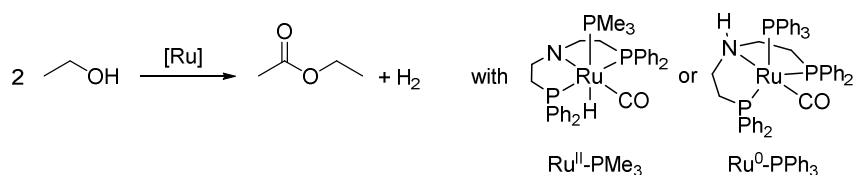


Scheme 3.28: Catalytic cycle for the Dub-type dehydrogenation of hemiacetal **51** to ethyl acetate (**EtOAc**). The Gibbs free energies ΔG^{383} (in kJ mol^{-1}) are given relative to $\text{Ru}^{\text{II}}\text{-PMe}_3$ complex **1** (black) and $\text{Ru}^0\text{-PPh}_3$ complex **4** (blue). Mass balance for additional stabilizing substrate equivalents is ensured in the entire scheme; RI-PBE0-D3(BJ)/def2-QZVPP//BP86/def2-SV(P); COSMO-RS (toluene).

Overall, the formation of the desired ester product can be achieved via a Tishchenko-like alcohol-aldehyde coupling pathway. Attempts to characterize a pathway for the formation of a hemiacetal were not successful. This is in good agreement with experimental observations by Gauvin and co-workers¹⁴⁴ and suggestions made by Dmitry G. Gusev for the SNS pincer ligand developed in his group.¹⁵³

3.4 Summary and Outlook

The base-free dehydrogenative coupling of alcohols to esters with two conceptually different ruthenium PNP catalysts was investigated.



Scheme 3.29: Ru-catalyzed base-free dehydrogenative coupling of ethanol to ethyl acetate.

Quantum-chemical calculations were employed to provide a rationale for the phosphine-dependent formation of Ru^{II}-PMe₃ and Ru⁰-PPh₃ (see Scheme 3.7) as well as their different behavior in stoichiometric reactions with alcohols (see Scheme 3.8). Furthermore, ruthenium dicarbonyl complexes have been suggested to be responsible for the inactivation observed when employing MeOH (see Scheme 3.9). Crystal structures of Ru^{II}-PMe₃ and Ru⁰-PPh₃ as well as a protonated onium complex and a Ru ethoxy complex have been used to evaluate the chosen geometry optimization method and demonstrated the capabilities to accurately calculate and predict structural parameters and conformational arrangements (see Tables 3.1 – 3.4). The commonly proposed Noyori-type mechanism was investigated (see Scheme 3.11) and compared to the recently introduced Dub-type pathways (see Scheme 3.13). The calculations showed that both pathways are feasible at the employed reaction conditions and that the Dub-type catalytic cycle is significantly preferred for the dehydrogenation of ethanol to acetaldehyde in the Ru-MACHO system. The stabilization of active sites by additional substrate molecules has been identified as key factor for the characterization of the different species (see Scheme 3.14). An alternative ‘slippage’-type pathway was found to be capable of generating the required on-cycle species completely without non-innocent metal-ligand cooperation, which might provide new approaches for rational catalyst design (see Scheme 3.15). A multitude of other reaction mechanisms was calculated to evaluate the influence of the ruthenium oxidation state and the employed phosphine for stabilization (see Schemes 3.16 – 3.22). These alternative pathways also included broad evaluation of PNP phosphine dissociation and CO ligand dissociation, which were both identified as not feasible. A Tishchenko-like pathway for the direct alcohol-aldehyde coupling to ethyl acetate was identified as preferred over the intermediary formation of a hemiacetal (see Scheme 3.23). As a proof of concept, the dehydrogenation of the corresponding hemiacetal to the desired ester was calculated and found to be feasible (see Schemes 3.27 and 3.28). The observation that both complexes, Ru^{II}-PMe₃ and Ru⁰-PPh₃, react via the same pathway means that no catalyst modifications can be based on Ru⁰ pathways, which would not be accessible from the Ru^{II} precatalyst, or alternative phosphine-

based pathways. However, the introduction of an apical phosphine ligand reduces catalyst degradation by providing a stabilized resting state without diminishing the catalyst activity (either by employing $\text{Ru}^{\text{II}}\text{-PMe}_3/\text{Ru}^0\text{-PPh}_3$ or by *in-situ* generation). This effect was investigated by mass spectrometry of the reaction mixture after catalysis and by kinetic studies over multiple subsequent runs.¹⁷¹ Although catalyst degradation could not be completely avoided, a significant improvement was observed and the initial reaction rate for subsequent runs was found to be more than twice as high (relative to the rate of the first run) for $\text{Ru}^0\text{-PPh}_3$ than for the commonly used combination of Ru-MACHO and $\text{KO}t\text{Bu}$ (see Figure 3.6). This behavior is also nicely visible in the quantum-chemical calculations where the resting states are found to be the most stable structures, but the phosphine dissociation does not represent the rate-determining step and is readily available. The required phosphine dissociation might also be the reason for the lower initial rate in the first run of the reaction.

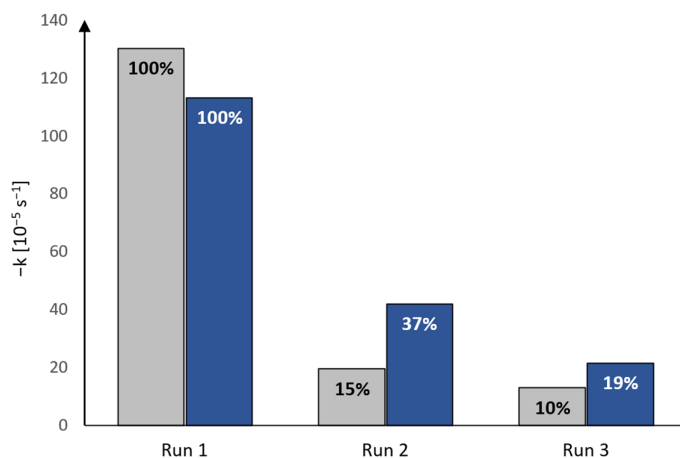


Figure 3.6: Column plot of the initial reaction rates ($-k$) of three consecutive runs of the dehydrogenative couplings of hexanol catalyzed by $\text{Ru-MACHO}/\text{KO}t\text{Bu}$ (grey) and the new $\text{Ru}^0\text{-PPh}_3$ complex (blue).

Further investigations into these improvements will need to be carried out to evaluate the influence of different complexes and phosphines as well as to understand long-term effects of the stabilization approach. Moreover, the combination of ‘slippage’- and Dub-type pathways might allow for (de-)hydrogenation without the regularly used NH group as long as a suitable functionality to build up a stabilizing hydrogen bonding is available. This could enable the design of a wide range of new catalysts and avoid the critical catalyst degradation in the first place. The prolonged scientific interest in the homogeneously catalyzed (de-)hydrogenation is also exemplified by recent mechanistic investigations in the groups of Milstein¹⁷² and Chianese¹⁷³ as well as large-scale reactions at GlaxoSmithKline,¹⁷⁴ which have been reported after our report on this topic has been published. The complexity of the available pathways renders the transfer to the other substrates and catalysts difficult, which is also supported by the results for hemiacetal dehydrogenation. Thus, when improving and altering the catalyst

system, quantum-chemical investigations should be employed to support these changes and ensure that no misinterpretations are made. It should also be noted that Dub *et al.* have recently investigated potassium-based catalytic pathways that also need to be considered in the base-induced (KO*t*Bu) systems.¹⁷⁵⁻¹⁷⁶ However, in base-free catalytic systems such as the Ru^{II}-PMe₃ and Ru⁰-PPh₃ complexes presented here, these pathways will not be accessible.

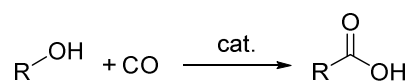
4

Carbonylation of Alcohols

Reproduced in part with permission from Sara Sabater, Maximilian Menche, Tamal Ghosh, Saskia Krieg, Katharina S. L. Rück, Rocco Paciello, Ansgar Schäfer, Peter Comba, A. Stephen K. Hashmi and Thomas Schaub, Mechanistic Investigation of the Nickel-Catalyzed Carbonylation of Alcohols. *Organometallics* **2020**, 39(6), 870-880. Copyright 2020 American Chemical Society. And reproduced in part from Niels Lichtenberger, Maximilian Menche, Katharina S. L. Rück, Rocco Paciello, Ansgar Schäfer, Peter Comba, A. Stephen K. Hashmi and Thomas Schaub, Revisiting Nickel-Catalyzed Carbonylations: Unexpected Observation of Substrate-dependent Mechanistic Differences. *manuscript in preparation* **2021**.

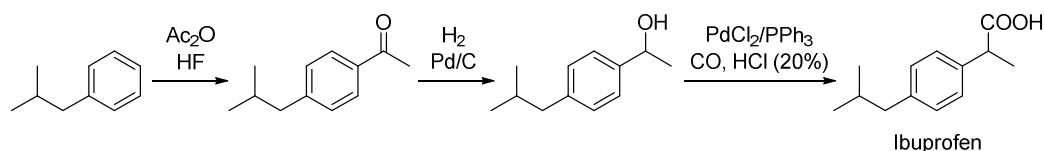
4.1 Motivation

The catalytic carbonylation of alcohols and olefins with carbon monoxide is of high interest in academic and industrial research as it provides a straightforward and atom-economic methodology for the synthesis of carboxylic acids (Scheme 4.1).¹⁷⁷⁻¹⁷⁸



Scheme 4.1: Carbonylation of alcohols to carboxylic acids with carbon monoxide.

At CO pressures below 100 bar, the use of precious metals¹⁷⁹ such as palladium,¹⁸⁰⁻¹⁸² rhodium¹⁸³⁻¹⁸⁴ or iridium¹⁸⁵⁻¹⁸⁶ is required for the industrial large-scale production of bulk chemicals like acetic acid¹⁸⁶⁻¹⁸⁷ and methyl propionate.¹⁸⁸ On the other hand, if non-precious metals are preferred, significantly harsher conditions are typically employed. For example, the BASF process for the production of propionic acid via the carbonylation of ethylene is achieved with cheap $\text{Ni}(\text{CO})_4$ but requires temperatures in the range from 250 to 320 °C and a CO pressure of 300 bar.¹⁸⁹ While this can be industrially achieved for simple substrates (like propionic acid), the conditions are not compatible with more complex substrates, which might be of interest in the synthesis of active pharmaceutical ingredients (APIs). For example, the BASF process for the production of *iso*-butylphenylpropanoic acid (ibuprofen) involves a late-stage carbonylation step. This synthesis route to ibuprofen starts with the Friedel-Crafts acylation of *iso*-butylbenzene, which is subsequently hydrogenated to 1-(4-*iso*-butylphenyl)ethanol. Carbonylation of the alcohol in the desired branched selectivity is achieved in a palladium phosphine catalyzed process run in HCl (20%) at a pressure of 100 bar (see Scheme 4.2).¹⁹⁰ It should be noted, that other routes for the synthesis of ibuprofen are available, but are less atom-efficient.¹⁹¹⁻¹⁹²



Scheme 4.2: Industrial synthesis route for the production of ibuprofen from *iso*-butylbenzene.¹⁹⁰

However, the harsh and corrosive conditions necessitate the use of expensive corrosion-resistant reactors. Furthermore, the continuously rising cost of palladium (ca. 10-fold increase in the last ten years)¹⁹³ leads to a considerable interest in employing cheaper earth-abundant metals for this transformation. Although some reports on the carbonylation of methanol, ethanol and *n*-propanol have been published,¹⁹⁴⁻¹⁹⁷ the carbonylation of more complex alcohol precursors has not been extensively studied (or reported) with only two patents dealing with this matter.¹⁹⁸⁻¹⁹⁹ Most notably, Nabil Rizkalla employed a nickel phosphine system in the presence of a variety of catalytic promoters to achieve the carbonylation of methanol at milder conditions.¹⁹⁴ In this context, the goal of this work was to perform a detailed mechanistic investigation of a Ni-based catalytic system, which would enable the atom-economic and regioselective carbonylation of complex alcohols to the corresponding branched carboxylic acids employing low-pressure and low-corrosivity conditions similar to the system patented by Mitsubishi.^{198,200}

In our mechanistic investigation – experiments and computations – 1-phenylethanol was used as the model substrate for ibuprofen. In the first catalyst screening, different Ni sources were evaluated (see Table 4.1). The use of NiI_2 and tri-*n*-butylphosphine ($\text{P}(\text{nBu})_3$; TBP)

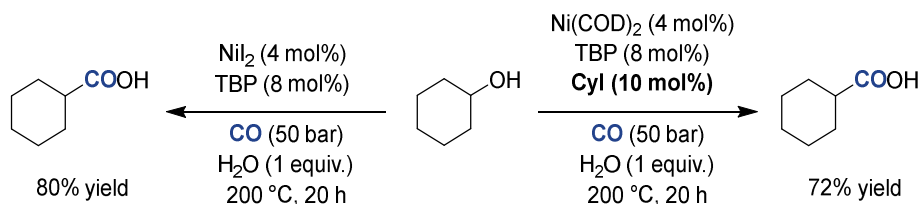
led to full conversion of 1-phenylethanol with regioselective formation of the branched 2-phenylpropanoic acid (**A**) with 83% yield (Table 4.1 - entry 1). Other observed side products are the dimeric 1,3-diphenyl-but-1-ene (**B**; 11%) and ethylbenzene (**C**; 4%). Dimeric reaction products could potentially be formed from some of the proposed reaction intermediates (*vide infra*) or from styrene, which could be formed via a competitive elimination reaction in 1-phenylethanol.²⁰¹ Similar to previous reports on the Ni-catalyzed carbonylation,¹⁹⁴⁻¹⁹⁵ the employed halide seems to have pivotal influence on the reaction outcome, and the use of Ni(OAc)₂ or Ni(OTf)₂ did not lead to any conversion. Throughout the course of the experimental investigations, control experiments such as reactions in the absence of nickel were carried out and all starting material was recovered. The commercially obtained NiI₂ was tested for palladium traces with inductively coupled plasma mass spectrometry (ICP-MS) to rule out the influence of unwanted Pd-catalyzed reaction pathways (Pd < 1 ppm). The screening revealed that the use of bis(cyclooctadiene)nickel (Ni(COD)₂) led to conversion when it was combined with TBP and an external source of HI (Table 4.1 – entries 2, 3, and 7). The absence of either of the two additives will stop the formation of the desired carbonylation product **A** (see Table 4.1 – entries 4 – 6), indicating that the combination of all three components is crucial in the catalytic cycle. Reduction of the catalyst loading to 2 mol% did significantly lower the conversion (16 %; see Table 4.1 – entry 8). Lastly, the influence of different additives that have been claimed to be beneficial for the carbonylation process have been tested.^{194-195, 197} Only the use of 8 mol% LiI led to beneficial results with 70% of 2-phenylpropanoic acid (**A**) being obtained at lower Ni loadings (2 mol%, 4 mol% TBP; Table 4.1 – entry 9). A detailed screening of different Ni precursors and additives can be found in the full publication and the corresponding supporting information.²⁰²

Table 4.1: Brief summary of the experimental screening in the nickel-catalyzed carbonylation of 1-phenylethanol to 2-phenylpropanoic acid.^[a] All experiments were carried out by Sara Sabater at CaRLa.

Entry	[Ni]	[L]	Additive	Yield A [%]	Yield B [%]	Yield C [%]
1	NiI ₂	TBP	-	83	11	4
2	Ni(COD) ₂	TBP	HI ^[b]	35	31	6
3	Ni(COD) ₂	TBPHI	-	68	25	8
4	Ni(COD) ₂	-	HI ^c	0	57	15
5	Ni(COD) ₂	TBP	-	0	0	0
6	Ni(COD) ₂	TBP	LiI	0	0	0
7	Ni(COD) ₂	TBP	LiI + HI ^[b]	92	2	5
8	NiI ₂ (2 mol%)	TBP (4 mol%)	-	16	24	3
9	NiI ₂ (2 mol%)	TBP (4 mol%)	LiI	70	17	5

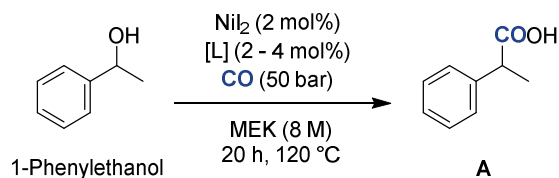
[a] A mixture of 1-phenylethanol (8.3mmol), [Ni] (2 or 4 mol%), TBP or TBPHI (4 or 8 mol%) and the corresponding additive (8 mol%), when indicated, was pressurized with CO at 50 bar, and stirred at 120 °C for 20 h. Yields were determined by GC-FID chromatography using anisole as internal standard after derivatization with *N*-methyl-*N*-(trimethylsilyl)trifluoroacetamide. [b] 57% in water.

To gain insights into the role of the external HI source that was required to achieve product formation, another experiment with Ni(COD)₂/TBP was performed with cyclohexanol, in which minor amounts of iodoethylbenzene were added (see Scheme 4.3). The observed reaction outcome was similar to the performance of the NiI₂/TBP system indicating that HI might be needed to convert the employed alcohol into the corresponding alkyl iodide. Concurring, the formation of iodoethylbenzene from model substrate 1-phenylethanol and HI has been previously reported and might play a major role during the reaction.²⁰³ Furthermore, when enantiomerically pure (*R*)-1-phenylethanol was employed as substrate, a racemic mixture of 2-phenylpropanoic acid was obtained suggesting that the mechanism of alkyl iodide formation follows a S_N1 pathway via an intermediate benzylic carbocation.



Scheme 4.3: Carbonylation of cyclohexanol using $\text{NiI}_2/\text{Ni(COD)}_2$, TBP and cyclohexyliodide to evaluate the role of the external HI source.

Subsequently, a detailed ligand screening was carried out to gain insights into the influence of the phosphine ligands and find suitable catalytic systems for the carbonylation procedure. Methyl ethyl ketone (MEK) was employed as solvent as it could solubilize the tested solid phosphine ligands and is used in the industrial ibuprofen production. The screening revealed an optimum Ni:TBP ratio of 1:2 (Table 4.2 – entries 1 – 3) as well as an increase in performance of bidentate phosphines with increasing backbone length (1,2-bis(diphenylphosphino)ethane (dppe): 13% ; 1,3-bis(diphenylphosphino)propane (dppp): 37%; see entries 4 – 5). As the quantum-chemical investigations into the reaction mechanism later revealed that the transition states with one phosphine coordinated to Ni are lower in energy than the corresponding transition states with two phosphines (see Section 4.3.1), further monodentate phosphines such as 2-dicyclohexylphosphino-2'-(*N,N*-dimethylamino)-biphenyl (DavePhos; see Table 4.2 – entry 6) and (2-Biphenyl)-dicyclohexylphosphin (CyJohnPhos) were investigated and found to be competent catalysts. The results also revealed that DavePhos (with its included amine functionality) performed significantly better at Ni:L ratios of 1:1 than CyJohnPhos or TBP. Experiments with non-coordinating Hünig's base and 2,6-lutidine revealed that replacing one equivalent of phosphine (TBP or CyJohnPhos) with base did not lead to a drop in activity and supported the results from the DFT calculations that only one phosphine ligand is coordinated to nickel. The full screening of different phosphine ligands can be found in the full publication and the corresponding supporting information.²⁰²

Table 4.2: Brief summary of the ligand screening in the nickel-catalyzed carbonylation of 1-phenylethanol to 2-phenylpropanoic acid.^[a] All experiments were carried out by Sara Sabater at CaRLa.

Entry	[L]	Yield A [%]
1	TBP (2 mol%)	14
2	TBP (4 mol%)	35
3	TBP (10 mol%)	23
4	dppe (2 mol%)	13
5	dppp (2 mol%)	37
6	 (2 mol%)	49

[a] A mixture of 1-phenylethanol (8.3 mmol), NiI_2 (2 mol%) and ligand [L] (2 or 4 mol%) in MEK (8 M) was pressurized with CO at 50 bar and stirred at 120 °C for 20 h. Yields were determined by GC-FID chromatography using anisole as internal standard after derivatization with *N*-methyl-*N*-(trimethylsilyl)trifluoroacetamide.

Once the targeted carbonylation of alcohols with earth-abundant nickel systems and simple phosphine ligands had been achieved, the focus shifted towards understanding the underlying catalytic cycle through a mixture of the presented experiments and a detailed mechanistic study with density functional theory. The gained insights were expected to allow for rational improvements of the catalytic system, e.g., via suggestions for the use of appropriate phosphine ligands that best facilitate the underlying reaction mechanism.

4.2 Computational Details

All geometry optimizations were carried out at the BP86/def2-SV(P)^{9, 39, 51} level of theory with relativistically corrected effective core potentials⁸⁴ (ECP) for iodine. Stationary points were verified via analysis of the vibrational frequencies at the level of geometry optimization. Final electronic energies were obtained by single-point calculations at the PBE0-D3(BJ)/def2-QZVPP^{38-39, 93} level of theory employing Grimme's D3 dispersion correction⁶⁹ incorporating Becke-Johnson damping.⁷⁴ All quantum-chemical calculations were carried out using the TURBOMOLE program⁸⁵⁻⁸⁸ (Version 7.3) with the resolution-of-identity (RI) approximation^{40, 60, 62-63} and the corresponding auxiliary basis sets¹⁴⁵⁻¹⁴⁶ implemented in the program. Zero-point vibrational energies and thermodynamic corrections were obtained at the level of geometry optimization ($T = 298.15$ K and $p = 1$ bar) and scaled to the given reaction temperatures (120 °C for the carbonylation of phenyl ethyl alcohol and 180 °C for the carbonylation of *tert*-butyl alcohol). For all species, the thermodynamic reference concentration was set to $x = 0.01$, except for CO ($p = 50$ bar). Solvent corrections to Gibbs free energies in 1-phenylethanol (carbonylation of phenyl ethyl alcohol) or in methyl ethyl ketone (MEK; carbonylation of *tert*-butyl alcohol) were calculated for all species, except CO and CO₂, with the conductor-like screening model for real solvents (COSMO-RS)⁷⁵⁻⁷⁶ carried out with the COSMOtherm program^{77, 89} (Version 18.0.0; Revision 4360; Parameters BP_TZVP_18.ctd). All energies discussed are Gibbs free energies (G) in kJ mol⁻¹. Connectivities between minima and transition states implied in figures and schemes were validated by intrinsic-reaction-coordinate (IRC) calculations.¹⁰³ Pictures of molecular structures were generated with the CYLview¹⁴⁷ program.

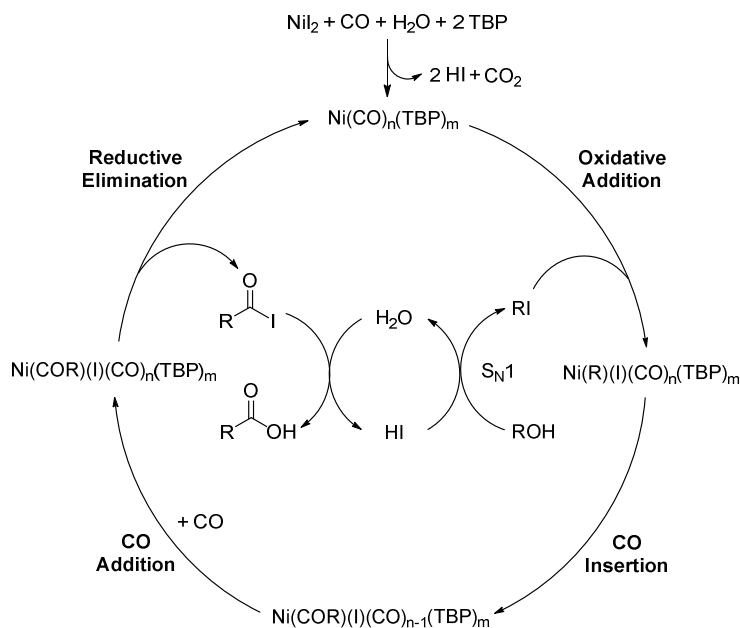
A multitude of geometrical isomers was analyzed for all complexes. Due to the vast number of structures, the herein reported structures are limited to the isomer lowest in energy for each species. All attempts to locate transition states for the homolytic cleavage of R–I or the radical recombination of the metal-centered radicals and R· were unsuccessful. Neither closed-shell nor open-shell methods (broken symmetry) nor potential energy surface scans revealed any significant barrier. It is therefore proposed that these steps are of barrierless nature, however, it cannot be excluded that this is an artefact of the single-reference methods.

Note that the numbering of the calculated and experimental structures is reset for every chapter.

4.3 Carbonylation of Phenyl Ethyl Alcohol

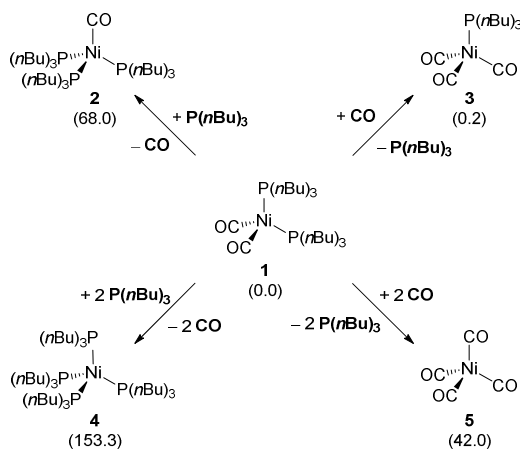
4.3.1 Neutral Reaction Pathways

Based on the experimental observations and commonly proposed reaction mechanisms,²⁰⁴⁻²¹⁵ a mechanistic scenario has been developed that sets the starting point for the detailed quantum-chemical investigations (see Scheme 4.4). Initially, the employed alcohol is converted into the corresponding alkyl halide species via an S_N1 substitution with HI. This reaction step is the reason for the high dependency of the catalytic system on the presence of a HI source to make sure coordinating species can be formed (*vide supra*). Other halides might also work, but as alkyl iodides exhibit the lowest alkyl-halide bond energy they were expected to be most suitable for the reaction. In the presented case, HI is formed during the reduction of the Ni^{II} halide to the Ni^0 species with CO, however, direct addition of HI, e.g., when using $Ni(COD)_2$ is also possible (see Table 4.1). Oxidative addition of the alkyl halide to the Ni^0 complex leads to the formation of on-cycle species suitable for CO insertion into the Ni–C bond. Subsequent CO addition and reductive elimination set the stage for the liberation of the carbonylated acyl halide species that is hydrolyzed to yield the desired carboxylic acid. Constant hydrolysis is required to regenerate HI, which is available only in small quantities with respect to the employed substrate to avoid the high corrosivity, which is of critical importance in the previously developed processes (see Scheme 4.2).



Scheme 4.4: Proposed catalytic cycle for the carbonylation of alcohols to carboxylic acids via alkyl halide intermediates ($n=1-3$; $m=0-2$; $n+m=2-4$).

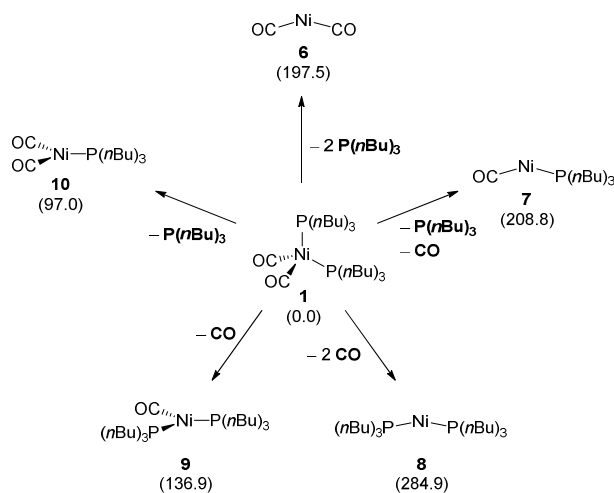
As experimental evidence for the proposed reaction steps or even the coordination environment was basically non-existent, the quantum-chemical investigations started by evaluating various possible species that could present resting states or reaction intermediates in the Ni-catalyzed carbonylation of alcohols/alkyl halides. Firstly, the stability of various four-coordinate Ni complexes with carbonyl (CO) and phosphine (P(*n*Bu)₃) ligands was compared (see Scheme 4.5). From the expected Ni-diphosphine-dicarbonyl complex **1**, exchange of one CO ligand for P(*n*Bu)₃ leads to the significantly less stable **2** ($\Delta G^{393} = 68.0 \text{ kJ mol}^{-1}$). On the other hand, exchange of one phosphine group for a third carbonyl ligand is energetically equal within the error limit of density functional theory (**1**→**3**: $\Delta G^{393} = 0.2 \text{ kJ mol}^{-1}$). The full substitution with P(*n*Bu)₃ and CO ligands leads to complexes **4** and **5**, respectively. The formation of both complexes is significantly endergonic (**4**: $\Delta G^{393} = 153.3 \text{ kJ mol}^{-1}$; **5**: $\Delta G^{393} = 42.0 \text{ kJ mol}^{-1}$). The initial evaluation shows that higher phosphine substitution is highly disfavored, which is caused by the high steric bulk of the large phosphine units. Due to the high energies and with at most two equivalents of phosphine in the reaction mixture, the formation of **2** and **4** as well as other higher phosphine-substituted reaction intermediates will not be relevant. The significantly lower stability of nickeltetracarbonyl (**5**) indicates that catalyst poisoning caused by high amounts of carbon monoxide gas is not to be expected in large amounts. While the mono- and disubstituted species **1** and **3** are equally suited as resting states, the following schemes will be referenced to the (slightly) more stable diphosphine-dicarbonyl complex **1**.



Scheme 4.5: Thermodynamic stabilities of the possible four-coordinate Ni-carbonyl-phosphine species. ΔG^{393} in kJ mol^{-1} ; RI-PBE0-D3(BJ)/def2-QZVPP//BP86/def2-SV(P); COSMO-RS (1-phenylethanol).

For oxidative addition to take place, the four-coordinate species will need to dissociate one or more ligands. Possible two- and three-coordinate reaction intermediates were calculated and are presented in Scheme 4.6. Three combinations of the two ligands can be considered for the two-coordinate species: two carbonyl ligands (**6**), two phosphine ligands (**8**) and one of each ligand (**7**). However, all three species are extremely unstable and are not considered

as realistic intermediates at the given reaction conditions (**6**: $\Delta G^{393} = 197.5 \text{ kJ mol}^{-1}$; **7**: $\Delta G^{393} = 208.8 \text{ kJ mol}^{-1}$; **8**: $\Delta G^{393} = 284.9 \text{ kJ mol}^{-1}$). The mono- and diphosphine-coordinated three-coordinate species **9** and **10** were also considered and found to be significantly more stable than the two-coordinate complexes. The diphosphine intermediate **9** is $136.9 \text{ kJ mol}^{-1}$ less stable than four-coordinate resting state **1**, while the respective molecule **10**, which carries only one phosphine ligand is 97.0 kJ mol^{-1} less stable than **1**. Although the formation of **9** and **10** is still strongly endergonic, these species represent more suitable on-cycle species than their two-coordinate equivalents.



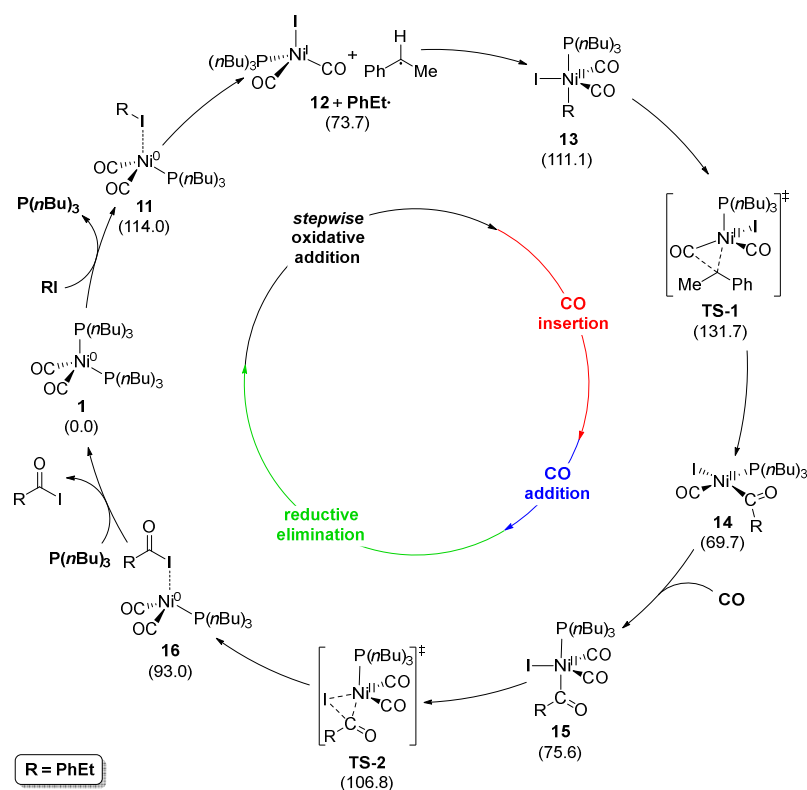
Scheme 4.6: Thermodynamic stabilities of the potential two- and three-coordinate key intermediates in the Ni-catalyzed carbonylation of alkyl- and benzyl iodides. ΔG^{393} in kJ mol^{-1} ; RI-PBE0-D3(BJ)/def2-QZVPP//BP86/def2-SV(P); COSMO-RS (1-phenylethanol).

From here, the proposed intermediates and transition states along the proposed reaction pathway were calculated starting with the monophosphine-substituted system (see Scheme 4.7), which was selected due to the lower energy of **10** compared to **9**. The availability of the alkyl halide substrate (**RI**) allows for the formation of the alkyl halide adduct of the three-coordinate species **10**, which leads to the tetrahedral intermediate **11** ($\Delta G^{393} = 114.0 \text{ kJ mol}^{-1}$). The direct two-electron oxidative addition (as proposed in the literature and incorporated into the expected catalytic cycle) was found to be not feasible at the employed reaction conditions (see Scheme 4.8). Prior investigations on the palladium-catalyzed carbonylation alkyl iodides reported stepwise oxidative addition mechanisms based on photocatalytically initiated single-electron transfer.²¹⁶⁻²¹⁷ The involvement of alkyl radicals, which are generated by single-electron transfer steps, in Ni-catalyzed reactions has previously been suggested by multiple research groups,^{204, 209-210, 212-213, 218} but to the best of our knowledge no in-depth investigation of the underlying reaction pathways had been carried out yet. Although adduct **11** is slightly less stable than non-adduct species **10** ($\Delta\Delta G^{393} = 17.0 \text{ kJ mol}^{-1}$), it was found to allow for barrierless homolytic cleavage of the C–I bond,

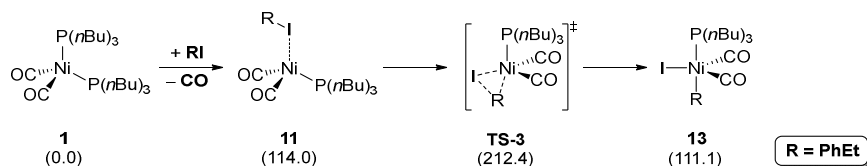
which leads to the significantly more stable Ni^I halide complex **12** and the phenylethyl radical (**PhEt•**; $\Delta G^{393} = 73.7 \text{ kJ mol}^{-1}$). All attempts to locate a transition state corresponding to this chemical transformation were unsuccessful, either employing closed-shell or open-shell broken symmetry methods. Scans along the R–I bond stretch reaction coordinate did not indicate a reaction barrier and led to the assumption of a barrierless reaction. Recombination of the two species leads to five-coordinate complex **13** ($\Delta G^{393} = 111.1 \text{ kJ mol}^{-1}$), in which the bulky phosphine and the alkyl substituent occupy the axial positions in the trigonal-bipyramidal geometry. As in the previous chapter on the dehydrogenative coupling of alcohols, a wide variety of configurational isomers was investigated for the four- and five-coordinate species and only the most stable isomer along the reaction pathway is shown here. **CO** insertion from **13** can take place via **TS-1** with a barrier of $131.7 \text{ kJ mol}^{-1}$. This leads to the square-planar Ni^{II} intermediate **14** being the first intermediate that carries the desired acyl unit ($\Delta G^{393} = 69.7 \text{ kJ mol}^{-1}$). Addition of another equivalent of **CO** will lead back to a trigonal-bipyramidal complex, in which the **P(*n*Bu)₃** and acyl groups once more occupy the axial positions (**15**; $\Delta G^{393} = 75.6 \text{ kJ mol}^{-1}$). This also places the equatorially positioned iodide ligand within a 90° angle to the acyl group and thus sets up the subsequent reductive elimination transition state (**TS-2**). With a barrier of $106.8 \text{ kJ mol}^{-1}$, reductive elimination can take place via **TS-2** and leads to the acyl halide adduct **16**, which is exhibiting the equivalent Ni–I contact as the initial alkyl halide adduct **11** (**16**: $\Delta G^{393} = 93.0 \text{ kJ mol}^{-1}$). Similar R–I adducts have been previously reported as computed intermediates for Ni²⁰⁵⁻²⁰⁶ and Pd²¹⁹ by the groups of Bottoni and Thiel. The formed acyl halide will subsequently be hydrolyzed to the desired carboxylic acid product as presented in the proposed catalytic cycle in Scheme 4.4. The overall reaction barrier of $131.7 \text{ kJ mol}^{-1}$ is in agreement with a slow reaction at the employed reaction temperature of 120°C . Once more, it should be noted that the comparison solely based on the activation barrier is not necessarily accurate but can only give general indications due to the complex factors at play in the system. For example, precatalyst equilibria such as the reduction of NiI₂ to the diphosphine-dicarbonyl-Ni⁰ complex **1** are not included in the computational investigation and can further influence the observed reaction rate and yield.

Similar to the reductive elimination leading to the acyl halide adduct (**16**), the two-electron oxidative addition pathway begins from the alkyl iodide adduct (**11**; see Scheme 4.8), which was also identified as key species in the stepwise oxidative addition pathway. The pathway proceeds via **TS-3**, which is associated with a barrier of over 200 kJ mol^{-1} and therefore significantly too high in energy to be feasible at the reaction conditions or to be competitive with the stepwise pathway presented above (**TS-3**: $\Delta G^\ddagger = 212.4 \text{ kJ mol}^{-1}$). The two-electron oxidative addition directly leads to the five-coordinate trigonal-bipyramidal intermediate **13** ($\Delta G^{393} = 111.1 \text{ kJ mol}^{-1}$). The most stable isomer, which was already shown as part of the stepwise pathway, with the alkyl substituent in axial position and the iodide ligand in

equatorial position exhibits the smallest possible R–Ru–I angle in a trigonal-bipyramidal system (90°) and is also formed via the two-electron oxidative addition transition state **TS-3**.



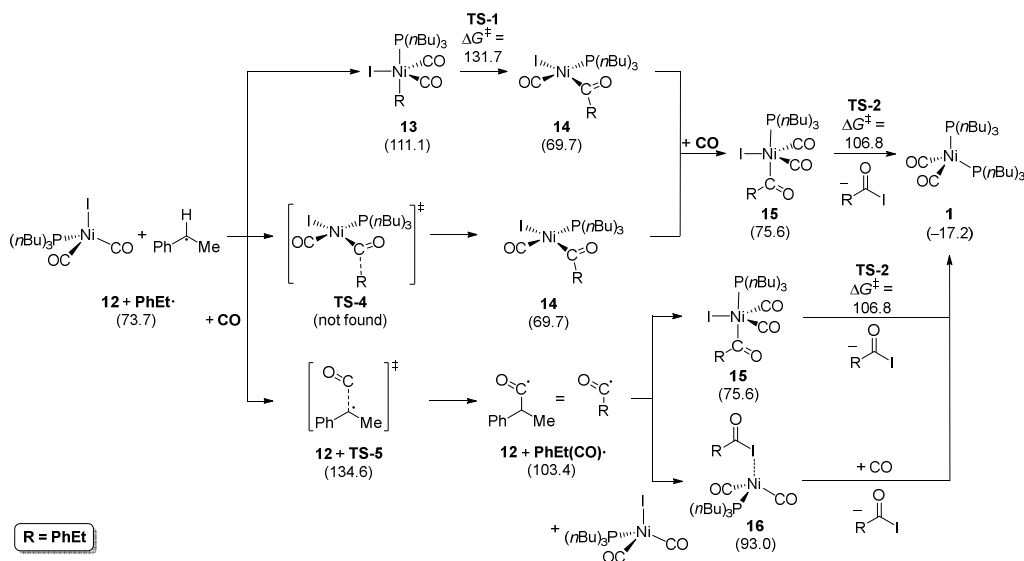
Scheme 4.7: Catalytic cycle for the carbonylation of iodoethylbenzene (**RI**) to the corresponding acyl iodide via a stepwise oxidative addition process over a Ni^I complex (**12**) and the phenylethyl radical species **PhEt•** in the catalytic system coordinated by one **P(nBu)₃** and two **CO** ligands. ΔG^{393} in kJ mol⁻¹; RI-PBE0-D3(BJ)/def2-QZVPP//BP86/def2-SV(P); COSMO-RS (1-phenylethanol).



Scheme 4.8: Reaction pathway for the carbonylation of **RI** to the corresponding acyl iodide via two-electron oxidative addition transition state **TS-3** in the catalytic system coordinated by one **P(nBu)₃** and two **CO** ligands. ΔG^{393} in kJ mol⁻¹; RI-PBE0-D3(BJ)/def2-QZVPP//BP86/def2-SV(P); COSMO-RS (1-phenylethanol).

To further investigate possible competing pathways, various radical recombination and reaction steps were calculated (see Scheme 4.9). Starting from **12** and **PhEt•**, which are formed via the previously discussed homolytic R–I cleavage (see Scheme 4.7), two alternative pathways have been identified next to the recombination to **13** (*vide supra*).

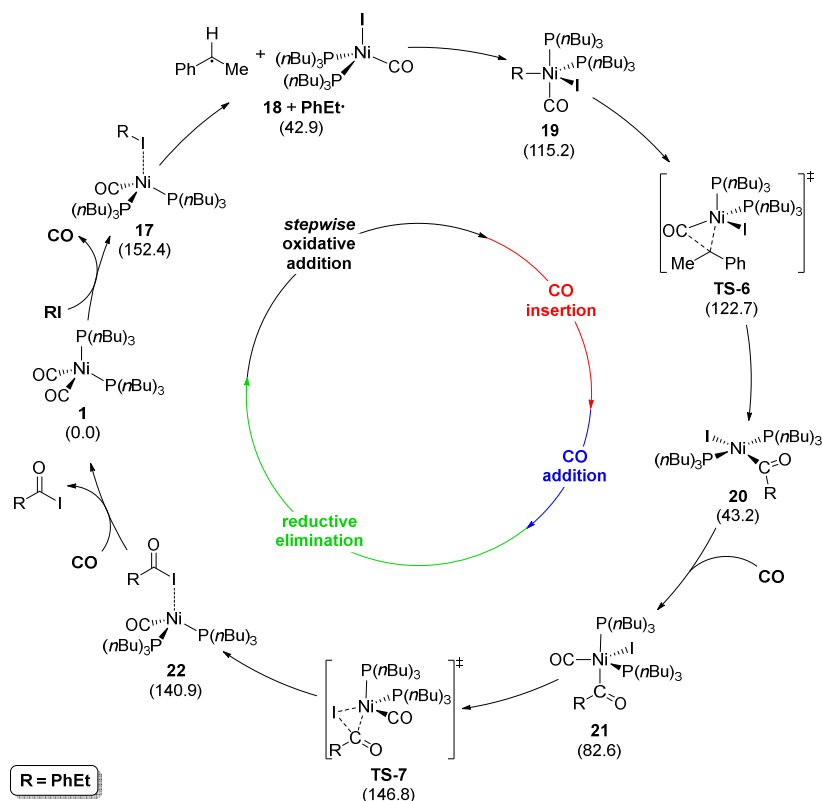
Firstly, the radical attack of **PhEt** \cdot to a carbonyl carbon atom of **12** was envisioned as a pathway to circumvent the rate-determining **CO** insertion transition state (**TS-1**). However, all attempts to locate **TS-4** were unsuccessful and led to other surrounding structures indicating that this transformation is significantly less feasible. A barrierless nature of this step was ruled out as an analysis revealed that the unpaired electron is located on the Ni center and barrierless recombination, as proposed above, would only be available between the Ni atom and an external radical. Secondly, this kind of radical reaction towards a carbonyl C atom can take place with a free **CO** molecule via **TS-5** ($\Delta G^\ddagger = 134.6 \text{ kJ mol}^{-1}$). The activation barrier for this recombination is slightly higher than the barrier of the **CO** insertion transition state (**TS-1**: $\Delta G^\ddagger = 131.7 \text{ kJ mol}^{-1}$) and leads to the formation of the free acyl radical **PhEt(CO)** \cdot (next to unchanged Ni^I complex **12**; $\Delta G^{393} = 103.4 \text{ kJ mol}^{-1}$). From here, two scenarios to complete the catalytic cycle are plausible. Recombination of the acyl radical with the Ni^I complex **12** (similar to the recombination of the alkyl radical to form **13**) leads to the formation of **15** ($\Delta G^{393} = 75.6 \text{ kJ mol}^{-1}$), which needs to undergo reductive elimination via the previously discussed **TS-2** ($\Delta G^\ddagger = 106.8 \text{ kJ mol}^{-1}$) to form the acyl halide product. Alternatively, a direct addition of **PhEt(CO)** \cdot to the iodide ligand in **12**, similar to the reverse reaction of the homolytic cleavage that led to radical generation in the first place, should be possible and would circumvent the reductive elimination step by directly generating the acyl halide adduct complex (**16**) in an outer-sphere mechanism (i.e., without the substrate ever coordinating to the Ni complex). In addition to the slightly larger activation barrier of **TS-5** to **TS-1** ($\Delta\Delta G^\ddagger = 2.9 \text{ kJ mol}^{-1}$), experimental evidence was used to support the postulated catalytic cycle in Scheme 4.7. Radical trapping experiments did only show a small drop in catalytic activity, leading to the assumption that the radical species has an extremely short lifetime and directly recombines with the Ni^I complex without ever escaping the solvent cage. A reaction of **PhEt** \cdot with **CO** would be expected to require a longer radical lifetime, in which the radical species can escape the solvent cage and can reach a CO unit. Consequently, this should lead to a more significant shutdown of the reaction performance when highly reactive radical traps are present, which would instantly react with the radical species once it can come into contact with other components. While this could also be interpreted as evidence against a radical mechanism altogether, the observation of EPR signals in the reaction of Ni(TBP)₂(CO)₂ with iodocyclohexane in MEK (X-band (9.638417 GHz) EPR spectrum at 203 K; $g_{\text{eff}} = 2.15$), which agree with previously reported Ni^I species,²²⁰⁻²²¹ was in favor of our assessment. For a complete description of the performed trapping experiments and EPR spectroscopy, please refer to the experimental section of the corresponding publication.²⁰²



Scheme 4.9: Possible recombination- and radical reaction pathways in the catalytic system coordinated by one $\text{P}(n\text{Bu})_3$ and two CO ligands. ΔG^{393} in kJ mol^{-1} ; referenced to **1** and **RI**; RI-PBE0-D3(BJ)/def2-QZVPP//BP86/def2-SV(P); COSMO-RS (1-phenylethanol).

After the investigation of the catalytic system coordinated by one phosphine ligand, the scope of the calculations was extended to reaction pathways with two $\text{P}(n\text{Bu})_3$ ligands coordinated to Ni (see Scheme 4.10) as well as a phosphine-free nickeltetracarbonyl system (see Scheme 4.11). The catalytic cycle for the diphosphine system, similarly to the previously shown reaction pathways, is based on $\text{Ni}(\text{TBP})_2(\text{CO})_2$ (**1**). From this resting state, CO dissociation leads to the three-coordinate complex **9** ($\Delta G^{393} = 136.9 \text{ kJ mol}^{-1}$), and the subsequent formation of the tetrahedral alkyl halide adduct species **17** is highly endergonic (**17**: $\Delta G^{393} = 152.4 \text{ kJ mol}^{-1}$). Once more, the adduct species is the prerequisite for the homolytic cleavage of the R–I bond leading to formation of a Ni^{I} complex and the phenylethyl radical PhEt^\bullet , which is significantly more stable than the Ni–I adduct complex **17** and also more stable than the monophosphine Ni^{I} complex presented above (**12**: $\Delta G^{393} = 73.8 \text{ kJ mol}^{-1}$; see Scheme 4.7). Recombination of the two species leads to the five-coordinate Ni^{III} complex **19** ($\Delta G^{393} = 115.2 \text{ kJ mol}^{-1}$) and subsequent CO insertion transition state **TS-6** ($\Delta G^\ddagger = 122.7 \text{ kJ mol}^{-1}$). **TS-6** is slightly more stable than the corresponding monophosphine transition state (**TS-1**: $\Delta G^\ddagger = 131.7 \text{ kJ mol}^{-1}$), indicating that the negative effects of bulky phosphine ligands being positioned in axial and equatorial position is counteracted by the underlying electronic effects. However, once the square-planar Ni^{III} complex **20** is formed via **TS-6**, in which the two $\text{P}(n\text{Bu})_3$ ligands are positioned *trans* to each other and thus minimize the steric pressure within the complex, the energetic difference between the mono- and diphosphine complexes significantly increases (**20**: $\Delta G^{393} = 43.2 \text{ kJ mol}^{-1}$; **14**: $\Delta G^{393} = 69.7 \text{ kJ mol}^{-1}$) indicating the steric influences in **19** and **TS-6**. These trends are also nicely observed when looking at the subsequent CO addition to form

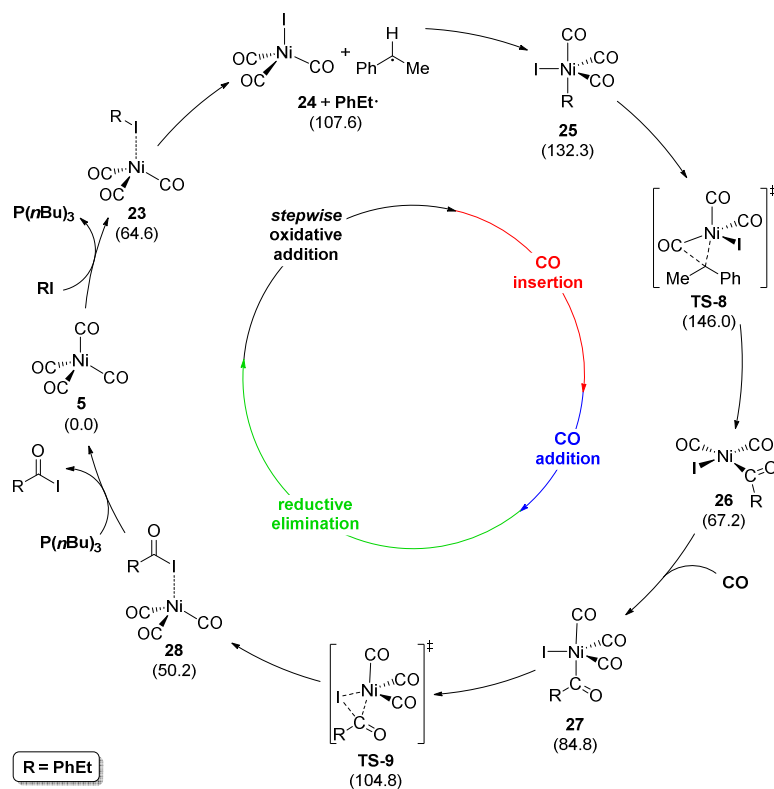
the five-coordinate acyl nickel complex **21** ($\Delta G^{393} = 82.6 \text{ kJ mol}^{-1}$). The structure of **21** features the same axial and equatorial placement of the phosphine ligands that has been observed in intermediate **19** and is found to be slightly less stable than the respective monophosphine system (**15**: $\Delta G^{393} = 75.6 \text{ kJ mol}^{-1}$). Other configurational isomers, which avoid the steric repulsion could be located, but do not facilitate the subsequent reductive elimination step. Overall, the activation barrier for diphosphine reductive elimination (**TS-7**) is higher in energy, which is in line with expectations that electron-poorer systems are preferred in reductive elimination steps (**TS-7**: $\Delta G^\ddagger = 148.8 \text{ kJ mol}^{-1}$). The formed adduct complex **22** can dissociate the acyl halide species for further hydrolysis to the desired carboxylic acid (**22**: $\Delta G^{393} = 140.9 \text{ kJ mol}^{-1}$). Overall, the diphosphine pathway is significantly less feasible than the catalytic cycle for the monophosphine complexes (cf. Scheme 4.7). Although experiments consistently achieved higher yields when two equivalents of phosphine were used, the more stable monophosphine pathway could be supported by experiments employing non-coordinating bases such as Hünig's base. In these, one equivalent of base was able to substitute one equivalent of phosphine in the catalytic system indicating that only one phosphine unit is actually coordinated (*vide supra*).



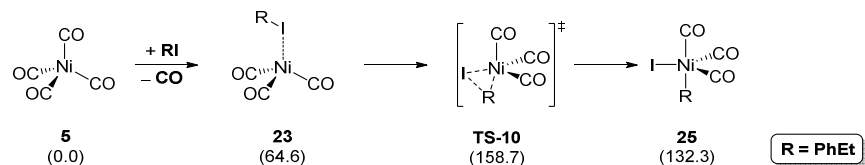
Scheme 4.10: Catalytic cycle for the carbonylation of iodoethylbenzene (**RI**) to the corresponding acyl iodide via a stepwise oxidative addition process over a Ni^{I} complex (**18**) and phenylethyl radical species **PhEt**• in the catalytic system coordinated by two $\text{P}(n\text{Bu})_3$ and one CO ligands. ΔG^{393} in kJ mol^{-1} ; RI-PBE0-D3(BJ)/def2-QZVPP//BP86/def2-SV(P); COSMO-RS (1-phenylethanol).

To gain further insights and to allow for comparison with phosphine-free experiments that did not lead to any product observation, the pathways in a phosphine-free catalytic system were investigated (see Scheme 4.11). The phosphine-free system starts from Ni(CO)₄ (**5**). From here, the **RI** adduct of tri-coordinate Ni(CO)₃ is formed (**23**: $\Delta G^{393} = 64.6 \text{ kJ mol}^{-1}$). It should be noted that these energies cannot be directly compared to the energies given in the two previously presented catalytic cycles as they are referenced to different structures (Schemes 4.7 and 4.10 to Ni(TBP)₂(CO)₂ (**1**) and Scheme 4.11 to Ni(CO)₄ (**5**). Homolytic R–I cleavage takes place from **23** and leads to Ni^I complex **24** and the phenyl ethyl radical **PhEt•** ($\Delta G^{393} = 107.6 \text{ kJ mol}^{-1}$). Interestingly, in contrast to the previous systems, the radical generation step (relative to the alkyl halide adduct) is endergonic (**23**→**24** + **PhEt•**: $\Delta G^{393} = 43.0 \text{ kJ mol}^{-1}$; **11**→**12** + **PhEt•**: $\Delta G^{393} = -40.3 \text{ kJ mol}^{-1}$; **17**→**18** + **PhEt•**: $\Delta G^{393} = -109.5 \text{ kJ mol}^{-1}$), which might be attributed to the electron-poorer nature of **23**. Radical recombination of **24** and **PhEt•** leads to the five-coordinate species **25** ($\Delta G^{393} = 132.3 \text{ kJ mol}^{-1}$), in which the alkyl group is located in an axial position and exhibits a 90° angle to two of the three carbonyl ligands. This structural arrangement sets the stage for **CO** insertion via **TS-8** with an activation barrier of 146.0 kJ mol⁻¹ and leads to the Ni^{II} complex **26** ($\Delta G^{393} = 67.2 \text{ kJ mol}^{-1}$). **CO** addition to **27** ($\Delta G^{393} = 84.8 \text{ kJ mol}^{-1}$) and subsequent reductive elimination via **TS-9** ($\Delta G^\ddagger = 104.8 \text{ kJ mol}^{-1}$) are significantly more feasible than the **CO** insertion step. The reductive elimination once more leads to the acyl halide adduct **28** ($\Delta G^{393} = 50.2 \text{ kJ mol}^{-1}$), which is hydrolyzed to the carboxylic acid after elimination from the complex. The high barrier for the **CO** insertion (**TS-8**), which is expected to not be feasible at the given reaction conditions (see Figure 2.1), is in good agreement with the experimental observations. On the other hand, the high stability of the alkyl halide adduct **23** and the relatively low barrier reductive elimination (**TS-9**) might present highly interesting species. However, due to the different reference points in the presented schemes, another contribution of 42 kJ mol⁻¹ must be added to the values given in Scheme 4.11 if phosphine is present in the reaction system (**1**→**5**: $\Delta G^{393} = 42.0 \text{ kJ mol}^{-1}$; see Scheme 4.5). Therefore, the three key species and steps of the phosphine-free catalytic cycle, i.e., the Ni^I complex/**PhEt•**, the **CO** insertion and reductive elimination, are all less feasible than the transition states, which were found for the phosphine-coordinated systems.

For completeness and motivated by the high stability of the alkyl halide adduct complex **23** ($\Delta G^{393} = 64.6 \text{ kJ mol}^{-1}$), the two-electron oxidative addition directly leading from intermediate **23** to **25**, as usually proposed in the literature,^{181, 205-206, 211-212, 218} was calculated (see Scheme 4.12). The resulting **TS-10** corresponding to this transformation was found to be significantly less feasible than the radical-based stepwise oxidative addition pathway over **24** and **PhEt•** (**TS-10**: $\Delta G^\ddagger = 158.7 \text{ kJ mol}^{-1}$) and ruled out in further considerations.



Scheme 4.11: Catalytic cycle for the carbonylation of iodoethylbenzene (**RI**) to the corresponding acyl iodide via a stepwise oxidative addition process over a Ni^{I} complex (**18**) and the phenylethyl radical species PhEt^\bullet in the catalytic system coordinated by three CO ligands. ΔG^{393} in kJ mol^{-1} ; RI-PBE0-D3(BJ)/def2-QZVPP//BP86/def2-SV(P); COSMO-RS (1-phenylethanol).



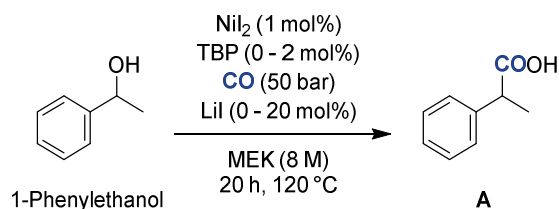
Scheme 4.12: Reaction pathway for the carbonylation of **RI** to the corresponding acyl iodide via two-electron oxidative addition transition state **TS-3** in the catalytic system coordinated by three CO ligands. ΔG^{393} in kJ mol^{-1} ; RI-PBE0-D3(BJ)/def2-QZVPP//BP86/def2-SV(P); COSMO-RS (1-phenylethanol).

All in all, the catalytic pathway, in which one $\text{P}(\text{nBu})_3$ ligand was coordinated to nickel was found to be significantly preferred over the catalytic systems without phosphine or with two phosphine ligands coordinated to Ni. This was contrary to what had initially been expected due to the higher yields with two equivalents of phosphine. However, the close collaboration between experiment and calculations at CaRLa with the ability to suggest decisive experiments with non-coordinating bases led to an understanding of the underlying processes and to the confirmation of the calculations.

4.3.2 Anionic Reaction Pathways

In combination with the quantum-chemical investigations of the neutral potential energy surfaces with different phosphine coordination motifs, further experiments on the role of the $\text{P}(n\text{Bu})_3$ ligand and the role of the lithium iodide (**LiI**) additive were conducted (see Table 4.3). The experiments revealed that the positive effects that had been initially observed (see Table 4.1) was highly dependent on the additive concentration (column 3). While small amounts of **LiI** (2 mol%) showed only a small increase in performance, loadings of 8 mol% of **LiI** achieved drastically higher yields. Increasing the **LiI** concentration to 20 mol% did not lead to significant further improvements. The use of only 1 mol% phosphine ligand (Ni:P ratio: 1:1) led to significantly worse performance when no **LiI** was added (entry 1). However, the addition of **LiI** led to the very similar yields being observed indicating that the difference between the two ligand loadings had nearly disappeared. To our surprise, when the appropriate control experiments without TBP were performed, an increase in yield was also observed (column 5). While the reaction without phosphine and **LiI** did not lead to any product, the use of 8 or 20 mol% **LiI** brought the performance of the phosphine-free system into line with the phosphine-containing reactions.

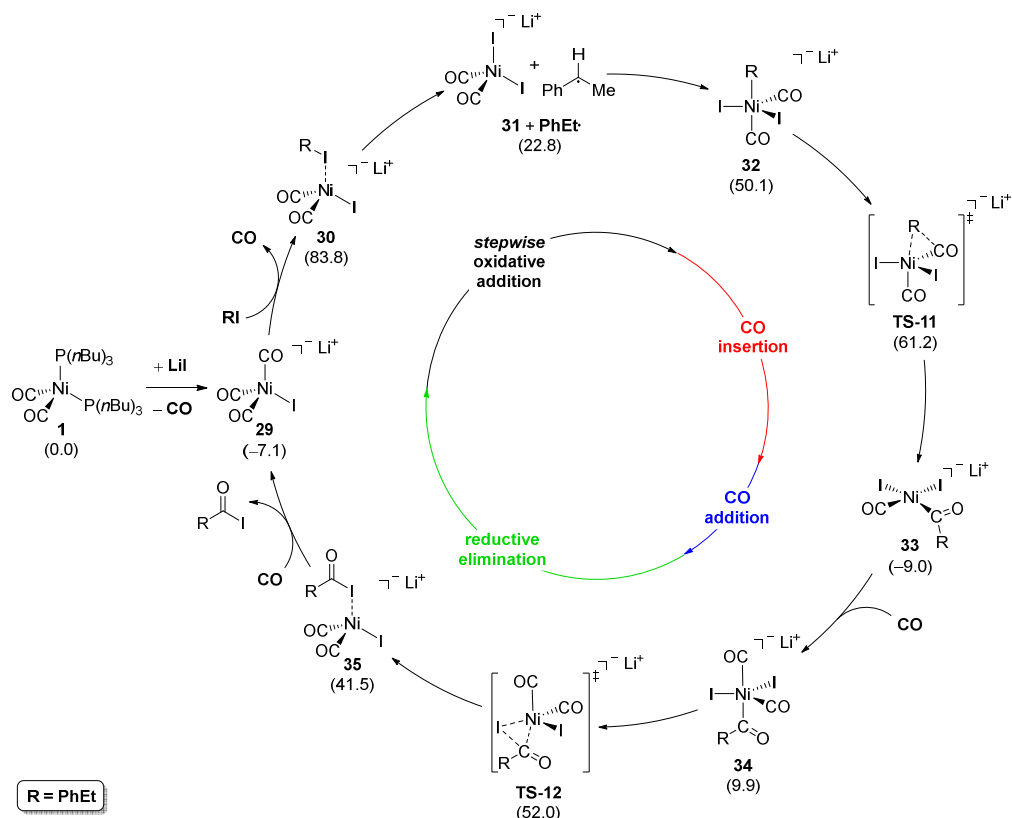
Table 4.3: Experimental screening of **LiI** and phosphine concentrations in the nickel-catalyzed carbonylation of alcohols to carboxylic acids.^[a] All experiments were carried out by Sara Sabater at CaRLa.



Entry	LiI	Yield A [%] (2 mol% TBP)	Yield A [%] (1 mol% TBP)	Yield A [%] (0 mol% TBP)
1	-	4	1	0
2	2 mol%	12	10	6
3	4 mol%	24	20	8
4	8 mol%	60	52	50
5	20 mol%	63	58	56

[a] A mixture of 1-phenylethanol (8.3mmol), NiI_2 (1 mol%), TBP (0 – 2 mol%) and LiI (0 - 20 mol%) was pressurized with CO at 50 bar and stirred at 120 °C for 20 h. Yields were determined by GC-FID chromatography using anisole as internal standard after derivatization with *N*-methyl-*N*-(trimethylsilyl)trifluoroacetamide.

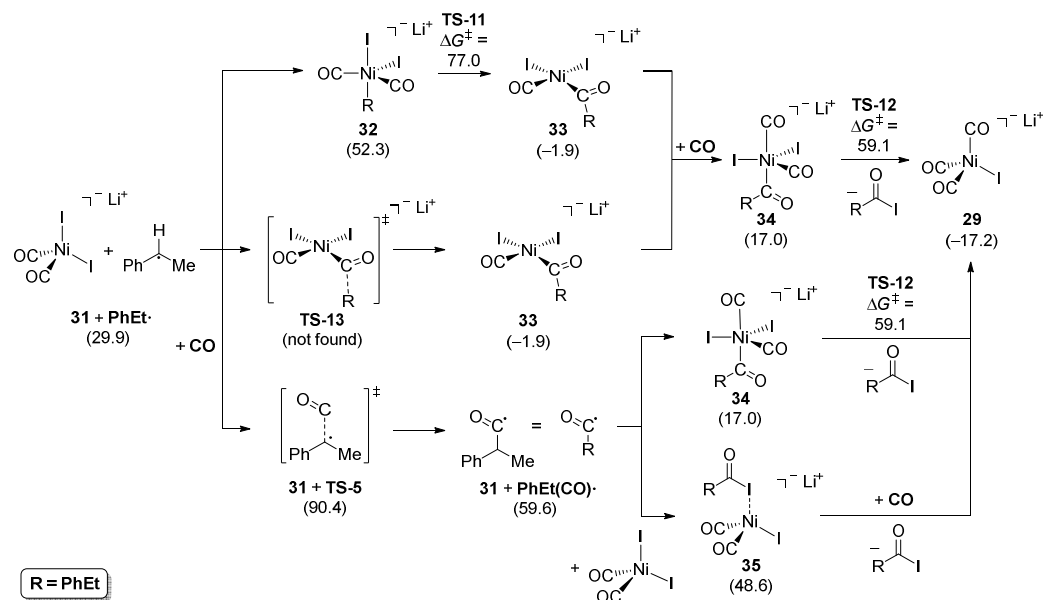
In light of this drastic change, it was clear that **LiI** would not just be supporting the initial reduction of the Ni^{II} species (NiI₂) to the Ni⁰ complex **1** or exhibit other small additive effects (e.g., interaction of Li⁺ with relevant species), but is capable of inducing a more significant mechanistic change. Due to the similar performance on the catalytic system with and without **P(*n*Bu)₃**, a pathway via phosphine-free species was assumed and investigated (see Scheme 4.13). As initial step of this pathway, the formation of an anionic tricarbonylnickelhalide complex (Li⁺[Ni(CO)₃I]⁻) was envisioned, the formation of which has been previously reported to take place from Ni(CO)₄ and **LiI** by Cassar and Foà in 1970²²² and proposed as intermediates in carbonylation reactions by Rizkalla in 1987.¹⁹⁴ The formation of the anionic complex **29** was calculated to be slightly exergonic ($\Delta G^{393} = -7.1 \text{ kJ mol}^{-1}$; see Scheme 4.13). This is contrary to the previous reports that subsequent addition of phosphine to the anionic nickel halide complex led to formation of the respective phosphine-coordinated complexes. Therefore, the modelling parameters were adjusted to room temperature, at which the experimental isolation of the species was reported ($\Delta G^{298} = 15.3 \text{ kJ mol}^{-1}$). A change in trends is observed that is in good agreement with the experimental observations and further indicates that the required species is formed at catalytic conditions. It should be noted that for the following intermediates and transition states only the anionic fragments were calculated and a constant interaction with Li⁺ was assumed. From **29** and the free alkyl halide **RI**, formation of the anionic alkyl halide adduct species **30**, which has been previously discussed for the neutral reaction pathways (**30**: $\Delta G^{393} = 83.8 \text{ kJ mol}^{-1}$). Homolytic cleavage of the R–I bond leads to formation of Ni^I dicarbonyl dihalide complex **31** and **PhEt·** ($\Delta G^{393} = 22.8 \text{ kJ mol}^{-1}$). Therefore, this step in the anionic phosphine-free iodide-coordinated system resembles the neutral phosphine systems, which also exhibited the strongly exergonic homolytic cleavage (relative to species **30**). Direct recombination of the two species leads to the five-coordinate anionic nickel alkyl complex **32** ($\Delta G^{393} = 50.1 \text{ kJ mol}^{-1}$). While the structure of **32**, which is shown in Scheme 4.13, was not found to be the most stable configurational isomer, it facilitated the most feasible **CO** insertion transition state (**TS-11**) and once more showed the high importance of calculating all possible isomer structures along all of the different reaction pathways. **TS-11** leads to the highly stable square-planar Ni^{II} complex **33**, in which the two iodide ligands are found in *cis* position (**TS-11**: $\Delta G^\ddagger = 61.2 \text{ kJ mol}^{-1}$; **33**: $\Delta G^{393} = -9.0 \text{ kJ mol}^{-1}$). The addition of a further equivalent of **CO** leads to the formation of the five-coordinate intermediate **34** ($\Delta G^{393} = 9.9 \text{ kJ mol}^{-1}$) and the subsequent reductive elimination transition state **TS-12** ($\Delta G^\ddagger = 52.0 \text{ kJ mol}^{-1}$) generates the acyl halide adduct species **35** ($\Delta G^{393} = 41.5 \text{ kJ mol}^{-1}$). Equally to the neutral catalytic system, the desired carboxylic acid product can be formed by hydrolysis of the free acyl halide after dissociation from the complex. With an activation barrier of 90.9 kJ mol^{-1} , the anionic reaction pathway is 40.8 kJ mol^{-1} more feasible than the monophosphine-substituted catalytic system (**TS-1**: $\Delta G^\ddagger = 131.7 \text{ kJ mol}^{-1}$).



Scheme 4.13: Catalytic cycle for the carbonylation of iodoethylbenzene (**RI**) to the corresponding acyl iodide via a stepwise oxidative addition process over a Ni^I complex (**31**) and phenylethyl radical species **PhEt•** in the LiI-induced anionic catalytic system. ΔG^{393} in kJ mol⁻¹; RI-PBE0-D3(BJ)/def2-QZVPP//BP86/def2-SV(P); COSMO-RS (1-phenylethanol).

To investigate whether the radical reaction and recombination steps behave any differently to the steps on the neutral potential energy surface, a detailed assessment of possible pathways was undertaken (see Scheme 4.14). From **31** and **PhEt•**, two additional pathways next to the previously discussed Ni radical recombination to **32** were investigated. Firstly, the transition state corresponding to the radical reaction of **PhEt•** with one of the two carbonyl ligands in **31** could not be located, and similarly to the discussion of this transition state in the investigation of the neutral catalytic system, it is assumed to not be of barrierless nature due to the localization of the unpaired electron within the Ni^I complex. It should be noted that it is conceptually not possible to prove the non-existence of this transition state and only a likely unfavorable nature of the transition state, which leads to the characterization of other species during optimization attempts, can be reported. The low barrier of the subsequent CO insertion step that would be avoided by the direct addition of **PhEt•** to the carbonyl group leads to the fact that the overall reaction barrier is not affected by this step and the general error that could be introduced by this is very low. Alternatively, the CO insertion can be replaced by the addition of CO to the free radical (**TS-5**: $\Delta G^\ddagger = 90.4$ kJ mol⁻¹) leading to

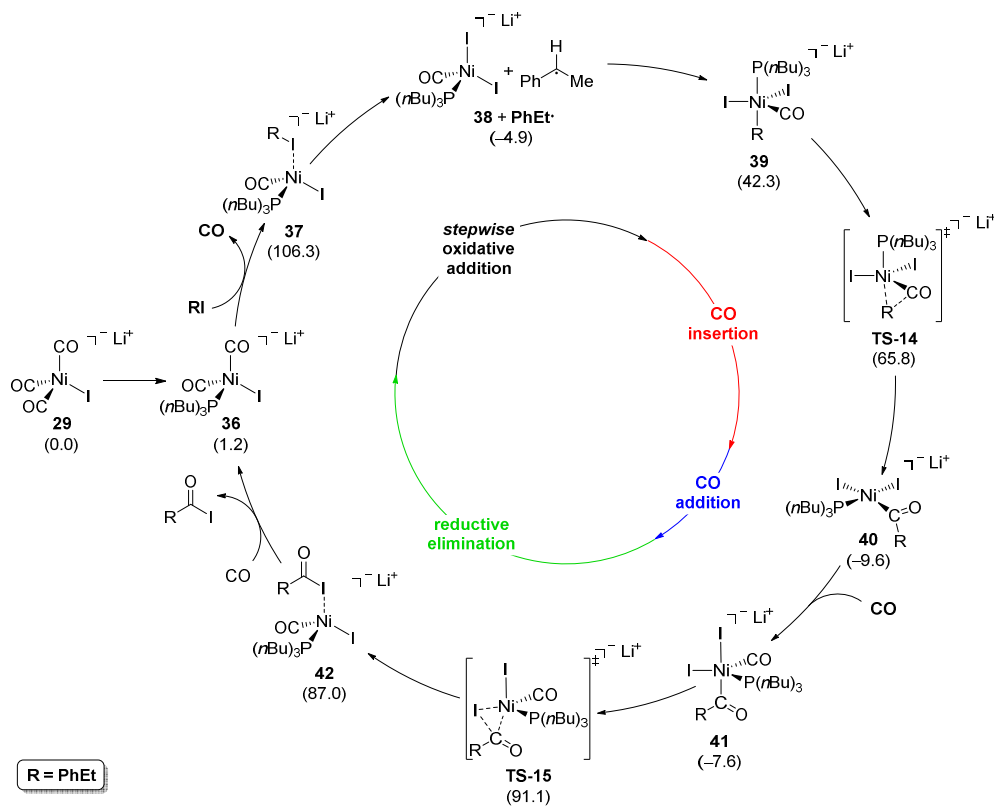
PhEt(CO)·. With a barrier of 90.4 kJ mol^{-1} , this pathway is less feasible than then barrierless recombination to **32** and subsequent **CO** insertion **TS-11** (**TS-11**: $\Delta G^\ddagger = 77.0 \text{ kJ mol}^{-1}$; $\Delta\Delta G^\ddagger = 13.4 \text{ kJ mol}^{-1}$) and led to the conclusion that recombination with the Ni atom of the complex will instantly take place, which is well in line with the experimental observations obtained with radical scavengers.



Scheme 4.14: Possible recombination- and radical reaction pathways in the **LiI**-induced anionic catalytic system. ΔG^{393} in kJ mol^{-1} ; referenced to **29** and **RI**; RI-PBE0-D3(BJ)/def2-QZVPP//BP86/def2-SV(P); COSMO-RS (1-phenylethanol).

Since slightly higher yields were observed in the phosphine-containing reaction mixture (see Table 4.3 – columns 3 and 5), an anionic phosphine-coordinated catalytic system was additionally investigated (see Scheme 4.15). The exchange of one carbonyl group in $\text{Li}^+[\text{Ni}(\text{CO})_3\text{I}]^-$ (**29**) with one **P(nBu)**₃ ligand was found to be nearly energetically equivalent to the fully carbonyl substituted complex (**36**: $\Delta G^{393} = 1.2 \text{ kJ mol}^{-1}$). The formation of the respective alkyl halide adduct complex that also carries one phosphine ligand (**37**: $\Delta G^{393} = 106.3 \text{ kJ mol}^{-1}$) is less feasible than the previously shown tricarbonyl equivalent (**30**: $\Delta G^{393} = 90.9 \text{ kJ mol}^{-1}$). The homolytic cleavage to **38** and **PhEt·**, in line with prior observations, is more exergonic when phosphine ligands are coordinated ($\Delta G^{393} = -4.9 \text{ kJ mol}^{-1}$; cf. Scheme 4.11 and corresponding discussion). Recombination leads to the five-coordinate species **39**, in which the bulkier **P(nBu)**₃ ligand and alkyl group are placed in the two axial positions of the trigonal-bipyramidal complex (**39**: $\Delta G^{393} = 42.3 \text{ kJ mol}^{-1}$). Low barrier **CO** insertion via **TS-14** leads to the square-planar Ni^{II} complex **40** ($\Delta G^{393} = -9.6 \text{ kJ mol}^{-1}$), which like the corresponding **CO** coordinated complex **33** features the two iodide ligands in *cis* configurations and subsequent **CO** addition leads to the acyl-coordinated complex **41** ($\Delta G^{393} = -7.6 \text{ kJ mol}^{-1}$). From here, reductive elimination can take

place with a barrier of $100.7 \text{ kJ mol}^{-1}$ due to the high stability of the four-coordinate species **40** ($\Delta G^{393} = -9.6 \text{ kJ mol}^{-1}$) and leads to the formation of **42** ($\Delta G^{393} = 87.0 \text{ kJ mol}^{-1}$). With barriers of over 100 kJ mol^{-1} for the formation of the alkyl halide adduct **37** and the reductive elimination step, the phosphine-coordinated pathway is less feasible than the phosphine-free pathway (**30**: $\Delta G^{393} = 90.9 \text{ kJ mol}^{-1}$; see Scheme 4.13). Thus, it was concluded that $\text{P}(\text{nBu})_3$ does not coordinate in the LiI -induced anionic system and that the slightly better performance is caused by other small effects that were not considered in the computational investigation (e.g., the initial Ni^{II} to Ni^0 step, the $\text{S}_{\text{N}}1$ substitution to form the alkyl halide, etc.).



Scheme 4.15: Catalytic cycle for the carbonylation of iodoethylbenzene (**RI**) to the corresponding acyl iodide via a stepwise oxidative addition process over a Ni^{I} complex (**38**) and the phenylethyl radical species PhEt^{\bullet} in the LiI -induced anionic catalytic system with one $\text{P}(\text{nBu})_3$ ligand. ΔG^{393} in kJ mol^{-1} ; RI-PBE0-D3(BJ)/def2-QZVPP//BP86/def2-SV(P); COSMO-RS (1-phenylethanol).

Overall, the quantum-chemical calculations can provide a rationale for the drastic effects observed when LiI is used as an additive in the Ni-catalyzed carbonylation of 1-phenylethanol to 2-phenylpropanoic acid. The additive provides access to new catalytic pathways on an anionic potential energy surface, which exhibit drastically lower activation barriers than all investigated neutral pathways. Although the calculation of the initial iodide coordination step (**1**→**29**: $\Delta G^{393} = -7.1 \text{ kJ mol}^{-1}$) might be associated with a small error due

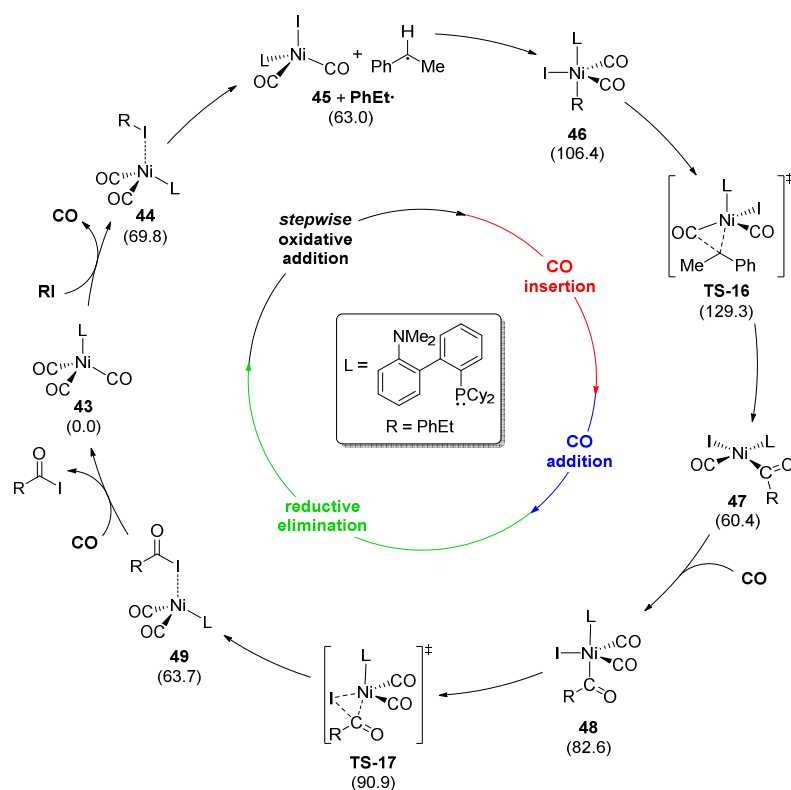
to the necessary approximations, the experimental observations provide a level of validation and are capable of providing an upper boundary for this deviation: The formation of $\text{Li}^+[\text{Ni}(\text{CO})_3\text{I}]^-$ (**29**) from $\text{Ni}(\text{CO})_4$ (**5**: $\Delta G^{298} = 43.3 \text{ kJ mol}^{-1}$) means that **29** must be more stable than **5**, while the subsequent experimental observation of Ni phosphine complexes indicates that these (**1**: $\Delta G^{298} = 0.0 \text{ kJ mol}^{-1}$; **3**: $\Delta G^{298} = 1.5 \text{ kJ mol}^{-1}$) must be more stable than **29**. This results in an energy range from 0 – 43 kJ mol^{-1} , which is in good agreement with the calculated value at 25 °C (**29**: $\Delta G^{298} = 15.3 \text{ kJ mol}^{-1}$). In any case, with a value of 90.9 kJ mol^{-1} (relative to **29**), the activation barrier is 40.8 kJ mol^{-1} lower than in the neutral catalytic system and, thus, even a small deviation at catalytic conditions would still lead to a predicted improvement in performance, which is also observed experimentally.

4.3.3 Catalytic Pathways with other Phosphine Ligands

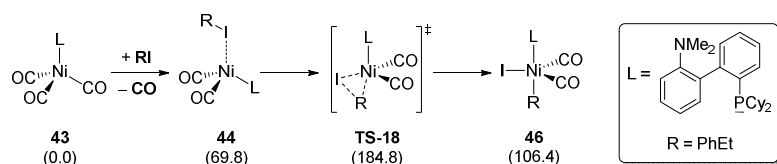
In the interest of understanding possible factors that could be used to influence and adjust the catalytic system, the calculations were repeated for other phosphine ligands employed in the experimental screening. Due to the calculated proposal that no phosphine ligand coordination takes place on the **LiI**-induced reaction pathway, only the neutral potential energy surface was investigated here. Additionally, the fact that barely any differences in reaction performance with various phosphines were observed when 20 mol% of **LiI** were added, further supported the hypothesis that phosphine influences can only be observed on the neutral pathways (see experimental sections in the corresponding publication).²⁰² The first ligand that was considered apart from **P(*n*Bu)₃** is the Buchwald-type 2-dicyclohexylphosphino-2'-(*N,N*-dimethylamino)-biphenyl (DavePhos; see Scheme 4.16), which was found to exhibit a higher activity than the other monodentate phosphines (**P(*n*Bu)₃**: 14% yield (Ni:L 1:1), 35% yield (Ni:L 1:2); DavePhos: 49% yield (Ni:L 1:1); see Table 4.2). The computed catalytic cycle starts from the monophosphine complex $\text{Ni}(\text{CO})_3\text{L}$ (**43**), which needs to dissociate one of the carbonyl ligands to allow for the formation of the alkyl halide adduct complex **44** ($\Delta G^{393} = 69.8 \text{ kJ mol}^{-1}$). From here, homolytic cleavage of the R–I bond leads to the generation of the **PhEt**· radical and the Ni^I complex **45** ($\Delta G^{393} = 63.0 \text{ kJ mol}^{-1}$). Recombination of the two species leads to the five-coordinate Ni^{II} species **46** ($\Delta G^{393} = 106.4 \text{ kJ mol}^{-1}$), which forms the precursor for the **CO** insertion via **TS-16**. This proceeds over a relatively high barrier of 129.3 kJ mol^{-1} to the square-planar Ni^{II} complex **47** ($\Delta G^{393} = 60.4 \text{ kJ mol}^{-1}$). **CO** addition to **48** ($\Delta G^{393} = 82.6 \text{ kJ mol}^{-1}$) and subsequent reductive elimination with an activation barrier of 90.9 kJ mol^{-1} (**TS-17**) leads to the formation of the acyl halide adduct complex **49** ($\Delta G^{393} = 63.7 \text{ kJ mol}^{-1}$). From here, liberation and hydrolysis to the desired carboxylic acids can take place as described for the other phosphine ligands and shown in Scheme 4.4. The rate-determining **CO** insertion activation barrier is only slightly smaller than the barrier for

$\text{P}(\text{nBu})_3$ ($\Delta\Delta G^\ddagger = 2.4 \text{ kJ mol}^{-1}$). This is within the error range of density functional theory and does not justify the difference in yield.

Alternatively, the two-electron oxidative addition step was also calculated (see Scheme 4.17). It proceeds from intermediate **44** ($\Delta G^{393} = 69.8 \text{ kJ mol}^{-1}$) via **TS-18** ($\Delta G^\ddagger = 184.8 \text{ kJ mol}^{-1}$) directly to the five-coordinate species **46** ($\Delta G^{393} = 106.4 \text{ kJ mol}^{-1}$) and is significantly less feasible than the stepwise oxidative addition over Ni^{I} .



Scheme 4.16: Catalytic cycle for the carbonylation of iodoethylbenzene (**RI**) to the corresponding acyl iodide via a stepwise oxidative addition process over a Ni^{I} complex (**45**) and the phenylethyl radical species **PhEt•** in the catalytic system coordinated by one DavePhos and two **CO** ligands. ΔG^{393} in kJ mol^{-1} ; RI-PBE0-D3(BJ)/def2-QZVPP//BP86/def2-SV(P); COSMO-RS (1-phenylethanol).

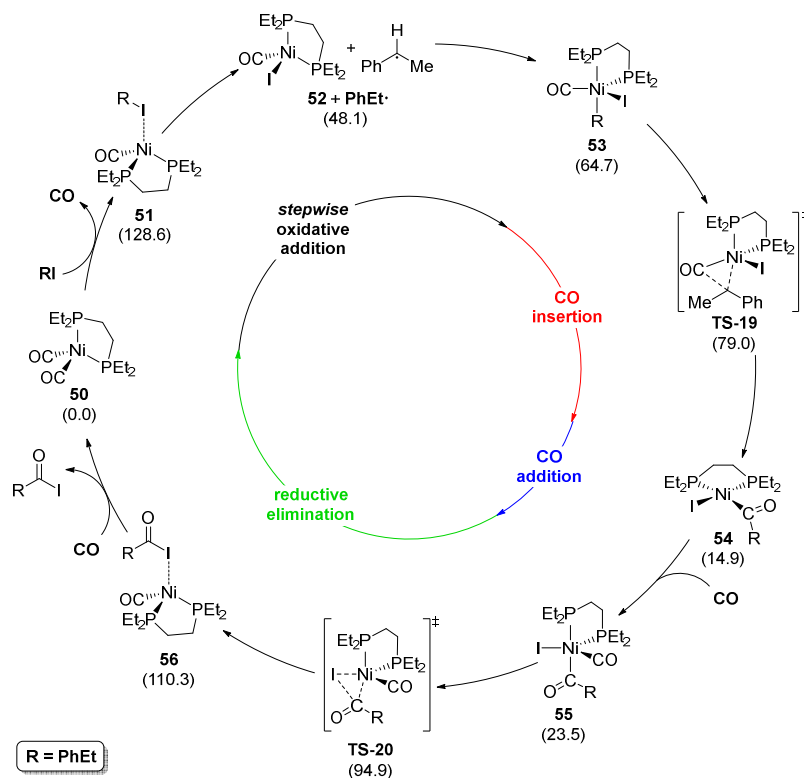


Scheme 4.17: Reaction pathway for the carbonylation of **RI** to the corresponding acyl iodide via two-electron oxidative addition transition state **TS-18** in the catalytic system coordinated by one DavePhos and two **CO** ligands. ΔG^{393} in kJ mol^{-1} ; RI-PBE0-D3(BJ)/def2-QZVPP//BP86/def2-SV(P); COSMO-RS (1-phenylethanol).

The similar rate-determining activation barriers for $\mathbf{P}(n\mathbf{Bu})_3$ and DavePhos – in contrast to the significantly superior performance of the DavePhos system – indicated other relevant influences. Based on the molecular structure of DavePhos and in combination with the results that showed that one equivalent of phosphine could be replaced by a non-coordinating nitrogen base such as Hünig's base, the assumption was made that the same phenomenon is at play here as DavePhos incorporates an additional amine functionality in the ligand. This was further supported by experiments with the CyJohnPhos ligand, which apart from the amine functionality is identical to DavePhos and led to significantly lower yields that were more in line with the performance $\mathbf{P}(n\mathbf{Bu})_3$. Once more, adding one equivalent of Hünig's base to the CyJohnPhos system, significantly improved the obtained yield. Attempts to calculate a bidentate coordination mode for DavePhos, in which both the phosphine and amine donor groups coordinate to nickel were unsuccessful. This led to the conclusion that chelated species, which would not be accessible with the CyJohnPhos system, are not responsible for the difference in performance.

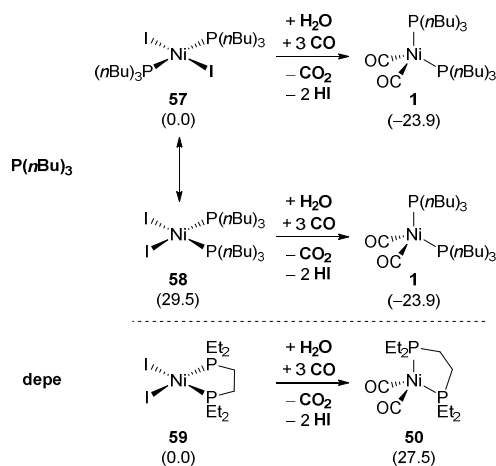
The second ligand, for which the catalytic pathway was recalculated, is the bidentate 1,2-bis(diethylphosphino)ethane (depe). The calculated cycle starts from the tetrahedral $\text{Ni}(\text{depe})(\text{CO})_2$ complex **50**, which is highly similar to the $\text{Ni}(\text{TBP})_2(\text{CO})_2$ (**1**), which served as reference points for most other calculations (see Scheme 4.18). From **50**, CO dissociation and alkyl halide (**RI**) adduct formation lead to the adduct complex **51** ($\Delta G^{393} = 128.6 \text{ kJ mol}^{-1}$). Similar to the catalytic pathways with two monodentate $\mathbf{P}(n\mathbf{Bu})_3$ ligands, the Ni^{I} complex **52** and \mathbf{PhEt}^{\cdot} , which are generated by a barrierless homolytic cleavage of the R–I bond, are significantly more stable than the preceding adduct species (**52** + \mathbf{PhEt}^{\cdot} : $\Delta G^{393} = 48.1 \text{ kJ mol}^{-1}$). The recombination reaction leads to the five-coordinate intermediate **53**, in which the two depe donor atoms are located in axial and equatorial position ($\Delta G^{393} = 64.7 \text{ kJ mol}^{-1}$). The subsequent CO insertion transition state **TS-19** exhibits a significantly lower barrier than the initial adduct formation and should readily proceed at the employed reaction conditions ($\Delta G^{\ddagger} = 79.0 \text{ kJ mol}^{-1}$). This leads to the square-planar Ni^{II} species **54**, in which the two donor atoms are forced into a *cis* position due to the short backbone length of depe (**54**: $\Delta G^{393} = 14.9 \text{ kJ mol}^{-1}$). Subsequent CO addition leads to **55** ($\Delta G^{393} = 23.5 \text{ kJ mol}^{-1}$), which exhibits the same coordination arrangement as the previously discussed alkyl complex **53**. Finally, the reductive elimination of the acyl halide proceeds over **TS-20** ($\Delta G^{\ddagger} = 94.9 \text{ kJ mol}^{-1}$) to adduct **56** ($\Delta G^{393} = 110.3 \text{ kJ mol}^{-1}$). To our surprise, the calculations for the depe ligand are associated with moderate reaction barriers, which are even lower than the required activation energy for the tri-*n*-butylphosphine system (depe: $\Delta G^{393} = 128.6 \text{ kJ mol}^{-1}$; $\mathbf{P}(n\mathbf{Bu})_3$: $\Delta G^{\ddagger} = 131.7 \text{ kJ mol}^{-1}$). This is contrary to the experimental observations, in which the similar 1,3-bis(diphenylphosphino)ethane (dppe) ligand only led to small yields and only bidentate ligands with larger alkyl chains in the backbone such as 1,3-bis(diphenylphosphino)propane (dppp) were able to achieve yields similar to $\mathbf{P}(n\mathbf{Bu})_3$. The

trend in experimental yields led to the hypothesis that a significant metallacycle ring strain might be present in the depe system, that would not be captured in the investigated catalytic cycle as the energetic reference structure would also be affected by this negative contribution. A closer look at the relationship between calculated energy and molecular structure (or more precisely the depe ligand bite angle), provided first indications for this assumption: The structures that exhibit a tetrahedral geometry with a bite angle of 109° like the reference structure **50** and **51**, **52**, and **56** generally seem to be less stable or in the case, where the structure has been significantly more stable in the previous systems the energetic difference significantly decreased. On the other hand, the structures with square-planar or trigonal-bipyramidal geometry, in which the depe bite angle can be reduced to 90° and therefore the ring strain compared to the reference structure is also reduced (**53**, **TS-19**, **54**, **55**, **TS-20**), seem to be generally more stable. Furthermore, the hypothetical ligand exchange from $\text{Ni}(\text{TBP})_2(\text{CO})_2$ (**1**) to $\text{Ni}(\text{depe})(\text{CO})_2$ (**50**) was found to be slightly endergonic ($\Delta G^{393} = 9.0 \text{ kJ mol}^{-1}$) and provides another indication that the assumed ring strain exists in complex **50**. Compound **50** is less stable than **1** even though the latter carries the bulkier tri-*n*-butylphosphine ligands.



Scheme 4.18: Catalytic cycle for the carbonylation of iodoethylbenzene (**RI**) to the corresponding acyl iodide via a stepwise oxidative addition process over a Ni^I complex (**45**) and phenylethyl radical species **PhEt $^\bullet$** in the catalytic system coordinated by the depe ligand and one **CO** ligand. ΔG^{393} in kJ mol^{-1} ; RI-PBE0-D3(BJ)/def2-QZVPP//BP86/def2-SV(P); COSMO-RS (1-phenylethanol).

To further test this assumption, a potential Ni^{II} to Ni⁰ reduction step was calculated (see Scheme 4.19). Here, the reductions of Ni(TBP)₂(I)₂ (**57** or **58**) and Ni(depe)(I)₂ (**59**) to Ni(TBP)₂(CO)₂ (**1**) and Ni(depe)(CO)₂ (**50**), respectively, were calculated. Starting from the square-planar Ni(TBP)₂(I)₂ species in *cis* or the more stable *trans* configuration (**57**: $\Delta G^{393} = 0.0$ kJ mol⁻¹; **58**: $\Delta G^{393} = 29.5$ kJ mol⁻¹), the two-electron reduction leads to the exergonic formation of the previously discussed tetrahedral complex **1** ($\Delta G^{393} = -23.9$ kJ mol⁻¹). Contrary, the depe-based Ni^{II} to Ni⁰ reduction can only take place from the *cis*-coordinated square-planar nickel complex (**59**: $\Delta G^{393} = 0.0$ kJ mol⁻¹) and the formation of Ni⁰ complex **50** is significantly endergonic ($\Delta G^{393} = 27.5$ kJ mol⁻¹). Direct comparison of the reaction energies for the *cis*-configured species reveals an even more drastic difference (**58**→**1**: $\Delta G^{393} = -53.4$ kJ mol⁻¹; **59**→**50**: $\Delta G^{393} = 27.5$ kJ mol⁻¹) that might indicate how large the ring strain in **50** is. This strain could severely hinder the formation of **50** at catalytic conditions and further increase the necessary activation energy for the reaction pathway, which would explain the bad catalytic performance that was observed in experiments.

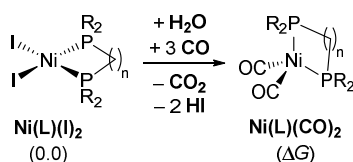


Scheme 4.19: Computed thermodynamic stabilities for the formation of Ni(TBP)₂(CO)₂ (**1**) and Ni(depe)(CO)₂ (**50**) via a Ni^{II} to Ni⁰ reduction step. ΔG^{393} in kJ mol⁻¹; RI-PBE0-D3(BJ)/def2-QZVPP//BP86/def2-SV(P); COSMO-RS (1-phenylethanol).

Based on this, the assumption was made that the severe strain in the Ni⁰ complex could be adjusted by increasing the ligand backbone length and lead to counteracting the endergonic nature of the Ni^{II} to Ni⁰ reduction step (depe: $\Delta G^{393} = 27.5$ kJ mol⁻¹). Therefore, the Ni^{II} to Ni⁰ reduction step was calculated for a number of different bidentate ligands: 1,2-bis(diethylphosphino)ethane (depe), 1,2-bis-(dicyclohexylphosphino)ethane (dcpe), 1,2-bis(diphenylphosphino)ethane (dppe), 1,2-bis(diethylphosphino)propane (depp), 1,2-bis-(dicyclohexylphosphino)propane (dcp), and 1,3-bis(diphenylphosphino)propane (dppp). The resulting Gibbs free energies for the reduction step are listed in Table 4.4. The comparison of the three ethane-linked bisphosphines (depe, dcpe, and dppe) shows a

significant dependence on the phosphine substituents. The observed differences can be explained by looking at the electron donation of the three ligands: dppe, which provides the least electron donation, leads to a more preferred reduction step, in which the metal center gains electron density ($\Delta G^{393} = 3.0 \text{ kJ mol}^{-1}$). depe can provide some electron donation via the positive inductive effect and thus stabilized the Ni^{II} center to a higher degree ($\Delta G^{393} = 27.5 \text{ kJ mol}^{-1}$). Lastly, dcpe with its higher carbon substitution exhibits a stronger inductive effect and leads to an even higher stabilization of the Ni^{II} complex ($\Delta G^{393} = 50.0 \text{ kJ mol}^{-1}$). Changing to longer ligand backbones, which leads to an increase in bite angle and reduction in ligand strain, was found to lead to significantly lower energy for the Ni^0 species across all three substituents (Et, Cy, and Ph). The Gibbs free energies of reduction for depp and dcpp are still slightly endergonic (depp: $\Delta G^{393} = 11.0 \text{ kJ mol}^{-1}$; dcpp: $\Delta G^{393} = 6.8 \text{ kJ mol}^{-1}$). The dppp ligand that was also able to facilitate the catalytic conversion on a similar level to the $\text{P}(\text{nBu})_3$ ligand is the only one of the six investigated ligands that was found to exhibit an exergonic Ni^{II} to Ni^0 reduction step ($\Delta G^{393} = -10.9 \text{ kJ mol}^{-1}$). These trends are interpreted as an indication that ring strain, dependent on the ligand backbone length, does indeed play a crucial role when considering bidentate ligands.

Table 4.4: Computed Gibbs free energies of reaction for the reduction of $\text{Ni}(\text{L})(\text{I})_2$ to $\text{Ni}(\text{L})(\text{CO})_2$ for a selection of bidentate ligands. ΔG^{393} in kJ mol^{-1} ; RI-PBE0-D3(BJ)/def2-QZVPP//BP86/def2-SV(P); COSMO-RS (1-phenylethanol).



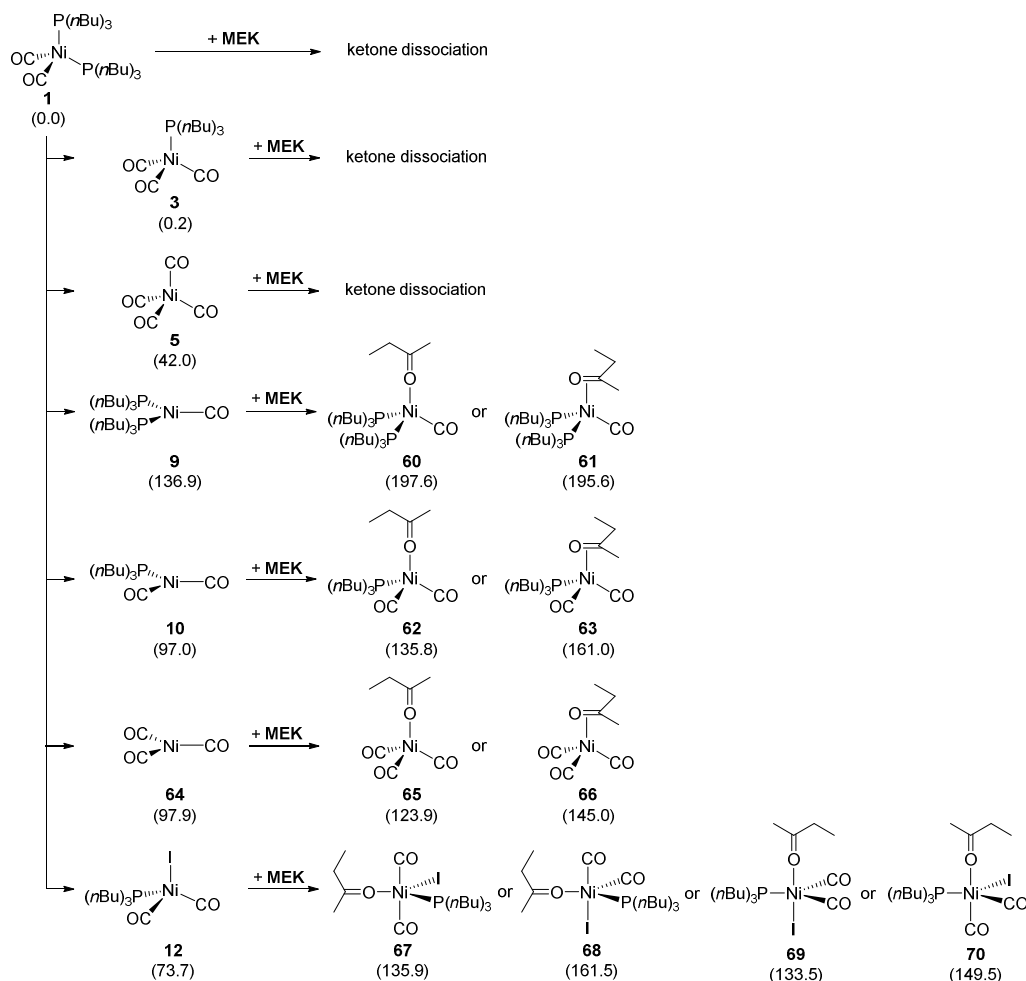
Entry	[L]	R	<i>n</i>	$\Delta G^{393} [\text{kJ mol}^{-1}]$
1	depe	Et	2	27.5
2	dcpe	Cy	2	50.0
3	dppe	Ph	2	3.0
4	depp	Et	3	11.0
5	dcpp	Cy	3	6.8
6	dppp	Ph	3	-10.9

All in all, the calculation provided a rationale for the experimental observations with the DavePhos and depe ligands, which generally act similarly to the previously investigated $\text{P}(\text{nBu})_3$ ligand. However, the calculations of the two ligands also served as a good example

of how difficult transferability between different ligands can be. Both ligands are assumed to exhibit secondary factors (i.e., non-coordinating amine base within the ligand itself or ligand strain in bidentate ligands) that were not captured by the initial model and required extra confirmation by experiments (DavePhos vs. CyJohnPhos and influence of Hünig's base) or by additional quantum-chemical calculations (ligand strain).

4.3.4 Investigation of Potentially Interfering Side Reactions

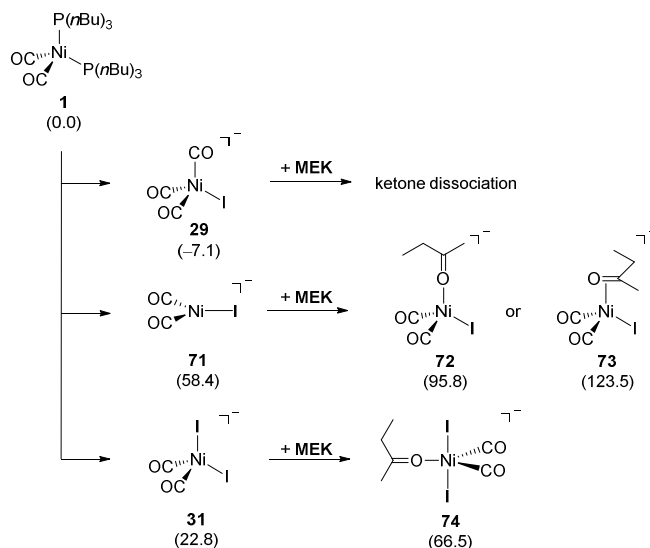
As initially unforeseen reaction pathways can have a crucial impact on the whole catalytic system, further calculations were employed to investigate a set of potential side reactions with a number of proposed reaction components. Firstly, possible interferences via coordination of methyl ethyl ketone (**MEK**) were studied (see Scheme 4.20). Attempts to compute the coordination of **MEK** to the tetrahedral Ni⁰ complexes **1**, **3**, and **5**, which are coordinated by two, one, and zero P(*n*Bu)₃ ligands, respectively, to form the corresponding five-coordinate Ni⁰ complexes were unsuccessful, and the geometry optimizations of these species repeatedly led to the dissociation of the ketone fragment. **MEK** coordination to the tri-coordinate Ni⁰ species **9**, **10**, and **64** can take place with two different ligand coordination motifs: η¹ oxygen coordination and η² coordination of the C=O bond. While these structures could all be characterized with quantum-chemical methods, the formation of the **MEK** complexes is strongly exergonic for **9** (**60** (η¹): ΔG³⁹³ = 197.6 kJ mol⁻¹; **61** (η²): ΔG³⁹³ = 195.6 kJ mol⁻¹), **10** (**62** (η¹): ΔG³⁹³ = 135.8 kJ mol⁻¹; **63** (η²): ΔG³⁹³ = 161.0 kJ mol⁻¹), and **64** (**65** (η¹): ΔG³⁹³ = 123.9 kJ mol⁻¹; **66** (η²): ΔG³⁹³ = 145.0 kJ mol⁻¹). In the tetrahedral non-chiral coordination environment only one isomer can be formed for these species. This is different for the formation of **MEK** complexes from the four-coordinate Ni^I complex **12**, which is assumed to form via barrierless homolytic cleavage of the alkyl halide bond. Four different isomers were located, all of which exhibited the η¹ coordination motif (**67**, **68**, **69**, and **70**). All attempts to characterize complexes with η² coordination remained unsuccessful, which was attributed to the higher steric demand of the η²-coordinated fragment in the sterically crowded five-coordinate species. Similar to the observations for the four-coordinate **MEK** species, the formation of the five-coordinate complexes is significantly endergonic (**67**: ΔG³⁹³ = 135.9 kJ mol⁻¹; **68**: ΔG³⁹³ = 161.5 kJ mol⁻¹; **69**: ΔG³⁹³ = 133.5 kJ mol⁻¹; **70**: ΔG³⁹³ = 149.5 kJ mol⁻¹). Based on the high relative energies, which in most cases exceed the energy of the rate-determining activation barrier, it was concluded that the coordination of **MEK** in the neutral catalytic system does not play a role in the underlying processes and that the improved performance with **MEK** is mainly based on the improved solubility of the phosphine components.



Scheme 4.20: Relative energies for the coordination of methyl ethyl ketone (**MEK**) to neutral Ni complexes that have been located along the reported reaction pathway (**1**, **3**, **5**, **9**, **10**, **12**, and **64**). ΔG^{393} in kJ mol^{-1} ; RI-PBE0-D3(BJ)/def2-QZVPP//BP86/def2-SV(P); COSMO-RS (1-phenylethanol).

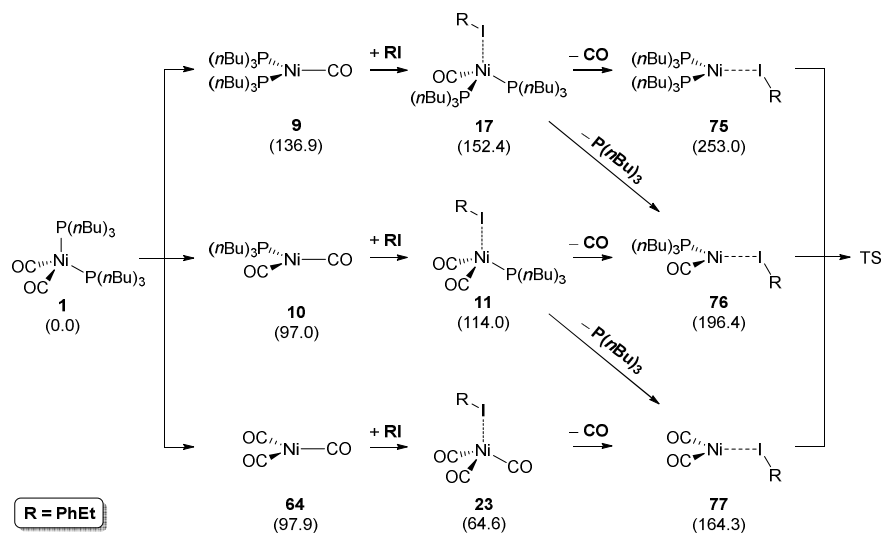
Additionally, the coordination of **MEK** on the LiI-induced anionic potential energy surface was investigated (see Scheme 4.21). Once more, this was calculated for the ketone coordination to the tetrahedral Ni^0 species (**29**), the three-coordinate Ni^0 complex after **CO** dissociation (**71**) and the tetrahedral Ni^I intermediate that is formed via barrierless homolytic cleavage (**31**). Like the attempted coordination of **MEK** to the neutral tetrahedral Ni^0 complexes **3**, **5**, and **9**, all geometry optimization attempts led to ketone dissociation indicating a lower stability of this species. The η^1 and η^2 coordination of **MEK** to **71** did lead to the intermediates **72** (η^1 ; $\Delta G^{393} = 95.8 \text{ kJ mol}^{-1}$) and **73** (η^2 ; $\Delta G^{393} = 123.5 \text{ kJ mol}^{-1}$). The η^1 coordination of the ketone ligand to **31** could also be located and led to structure **74** ($\Delta G^{393} = 66.5 \text{ kJ mol}^{-1}$). In agreement with the high energies of the structures of neutral **MEK** complexes, the anionic complexes **72** and **73** are also strongly exergonic. On the other hand, the five-coordinate Ni^I species **74** is relatively stable ($\Delta G^{393} = 66.5 \text{ kJ mol}^{-1}$), however, it still

remains less feasible than the direct recombination of the **PhEt** \cdot radical and the anionic Ni^I complex **31** to **32** ($\Delta G^{393} = 50.1 \text{ kJ mol}^{-1}$). Therefore, unexpected influences due to ketone coordination were not expected based on quantum chemistry.



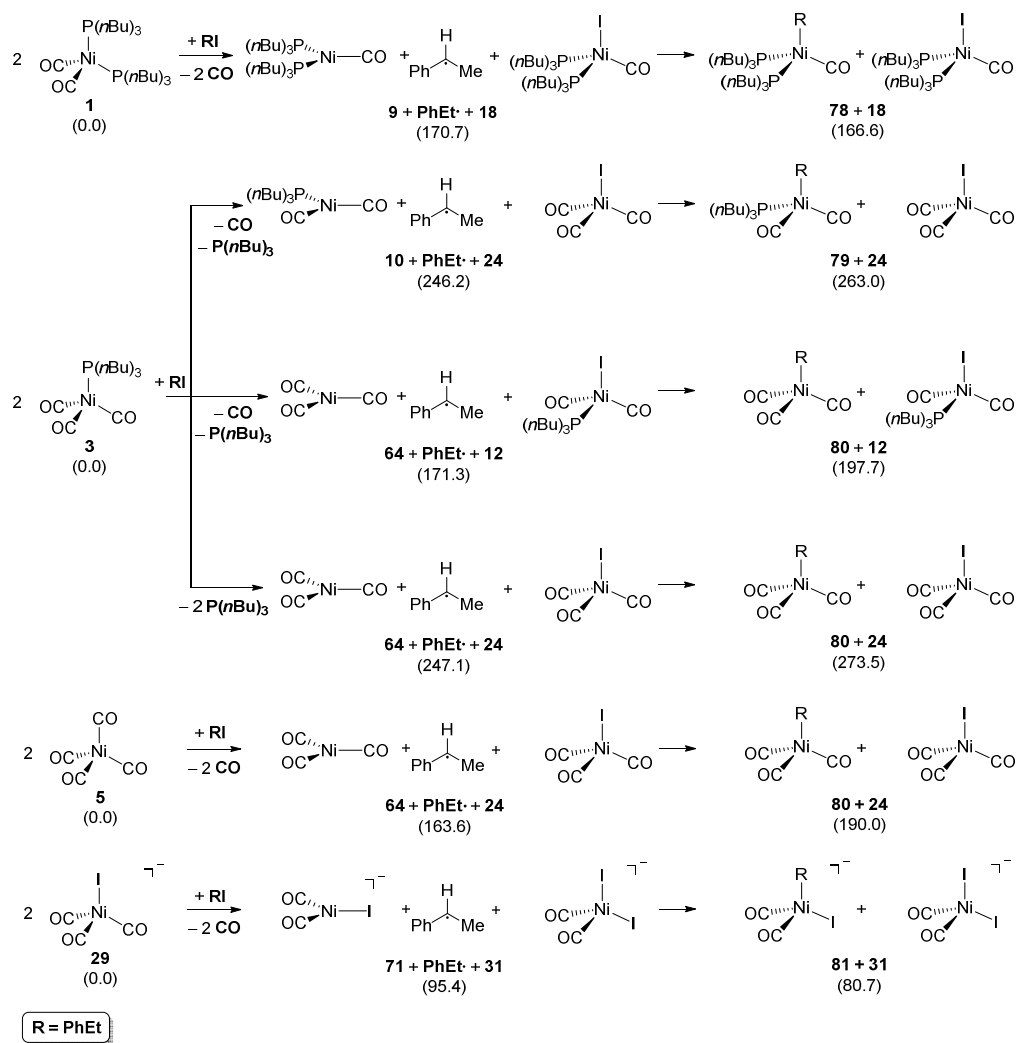
Scheme 4.21: Relative energies for the coordination of methyl ethyl ketone (**MEK**) to anionic Ni complexes that have been located along the reported reaction pathway (**29**, **31**, and **71**). ΔG^{393} in kJ mol⁻¹; RI-PBE0-D3(BJ)/def2-QZVPP//BP86/def2-SV(P); COSMO-RS (1-phenylethanol).

As an alternative reaction pathway, the dissociation of one of the phosphine or carbonyl ligands from the tetrahedral alkyl halide adduct complexes was calculated (see Scheme 4.22). The three investigated species were the neutral **RI**-coordinated monophosphine, diphosphine and tricarbonyl species (**11**, **17**, and **23**, respectively), which are formed via the free trigonal Ni⁰ complexes **9**, **10**, and **64**. **CO** dissociation from **17** along the diphosphine pathway leads to the trigonal complex **75** ($\Delta G^{393} = 253.0 \text{ kJ mol}^{-1}$). Equivalent **CO** dissociation from **11** (or **P(*n*Bu)₃** dissociation from **17**) generates the monophosphine intermediate **76** ($\Delta G^{393} = 196.4 \text{ kJ mol}^{-1}$). **CO** dissociation from the tricarbonyl system **23**, which does not carry any phosphine ligands, or phosphine dissociation from monophosphine system **11** leads to the formation of **77**, which is also of strongly endergonic nature ($\Delta G^{393} = 164.3 \text{ kJ mol}^{-1}$). The characterization of subsequent oxidative addition transition states, which lead to the four-coordinate Ni^{II} complexes was not attempted due to the unfeasible energetic nature of **75**, **76**, and **77**.



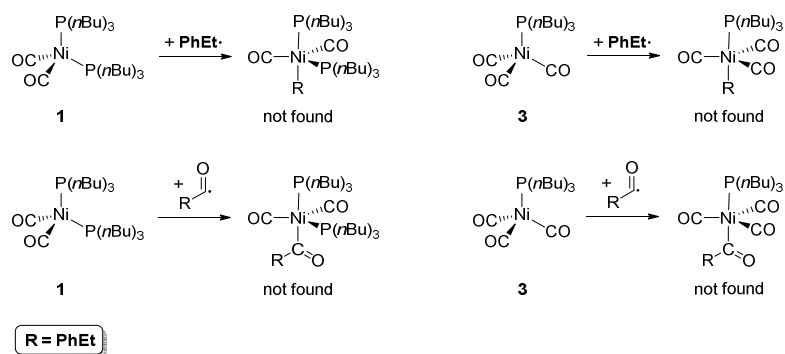
Scheme 4.22: Relative energies for the generation of trigonal alkyl halide adduct Ni⁰ complexes (**75**, **76**, and **77**) via ligand dissociation of the respective tetragonal adduct complexes (**11**, **17**, and **23**). ΔG^{393} in kJ mol⁻¹; RI-PBE0-D3(BJ)/def2-QZVPP//BP86/def2-SV(P); COSMO-RS (1-phenylethanol).

Although radical trapping experiments have indicated an instant recombination inside the solvent cage (*vide supra*), the addition of the intermediary phenylethyl radical (**PhEt**[•]) to various trigonal complexes (formed from a second equivalent of **1**, **3**, **5** or **29**) was investigated for completeness's sake (see Scheme 4.23). The phenylethyl radical itself priorly needs to be formed via barrierless homolytic cleavage, which leads to the fact that an additional Ni^I complex is also present in solution and provides the possibility for a barrierless recombination, which competes with the presented reactions. Formation of the neutral trigonal Ni⁰ species (by **CO** or **P(nBu)₃** dissociation) next to the Ni^I complexes and **PhEt**[•] is already strongly endergonic for all investigated species (ΔG^{393} from 163.6 to 247.1 kJ mol⁻¹). All subsequent generations of pairs of Ni^I complexes (**78** + **18/79** + **24/80** + **12/80** + **24**) were found to be equally too high in energy to be feasible intermediates on the neutral potential energy surface (ΔG^{393} ranging from 166.6 to 273.5 kJ mol⁻¹). Once more, the structures on the anionic potential energy surface are significantly more stable with the generation of **71** + **31** + **PhEt**[•] ($\Delta G^{393} = 95.4$ kJ mol⁻¹) and the subsequent Ni^I generation (**81** + **31**: $\Delta G^{393} = 80.7$ kJ mol⁻¹) being in an energy range that might be feasible at the employed reaction conditions. However, even these pathways cannot compete with the low barriers of the previously investigated carbonylation pathway and led to these pathways being ruled out.



Scheme 4.23: Relative energies for the reaction of the phenylethyl radical (**PhEt** \cdot) with three-coordinate Ni⁰ complexes (**9**, **10**, **64**, and **71**). ΔG^{393} in kJ mol⁻¹; RI-PBE0-D3(BJ)/def2-QZVPP//BP86/def2-SV(P); COSMO-RS (1-phenylethanol).

Lastly, the addition of the calculated radicals **PhEt** \cdot and **PhEt(CO)** \cdot to the mono- and diphosphine complexes Ni(TBP)(CO)₃ (**3**) and Ni(TBP)₂(CO)₂ (**1**) to form the five-coordinate Ni^I complexes was attempted (see Scheme 4.24). However, none of these complexes could be located and these reaction pathways were not considered further.

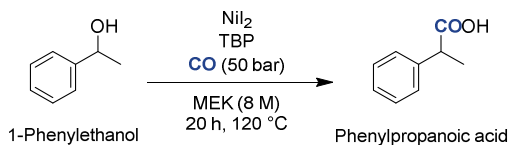


Scheme 4.24: Possible reaction products for the addition of alkyl radical **PhEt·** and acyl radical **PhEt(CO)·** to tetragonal Ni⁰ complexes **1** and **3**. The characterization of all configurational isomers of the shown five-coordinate complexes was attempted but was not successful. ΔG^{393} in kJ mol⁻¹; RI-PBE0-D3(BJ)/def2-QZVPP//BP86/def2-SV(P); COSMO-RS (1-phenylethanol).

The calculations concerned with a number of side reaction pathways (including methyl ethyl ketone coordination, trigonal alkyl halide adduct complexes and radical addition to various species) revealed that none of the investigated pathways is able to compete with the previously presented pathway for carbonylation of 1-phenylethanol to 2-phenylpropanoic acid on the neutral and anionic potential energy surfaces.

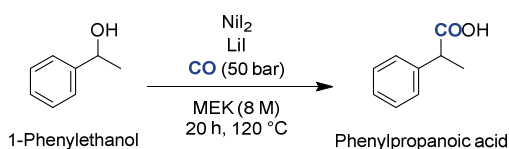
4.3.5 Summary and Outlook

The carbonylation of benzylic alcohols to the corresponding carboxylic acids with earth-abundant nickel phosphine catalysts has been thoroughly studied. In this catalytic system, the *in-situ* formation of HI leads to significantly lower acid concentrations and, thus, corrosivity, which represents a problem in the currently applied processes.



Scheme 4.25: Carbonylation of 1-phenylethanol to 2-phenylpropanoic acid with an earth-abundant Ni catalyst and a simple phosphine ligand.

The use of quantum-chemical calculations allowed to identify of relevant intermediates (see Schemes 4.5 and 4.6), which laid the foundation for the subsequently investigated reaction pathways. The computation of different coordination environments with two, one, and zero phosphine ligands coordinated to the metal center (Schemes 10, 7 and 11, respectively) allowed for the suggestion of ligand-based effects, which were later confirmed by experiments. The reaction was found to proceed via a stepwise oxidative addition with two one-electron oxidation steps instead of the typically proposed two-electron oxidative addition (see Scheme 4.8), and the proposed radical intermediates could be observed in EPR spectroscopy. A variety of different radical recombination pathways were investigated to ensure that the underlying molecular transformation steps are well-understood (see Scheme 4.9). Possible side reaction pathways with methyl ethyl ketone, trigonal alkyl halide complexes and radical species were investigated and found not to interfere with the reaction (see Schemes 4.20 – 4.24). A second catalytic pathway based on the use of LiI as an additive has been studied (see Scheme 4.13). It was found to proceed in parallel to the neutral potential energy surface via the same key reaction steps and is significantly more feasible than any the lowest energy pathway of the neutral regime (see Figure 4.1). Once more, experimental observations agreed with the computational results and the development of a phosphine-free reaction was possible.



Scheme 4.26: Carbonylation of 1-phenylethanol to 2-phenylpropanoic acid with an earth-abundant Ni catalyst and LiI without the need of a phosphine ligand.

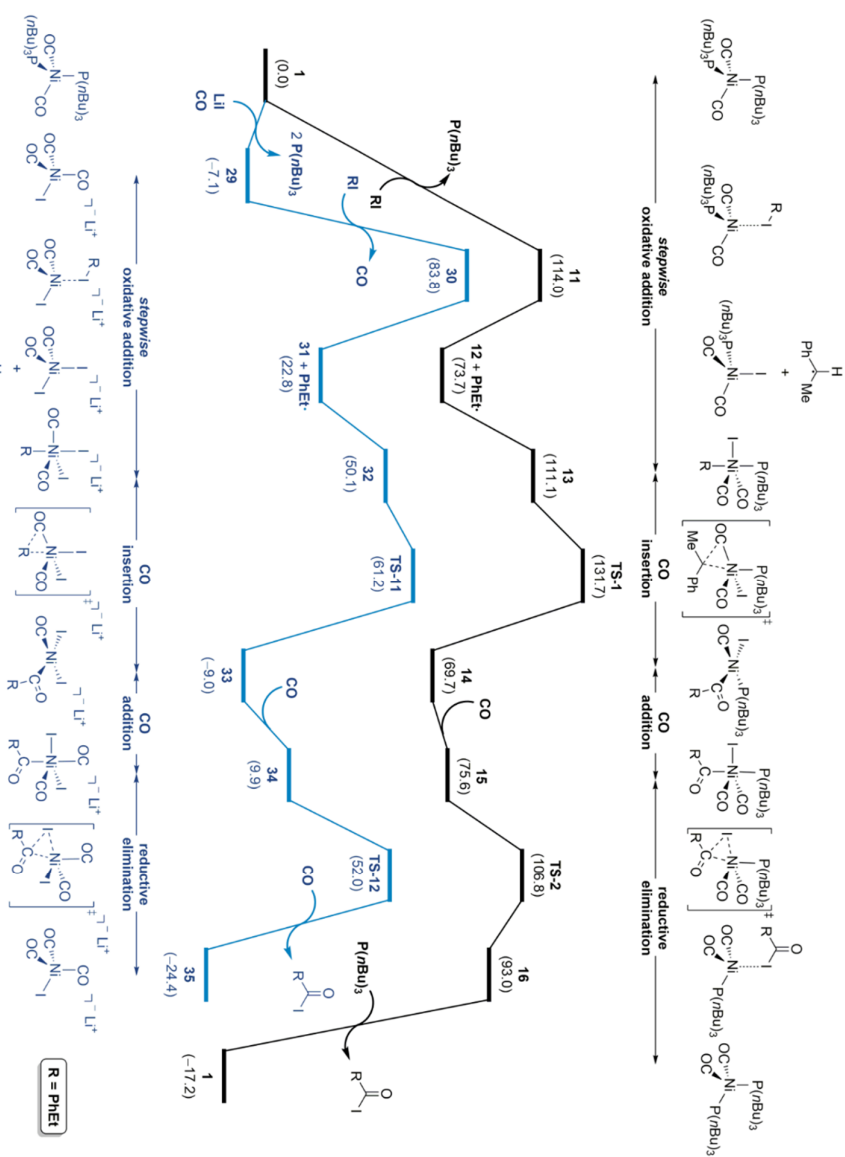


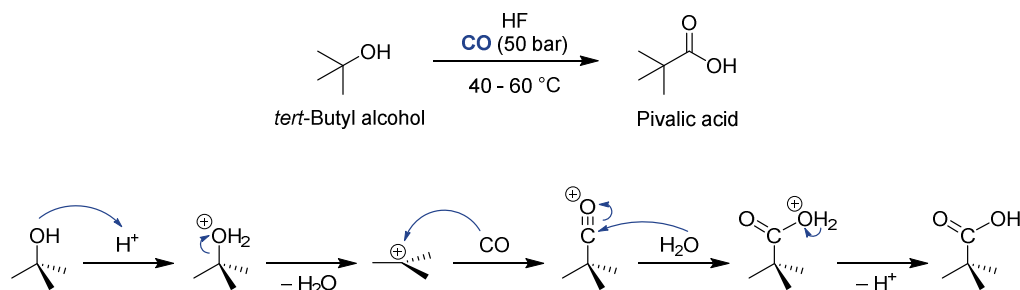
Figure 4.1: Potential energy surface plot for the carbonylation of iodoethybenzene (**RI**) to the corresponding acyl iodide comparing the neutral reaction pathway with one phosphine ligand coordinated to Ni (**RI**; upper pathway) with the **L1**-induced phosphine-free reaction pathway (blue, lower pathway). ΔG^{393} in kJ mol⁻¹; RI-PBE0-D3(BJ)/def2-QZVPP//BP86/def2-SV(P); COSMO-RS (1-phenylethanol).

Furthermore, rationalization of various specific ligand effects with DavePhos and bidentate phosphine donor ligands such as depe could be provided (see Schemes 4.16 and 4.18) and, again, be validated with experimental results.

After the quantum-chemical insights had been obtained and the catalytic system has been improved, several aliphatic alcohols were tested and the broad range of applicability of the methodology was demonstrated. This also included more complex and industrially relevant substrates such as 1-(4-*iso*-butylphenyl)ethanol and 1-(6-methoxy-2-naphthyl)ethanol (leading to the formation of ibuprofen and naproxene, respectively). Although the use of primary and secondary aliphatic alcohols required higher reaction temperatures (200 °C vs. 120 °C), a range of cyclic and linear aliphatic systems was generally suitable for carbonylation with the catalytic system. In terms of future steps, which might increase the relevance of this system, a more detailed reaction optimization directly targeting the industrially relevant API products could be undertaken. Apart from this optimization, upscaling studies and recycling experiments would set the cornerstone for real-world application. Based on these larger scale reactions and reaction improvements, the economic feasibility of this reaction for a selection of relevant substrates can be evaluated. Lastly, an extension of the methodology to Koch-type carbonylation products was envisioned and subsequently investigated (see Section 4.4: *Carbonylation of tert-Butyl Alcohol*).

4.4 Carbonylation of *tert*-Butyl Alcohol

Apart from looking into alternative synthesis methodologies for ibuprofen and related compounds as discussed in the previous chapter, the protocol could also be of interest for more simple aliphatic compounds. Classically, the industrial synthesis of basic aliphatic carboxylic acids is mainly accomplished in one of three ways:¹⁷⁷⁻¹⁷⁸ Firstly, the most economic process starts with the catalytic hydroformylation of olefins with syngas (H_2/CO) to the corresponding aldehyde (oxo synthesis), which is subsequently oxidized with air or O_2 to the carboxylic acid. The method is applicable to a wide range of olefins.¹⁷⁸ Secondly, the direct (Reppe) hydroxy carbonylation of olefins can be achieved and commonly employs nickel compounds.²²³⁻²²⁴ However, commercial application is limited to the conversion of ethylene into propionic acid and the reaction – similar to the hydroformylation step – tends to form the (linear) *n*-products when employing larger alkanes.²²⁴ Branched carboxylic acids are typically accessed via the Koch reaction (also Koch-Haaf carbonylation when formic acid is used for CO generation).²²⁵⁻²²⁶ Here, the carbonylation of alcohols or olefins is achieved with strong mineral acids such as HF or H_2SO_4 and the preferred formation of the tertiary carboxylic acids is observed. The large-scale application of this methodology requires expensive corrosion-resistant equipment, complex separation procedures for the products as well as the capabilities to deal with the large amounts of waste generated during the reaction. Furthermore, Koch reactions can lead to several side products that are generally based on the instability of the formed carbocations (see Scheme 4.27),²²⁷ and dimeric reaction products have already been reported by Koch and Haaf in 1958.²²⁵ Therefore, a number of reports have been published to find alternative catalysts such as Nafion-H,²²⁸ ionic liquids,²²⁹ Cu²³⁰, Au²³¹ or Pd²³²⁻²³³ complexes for this reaction that can accomplish the desired reactivity at milder conditions, but are regularly leading to linear selectivity.²³²⁻²³³ It should be noted that the use of metal complexes for this reaction might rather be considered as a variation of the Reppe carbonylation but is motivated by the same factors.

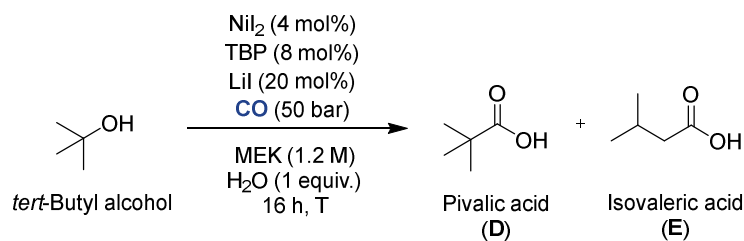


Scheme 4.27: Proposed reaction mechanism for the Koch carbonylation of *tert*-butyl alcohol to pivalic acid with CO and HF. The use of isobutene similarly leads to the pivalic acid product.²²⁷

On the basis of the previous investigation into the Ni-catalyzed carbonylation of phenyl ethyl alcohol with NiI_2 , TBP, and LiI that has revealed excellent branched selectivity and a radical-

based oxidative addition step (see Section 4.3), the catalytic system was expected to be an interesting candidate for the carbonylation of Koch-type (tertiary) alcohols, which (to the best of our knowledge) has not been studied yet. Firstly, the *tert*-butyl radical should be significantly favored over the other isomers. Secondly, the *in-situ* conversion of the employed alcohol to the corresponding alkyl iodide, which represents the actual substrate species coordinating to the Ni atom, is formed via an S_N1 mechanism (see Scheme 4.4). Both steps would be expected to strongly favor the tertiary reaction product over the respective linear species. To test this hypothesis, *tert*-butyl alcohol (*t*BuOH) was used as a model substrate for further carbonylation experiments. It is especially suited for this investigation as the alcohol itself as well as the relevant related compounds, *iso*-butyl alcohol (*i*BuOH) and isobutene, are readily available and the formed product, pivalic acid, is of importance as an intermediate in chemical industry (e.g., for the production of pivaloyl chloride²³⁴ or vinyl pivalate²³⁵). As the catalytic system has already been tested and optimized in the first part of the study,²⁰² the catalytic conditions were initially directly transferred to the adapted *t*BuOH substrate. At 120 °C, which was the reaction temperature employed for the carbonylation of phenyl ethyl alcohol, pivalic acid (**D**) as well as the corresponding isomerization product isovaleric acid (**E**) could only be observed in traces (see Table 4.5 – entry 1). Increasing the reaction temperature to 160 and 200 °C significantly increased the formation of the target compounds, however, the formed ratios of **D** and **E** were contrary to the initial expectations (Table 4.5 – entries 2 and 3).

Table 4.5: Initial experimental tests in the Ni-catalyzed carbonylation of *tert*-butyl alcohol to pivalic acid.^[a] All experiments were carried out by Niels Lichtenberger at CaRLa.



Entry	T [°C]	Yield [%]	Yield D [%]	Yield E [%]	Ratio D : E
1	120	traces	<1	<1	n.d.
2	160	6	3	3	1:1
3	200	31	13	18	1:1.4

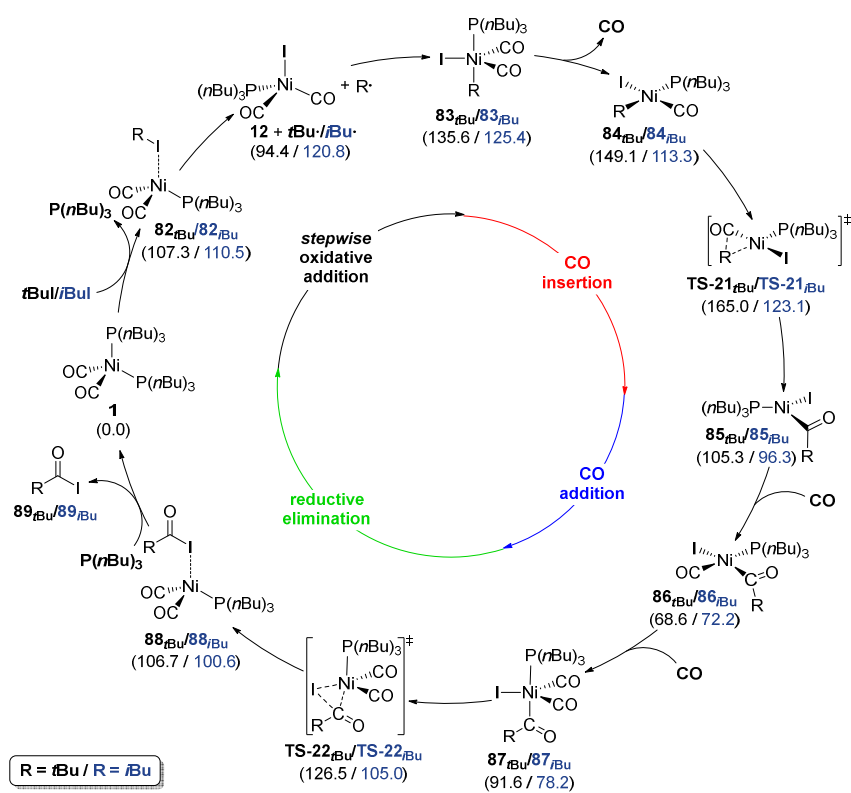
[a] A mixture of *tert*-butyl alcohol (21 mmol), NiI₂ (4 mol%), TBP (8 mol%) and LiI (20 mol%) was pressurized with CO at 50 bar in MEK (1.2 M) and H₂O (1 equiv.) and stirred at the given temperature for 16 h. Yields were determined by GC-FID chromatography using anisole as internal standard.

As this was contrary to the initially expected branched selectivity of the catalytic system, the conclusion was drawn that the reaction pathways for the formation of pivalic acid must either be accompanied by additional isomerization steps or follow a different reaction mechanism altogether. To gather evidence towards this hypothesis, a quantum-chemical investigation into the previously established radical-based reaction mechanism adapted to *tert*-butyl alcohol was carried out.

4.4.1 Investigation of Previously Established Catalytic Cycles

In the DFT investigation of the Ni-catalyzed carbonylation of *tert*-butyl alcohol to pivalic acid, the reaction was assumed to take place via the same mechanistic steps, which have been described for phenyl ethyl alcohol. The alcohol is converted to the corresponding alkyl iodide via a S_N1 mechanism (see Scheme 4.4), which is then acting as the coordinating fragment either in a neutral phosphine-coordinated or in a LiI-induced anionic catalytic cycle (see Schemes 4.7 and 4.13, respectively). These reaction pathways were then adapted to the *tert*-butyl alcohol (*t*BuOH) as well as *iso*-butyl alcohol (*i*BuOH), which are carbonylated to the corresponding acyl halides and can subsequently be hydrolyzed to the desired carbonylation products, pivalic acid and isovaleric acid (see Scheme 4.28). The catalytic cycle starts from Ni(TBP)₂(CO)₂ (**1**), from which dissociation of one P(*n*Bu)₃ ligand and adduct formation with the alkyl halide leads to the intermediates **82_{tBu}** and **82_{iBu}** ($\Delta G^{453} = 107.3$ and 110.5 kJ mol⁻¹, respectively). Barrierless homolytic cleavage of the C–I bond in the **tBuI** or **iBuI** fragment of **82_{tBu}** or **82_{iBu}** leads to the formation of Ni^I complex **12**, which is identical to the Ni^I complex formed in the reaction with phenyl ethyl alcohol, and the respective *tert*-butyl or *iso*-butyl radical (**12** + **tBu·**: $\Delta G^{453} = 94.4$ kJ mol⁻¹; **12** + **iBu·**: $\Delta G^{453} = 120.8$ kJ mol⁻¹). Fully in line with our envisioned selectivity, the *tert*-butyl radical is significantly more stable than the respective *iso* species ($\Delta\Delta G^{453} = 26.4$ kJ mol⁻¹). However, once recombination of the two species takes place and forms the five-coordinate alkyl Ni^{III} species **83_{tBu}** or **83_{iBu}**, the energetic trend changes and the *iso*-butyl-coordinated intermediate is favored (**83_{tBu}**: $\Delta G^{453} = 135.6$ kJ mol⁻¹; **83_{iBu}**: $\Delta G^{453} = 125.4$ kJ mol⁻¹). Opposite to the catalytic pathways for the carbonylation of phenyl ethyl alcohol, the CO insertion step was found to be favored in a four-coordinate system. Therefore, CO is dissociated from the five-coordinate **83_{tBu}**/**83_{iBu}** leading to the four-coordinate square-planar Ni^{II} complexes **84_{tBu}** or **84_{iBu}** (**84_{tBu}**: $\Delta G^{453} = 149.1$ kJ mol⁻¹; **84_{iBu}**: $\Delta G^{453} = 113.3$ kJ mol⁻¹), which lead to the CO insertion transition states **TS-21_{tBu}** and **TS-21_{iBu}** ($\Delta G^\ddagger = 165.0$ and 123.1 kJ mol⁻¹, respectively). A comparison of the four- and five-coordinate CO insertion pathways was also performed (*vide infra*). The trend of the more stable *i*Bu structures continues throughout this four-coordinate insertion pathway and becomes significantly smaller from the formed trigonal intermediate **85_{tBu}**/**85_{iBu}** and onwards (**85_{tBu}**: $\Delta G^{453} = 105.3$ kJ mol⁻¹; **85_{iBu}**: $\Delta G^{453} = 96.3$ kJ mol⁻¹), which can be explained with the chain extension by CO that moves the

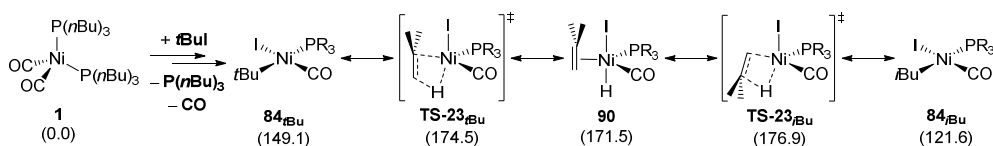
decisive alkyl unit further away from the crowded metal center. The addition of two equivalents of **CO** leads to **86_{tBu}**/**86_{iBu}** (**86_{tBu}**: $\Delta G^{453} = 68.6 \text{ kJ mol}^{-1}$; **86_{iBu}**: $\Delta G^{453} = 72.2 \text{ kJ mol}^{-1}$) and **87_{tBu}**/**87_{iBu}** ($\Delta G^{453} = 91.6$ and 78.2 kJ mol^{-1} , respectively), which sets up the systems for reductive elimination. This transformation takes place via **TS-22_{tBu}** or **TS-22_{iBu}** to form the *t*Bu acyl halide and *i*Bu acyl halide, respectively (**TS-22_{tBu}**: $\Delta G^\ddagger = 126.5 \text{ kJ mol}^{-1}$; **TS-22_{iBu}**: $\Delta G^\ddagger = 105.0 \text{ kJ mol}^{-1}$). No transition states corresponding to a four-coordinate reductive elimination could be located, which was therefore ruled out. In the last step, the adduct complexes **88_{tBu}** and **88_{iBu}** need to liberate the acyl halide unit, which is subsequently hydrolyzed to pivalic acid or isovaleric acid (**88_{tBu}**: $\Delta G^{453} = 106.7 \text{ kJ mol}^{-1}$; **88_{iBu}**: $\Delta G^{453} = 100.6 \text{ kJ mol}^{-1}$).



Scheme 4.28: Calculated lowest energy pathways for the carbonylation of *tert*-butyl iodide (**tBuI**; black) and *iso*-butyl iodide (**iBuI**; blue) via the previously reported neutral radical-based reaction mechanism. ΔG^{453} in kJ mol^{-1} ; RI-PBE0-D3(BJ)/def2-QZVPP//BP86/def2-SV(P); COSMO-RS (MEK).

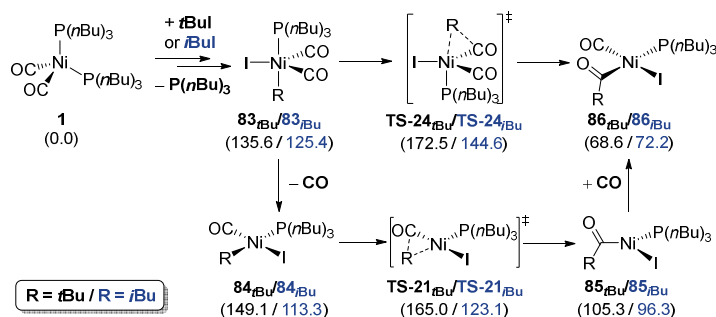
Motivated by the observed isomerization during carbonylation of *t*BuOH leading to the simultaneous formation of pivalic acid (*t*BuCOOH) and isovaleric acid (*i*BuCOOH), a possible *tert/iso* isomerization pathway based on β hydride elimination and hydride transfer was investigated (see Scheme 4.29). This isomerization pathway leads from **84_{tBu}**, which is formed via **CO** dissociation after the alkyl fragment has been transferred onto the Ni center (see Scheme 4.28) to the corresponding *iso* species, **84_{iBu}**. Firstly, β hydride elimination via

TS-23_{tBu} leads to the five-coordinate Ni^{II} isobutene complex **90** (**TS-23_{tBu}**: $\Delta G^\ddagger = 174.5 \text{ kJ mol}^{-1}$; **90**: $\Delta G^{453} = 171.5 \text{ kJ mol}^{-1}$). After rearrangement of the isobutene ligand the reverse reaction, hydride transfer from the metal to the tertiary carbon atom, can lead to the generation of the *iso*-butyl group and to the more stable **84_{tBu}**, which is also formed along the carbonylation pathway starting from **iBuI** (**TS-23_{iBu}**: $\Delta G^\ddagger = 176.9 \text{ kJ mol}^{-1}$; **84_{iBu}**: $\Delta G^{453} = 121.6 \text{ kJ mol}^{-1}$). With the significantly higher barrier of $176.9 \text{ kJ mol}^{-1}$ (compared to the activation energy of $165.0 \text{ kJ mol}^{-1}$ for the carbonylation to pivalic acid), a relevant amount of *t*Bu/*i*Bu isomerization would not be expected. Equally, the isomerization of the *iso*-butyl group in **84_{iBu}** to the *tert*-butyl group (leading to the formation of **84_{tBu}** and subsequently to pivalic acid) would not be assumed to take place as it is associated with a reaction barrier of $168.6 \text{ kJ mol}^{-1}$ (**TS-23_{tBu}**).



Scheme 4.29: Reaction pathway for the *t*Bu/*i*Bu isomerization from **84_{tBu}** to **84_{iBu}** in the phosphine-coordinated system via hydride transfer and β hydride elimination transition states. ΔG^{453} in kJ mol^{-1} ; RI-PBE0-D3(BJ)/def2-QZVPP//BP86/def2-SV(P); COSMO-RS (MEK).

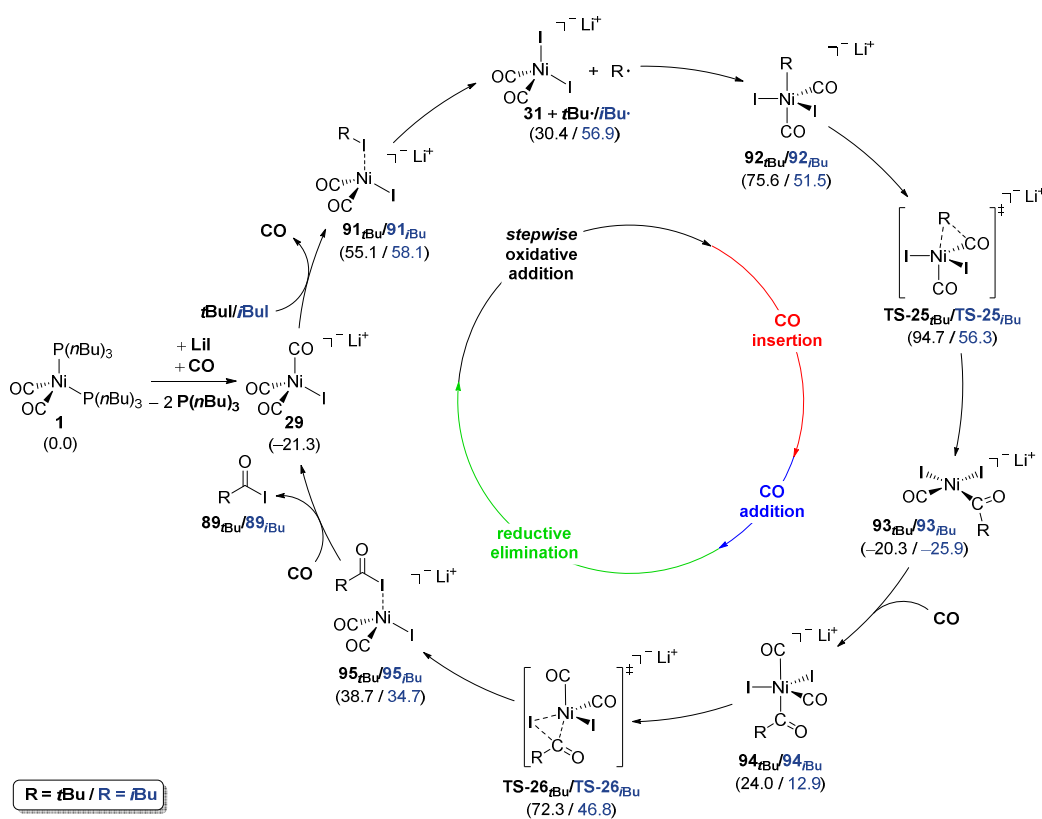
The investigation into the mechanistic pathways for the carbonylation of **tBuI** to **tBu(CO)I** (**89_{tBu}**) led to the characterization of four- and five-coordinate reaction pathways for the **CO** insertion step (see Scheme 4.30). The four-coordinate transition state **TS-21_{tBu}**/**TS-21_{iBu}**, which was presented in detail before (see Scheme 4.28), requires prior **CO** dissociation from species **83_{tBu}**/**83_{iBu}** to **84_{tBu}**/**84_{iBu}** (**83_{tBu}**: $\Delta G^{453} = 135.6 \text{ kJ mol}^{-1}$; **83_{iBu}**: $\Delta G^{453} = 125.4 \text{ kJ mol}^{-1}$; **84_{tBu}**: $\Delta G^{453} = 149.1 \text{ kJ mol}^{-1}$; **84_{iBu}**: $\Delta G^{453} = 113.3 \text{ kJ mol}^{-1}$) and subsequent recoordination of the ligand to the formed trigonal complex **85_{tBu}**/**85_{iBu}** ($\Delta G^{453} = 105.3$ and 96.3 kJ mol^{-1} for *t*Bu and *i*Bu, respectively). On the other hand, the five coordinate **CO** insertion transition state directly leads from **83_{tBu}**/**83_{iBu}** to **86_{tBu}**/**86_{iBu}** (**86_{tBu}**: $\Delta G^{453} = 68.6 \text{ kJ mol}^{-1}$; **86_{iBu}**: $\Delta G^{453} = 72.2 \text{ kJ mol}^{-1}$). However, with a barrier of 172.5 and $144.6 \text{ kJ mol}^{-1}$ for the carbonylation of **tBuI** and **iBuI**, respectively, the five-coordinate transition states **TS-24_{tBu}** and **TS-24_{iBu}** are less feasible than the previously presented reaction pathways and are expected to be of no relevance on the overall potential energy surface.



Scheme 4.30: Reaction pathways for the four- and five-coordinate **CO** insertion steps in the phosphine-coordinated system. ΔG^{453} in kJ mol^{-1} ; RI-PBE0-D3(BJ)/def2-QZVPP//BP86/def2-SV(P); COSMO-RS (MEK).

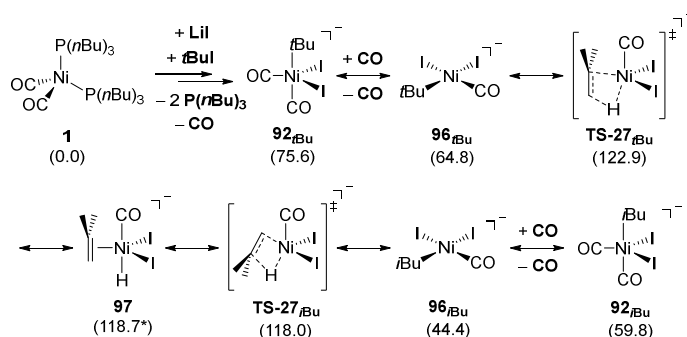
Although the activation barrier for the carbonylation of **tBuI** is significantly higher than the previously calculated activation barrier for the carbonylation of phenyl ethyl alcohol, it might still barely fall below the upper limit for a reaction at 160 – 200 °C (with a high dependence on the reaction temperature as observed in the experiments). On the other hand, the carbonylation of **iBuI** to the corresponding acyl halide **89_{iBu}** (for subsequent hydrolysis to isovaleric acid) was found to have a significantly lower activation barrier, which is approximately as high as the reaction barrier that was computed for phenyl ethyl alcohol. After the differences for mono- and diphosphine-substituted as well as for the tricarbonyl coordinated system have been discussed in detail before and have shown drastically better performance in the case of exactly one **P(nBu)₃** ligand (see Section 4.3.1), the adaptation of the catalytic system to pivalic acid and isovaleric acid was limited to this case and the other two systems were not investigated specifically. However, with the drastic effect that was demonstrated for **LiI** by enabling access to an anionic potential energy surface and the fact that the initial experimental tests did also include this component, the calculation of the anionic pathways was also crucial to gain a comprehensive understanding of the underlying reactivity (see Scheme 4.31). The catalytic cycle was assumed to start with the formation of the anionic Ni tricarbonyl halide complex **29** from **Ni(TBP)₂(CO)₂** (**1**) based on literature reports of this species^{194,222} and is moderately exergonic ($\Delta G^{453} = -21.3 \text{ kJ mol}^{-1}$). Please note that the difference in reaction energy to the previously calculated value in the phenyl ethyl alcohol system is caused by the adjusted thermodynamic corrections for the higher reaction temperature. The alkyl halide adduct formation leads endergonically to **91_{tBu}** and **91_{iBu}** ($\Delta G^{453} = 55.1$ and 58.1 kJ mol^{-1} , respectively), from which barrierless homolytic cleavage takes place. This cleavage step leads to the formation of anionic Ni^I complex **31** and **tBu·/iBu·** (**31** + **tBu·**: $\Delta G^{453} = 30.4 \text{ kJ mol}^{-1}$; **31** + **iBu·**: $\Delta G^{453} = 56.9 \text{ kJ mol}^{-1}$), which can readily recombine to form the five-coordinate **92_{tBu}** and **92_{iBu}** ($\Delta G^{453} = 75.6$ and 51.5 kJ mol^{-1} , respectively). Once more, this step perfectly exemplifies the motivation behind the transfer of the methodology to Koch-type carbonylation targets as the *tert*-butyl radical species is over 25 kJ mol^{-1} more stable than the *iso*-butyl isomer. Like the results on the neutral

potential energy surface after radical recombination, the five-coordinate anionic complexes **92_{tBu}** and **92_{iBu}** reverse this trend and the more sterically demanding *t*Bu group causes a lower feasibility of the tertiary isomer. Interestingly, the five-coordinate **CO** insertion transition state was found to be more stable than the four-coordinate pathway (*vide infra*), which is different to the neutral catalytic cycle (see Scheme 4.30). With barriers of 116.0 kJ mol⁻¹ and 77.6 kJ mol⁻¹, this step is rate-determining for the anionic reaction pathway (**TS-25_{tBu}** and **TS-25_{iBu}**). Due to the five-coordinate motif of the **CO** insertion, the subsequent intermediate is the square-planar Ni^{II} complex **93_{tBu}**/**93_{iBu}** as opposed to the trigonal intermediate in the neutral phosphine-coordinated catalytic cycle (**93_{tBu}**: $\Delta G^{453} = -20.3$ kJ mol⁻¹; **93_{iBu}**: $\Delta G^{453} = -25.9$ kJ mol⁻¹; cf. step **TS-21**→**85** in Scheme 4.28). Addition of the second carbonyl ligand leads to the intermediates **94_{tBu}** and **94_{iBu}** ($\Delta G^{453} = 24.0$ and 12.9 kJ mol⁻¹, respectively) and subsequent reductive elimination (**TS-26_{tBu}**: $\Delta G^\ddagger = 72.3$ kJ mol⁻¹; **TS-26_{iBu}**: $\Delta G^\ddagger = 46.8$ kJ mol⁻¹) to the acyl halide adduct complexes **95_{tBu}** and **95_{iBu}** ($\Delta G^{453} = 38.7$ and 34.7 kJ mol⁻¹, respectively).



Scheme 4.31: Calculated lowest energy pathways for the carbonylation of *tert*-butyl iodide (**tBuI**; black) and *iso*-butyl iodide (**iBuI**; blue) via the previously reported **LiI**-induced anionic radical-based reaction mechanism. ΔG^{453} in kJ mol⁻¹; RI-PBE0-D3(BJ)/def2-QZVPP//BP86/def2-SV(P); COSMO-RS (MEK).

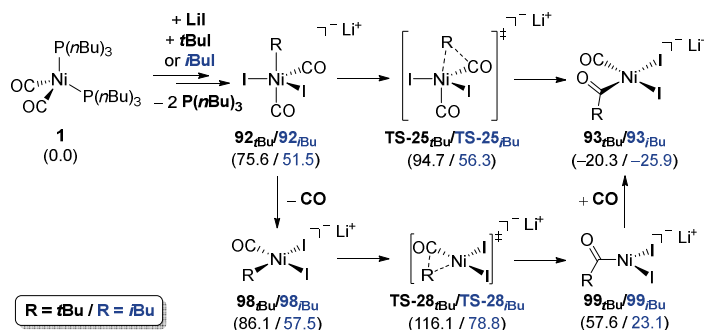
Furthermore, the *t*Bu/*i*Bu isomerization pathway over isobutene was also investigated for the anionic reaction, which takes place starting from **92_{tBu}** and leads to the respective *i*Bu isomer (see Scheme 4.32). Opposite to the neutral pathway, which – due to the four-coordinate CO insertion step – already proceeded over the four-coordinate square-planar Ni^{II} complex, initial CO dissociation from **92_{tBu}** to **96_{tBu}** is required in the anionic regime (cf. Scheme 4.29). From here, β hydride elimination via **TS-27_{tBu}** leads to the formation of anionic Ni isobutene complex **97** (**TS-27_{tBu}**: $\Delta G^\ddagger = 122.9 \text{ kJ mol}^{-1}$; **97**: $\Delta G^{453} = 118.7 \text{ kJ mol}^{-1}$). The fully-optimized minimum geometry of **97** could not be located and the I–Ni–H bond angle had to be frozen during optimization to ensure that a stationary point with no imaginary frequencies was obtained. However, this leads to a slightly higher energy than compared to the true geometry and results in the subsequent transition state being (unrealistically) lower in energy than the preceding intermediate. This hydride transfer transition state (**TS-27_{tBu}**) regenerates the nickel-bound alkyl group and leads to **96_{iBu}** (**TS-27_{tBu}**: $\Delta G^\ddagger = 118.0 \text{ kJ mol}^{-1}$; **96_{iBu}**: $\Delta G^{453} = 44.4 \text{ kJ mol}^{-1}$). Recoordination of the CO ligand, which was dissociated from the Ni complex in the initial step leads to **92_{iBu}**, the desired isomer of **92_{tBu}** (**92_{iBu}**: $\Delta G^{453} = 59.8 \text{ kJ mol}^{-1}$). Similar to the investigation on the neutral potential energy surface, the *t*Bu/*i*Bu as well as the *i*Bu/*t*Bu isomerization barrier are significantly less feasible than the respective carbonylation pathways from *tert*-butyl alcohol to pivalic acid and *iso*-butyl alcohol to isovaleric acid ($\Delta\Delta G^\ddagger = 28.2$ and 58.3 kJ mol^{-1} for the *t*Bu/*i*Bu and *i*Bu/*t*Bu isomerizations, respectively). Thus, the isomerization was ruled out and the found pathways did not rationalize the observed product formation.



Scheme 4.32: Reaction pathway for the *t*Bu/*i*Bu isomerization from **92_{tBu}** to **92_{iBu}** in the phosphine-coordinated system via hydride transfer and β hydride elimination transition states. *The structure of **97** could only be located by freezing the I–Ni–H bond angle. The real energy should be slightly lower than the given value and the energy of the subsequent transition state. ΔG^{453} in kJ mol^{-1} ; RI-PBE0-D3(BJ)/def2-QZVPP//BP86/def2-SV(P); COSMO-RS (MEK).

Lastly, the four-coordinate CO insertion transition state **TS-28_{tBu}**/**TS-28_{iBu}** was compared to the five-coordinate species (**TS-25_{tBu}**/**TS-25_{iBu}**; see Scheme 4.33). While **TS-25_{tBu}** and **TS-25_{iBu}** directly lead from **92_{tBu}** or **92_{iBu}** to **93_{tBu}** or **93_{iBu}**, respectively, **TS-28_{tBu}** and **TS-28_{iBu}** require prior dissociation of one of the carbonyl ligands to form **98_{tBu}** and **98_{iBu}** ($\Delta G^{453} = 86.1$

and 57.5 kJ mol^{-1} , respectively). Subsequently, **TS-28**_{*t*Bu} and **TS-28**_{*i*Bu} transform the four-coordinate Ni^{II} complexes into the trigonal species **99**_{*t*Bu} or **99**_{*i*Bu}, from which on-cycle species **93**_{*t*Bu}/**93**_{*i*Bu} can be accessed by CO association (**TS-28**_{*t*Bu}: $\Delta G^\ddagger = 116.1 \text{ kJ mol}^{-1}$; **TS-28**_{*i*Bu}: $\Delta G^\ddagger = 78.8 \text{ kJ mol}^{-1}$; **99**_{*t*Bu}: $\Delta G^{453} = 57.6 \text{ kJ mol}^{-1}$; **99**_{*i*Bu}: $\Delta G^{453} = 23.1 \text{ kJ mol}^{-1}$).



Scheme 4.33: Reaction pathways for the four- and five-coordinate CO insertion steps in the LiI-induced anionic catalytic system. ΔG^{453} in kJ mol^{-1} ; RI-PBE0-D3(BJ)/def2-QZVPP//BP86/def2-SV(P); COSMO-RS (MEK).

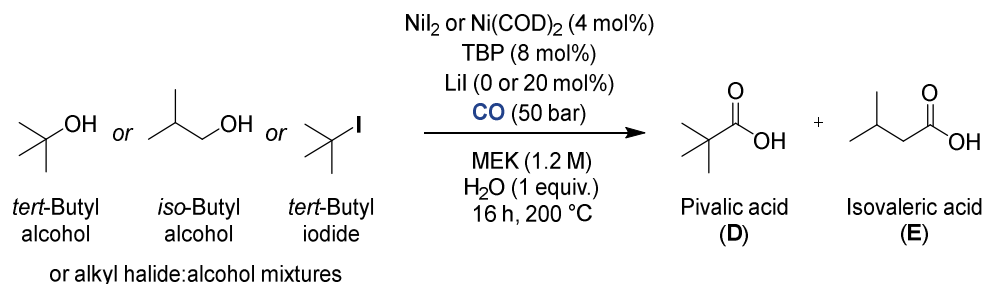
In summary, the calculations on the carbonylation of *tert*-butyl alcohol to pivalic acid and *iso*-butyl alcohol to isovaleric acid based on the initial $\text{S}_{\text{N}}1$ -type generation of alkyl halides suggest that the reaction pathways are feasible at experimental conditions. Moreover, the results show that isomerization between the *tert*-butyl and *iso*-butyl pathways is significantly less feasible and selective formation of the carboxylic acid from the corresponding alcohol should be observed. However, the initial experimental tests had clearly revealed the opposite and a mixture of both isomers was observed. Therefore, a more fundamental change in the underlying catalytic system must have occurred in the adaption from synthesizing ibuprofen analogues (from phenyl ethyl alcohol) to synthesizing Koch-type carbonylation targets.

4.4.2 Isobutene-based Reaction Pathways

On the basis of the mismatch between experimental observations and the computed catalytic pathways for the carbonylation of *tert*-butyl and *iso*-butyl iodide, further experiments were conducted to gain indications on the differences between the two systems and phenyl ethyl alcohol with a special focus on finding and confirming the true substrate of the catalytic cycle. Therefore, the initial approach was to directly employ *tert*-butyl iodide and *iso*-butyl iodide, which were postulated to be formed *in-situ* via a simple $\text{S}_{\text{N}}1$ reaction from the corresponding alcohols. In the work on the carbonylation of phenyl ethyl alcohol,²⁰² experiments were able to indicate the role of the external HI source by use of a 1:9 mixture of iodocyclohexane and cyclohexanol with a $\text{Ni}(\text{COD})_2$ precursor, which led to similar yields as the $\text{NiI}_2/\text{cyclohexanol}$ system (*vide supra* and see the corresponding publication). To adapt this for the synthesis of pivalic acid and isovaleric acid, experiments were performed with $\text{Ni}(\text{COD})_2$ and *tert*-butyl iodide/*iso*-butyl iodide as well as the equivalent 1:9 mixtures of

alkyl halide and alcohol (see Table 4.6). The use of only alkyl iodide as substrate led to the formation of a mixture of undefined products and analysis did not show any free carboxylic acid species (see entry 3). This was a clear sign for decomposition or favored side reactions that had not been considered in the computational investigation. Interestingly, the use of 1:9 mixtures of *t*BuI or *i*BuI and *t*BuOH or *i*BuOH did lead to the formation of pivalic acid and isovaleric acid in very similar amounts and ratios as compared to the use of pure *t*BuOH or *i*BuOH (see entries 1,2,4 and 5). It was especially striking that both the use of *t*BuOH and *i*BuOH (or of the respective iodide:alcohol mixtures) led to highly similar ratios indicating a common substrate for both alcohols. If the alkyl halides were the metal-coordinating substrates along the reaction pathway, a significant impact on the formed product ratios would be expected for the addition of *t*BuI and *i*BuI, which was not the case.

Table 4.6: Control experiments employing *t*BuI as well as *t*BuI:*t*BuOH and *i*BuI:*t*BuOH mixtures to investigate substrate influences in the Ni-catalyzed carbonylation of *t*BuOH and *i*BuOH.^[a] All experiments were carried out by Niels Lichtenberger at CaRLa.

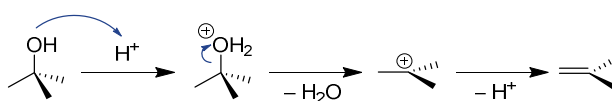
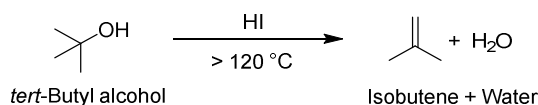


Entry	Substrate	Yield [%]	Yield D [%]	Yield E [%]	Ratio D:E
1	<i>t</i> BuOH	41	21	20	1:1
2	<i>i</i> BuOH	31	16	15	1:0.9
3	<i>t</i> BuI	decomposition			
4	<i>t</i> BuI: <i>t</i> BuOH (1:9)	29	12	17	1:1.4
5	<i>i</i> BuI: <i>t</i> BuOH (1:9)	31	14	17	1:1.2

[a] A mixture of *t*BuOH, *i*BuOH, *t*BuI:*t*BuOH (1:9) or *i*BuI:*t*BuOH (1:9), NiI_2 or $\text{Ni}(\text{COD})_2$ (for alkyl halide:alcohol mixtures; 4 mol%), TBP (8 mol%) and LiI (in the case of pure systems; entries 1-3; 20 mol%) was pressurized with CO at 50 bar in MEK (1.2 M) and H_2O (1 equiv.) and stirred at 200 °C for 16 h. Yields were determined by GC-FID chromatography using anisole as internal standard.

To further support these claims, individual alkyl halides and the same 1:9 alkyl halide/alcohol mixtures (diluted in methyl ethyl ketone) were heated to 120 °C and the reaction mixture was analyzed. The *t*BuI-containing system had rapidly afforded a dark brown solution, which strongly indicated decomposition of the alkyl halide species. Although the use of cyclohexyl

iodide (as used in the control experiments of the first project phase) did also lead to a pale-yellow solution, the results indicate that decomposition plays a significantly lower role in this system and both, CyI and CyOH, could be observed by GC chromatography. These results led to the conclusion that *t*BuI and *i*BuI are most likely not formed during the reaction or if they are formed, will quickly undergo thermal decomposition. Due to the observed trends and the known use of olefins in Reppe-type or Koch-type carbonylation reactions,^{177-178, 224-226} the formation and subsequent carbonylation of isobutene was envisioned as a possible explanation for the selectivity phenomena at play in the catalytic system. Therefore, *t*BuOH and *i*BuOH were heated in the presence of HI and water elimination was found to occur at 120 °C and higher leading to the formation of significant amounts of isobutene at catalytic conditions. The fact that unimolecular (E_1) elimination should more readily occur from the tertiary *t*BuOH than from *i*BuOH might also provide an explanation for the higher yields that are observed with *t*BuOH (see Table 4.6 – entries 1 and 2 and Scheme 4.34). Similar elimination has also been observed in Pd-catalyzed carbonylation reactions of *t*BuOH to isovalerate esters.²³⁶



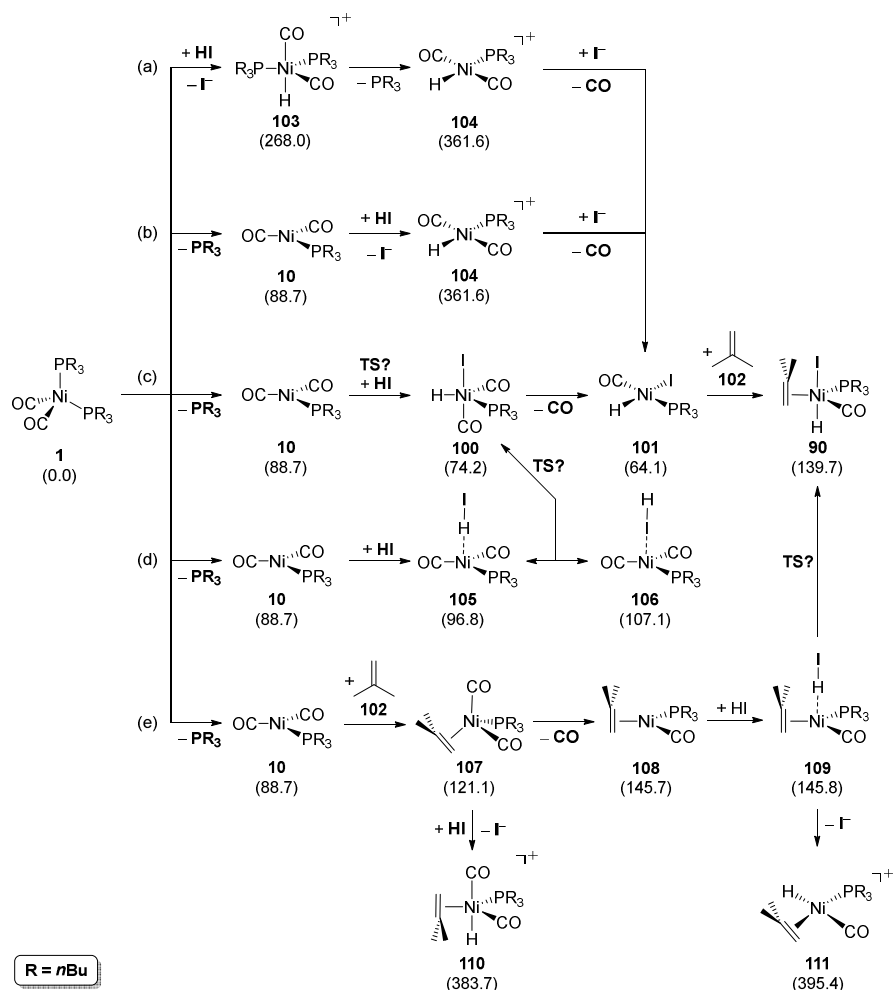
Scheme 4.34: Proposed reaction mechanism for the E_1 elimination of water from *tert*-butyl alcohol.

Lastly, as the initial reaction steps of the E_1 elimination are identical to the proposed reaction mechanism for the Koch-type carbonylation reaction (cf. Scheme 4.27), the possibility of a solely HI-catalyzed reaction was investigated. Thus, a mixture of *t*BuOH with 8 mol% HI (57 wt% in H_2O) was pressurized with CO at 50 bar and stirred at 200 °C for 23 h. The reaction did not afford any carbonylation products and the simple occurrence of a Koch reaction was excluded.

On this basis, further quantum-chemical calculations were carried out to study an adapted mechanism, which would incorporate isobutene as coordinating substrate instead of *tert*-butyl iodide or *iso*-butyl iodide. Once more, multiple possible systems can be formed, and the investigations began with the monophosphine-coordinated Ni complexes as these had been found to be most feasible in the previous investigation on the carbonylation of phenyl ethyl alcohol (see Scheme 4.35). Herein, the initial step was expected to be $P(nBu)_3$ ligand dissociation from $Ni(TBP)_2(CO)_2$ (**1**) after generation of this species in the Ni^{II} to Ni^0 reduction step (to **10**: $\Delta G^{453} = 88.7 \text{ kJ mol}^{-1}$). Subsequently, **HI** (by oxidative addition to form a hydride and iodide ligand) and isobutene (**102**) need to coordinate to the trigonal

Ni⁰ complex **10**, which requires additional CO dissociation. The shown pathway proceeds via initial oxidative addition of **HI** to the metal atom forming the five-coordinate Ni^{II} complex **100** ($\Delta G^{453} = 74.2 \text{ kJ mol}^{-1}$). Subsequent CO dissociation leads to the species **101** ($\Delta G^{453} = 64.1 \text{ kJ mol}^{-1}$), to which isobutene (**102**) can coordinate forming the five-coordinate intermediate **90** ($\Delta G^{453} = 139.7 \text{ kJ mol}^{-1}$), which was already investigated as part of the *t*Bu/*i*Bu isomerization pathway (see Scheme 4.29). Other possible pathways for the coordination of **HI** and isobutene were also investigated and compared to these species (*vide infra*). From **90**, the two hydride transfer transition states, which also have been discussed as part of the isomerization pathway, lead to the formation of the alkyl ligands, *t*Bu and *i*Bu for **TS-23_{tBu}** and **TS-23_{iBu}**, respectively (**TS-23_{tBu}**: $\Delta G^\ddagger = 142.8 \text{ kJ mol}^{-1}$; **TS-23_{iBu}**: $\Delta G^\ddagger = 145.1 \text{ kJ mol}^{-1}$). The formed square-planar Ni^{II} complexes, **84_{tBu}** and **84_{iBu}**, can directly undergo CO insertion via the four-coordinate **TS-21_{tBu}** and **TS-21_{iBu}**, respectively (**84_{tBu}**: $\Delta G^{453} = 117.4 \text{ kJ mol}^{-1}$; **84_{iBu}**: $\Delta G^{453} = 89.8 \text{ kJ mol}^{-1}$; **TS-21_{tBu}**: $\Delta G^\ddagger = 133.2 \text{ kJ mol}^{-1}$; **TS-21_{iBu}**: $\Delta G^\ddagger = 99.6 \text{ kJ mol}^{-1}$). A comparison to the less feasible five-coordinate CO insertion pathway can be found in Scheme 4.30. The formed trigonal Ni^{II} species **85_{tBu}** and **85_{iBu}** ($\Delta G^{453} = 73.5$ and 72.8 kJ mol^{-1} , respectively) require addition of two carbonyl ligands (over **86_{tBu}**: $\Delta G^{453} = 48.3 \text{ kJ mol}^{-1}$ to **87_{tBu}**: $\Delta G^{453} = 64.6 \text{ kJ mol}^{-1}$; over **86_{iBu}**: $\Delta G^{453} = 45.0 \text{ kJ mol}^{-1}$ to **87_{iBu}**: $\Delta G^{453} = 55.3 \text{ kJ mol}^{-1}$) before reductive elimination. The reductive elimination transition states **TS-22_{tBu}** and **TS-22_{iBu}** form the free *tert*-butyl acyl iodide (**89_{tBu}**) and *iso*-butyl acyl iodide (**89_{iBu}**) via the corresponding acyl iodide adduct complexes, which have been shown in the alkyl iodide-based reaction pathways (**88_{tBu}** and **88_{iBu}**; see Scheme 4.28). The calculated pathways show that both for the formation of pivalic acid as well as isovaleric acid the rate-determining step is the hydride transfer transition state (**TS-23_{tBu}**/**TS-23_{iBu}**). With barriers of $142.8 \text{ kJ mol}^{-1}$ and $145.1 \text{ kJ mol}^{-1}$, the activation barriers for these two pathways are in line with a number of experimental observations: Firstly, the two transition states are quite close in energy (and would most likely fall into the common error range of DFT). This is in very good agreement with the observed 1:1 ratios for pivalic acid and isovaleric acid. Furthermore, as discussed when the comparison of calculated activation energies and experimental parameters has been introduced (see Section 2.3.3), many parameters need to be considered. Although the slightly lower barrier in the *t*Bu system does not fully correlate with the slightly higher percentages of isovaleric acid, the consideration of the complete potential energy surface is crucial, on which the subsequent intermediates and CO insertion barriers are significantly favored for the formation of isovaleric acid (**TS-21_{tBu}** vs. **TS-21_{iBu}**: $\Delta G^\ddagger = 133.2$ vs. 99.6 kJ mol^{-1}). Moreover, the fact that certain steps of the catalytic cycle were not considered in the DFT investigations such as the Ni^{II} to Ni⁰ reduction steps, which form the crucial **HI** equivalents, or the hydrolysis of the acyl halides to the carboxylic acids leads to further deviations from real world conditions.

After the hydride transfer, **CO** insertion and reductive elimination steps have been calculated, a detailed exploration of possible **HI** and isobutene coordination schemes was performed (see Scheme 4.36). Firstly, the tetrahedral reference complex **1** could be directly protonated by *in-situ* formed **HI** (pathway a). This would lead to the cationic trigonal-bipyramidal complex **103** ($\Delta G^{453} = 268.0 \text{ kJ mol}^{-1}$), which would need to eliminate one of the five substituents (**P**(*n***Bu**)₃) forming cationic square-planar intermediate **104** ($\Delta G^{453} = 361.6 \text{ kJ mol}^{-1}$). Iodide (**I**⁻) addition (with or without **CO** dissociation) leads to the formation of intermediates **100** or **101** (**100**: $\Delta G^{453} = 74.2 \text{ kJ mol}^{-1}$; **101**: $\Delta G^{453} = 64.1 \text{ kJ mol}^{-1}$). However, the two cationic species, **103** and **104** are strongly endergonic and will not be viable intermediates in the reaction. Secondly, after phosphine dissociation from **1** (**1**→**10**: $\Delta G^{453} = 88.7 \text{ kJ mol}^{-1}$), protonation of **10** could directly lead to **104** ($\Delta G^{453} = 361.6 \text{ kJ mol}^{-1}$; pathway b), however, this suffers from the same instability of the cationic species. The third possibility (pathway c) represents the previously discussed direct addition of **HI** to trigonal intermediate **10** (forming **100**: $\Delta G^{453} = 74.2 \text{ kJ mol}^{-1}$), followed by **CO** dissociation (forming **101**: $\Delta G^{453} = 64.1 \text{ kJ mol}^{-1}$) and finally, isobutene addition leading to the five-coordinate η^2 isobutene complex **90** ($\Delta G^{453} = 139.7 \text{ kJ mol}^{-1}$). However, all attempts to characterize the oxidative addition transition state failed. Alternatively, the addition of **HI** to **10** can yield the **HI** adduct complexes **105** and **106** (Ni–H contact: $\Delta G^{453} = 96.8 \text{ kJ mol}^{-1}$; Ni–I contact: $\Delta G^{453} = 107.1 \text{ kJ mol}^{-1}$), which could lead to the desired formation of **100**, but, once more, the appropriate transition state could not be located (pathway d). Lastly, the sequence could be reversed, and isobutene (**102**) could be added to the trigonal intermediate first (**10**→**107**: $\Delta G^{453} = 121.1 \text{ kJ mol}^{-1}$). Subsequent **CO** dissociation and **HI** addition would lead to **108** und **109**, respectively (**108**: $\Delta G^{453} = 145.7 \text{ kJ mol}^{-1}$; **109**: $\Delta G^{453} = 145.8 \text{ kJ mol}^{-1}$), which itself could be protonated to form further strongly endergonic cationic species (**110**: $\Delta G^{453} = 383.7 \text{ kJ mol}^{-1}$; **111**: $\Delta G^{453} = 395.4 \text{ kJ mol}^{-1}$). Generally, the addition of isobutene before **HI** seems to be significantly less feasible and was not considered as relevant.



Scheme 4.36: Possible reaction pathways for the **HI** and isobutene (**102**) coordination to $\text{Ni}(\text{PR}_3)_2(\text{CO})_2$ (**1**) and $\text{Ni}(\text{PR}_3)(\text{CO})_2$ (**10**) in the phosphine-coordinated system. ΔG^{453} in kJ mol^{-1} ; RI-PBE0-D3(BJ)/def2-QZVPP//BP86/def2-SV(P); COSMO-RS (MEK).

After all attempts to characterize one of the transition states (e.g., leading from **10** or **105** to the five-coordinate intermediate **100**) had failed, a scan of the Ni–I bond length in complex **100** had been performed (see Figure 4.2) and the resulting potential energy surface revealed a barrierless reaction from **100** to the **HI** adduct complex **105**. The transformation proceeds to continuously higher electronic energies along the reaction coordinate, which is in good agreement with endergonic nature of the step (**100**→**105**: $\Delta G^{453} = 22.6 \text{ kJ mol}^{-1}$). The small dent towards the end of the bond length scan corresponds to a small change in conformation and does not represent a reaction barrier. Therefore, the addition of **HI** to the Ni center can readily occur during the reaction and will proceed over the lowest energy path of the intermediates (**1**→**10**→**105**→**100**).

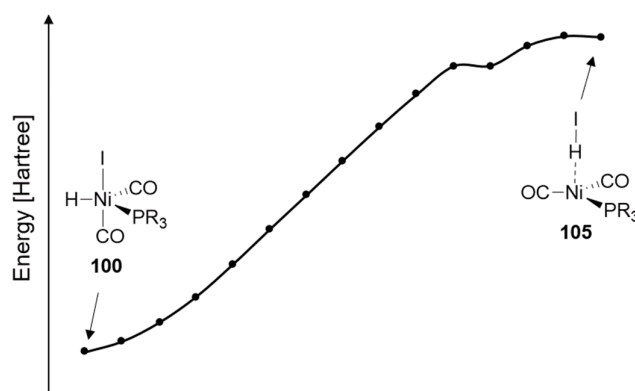
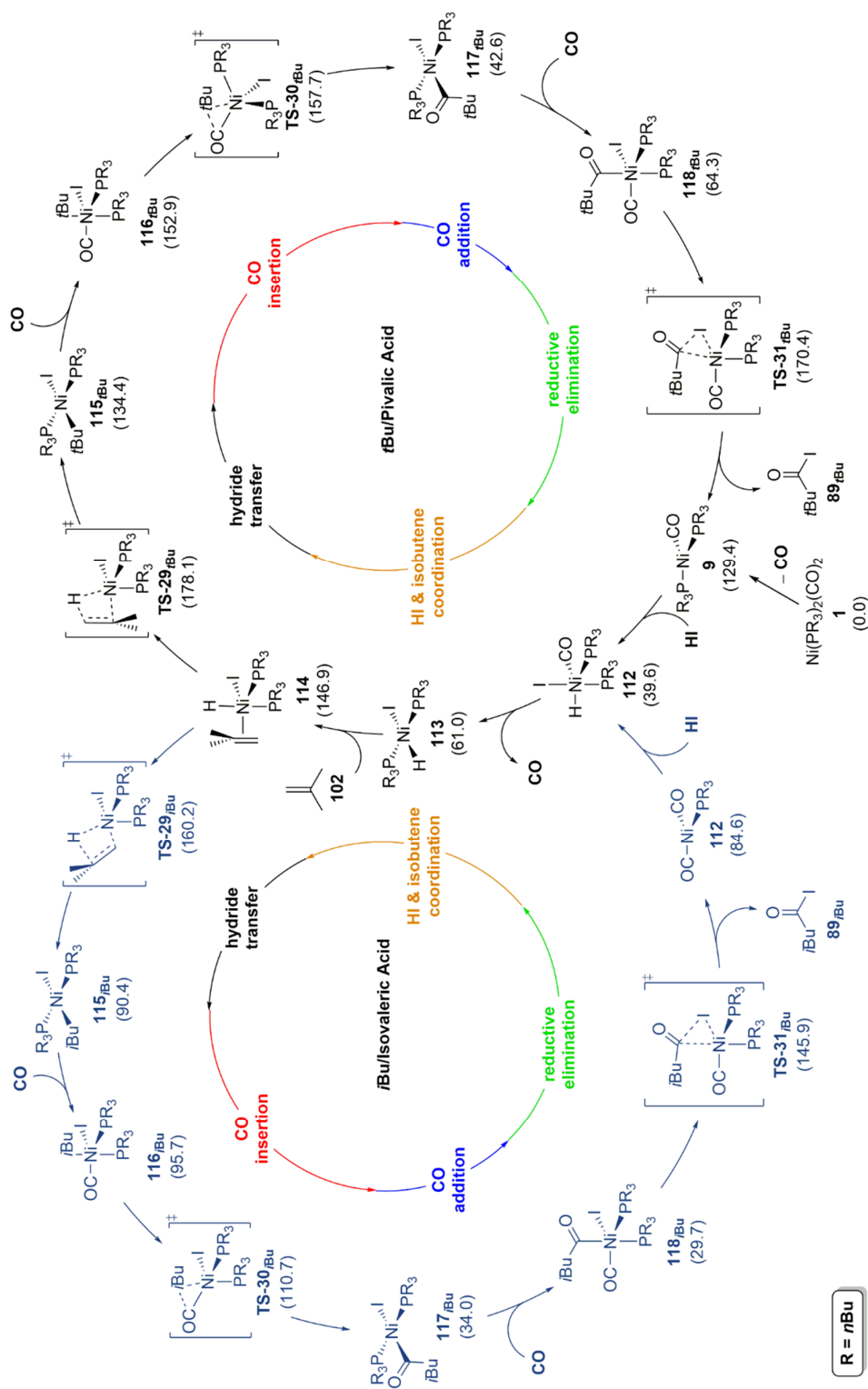


Figure 4.2: Potential energy surface for the scan of the Ni–I bond length in the phosphine-coordinated system, during which the hydride is concertedly abstracted from the Ni center. ΔE^{453} in kJ mol^{-1} ; RI-PBE0-D3(BJ)/def2-QZVPP//BP86/def2-SV(P); COSMO-RS (MEK).

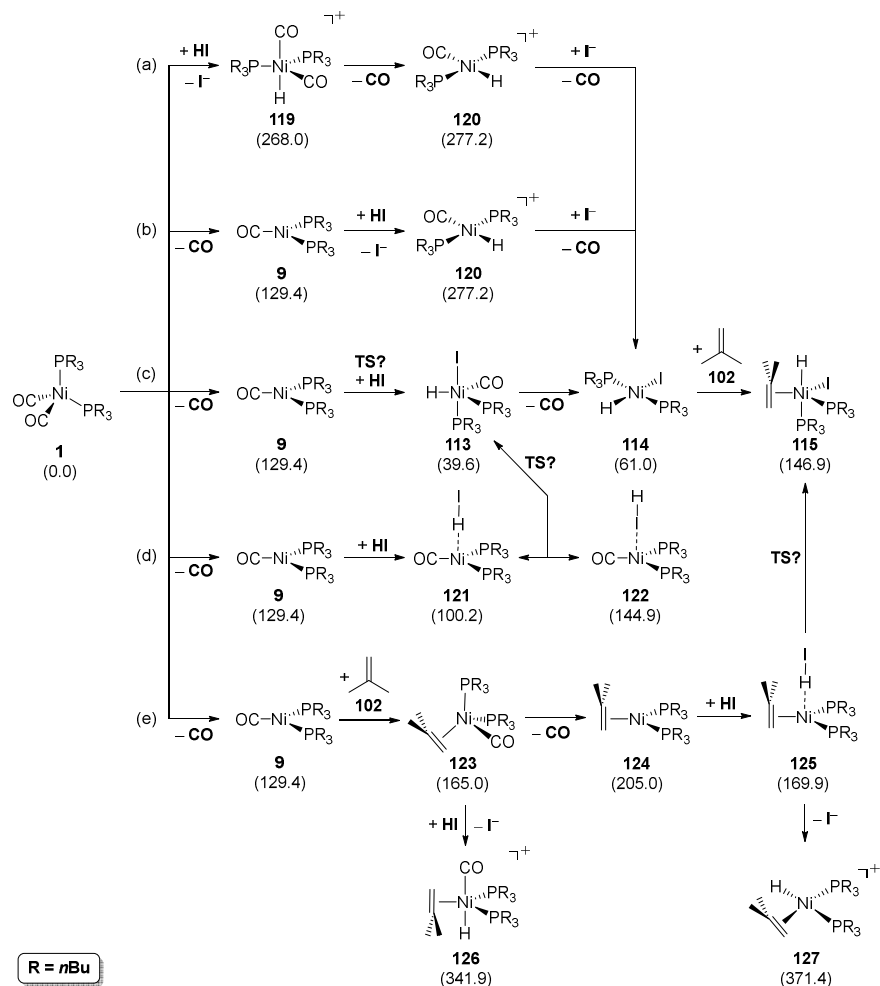
After the catalytic cycles for the monophosphine-coordinated system had been calculated and evaluated, the attention was directed towards alternative catalytic systems, which could also be formed at catalytic conditions. Like the alternative pathways in the investigation concerning phenyl ethyl alcohol, this included the diphosphine system (see Scheme 4.37). This reaction pathway equally starts from $\text{Ni}(\text{TBP})_2(\text{CO})_2$ (**1**) but proceeds via **CO** dissociation (instead of the dissociation of $\text{P}(\text{nBu})_3$) to the trigonal structure **9** ($\Delta G^{453} = 129.4 \text{ kJ mol}^{-1}$). Direct addition of **HI** leading to **112** ($\Delta G^{453} = 39.6 \text{ kJ mol}^{-1}$) was assumed to take place similar to the monophosphine system and is followed by **CO** dissociation, which leads to formation of the square-planar Ni^{II} complex **113** ($\Delta G^{453} = 61.0 \text{ kJ mol}^{-1}$). Subsequent isobutene addition to **114** ($\Delta G^{453} = 146.9 \text{ kJ mol}^{-1}$) prepares the system for the decisive hydride transfer transition states **TS-29_{tBu}** and **TS-29_{iBu}** that form the metal-bound alkyl ligands ($\Delta G^\ddagger = 178.1$ and $160.2 \text{ kJ mol}^{-1}$, respectively). From **115_{tBu}**/**115_{iBu}** (**115_{tBu}**: $\Delta G^{453} = 134.4 \text{ kJ mol}^{-1}$; **115_{iBu}**: $\Delta G^{453} = 90.4 \text{ kJ mol}^{-1}$), **CO** insertion – opposite to the monophosphine system – takes place via the five-coordinate pathway as no carbonyl ligand is coordinated in the four-coordinate square-planar systems that could insert. After **CO** coordination (to **116_{tBu}**: $\Delta G^{453} = 152.9 \text{ kJ mol}^{-1}$ or **116_{iBu}**: $\Delta G^{453} = 95.7 \text{ kJ mol}^{-1}$), the transformation is achieved via **TS-30_{tBu}** or **TS-30_{iBu}** ($\Delta G^\ddagger = 157.7$ and $110.7 \text{ kJ mol}^{-1}$, respectively). In accordance with other *tBu*/*iBu* complexes in this thesis, the more sterically demanding *tBu* group leads to significantly higher energies for **115_{tBu}**, **116_{tBu}** and **TS-30_{tBu}** (compared to **115_{iBu}**, **116_{iBu}** and **TS-30_{iBu}**, respectively) and is further elevated by the two bulky $\text{P}(\text{nBu})_3$ ligands in this system. After **CO** addition to **117_{tBu}**/**117_{iBu}** (**117_{tBu}**: $\Delta G^{453} = 42.6 \text{ kJ mol}^{-1}$; **117_{iBu}**: $\Delta G^{453} = 34.0 \text{ kJ mol}^{-1}$), which leads to the formation of the five-coordinate **118_{tBu}** and **118_{iBu}** ($\Delta G^{453} = 64.3$ and 29.7 kJ mol^{-1} , respectively), reductive elimination takes place via **TS-31_{tBu}** or **TS-31_{iBu}** (**TS-31_{tBu}**: $\Delta G^\ddagger = 170.4 \text{ kJ mol}^{-1}$; **TS-31_{iBu}**: $\Delta G^\ddagger = 145.9 \text{ kJ mol}^{-1}$). Overall, the rate-determining steps are, similar to the previously

investigated monophosphine isobutene pathway (see Scheme 4.34), the hydride transfer transition states **TS-29_{tBu}** and **TS-29_{iBu}**. The barriers associated with these transformations are significantly higher than when only one **P(*n*Bu)₃** ligand is coordinated to nickel (towards pivalic acid: $\Delta\Delta G^\ddagger = 35.3 \text{ kJ mol}^{-1}$; towards isovaleric acid: $\Delta\Delta G^\ddagger = 15.1 \text{ kJ mol}^{-1}$). These differences, which are significantly larger for the *tert*-butyl system, once more exemplify the drastic steric hinderance occurring in the *t*Bu pathways of the diphosphine systems.



Scheme 4.37: Calculated lowest energy pathway for the carbonylation of isobutene leading to pivalic acid (*tert*-butyl product; black) and isovaleric acid (*iso*-butyl product; blue) by a neutral double phosphine coordinated system. ΔG^{\ddagger} in kJ mol^{-1} ; RI-PBE0-D3(B)/def2-QZVPP//BP86/def2-SV(P); COSMO-RS (MEK).

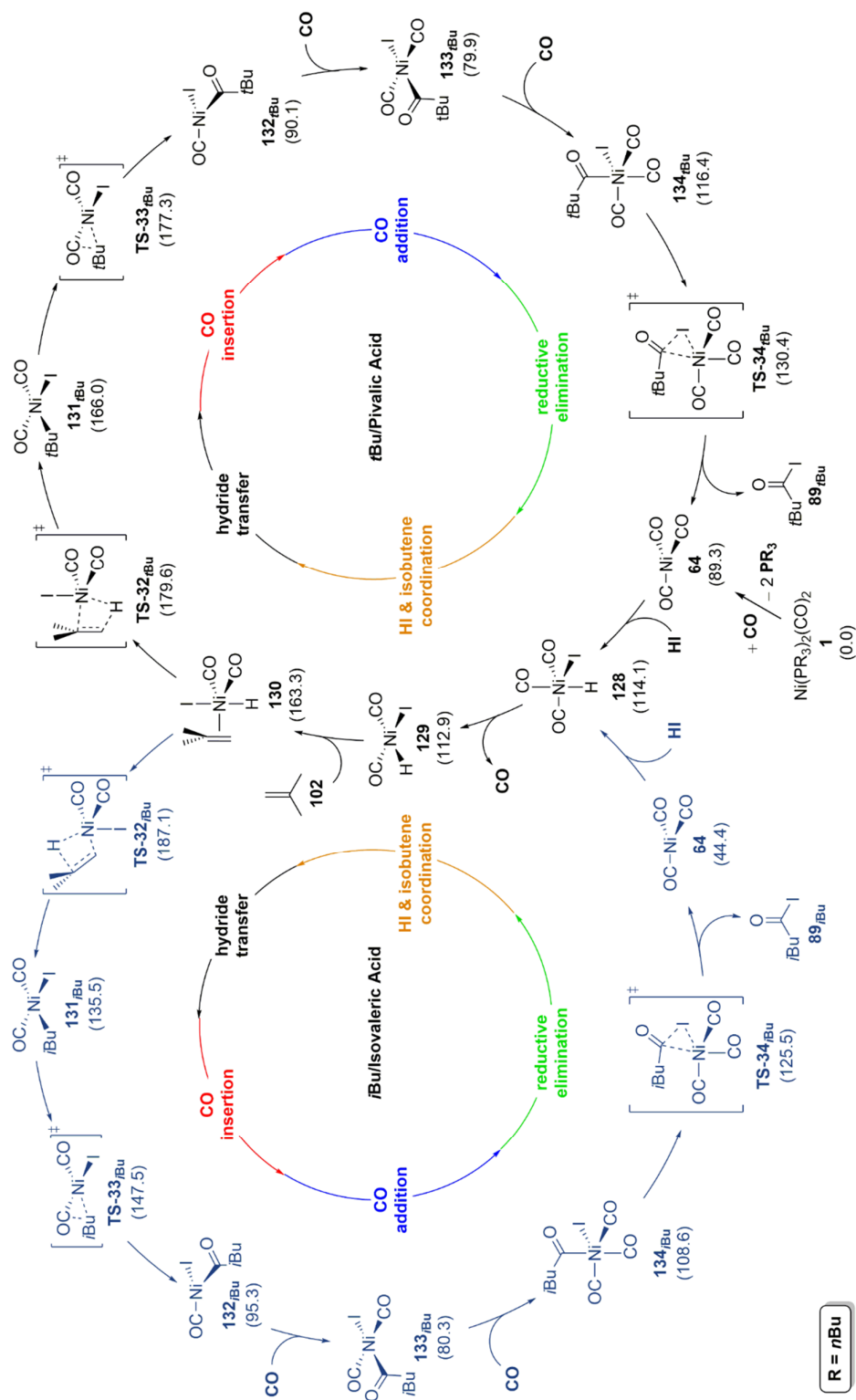
A detailed investigation of **HI** and isobutene addition pathways was also carried out for the catalytic system coordinated by two **P(*n*Bu)₃** ligands (see Scheme 4.38). The pathways leading to the formation of cationic species **119** and **120** (**119**: $\Delta G^{453} = 268.0 \text{ kJ mol}^{-1}$; **120**: $\Delta G^{453} = 277.2 \text{ kJ mol}^{-1}$) either via direct protonation of **1** (**1**→**119**→**120**) or via protonation of **9** ($\Delta G^{453} = 129.4 \text{ kJ mol}^{-1}$) after **CO** dissociation (**1**→**9**→**120**) are too high in energy to be feasible at the experimentally employed reaction conditions (pathways a and b). Next to pathway c, which is presented as part of Scheme 4.37, two more pathway were envisioned and calculated. Of these, the formation of **HI** adducts of Ni(TBP)₂(CO) (**9**) either with a Ni–H contact (**121**: $\Delta G^{453} = 100.2 \text{ kJ mol}^{-1}$) or (significantly less feasible) with a Ni–I interaction (**122**: $\Delta G^{453} = 144.9 \text{ kJ mol}^{-1}$) and barrierless transformation of **121** into **113** was found to be the most logical pathway for **HI** and isobutene coordination (pathway d; cf. Figure 4.2). On the other hand, pathway e is based on the initial η^2 coordination of the isobutene substrate but the formed intermediate **123** as well as subsequent complexes **124** and **125** or protonation to **126** and **127** were found to be significantly less stable than pathways c/d (**123**: $\Delta G^{453} = 165.0 \text{ kJ mol}^{-1}$; **124**: $\Delta G^{453} = 205.0 \text{ kJ mol}^{-1}$; **125**: $\Delta G^{453} = 169.9 \text{ kJ mol}^{-1}$; **126**: $\Delta G^{453} = 341.9 \text{ kJ mol}^{-1}$; **127**: $\Delta G^{453} = 371.4 \text{ kJ mol}^{-1}$). The characterization of any transition states along these reaction pathways was not successful and a barrierless reaction was assumed.



Scheme 4.38: Possible reaction pathways for the **HI** and isobutene (**102**) coordination to $\text{Ni}(\text{PR}_3)_2(\text{CO})_2$ (**1**) and $\text{Ni}(\text{PR}_3)_2(\text{CO})$ (**9**) in the double phosphine-coordinated system. ΔG^{453} in kJ mol^{-1} ; RI-PBE0-D3(BJ)/def2-QZVPP//BP86/def2-SV(P); COSMO-RS (MEK).

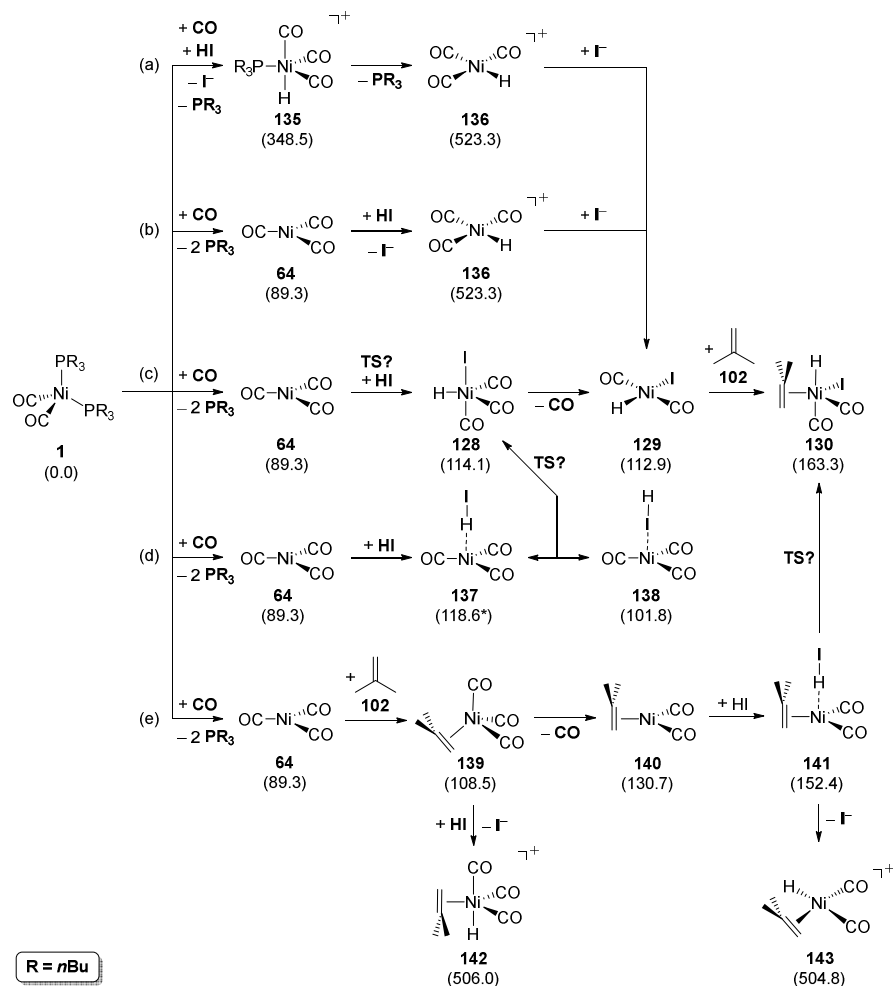
Furthermore, the phosphine-free catalytic system, in which only carbonyl groups were employed, was calculated (see Scheme 4.39) and enabled comparison to the control experiments, which had shown that no conversion was observed when neither phosphine nor **LiI** were employed. For better comparability with the other reaction pathways, this was also referenced to $\text{Ni}(\text{TBP})_2(\text{CO})_2$ (**1**). From **1**, both phosphine ligands need to dissociate from the Ni complex to form the trigonal intermediate **64** ($\Delta G^{453} = 89.3 \text{ kJ mol}^{-1}$). Subsequent **HI** addition (**128**: $\Delta G^{453} = 114.1 \text{ kJ mol}^{-1}$), **CO** dissociation (**129**: $\Delta G^{453} = 112.9 \text{ kJ mol}^{-1}$) and isobutene coordination (**130**: $\Delta G^{453} = 163.3 \text{ kJ mol}^{-1}$) proceed via the same steps as in the other catalytic systems (cf. Schemes 4.35 and 4.37). In the following step, the catalytic cycle divides into the two pathways leading to pivalic acid (**TS-32**_{*t*Bu}: $\Delta G^\ddagger = 179.6 \text{ kJ mol}^{-1}$) and to isovaleric acid (**TS-32**_{*i*Bu}: $\Delta G^\ddagger = 187.1 \text{ kJ mol}^{-1}$). The transition states lead to the square-planar Ni^{II} complexes **131**_{*t*Bu} and **131**_{*i*Bu} ($\Delta G^{453} = 166.0$ and $135.5 \text{ kJ mol}^{-1}$, respectively).

Opposite to the diphosphine system (see Scheme 4.37), the four-coordinate complexes carry **CO** ligands and are, thus, capable of accessing the four-coordinate **CO** insertion pathways (**TS-33_{iBu}**: $\Delta G^\ddagger = 177.3 \text{ kJ mol}^{-1}$; **TS-33_{iBu}**: $\Delta G^\ddagger = 147.5 \text{ kJ mol}^{-1}$), which were found to be more feasible than the respective five-coordinate pathways. The formed trigonal intermediates **132_{iBu}** and **132_{iBu}** ($\Delta G^{453} = 90.1$ and 95.3 kJ mol^{-1} , respectively) add carbon monoxide in two steps (**133_{iBu}**: $\Delta G^{453} = 79.9 \text{ kJ mol}^{-1}$; **133_{iBu}**: $\Delta G^{453} = 80.3 \text{ kJ mol}^{-1}$; **134_{iBu}**: $\Delta G^{453} = 116.4 \text{ kJ mol}^{-1}$; **134_{iBu}**: $\Delta G^{453} = 108.6 \text{ kJ mol}^{-1}$). Finally, reductive elimination takes place via **TS-34_{iBu}** and **TS-34_{iBu}** with barriers of 130.4 and $125.5 \text{ kJ mol}^{-1}$, respectively. Generally, the same trends for the different four- and five-coordinate complexes were observed as for the two previous catalytic systems coordinated either with one or with two phosphine ligands and have been discussed in detail before. The rate-determining transition states of the phosphine-free reaction pathways towards pivalic acid and isovaleric acid are **TS-32_{iBu}** and **TS-32_{iBu}**, thus, once more the hydride transfer step. With activation energies of 179.6 and $187.1 \text{ kJ mol}^{-1}$, the pathways will not be able to compete with the monophosphine-coordinated pathway, which exhibited barriers of 143 - 145 kJ mol^{-1} . However, the system drastically gains relevance when phosphine-free experimental conditions are considered. In this case, the formation of **1** (in the Ni^{II} to Ni^0 reduction step from NiL_2) will no longer be possible and only nickeltetracarbonyl (**5**: $\Delta G^{453} = 41.1 \text{ kJ mol}^{-1}$; referenced to **1** and additional **CO** ligands) might be available as off-cycle resting state. Due to the significantly less stable reference point, the calculated activation energy of the rate-determining steps will be lowered and might fall into a reasonable regime (**TS-32_{iBu}**: $\Delta G^\ddagger = 138.5 \text{ kJ mol}^{-1}$; **TS-32_{iBu}**: $\Delta G^\ddagger = 146.0 \text{ kJ mol}^{-1}$; referenced to **5** and necessary reagents). Based on this, a similar performance as the Ni-phosphine system would be expected, which is contrary to the low conversion that was observed experimentally. It was concluded that this might be caused by a low viability of the initial Ni^{II} to Ni^0 reduction step, which leads to the fact that only very small amounts of active catalyst are present in the reaction and do not suffice to generate relevant amounts of the desired carboxylic acids.



Scheme 4-39: Calculated lowest energy pathway for the carbonylation of isobutene leading to pivalic acid (*tert*-butyl pathway; black) and isovaleric acid (*iso*-butyl pathway; blue) by a neutral non-phosphine coordinated system. ΔG^{\ddagger} in kJ mol^{-1} ; RI-PBE0-D3(BJ)/def2-QZVPP//BP86/def2-SV(P); COSMO-RS (MEK).

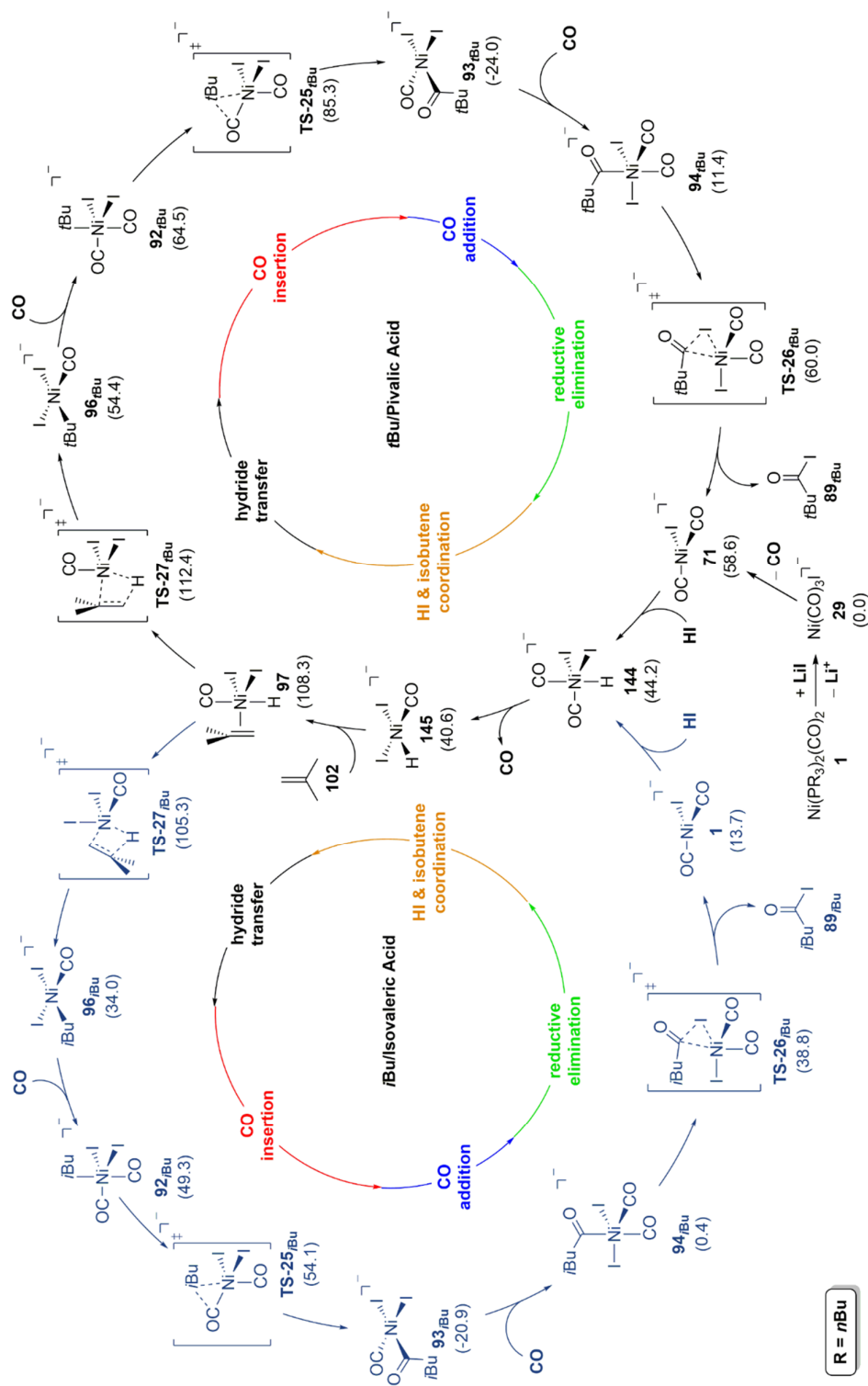
As final part of the DFT calculations of possible catalytic systems in the neutral regime, an investigation into the possible **HI** and isobutene (**102**) coordination pathways was undertaken (see Scheme 4.40). Identically to the previous two catalytic systems, the cationic species are extremely high in energy (**135**: $\Delta G^{453} = 348.5 \text{ kJ mol}^{-1}$; **136**: $\Delta G^{453} = 523.3 \text{ kJ mol}^{-1}$; **142**: $\Delta G^{453} = 506.0 \text{ kJ mol}^{-1}$; **143**: $\Delta G^{453} = 504.8 \text{ kJ mol}^{-1}$) and pathways a and b that rely on the formation of these complexes can be disregarded. Pathway c, which has been presented in Scheme 4.39, is accompanied by the formation of **HI** adduct complexes (**137**: $\Delta G^{453} = 118.6 \text{ kJ mol}^{-1}$; **138**: $\Delta G^{453} = 101.8 \text{ kJ mol}^{-1}$; pathway d). Compared to the phosphine-coordinated pathways, the coordination of isobutene prior to the coordination of **HI** was found to be surprisingly competitive (pathway e). After formation of $\text{Ni}(\text{CO})_3$ (**64**: $\Delta G^{453} = 89.3 \text{ kJ mol}^{-1}$), isobutene coordination leads to the tetrahedral Ni^0 complex **139** ($\Delta G^{453} = 108.5 \text{ kJ mol}^{-1}$). Subsequent **CO** dissociation leads back to the trigonal structural motif, **140** ($\Delta G^{453} = 130.7 \text{ kJ mol}^{-1}$). The alternative pathway via dissociation of **CO** from **64** leading to $\text{Ni}(\text{CO})_2$ (**6**) is less feasible due to the high instability of all two-coordinate species (see Scheme 4.6). From **140**, **HI** adduct formation leading to **141** is slightly endergonic ($\Delta G^{453} = 152.4 \text{ kJ mol}^{-1}$) and a transition state for the subsequent oxidative addition of the acid, which was envisioned to lead to **130** ($\Delta G^{453} = 163.3 \text{ kJ mol}^{-1}$), could not be located. As indicated above, the protonation of species **139** and **141** to **142** and **143**, respectively, is strongly exergonic and, thus, not of relevance compared to the other reaction pathways.



Scheme 4.40: Possible reaction pathways for the **HI** and isobutene (**102**) coordination to $\text{Ni}(\text{PR}_3)_2(\text{CO})_2$ (**1**) and $\text{Ni}(\text{CO})_3$ (**64**) in the non-phosphine coordinated system. *The structure of **137** could only be located by freezing the Ni–I bond length. The real energy should be slightly lower than the given value. ΔG^{453} in kJ mol^{-1} ; RI-PBE0-D3(BJ)/def2-QZVPP//BP86/def2-SV(P); COSMO-RS (MEK).

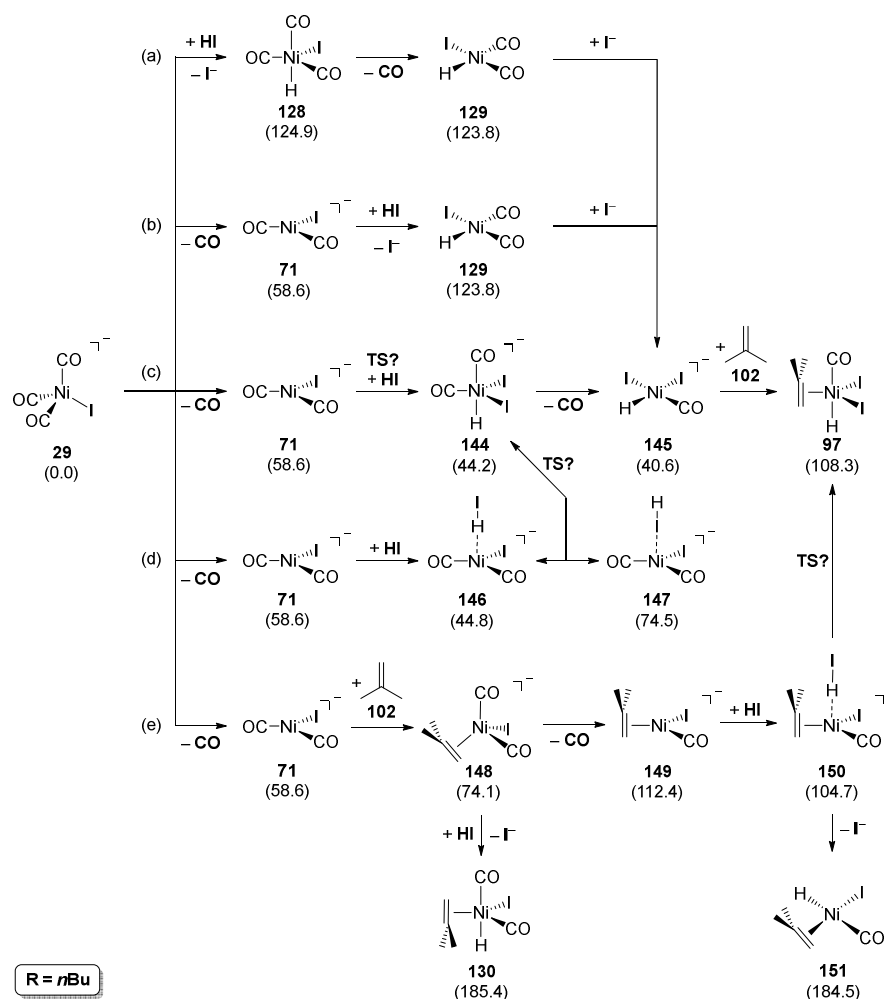
After the three neutral catalytic systems were investigated, the calculations were extended to the **LiI**-induced anionic reaction pathways, which had been shown to have a drastic impact on the carbonylation of phenyl ethyl alcohol (see Scheme 4.41). Interestingly, initial experiments had indicated that the addition of **LiI** had no beneficial influence on the catalytic system. In any case, the thorough investigation of the anionic species is crucial to identify possible side reaction pathways as well as to understand the different behavior of the system in the presence of **LiI**. After formation of $\text{Li}^+[\text{Ni}(\text{CO})_3\text{I}]^-$ (**29**) from $\text{Ni}(\text{TBP})_2(\text{CO})_2$ (**1**), which has been experimentally reported and calculated as part of the previous in-depth investigation into the **LiI** additive,^{194, 202, 222} the envisioned pathway proceeds via **CO** dissociation to the trigonal species **71** ($\Delta G^{453} = 58.6 \text{ kJ mol}^{-1}$). Oxidative addition of **HI** to **71** leads to the endergonic formation of **144** ($\Delta G^{453} = 44.2 \text{ kJ mol}^{-1}$). Dissociation of **CO**

generates the square-planar complex **145**, in which the two iodide ligands are found in *cis* position (**145**: $\Delta G^{453} = 40.6 \text{ kJ mol}^{-1}$). After formation of the five-coordinate Ni-isobutene complex **97** ($\Delta G^{453} = 108.3 \text{ kJ mol}^{-1}$), the pathways for the formation of pivalic acid and isovaleric acid are determined by **TS-27_{tBu}** and **TS-27_{iBu}** ($\Delta G^\ddagger = 112.4$ and $105.3 \text{ kJ mol}^{-1}$, respectively), which either lead to generation of the Ni-*t*Bu and Ni-*i*Bu moiety (**96_{tBu}**: $\Delta G^{453} = 54.4 \text{ kJ mol}^{-1}$; **96_{iBu}**: $\Delta G^{453} = 34.0 \text{ kJ mol}^{-1}$). CO insertion takes place via the five-coordinate species **92_{tBu}** and **TS-25_{tBu}** or **92_{iBu}** and **TS-25_{iBu}** (**92_{tBu}**: $\Delta G^{453} = 64.5 \text{ kJ mol}^{-1}$; **92_{iBu}**: $\Delta G^{453} = 49.3 \text{ kJ mol}^{-1}$; **TS-25_{tBu}**: $\Delta G^\ddagger = 85.3 \text{ kJ mol}^{-1}$; **TS-25_{iBu}**: $\Delta G^\ddagger = 54.1 \text{ kJ mol}^{-1}$). The comparison of the four- and five-coordinate insertion pathways was discussed as part of the investigation into the alkyl iodide-based catalytic cycle (see Scheme 4.33). After **TS-25_{tBu}**/**TS-25_{iBu}**, another set of square-planar Ni^{II} complexes is formed, **93_{tBu}** and **93_{iBu}** ($\Delta G^{453} = -24.0$ and $-20.9 \text{ kJ mol}^{-1}$, respectively), which require the addition of another CO ligand before reductive elimination (to avoid unfavorable two-coordinate complexes). From **94_{tBu}** and **94_{iBu}** ($\Delta G^{453} = 11.4$ and 0.4 kJ mol^{-1} , respectively), this step proceeds via **TS-26_{tBu}** and **TS-26_{iBu}** with barriers of 84.0 and $59. \text{ kJ mol}^{-1}$. The desired carboxylic acids, pivalic acid and isovaleric acid, are generated by hydrolysis of the formed acyl halides (**89_{tBu}**/**89_{iBu}**) after the actual catalytic cycle and regenerate the acid (**HI**) required for the next turnover.



Scheme 4.41: Calculated lowest energy pathway for the carbonylation of isobutene leading to pivalic acid (*tert*-butyl pathway; black) and isovaleric acid (*iso*-butyl pathway; blue) for a LiI-induced anionic catalyst species. ΔG^{\ddagger} in kJ mol⁻¹; RI-PBE0-D3(BJ)/def2-QZVPP//BP86/def2-SV(P); COSMO-RS (MEK).

As for the previous catalytic systems, an in-depth investigation into the **HI** and isobutene coordination steps was performed to evaluate whether any changes between the neutral and the **LiI**-induced anionic potential energy surfaces are present (see Scheme 4.42). Due to the anionic nature of the initial species, $[\text{Ni}(\text{CO})_3\text{I}]^-$ (**29**) and $[\text{Ni}(\text{CO})_2\text{I}]^-$ (**71**: $\Delta G^{453} = 58.6 \text{ kJ mol}^{-1}$), the protonation does not lead to cationic species as before but generates neutral complexes (**128**: $\Delta G^{453} = 124.9 \text{ kJ mol}^{-1}$; **129**: $\Delta G^{453} = 123.8 \text{ kJ mol}^{-1}$; see pathways a and b). These complexes have already been characterized as part of the tricarbonyl catalytic system (see Scheme 4.39) and are significantly more stable than the cationic complexes (cf. Scheme 4.36, 4.38 and 4.40). However, the 'classical' pathway over **71**, **144** and **145** to **97** is still significantly lower in energy (**144**: $\Delta G^{453} = 44.2 \text{ kJ mol}^{-1}$; **145**: $\Delta G^{453} = 40.6 \text{ kJ mol}^{-1}$; **97**: $\Delta G^{453} = 108.3 \text{ kJ mol}^{-1}$; see pathway c). Furthermore, the two **HI** adducts, **146** (with a $\text{Ni}\cdots\text{H}$ interaction: $\Delta G^{453} = 44.8 \text{ kJ mol}^{-1}$; see pathway d) and **147** (with a $\text{Ni}\cdots\text{I}$ interaction: $\Delta G^{453} = 74.5 \text{ kJ mol}^{-1}$) are also more stable and **146** should be readily formed from **71** as the formation is slightly exergonic (**71**→**146**: $\Delta G^{453} = 13.8 \text{ kJ mol}^{-1}$). Lastly, the initial addition of isobutene to **71** results in the tetrahedral motif **148** ($\Delta G^{453} = 74.1 \text{ kJ mol}^{-1}$; see pathway e). From here, dissociation of **CO** (to **149**: $\Delta G^{453} = 112.4 \text{ kJ mol}^{-1}$) or protonation to the neutral five-coordinate Ni^{II} complex **130** ($\Delta G^{453} = 185.4 \text{ kJ mol}^{-1}$) can be envisioned. The initial isobutene coordination step as well as the protonation to **130** are significantly less feasible than other possibilities (pathways c and d) and are highly unlikely to be competitive. The subsequent motifs along pathway e are equally higher in energy than the lowest energy pathway and will not be relevant species in the catalytic system (**150**: $\Delta G^{453} = 104.7 \text{ kJ mol}^{-1}$; **151**: $\Delta G^{453} = 184.5 \text{ kJ mol}^{-1}$).



Scheme 4.42: Possible reaction pathways for the **HI** and isobutene (**102**) coordination to $[\text{Ni}(\text{CO})_3\text{I}]^-$ (**29**) and $[\text{Ni}(\text{CO})_2\text{I}]^-$ (**71**) in the **LiI**-induced system. ΔG^{453} in kJ mol^{-1} ; RI-PBE0-D3(BJ)/def2-QZVPP//BP86/def2-SV(P); COSMO-RS (MEK).

Based on the previous results, which had indicated a barrierless reaction for the oxidative addition of **HI** (coordinated to the Ni atom in the form of **HI** adduct **146**), a Ni–I bond length scan in complex **144** was performed (see Figure 4.3). In contrast to the previous bond length scan on the neutral potential energy surface (cf. Figure 4.2), the scan revealed a reaction barrier along the reaction coordinate. Consequently, the obtained structures were used as a starting point for subsequent transition state geometry optimizations and led to the characterization of **TS-35** (see Scheme 4.43). Intrinsic reaction coordinate (IRC) calculations confirmed that the obtained transition state leads from the **HI** adduct of $[\text{Ni}(\text{CO})_2\text{I}]^-$ (**146**: $\Delta G^{453} = 44.8 \text{ kJ mol}^{-1}$) to the anionic five-coordinate species **144** ($\Delta G^{453} = 44.2 \text{ kJ mol}^{-1}$) with a low barrier that can readily occur at reaction conditions (**TS-35**: $\Delta G^\ddagger = 56.9 \text{ kJ mol}^{-1}$). Although it is highly surprising that this oxidative addition reaction only exhibits a reaction barrier on the anionic potential energy surface, it can also be interpreted

as a confirmation of the previous conclusions. This result demonstrated the good capability of the Ni–I bond length scan to find a transition state along the reaction coordinate and strengthens the conclusion that the reactions on the neutral potential energy surface are in fact barrierless (cf. Figure 4.2).

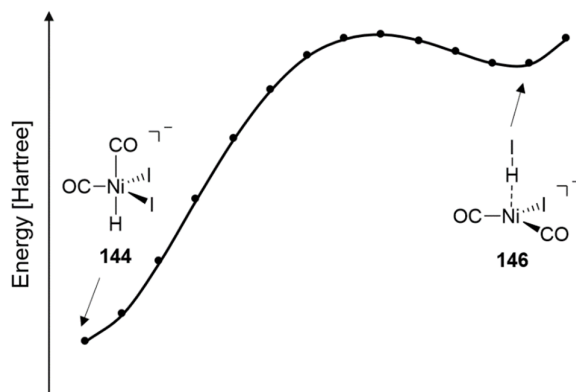
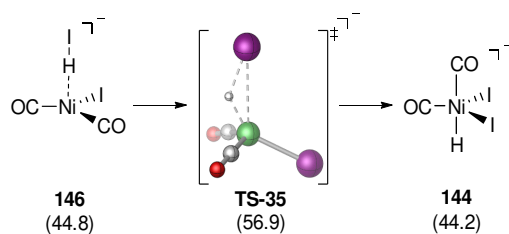


Figure 4.3: Potential energy surface for the scan of the Ni–I bond length in the **LiI**-induced system, during which the hydride is concertedly abstracted from the Ni atom. ΔE^{453} in kJ mol^{-1} ; RI-PBE0-D3(BJ)/def2-QZVPP//BP86/def2-SV(P); COSMO-RS (MEK).

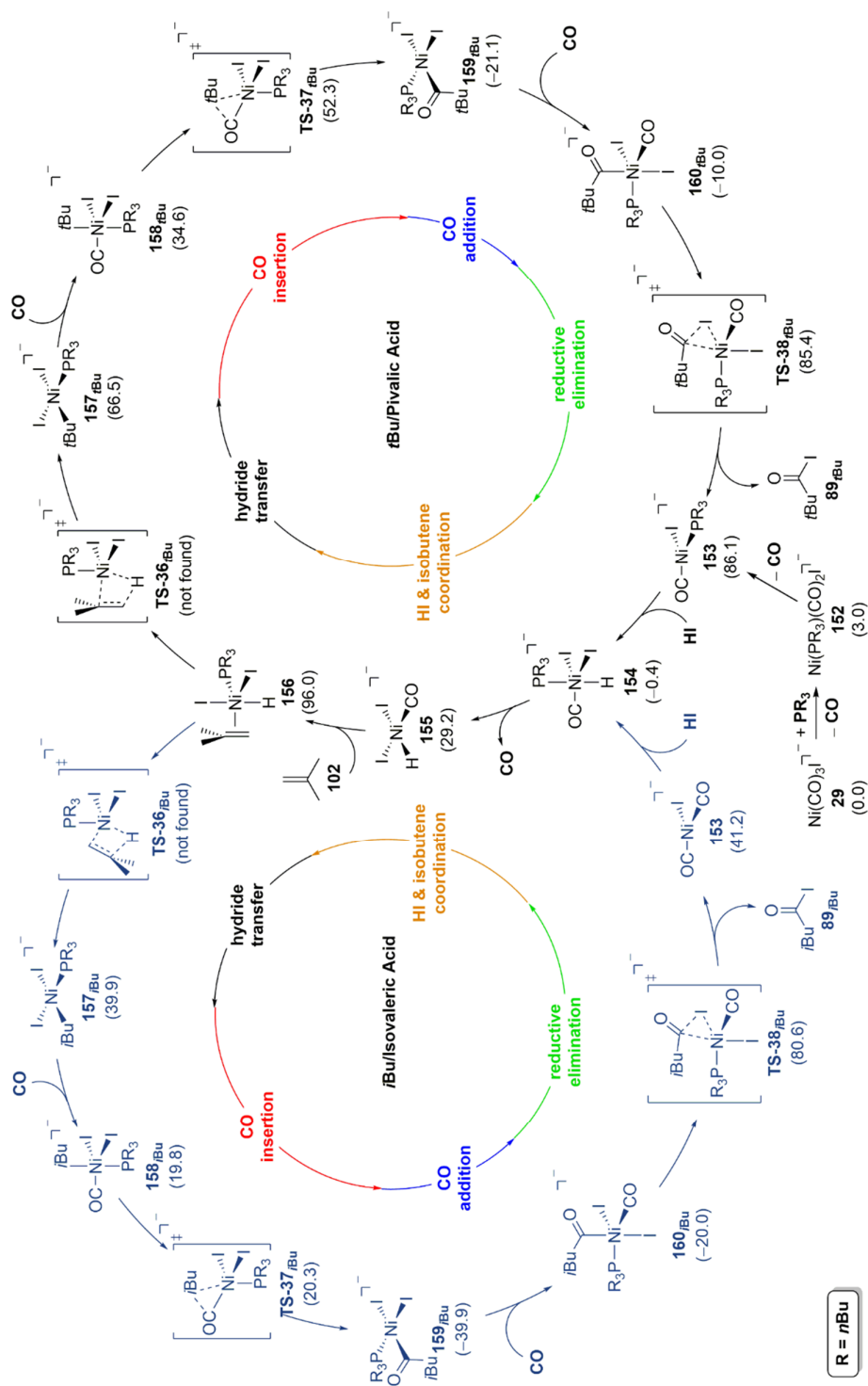


Scheme 4.43: Molecular structure of the **HI** addition transition state **TS-35** in the **LiI**-induced system. ΔG^{453} in kJ mol^{-1} ; referenced to **29** and **HI**; RI-PBE0-D3(BJ)/def2-QZVPP//BP86/def2-SV(P); COSMO-RS (MEK).

In summary, the calculations on the anionic **LiI**-induced phosphine-free reaction mechanism clearly indicated that the reaction should be significantly more feasible when **LiI** is added to the reaction mixture ($\Delta\Delta G^\ddagger = 30.4$ and 39.8 kJ mol^{-1} for the formation of pivalic acid and isovaleric acid, respectively). The similar activation barriers for both pathways (**TS-27**_{*iBu*}: $\Delta G^\ddagger = 112.4 \text{ kJ mol}^{-1}$; **TS-27**_{*iBu*}: $\Delta G^\ddagger = 105.3 \text{ kJ mol}^{-1}$) suggest a similar isomer ratio for the **LiI**-induced carbonylation mechanism as for the reaction along the neutral pathways (see Scheme 4.35), which are expected to take place in the additive-free reactions. Under the premise that the transition state energies are quantitatively correct and small differences can be compared, the calculations with the slightly more feasible activation barrier toward the *iBu*-configured product (**TS-27**_{*iBu*} to isovaleric acid) are in good agreement with the slightly

larger amounts of isovaleric acid being isolated from the catalytic mixtures (1:1.4; see Table 4.5 – entry 3). After these results have been obtained, further experiments were carried out to understand the bad experimental performance, and the differences could be traced back to interferences caused by the reaction autoclave (possibly due to the aggressivity of **HI**). After repeating the experiments in appropriate reaction equipment, the results confirmed the predicted observations by exhibiting the expected increased performance after **LiI** addition. Interestingly, the experimental investigation had also revealed another difference between the carbonylation of phenyl ethyl alcohol and *tert*-butyl alcohol: the direct replacement of **P(*n*Bu)₃** with **LiI**. In the carbonylation of phenyl ethyl alcohol, **LiI** can replace the phosphine without a significant drop in yield. Contrary, a significant drop in performance is observed for formation of pivalic acid and isovaleric acid, when **LiI** is used without **P(*n*Bu)₃**. Therefore, a phosphine-coordinated anionic catalytic system, which had been shown to be less feasible in the carbonylation of phenyl ethyl alcohol (see Scheme 4.15), was also investigated for the olefin-based reaction mechanism (see Scheme 4.44). The initial phosphine-coordinated anionic species $[\text{Ni}(\text{TBP})(\text{CO})_2\text{I}]^-$ (**152**) is generated from the stable Ni tricarbonyl halide complex **29**, which already was the reference structure for the previous investigations into the anionic catalytic systems (*vide supra*). The formation of **152** is nearly energetically equivalent and sets the stage for carbonyl dissociation leading to trigonal complex **153** (**152**: $\Delta G^{453} = 3.0 \text{ kJ mol}^{-1}$; **153**: $\Delta G^{453} = 86.1 \text{ kJ mol}^{-1}$). The coordination changes were envisioned to occur over the same steps as in all previous systems starting with **HI** coordination. This leads to the formation of five-coordinate Ni^{II} intermediate **154**, which undergoes **CO** dissociation to form square-planar complex **155** with *cis* configuration of the iodide ligands (**154**: $\Delta G^{453} = -0.4 \text{ kJ mol}^{-1}$; **155**: $\Delta G^{453} = 29.2 \text{ kJ mol}^{-1}$). Interestingly, **154** is significantly more stable than the equivalent five-coordinate complex in the phosphine-free catalytic cycle (**144**: $\Delta G^{453} = 44.2 \text{ kJ mol}^{-1}$; see Scheme 4.41). Isobutene coordination regenerates the trigonal-bipyramidal structural motif (**156**: $\Delta G^{453} = 96.0 \text{ kJ mol}^{-1}$). Despite several attempts, the subsequent hydride transfer transition states, **TS-36_{tBu}** and **TS-36_{iBu}**, could not be located. Geometry optimization frequently led to dissociation of one of the ligands or to the adjacent intermediates indicating that the desired transition states are highly instable. The characterizable species resume with the square-planar Ni^{II} intermediates **157_{tBu}** and **157_{iBu}**, to which another **CO** ligand coordinates to form the next set of five-coordinate trigonal-bipyramidal intermediates (**157_{tBu}**: $\Delta G^{453} = 66.5 \text{ kJ mol}^{-1}$; **157_{iBu}**: $\Delta G^{453} = 39.9 \text{ kJ mol}^{-1}$). The formed species **158_{tBu}** and **158_{iBu}** are the precursors for **CO** insertion (**158_{tBu}**: $\Delta G^{453} = 34.6 \text{ kJ mol}^{-1}$; **158_{iBu}**: $\Delta G^{453} = 19.8 \text{ kJ mol}^{-1}$), which takes place via **TS-37_{tBu}**/**TS-37_{iBu}** ($\Delta G^\ddagger = 52.3$ and 20.3 kJ mol^{-1} for *t*Bu and *i*Bu, respectively) and leads to the strongly exergonic formation of the square-planar species **159_{tBu}**/**159_{iBu}** ($\Delta G^{453} = -21.1$ and $-39.9 \text{ kJ mol}^{-1}$ for *t*Bu and *i*Bu, respectively). After **CO** association (to **160_{tBu}**: $\Delta G^{453} = -10.0 \text{ kJ mol}^{-1}$; to **160_{iBu}**: $\Delta G^{453} = -20.0 \text{ kJ mol}^{-1}$), the

catalytic cycle is completed via reductive elimination with barriers of 106.5 and 120.5 kJ mol⁻¹ for **TS-38**_{*t*Bu} and **TS-38**_{*i*Bu}, respectively. The final reductive elimination step is significantly less feasible than in the previously investigated system and reaches a similar barrier height (*t*Bu) or even surpasses the activation energy (*i*Bu) compared to the phosphine-free catalytic cycle (cf. Scheme 4.41). This, combined with the implied instability of the hydride transfer (*vide supra*), led to the conclusion that the phosphine-coordinated pathways are not competitive, and the observed experimental activities must originate from effects that cannot be captured by the computational investigations.

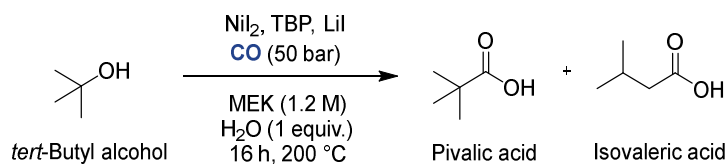


Scheme 4.44: Calculated lowest energy pathway for the carbonylation of isobutene leading to pivalic acid (*tert*-butyl pathway; black) and isovaleric acid (*isobutyl* pathway; blue) for a **LiI**-induced anionic phosphine-coordinated catalyst species. ΔG^{453} in kJ mol⁻¹; RI-PBE0-D3(BJ)/def2-QZVPP//BP86/def2-SV(P); COSMO-RS (MEK).

In summary, the DFT investigation into the anionic catalytic cycles enabled the accurate prediction of an improvement of the Ni-catalyzed carbonylation of *tert*-butyl alcohol with **LiI**. The reaction, like the alkyl iodide-based carbonylation of phenyl ethyl alcohol, was found to proceed via the same transformation steps in the neutral and anionic systems. The coordination of **P(*n*Bu)₃** was calculated to be less feasible than the anionic phosphine-free catalytic system, for which further investigations are needed to precisely evaluate the combined effects of phosphine and **LiI** additive. Lastly, a further experimental observation that is in line with the calculated reaction pathways is the influence of the employed **CO** pressure. Higher pressures were identified to lower the activity of the catalytic system, which can be explained by the need for **CO** dissociation before the rate-determining hydride transfer transition states. The addition of **CO** to the systems (both along the neutral and anionic pathways) only occurs after this step and does not influence the rate-determining activation barrier.

4.4.3 Summary and Outlook

The previously developed catalytic system could be adapted to the carbonylation of *tert*-butyl alcohol to the corresponding Koch-type carboxylic acid. However, the observed reactivity was contrary to the initial assumption and did not lead to the sole formation of pivalic acid.



Scheme 4.45: Carbonylation of *tert*-butyl alcohol to pivalic acid and isovaleric acid with NiI_2 , $\text{P}(n\text{Bu})_3$ and LiI .

The established mechanism was recalculated for the adapted substrates and found to be feasible (see Schemes 4.28 and 4.31) but did not provide an explanation for the observed isomerization (see Schemes 4.29 and 4.32). A set of control experiments demonstrated the decomposition of the *in-situ* formed alkyl iodides and was able to suggest an olefin-based reaction employing isobutene (see Table 4.6 and Scheme 4.34). Consequently, new reaction mechanisms were studied with neutral monophosphine, diphosphine and tricarbonyl species (see Schemes 4.35, 4.37 and 4.39, respectively) as well as with anionic phosphine-free and phosphine-coordinated species (see Schemes 4.41 and 4.44, respectively), which provided an explanation for the observed phenomena. Impressively, the calculations on the anionic potential energy surface are able to predict the beneficial nature of the LiI additive, while experiments have still shown the opposite effect. In the end, the computational results prevailed, and the differing results were traced back to problematic autoclave effects (see Figure 4.4). The calculations on the anionic phosphine-coordinated potential energy surface suggest that the reaction does not proceed via these pathways even if tri-*n*-butylphosphine is added. As in the carbonylation of phenyl ethyl alcohol, the combination of experimental and computational investigations led to a consistent interpretation and improved the mechanistic analysis. However, the required use of a combination of the phosphine ligand with LiI could not yet be explained by the DFT investigations and should be further studied by experimental and computational means.

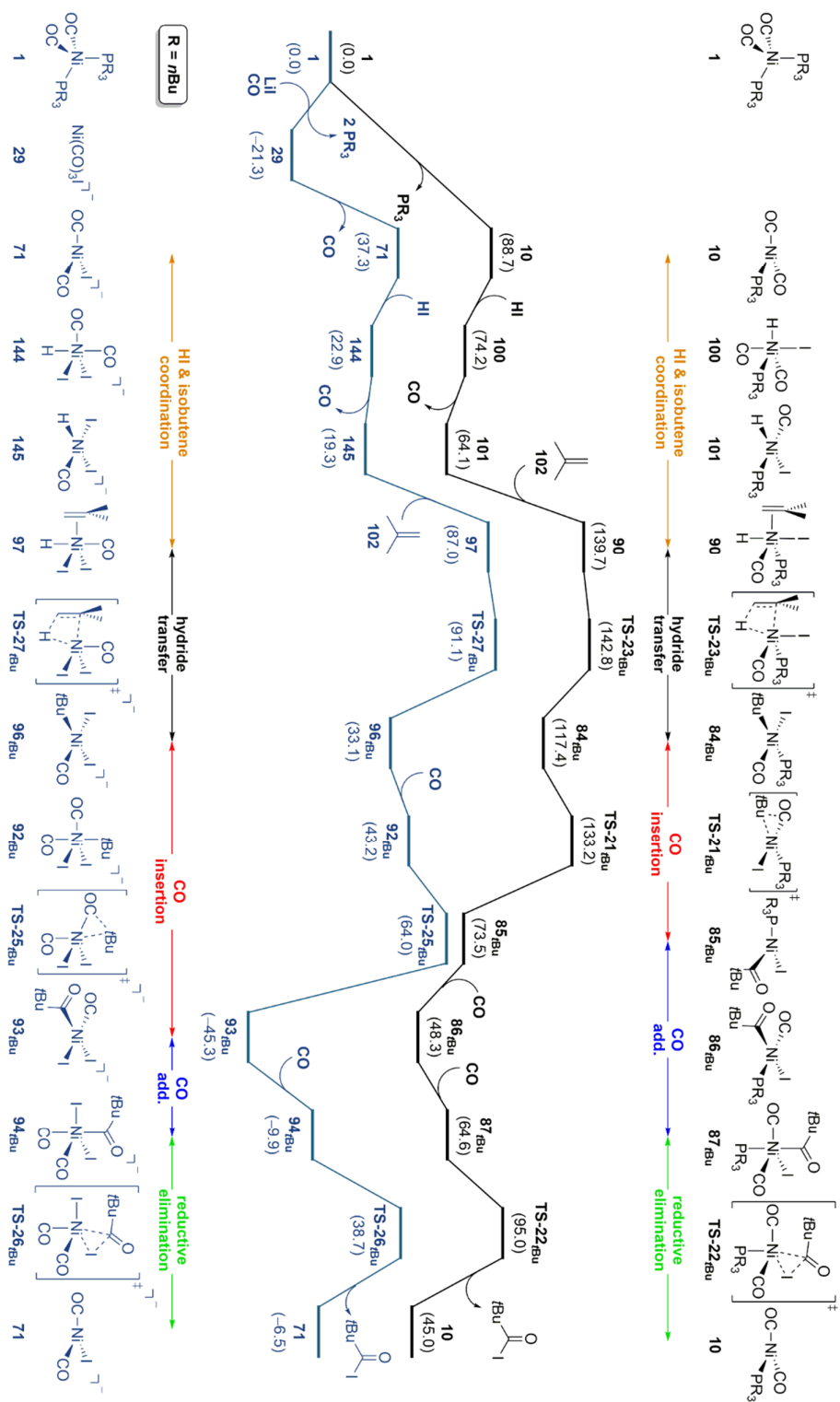


Figure 4.4: Potential energy surface plot for the carbonylation of isobutene (**102**) to the pivalic acid comparing the neutral reaction pathway with one phosphine ligand coordinated to Ni (black; upper pathway) with the LiH-induced phosphine-free reaction pathway (blue; lower pathway). ΔG^{453} in kJ mol^{-1} ; RI-PBE0-D3(BJ)/def2-QZVPP//BP86/def2-SV(P); COSMO-RS (MEK).

Further experiments could be conducted to test the applicability of the methodology to other alcohols and especially olefins, of which only isobutene has been employed so far for control experiments. This should be done with special care as the adaption from phenyl ethyl alcohol to *tert*-butyl alcohol (and *iso*-butyl alcohol) has already demonstrated the drastic effects that can arise from such an exchange. Although the pivalic acid:isovaleric acid ratios have been very similar across most experiments, a more detailed investigation into possible approaches to control this value would be desirable. For example, the use of more complex monodentate ligands (e.g., Buchwald-type ligands, which have shown good performance in the carbonylation of phenyl ethyl alcohol) once the lack of clarity regarding the combined use of phosphine and LiI has been resolved (*vide supra*). Alternatively, the adjustment of various reaction parameters might be a suitable starting point for attempting to influence the catalytic system. As part of these efforts, one should try to define the yield-limiting factors and identify any other species that are formed during the reaction as full conversion is achieved but only limited amounts of products are isolated. Initial tests have revealed olefin isomerization for more complex substrates. Further experiments and quantum-chemical calculations could be employed to gain an in-depth understanding of the underlying processes. The full experimental results will be reported in a combined publication of experiments and quantum chemistry, which will be submitted shortly.²³⁷

4.5 Summary and Outlook

The carbonylation of phenyl ethyl alcohol and *tert*-butyl alcohol with an earth-abundant Ni catalyst, which provides a straightforward and atom-economic methodology for the synthesis of the corresponding carboxylic acids, 2-phenylpropanoic acid and pivalic acid, was extensively investigated. These represent model substrates for important products in chemical industry such as ibuprofen, naproxene or tertiary Koch-type compounds. The catalytic system was found to be highly effective with the cheap NiI₂ precursor, tri-*n*-butylphosphine and LiI at a CO pressure of 50 bar. Quantum-chemical investigations were able to provide an in-depth understanding of the underlying reaction mechanism for the carbonylation of phenyl ethyl alcohol and to explain the crucial role of the LiI additive, which enables access to an anionic potential energy surface with significantly lower activation energies. Several side reaction pathways have been investigated to ensure the accuracy of the calculations. However, the carbonylation of branched aliphatic alcohols with the developed catalytic system afforded a mixture of multiple isomers, which was not expected based on the previous mechanistic insights on benzylic alcohols. The transfer of the determined reaction mechanism proved as highly complex as the coordinating substrate species in the catalytic cycle changed from alkyl halides to olefins. Thus, a complete reevaluation of the catalytic cycles was necessary to provide an understanding of the role of the individual components. Control experiments were able to provide experimental indications for both mechanisms separately, with phenyl ethyl alcohol and with *tert*-butyl alcohol. A range of strategies to develop further improvements have been suggested, which go hand in hand with experimental observations that still need to be rationalized. Many of these steps fall out of the reach of DFT investigations (e.g., the Ni^{II}→Ni⁰ reduction step starting from NiI₂) or would significantly benefit from experimental indications that would help to guide the calculations towards the right direction in the highly complex chemical space. The combination of experimental and computational investigations run in parallel enabled the improvements and progress in mechanistic understanding, which allowed to move this project forward and to adjust to new results such as access to the anionic reaction pathways or the substrate-dependent reaction mechanisms.

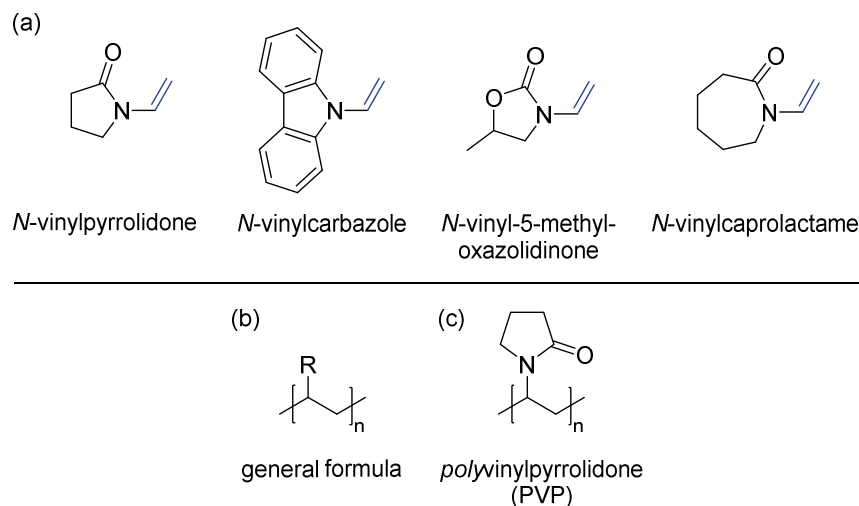
5

Vinylation of Pyrrolidone

Reproduced in part with permission from Nikolai A. Sitte, Maximilian Menche, Pavel Tužina, Frank Bienewald, Ansgar Schäfer, Peter Comba, Frank Rominger, A. Stephen K. Hashmi and Thomas Schaub, Phosphine-catalyzed Vinylation at Low Acetylene Pressure, *The Journal of Organic Chemistry* **2021**, *manuscript accepted*. Copyright 2021 American Chemical Society.

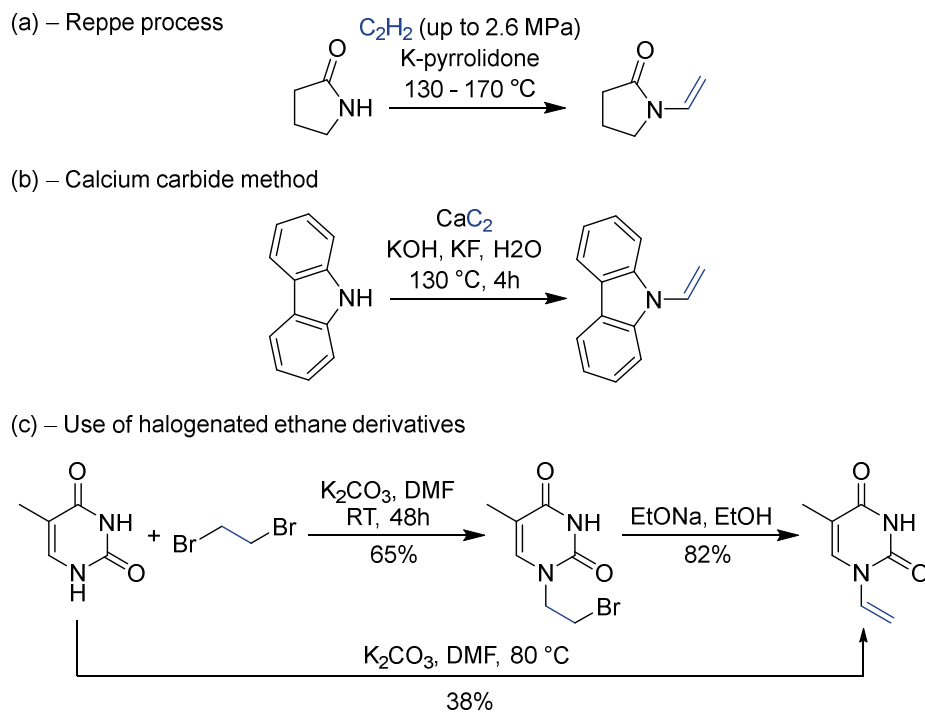
5.1 Motivation

N-vinyl compounds represent an important class of monomers for the synthesis of polymers with a versatile set of properties. One commonly used example of this substance class is *N*-vinylpyrrolidone (NVP; Scheme 5.1a), which is extensively used in the pharmaceutical, cosmetic and food industries, either directly as poly(*N*-vinylpyrrolidone) (PVP; Scheme 5.1c) or in the form of various copolymers.²³⁸⁻²⁴⁰ Apart from NVP, a wide range of other commercially employed monomers is available for direct or copolymer use (e.g., *N*-vinylcarbazole,²⁴¹ *N*-vinylcaprolactame,²⁴²⁻²⁴³ or *N*-vinyl-5-methyloxazolidinone;²⁴⁴⁻²⁴⁶ see Scheme 5.1a).



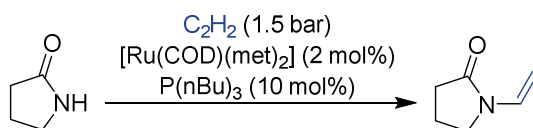
Scheme 5.1: (a) Chemical structures of important *N*-vinyl monomers, (b) General formula for the polymer compounds resulting from the above monomers and (c) formula of polyvinylpyrrolidone (PVP), which is formed from *N*-vinylpyrrolidone.

Due to this extended commercial application, a widely applicable and economically feasible synthesis of *N*-vinyl compounds is highly desirable. The current industrial synthesis of these *N*-vinyl monomers is achieved in a high-pressure process with acetylene in presence of a strong base as described by Walter Reppe (see Scheme 5.2a).^{240,247} While other approaches for the synthesis of these compounds have also been reported (e.g., using calcium carbide²⁴⁸⁻²⁴⁹ or halogenated ethane derivatives;²⁵⁰ Scheme 5.2b-c), the direct utilization of acetylene for the vinylation reaction remains more desirable than these other possibilities based on the atom efficiency of this route.²⁵¹⁻²⁵² On the other hand, the strongly basic conditions and high acetylene pressures up to 20 bar substantially limit the range of substrates and requires expensive high-pressure reactors and equipment to ensure appropriate safety during the synthesis.²⁵³⁻²⁵⁴ Base-sensitive substrates need to be synthesized via other, mostly less atom-economic processes. Consequently, an envisioned protocol for this transformation should ideally improve on at least one of these critical aspects without losing economic feasibility out of sight.



Scheme 5.2: Reaction schemes for (a) the industrially widely-used Reppe process directly employing C_2H_2 ,²⁴⁰ (b) the calcium carbide based method presented by Ananikov and co-workers²⁴⁹ and (c) the use of halogenated ethane derivatives as intermediates in the *N*-vinyl compound synthesis.²⁵⁰

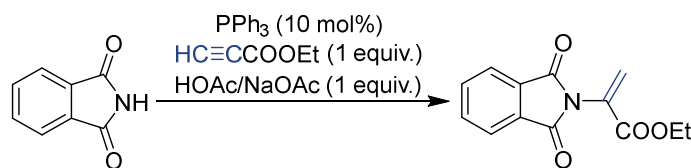
A variety of scientific publications has addressed these issues and provided substantial improvements to the synthesis of *N*-vinyl compounds,²⁵⁵ many of which employed ruthenium complexes for the hydroamination²⁵⁶ and hydroamidation²⁵⁷⁻²⁵⁹ of alkyne compounds. On this basis, our own group has also reported the Ru-catalyzed low-pressure hydroamidation of acetylene in 2020 from pyrrolidone (see Scheme 5.3),²⁶⁰ which itself can be easily synthesized from γ -butyrolactone and ammonia.²⁴⁰ However, the use of an expensive ruthenium catalyst significantly reduces the economic feasibility of a potential process as a highly efficient catalyst recycling methodology is required, which will also come with significant costs of its own.



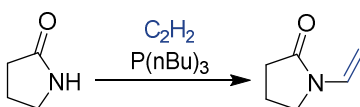
Scheme 5.3: Reaction scheme for the ruthenium-catalyzed vinylation of pyrrolidone previously reported by our group.²⁶⁰

Therefore, the development of a system that employs either cheap, earth-abundant metals or even works metal-free was set as the target of our investigation, while preserving the capability for low-pressure vinylation of base-sensitive substrates. To achieve this, previous

work from the past decades on the utilization of nucleophilic phosphine catalysis for the activation of electron deficient alkenes and alkynes was taken into consideration.²⁶¹⁻²⁶² Hereby, the seminal work by Trost and Dake,²⁶³ in which they described a triphenylphosphine-catalyzed vinylation of *N*-nucleophiles that is achieved by an α -umpolung addition of electron-deficient alkynes, set the foundation for our approach (see Scheme 5.4). However, in over 20 years following the publication, this reactivity could never be transferred to acetylene or even to non-activated alkynes, which represented the desired starting material in our methodology (see Scheme 5.5).



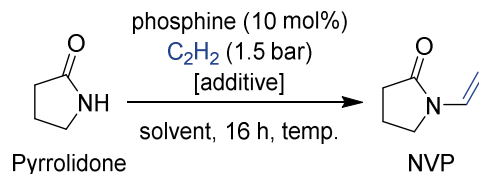
Scheme 5.4: Reaction scheme for the PPh_3 -catalyzed α -umpolung addition of phthalimide to ethyl propiolate developed by Trost *et al.*²⁶³



Scheme 5.5: Reaction scheme for the desired phosphine-catalyzed vinylation of the model substrate pyrrolidone directly employing acetylene at low pressures.

A brief exert of the screening of reaction components and conditions is shown in Table 5.1. Initially, the reaction system reported by Trost *et al.* was applied to the model substrate pyrrolidone and acetylene (Table 5.1 – entry 1). No reactivity was observed either with or without the AcOH/NaOAc additive that had been used by Trost *et al.* (Table 5.1 – entries 1-2) and the same reactions employing dimethylacetamide (DMAA) as solvent were not showing any activity either (Table 5.1 – entries 3-4). However, while increased temperatures of $140\text{ }^\circ\text{C}$ did not afford any yield in toluene, the reaction did show traces of the desired NVP product in DMAA (Table 5.1 – entry 5). Replacing the employed phosphine with a phosphine with increased nucleophilicity to facilitate the activation of acetylene proved crucial and lead to a yield of 63% when using tri-*n*-butylphosphine ($\text{P}(\text{nBu})_3$; Table 5.1 – entry 6). A detailed screening of solvents and phosphines was carried out and can be found in the corresponding publication.²⁶⁴ Throughout this screening the combination of DMAA and $\text{P}(\text{nBu})_3$ remained the best performing catalytic system and was used as standard for all further experiments (except when specifically noted).

Table 5.1: Brief summary of the experimental screening in the phosphine-catalyzed direct vinylation with acetylene.^[a] All experiments were carried out by Nikolai Sitte at CaRLa.



Entry	Phosphine	Additive (equiv.)	Solvent	Temp [°C]	Yield ^[b] [%]
1	PPh ₃	AcOH/NaOAc (1.0)	Toluene	110	0
2	PPh ₃	-	Toluene	110	0
3	PPh ₃	AcOH/NaOAc (1.0)	DMAA	110	0
4	PPh ₃	-	DMAA	110	0
5	PPh ₃	-	DMAA	140	trace
6	P(<i>n</i> Bu) ₃	-	DMAA	140	63

[a] Reactions were performed with 1 equiv. of pyrrolidone in solvent (0.435 M), 0.5 equiv. of AcOH and 0.5 equiv. of NaOAc (when indicated), 10 mol% of phosphine (PPh₃ or P(*n*Bu)₃), and 1.5 bar C₂H₂ at 110 °C or 140 °C for 16 h. [b] Yield was determined by calibrated gas chromatography.

After the desired reactivity had been achieved, our interest turned to performing an in-depth mechanistic investigation, both with experimental and quantum-chemical methods, to understand the underlying reaction steps and to suggest further actions for improving the catalytic system. These improvements might include avoiding unwanted side reactions, which drastically lower the system's catalytic performance. The efforts to understand the degradation pathways was additionally driven by the observation of phosphine oxide formation in many of the experiments as well as the significant loss of phosphine due to its reaction with acetylene.

5.2 Computational Details

All geometry optimizations were carried out at the BP86/def2-SV(P)^{9, 39, 51} level of theory. Stationary points were verified via analysis of the vibrational frequencies at the level of geometry optimization. Final electronic energies were obtained by single-point calculations at the PBE0-D3(BJ)/def2-QZVPP^{38-39, 93} level of theory employing Grimme's D3 dispersion correction⁶⁹ incorporating Becke-Johnson damping.⁷⁴ All quantum-chemical calculations were carried out using the TURBOMOLE program⁸⁵⁻⁸⁸ (Version 7.3) with the resolution-of-identity (RI) approximation^{40, 60, 62-63} and the corresponding auxiliary basis sets¹⁴⁵⁻¹⁴⁶ implemented in the program. Zero-point vibrational energies and thermodynamic corrections were obtained at the level of geometry optimization (T = 298.15 K and p = 1 bar) and scaled to 140 °C. For all species, the thermodynamic reference concentration was set to $x = 0.01$. Solvent corrections to Gibbs free energies in DMF were calculated for all species with the conductor-like screening model for real solvents (COSMO-RS)⁷⁵⁻⁷⁶ carried out with the COSMOtherm program^{77, 89} (Version 18.0.0; Revision 4360). All energies discussed are Gibbs free energies at 140 °C (ΔG^{413}) in kJ mol^{-1} accounting for solvent corrections. Connectivities between minima and transition states implied in Figures and Schemes were validated by intrinsic-reaction-coordinate (IRC) calculations.¹⁰³ Pictures of molecular structures were generated with the CYLview¹⁴⁷ program.

In the whole investigation, the full catalytic system was employed in the calculations without any truncation of the pyrrolidone substrate or the phosphine.

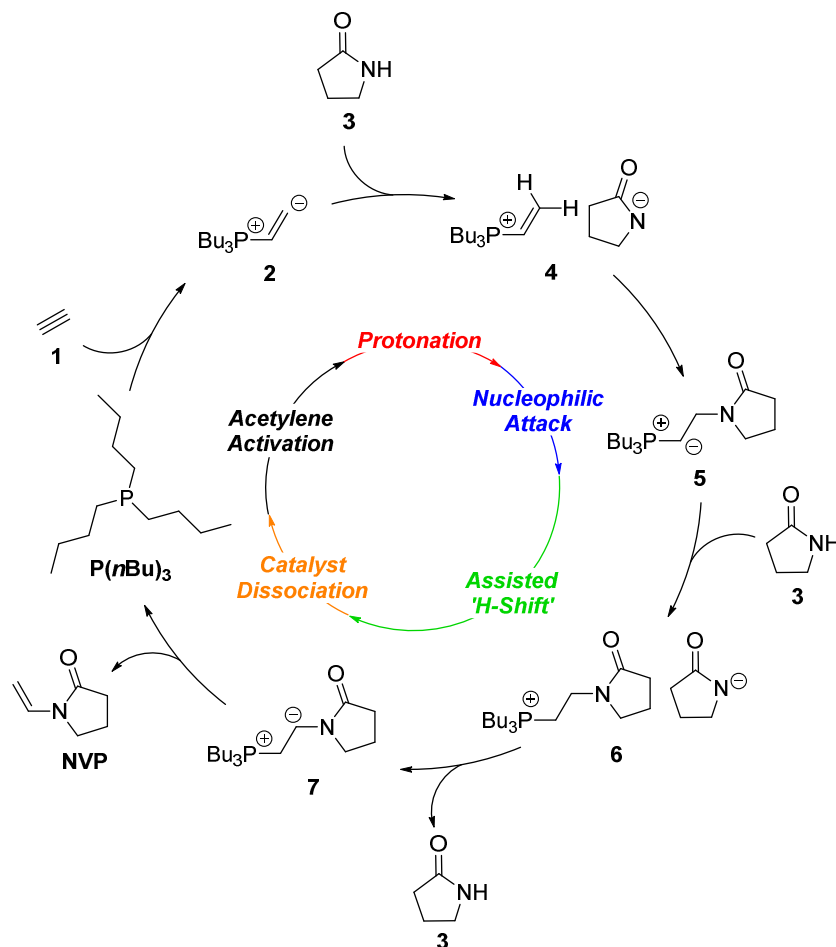
Note that the numbering of the calculated and experimental structures is reset for every chapter.

5.3 Results and Discussion

5.3.1 Investigation of a Nucleophilic Reaction Mechanism

The first catalytic cycle that is proposed and investigated is based on the phosphine-induced activation of acetylene, which at a later stage enables a nucleophilic attack of the substrate, which ultimately leads to the desired product formation. Similar activation steps have been proposed by Trost and Dake in their previously discussed publication²⁶³ and by Kwon and co-workers^{261, 265} as well as Ziegenbalg *et al.*²⁶⁶ in their work on phosphine-initiated Michael additions but have not been investigated in detail. This hypothesis was further supported by the experimental observation that amine bases did not exhibit any activity, which indicates a phosphine-based activation step.

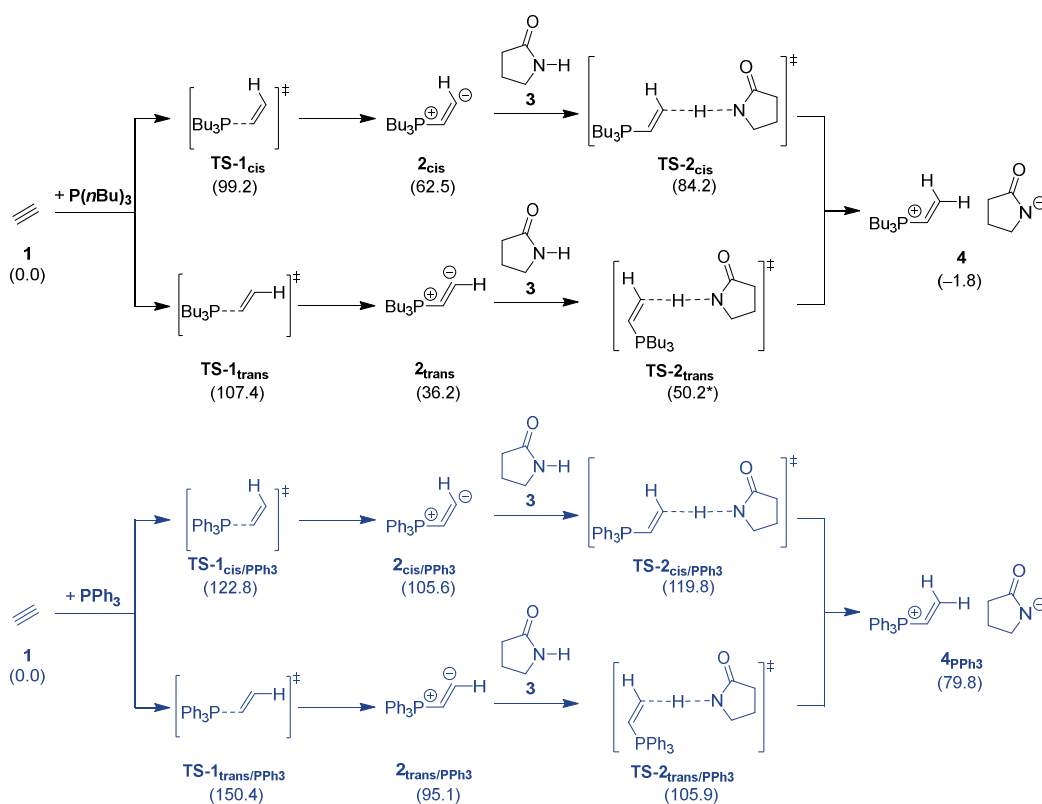
The first proposed catalytic cycle includes five key steps: (a) acetylene activation, (b) protonation, (c) nucleophilic attack, (d) assisted hydrogen shift and (e) catalyst/product dissociation (see Scheme 5.6). First, the phosphine catalyst (**P**(*n*Bu)₃) will need to activate the acetylene molecule (**1**). Due to the direct use of acetylene instead of an activated building block (e.g., ethyl propiolate in the work of Trost *et al.*), it is expected that this represents a significant reaction barrier. The importance of this activation barrier is further supported by the drastic change in activity when switching from **PPh**₃ to **P**(*n*Bu)₃ and that no conversion has been observed without **P**(*n*Bu)₃ (see Table 3.1). This activated acetylene intermediate (**2**) can receive the NH proton of the pyrrolidone substrate (**3**) forming ion pair **4**. The two ions of **4** can undergo a nucleophilic addition of the pyrrolidone unit to the terminal carbon atom of the cation to form a zwitterionic ylide (**5**). A H-shift from the β position to the α position (with respect to the phosphorus unit), which could possibly be assisted by a second equivalent of pyrrolidone (via intermediary species **6**), leads to intermediate **7**, which can split up in order to form the desired **NVP** product and to regenerate the phosphine catalyst **P**(*n*Bu)₃ and thus complete the catalytic cycle. To understand the underlying reaction pathways and to be able to validate our quantum-chemical investigation against the drastic effect of the choice of phosphine that was observed in the experiments (*vide supra*), the calculations were performed employing **P**(*n*Bu)₃ as well as **PPh**₃. Based on the observed reactivities, a significantly more feasible reaction pathway for **P**(*n*Bu)₃ was expected.



Scheme 5.6: Proposed catalytic cycle for the direct vinylation of pyrrolidone with $P(nBu)_3$ and acetylene (1).

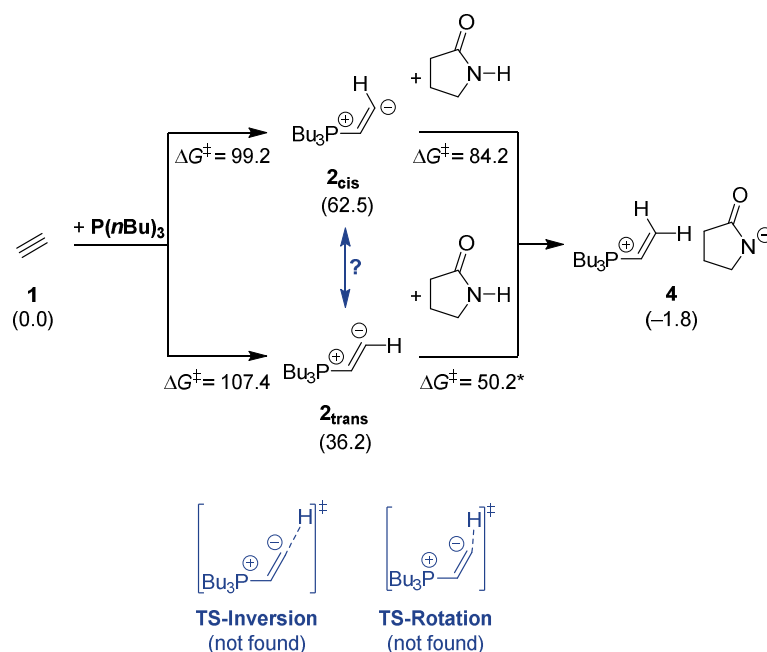
When investigating the initial activation step of the proposed catalytic cycle, leading from **1** and $P(nBu)_3$ to **2**, two configurations must be considered (see Scheme 5.7). Firstly, $P(nBu)_3$ can activate **1** in a fashion, where the hydrogen atom connected to the carbon atom in β position is found in a *cis* configuration to the phosphine. In this case, transition state **TS-1_{cis}** leads to **2_{cis}** ($\Delta G^{413} = 62.5 \text{ kJ mol}^{-1}$) with a barrier of 99.2 kJ mol^{-1} . On the other hand, **TS-1_{trans}** ($\Delta G^\ddagger = 107.4 \text{ kJ mol}^{-1}$), in which the hydrogen atom is positioned *trans* to the activating phosphine unit exhibits a slightly larger energy barrier ($\Delta\Delta G^\ddagger = 8.2 \text{ kJ mol}^{-1}$) but leads to the significantly more stable intermediate **2_{trans}** ($\Delta G^{413} = 36.2 \text{ kJ mol}^{-1}$; $\Delta\Delta G^{413} = 26.3 \text{ kJ mol}^{-1}$). Subsequent proton transfer of the NH proton in **3** to the negatively charged carbon atom in **2_{cis}** and **2_{trans}** leads to the recombination of the two *cis* and *trans* pathways (via **TS-2_{cis}**: $\Delta G^\ddagger = 84.2 \text{ kJ mol}^{-1}$; via **TS-2_{trans}**: $\Delta G^\ddagger = 50.2 \text{ kJ mol}^{-1}$) and forms the ion pair **4** ($\Delta G^{413} = -1.8 \text{ kJ mol}^{-1}$). While this proton transfer is significantly more feasible in the *trans* configuration, the energy barriers for both transition states remain below the energies of **TS-1_{cis}** and **TS-1_{trans}** and, therefore, the *cis* pathway remains favored for the overall

conversion of $\mathbf{P}(\mathbf{nBu})_3$ and $\mathbf{1}$ to $\mathbf{4}$ with a barrier of 99.2 kJ mol^{-1} . Similarly, this step was investigated employing triphenylphosphine (\mathbf{PPh}_3) for the activation of acetylene (see Scheme 5.7). The activation of $\mathbf{1}$ with \mathbf{PPh}_3 was found to be significantly less feasible than for $\mathbf{P}(\mathbf{nBu})_3$ ($\mathbf{TS-1}_{\text{cis}/\text{PPh}_3}$: $\Delta G^\ddagger = 122.8 \text{ kJ mol}^{-1}$; $\mathbf{TS-1}_{\text{trans}/\text{PPh}_3}$: $\Delta G^\ddagger = 150.4 \text{ kJ mol}^{-1}$). Comparing these two activation barriers reveals that the gap between *cis* and *trans* configurations has also significantly increased from $\mathbf{P}(\mathbf{nBu})_3$ ($\Delta\Delta G^\ddagger = 8.2 \text{ kJ mol}^{-1}$) to \mathbf{PPh}_3 ($\Delta\Delta G^\ddagger = 27.6 \text{ kJ mol}^{-1}$). After the activation step, the *cis* pathway proceeds via proton transfer from $\mathbf{2}_{\text{cis}/\text{PPh}_3}$ ($\Delta G^{413} = 105.6 \text{ kJ mol}^{-1}$) to $\mathbf{4}_{\text{PPh}_3}$ ($\Delta G^{413} = 79.8 \text{ kJ mol}^{-1}$) with a barrier of $119.8 \text{ kJ mol}^{-1}$ ($\mathbf{TS-2}_{\text{cis}/\text{PPh}_3}$). On the other hand, the *trans*-configured steps proceed from $\mathbf{2}_{\text{trans}/\text{PPh}_3}$ ($\Delta G^{413} = 95.1 \text{ kJ mol}^{-1}$) over $\mathbf{TS-2}_{\text{trans}/\text{PPh}_3}$ ($\Delta G^\ddagger = 105.9 \text{ kJ mol}^{-1}$) to $\mathbf{4}_{\text{PPh}_3}$ ($\Delta G^{413} = 79.8 \text{ kJ mol}^{-1}$). In resemblance to the $\mathbf{P}(\mathbf{nBu})_3$ -catalyzed pathways, the *trans* configuration of $\mathbf{2}_{\text{PPh}_3}$ and $\mathbf{TS-2}_{\text{PPh}_3}$ is significantly more stable than the *cis* configuration but $\mathbf{TS-2}_{\text{cis}/\text{PPh}_3}$ is (slightly) more feasible than $\mathbf{TS-1}_{\text{cis}/\text{PPh}_3}$ and therefore does not influence the overall selectivity-determining barrier of the pathway ($\Delta G^\ddagger = 122.8 \text{ kJ mol}^{-1}$).



Scheme 5.7: Catalytic pathways for the *cis*- and *trans*-activation of acetylene ($\mathbf{1}$) with $\mathbf{P}(\mathbf{nBu})_3$ (top, black) and \mathbf{PPh}_3 (bottom, blue). ΔG^{413} in kJ mol^{-1} ; RI-PBE0-D3(BJ)/def2-QZVPP//BP86/def2-SV(P); COSMO-RS (DMF). *A converged structure of $\mathbf{TS-2}_{\text{trans}}$ could not be located. The reported energy is from a structure close to the minimum, for which some bond distances have been frozen.

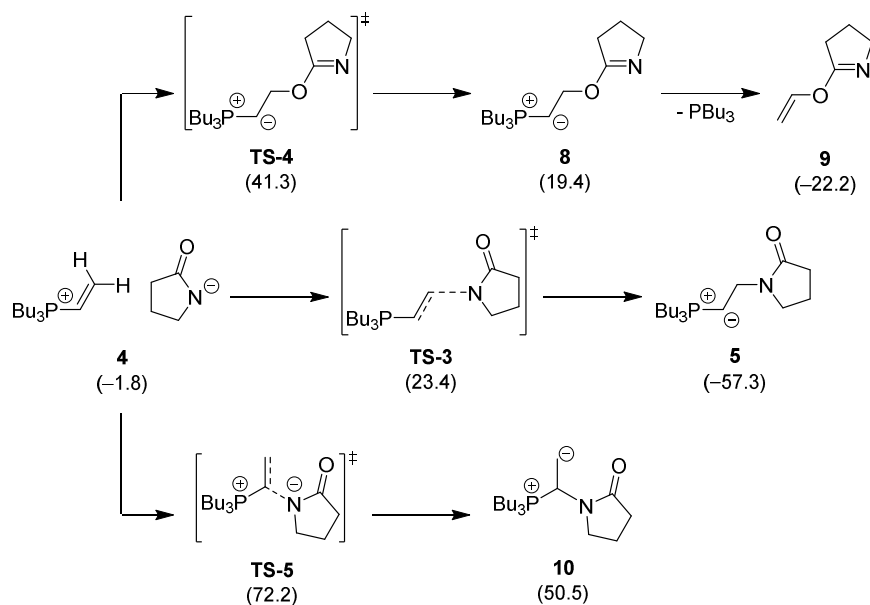
For this assessment of the role of **TS-2_{trans}** and **TS-2_{trans}/PPh₃** to be correct, it is crucial that no isomerization pathways between **2_{cis}** and **2_{trans}** (or **2_{cis}/PPh₃** and **2_{trans}/PPh₃**) exist that could provide access to the more stable *trans* intermediates and the subsequent transition states. While this does not have an influence on the overall energy barrier from **1** to **4** (or **1** to **4_{PPh₃}**), the identification of the most feasible reaction pathways remains one of the main concepts behind this thesis and sets the foundation for all further improvements of the system. An investigation into the *cis-trans* isomerization pathways from **2_{cis}** to **2_{trans}**, either via inversion or rotation, was carried out (see Scheme 5.8, blue structures). Despite all attempts, neither a transition state exhibiting an inversion mode nor a transition state with a rotation mode could be located. Non-converged structures resulting from pre-optimizations, which exhibited the desired inversion or rotation motifs and are expected to be close to the fully optimized structure, resulted in significantly higher energies than the surrounding transition states **TS-1_{cis}**, **TS-1_{trans}**, **TS-2_{cis}**, and **TS-2_{trans}**. (ΔG^\ddagger between 50.2 and 107.4 kJ mol⁻¹). Due to these indications, it was concluded that *cis-trans* isomerization does not play a role in this catalytic system.



Scheme 5.8: Potential isomerization pathways between **2_{cis}** and **2_{trans}** via inversion or rotation. Both transition states could not be located, however, energies from structures exhibiting the desired reaction mode were significantly higher in energy than **TS-1_{cis}**, **TS-1_{trans}**, **TS-2_{cis}** and **TS-2_{trans}**. ΔG^{413} in kJ mol⁻¹; RI-PBE0-D3(BJ)/def2-QZVPP//BP86/def2-SV(P); COSMO-RS (DMF). *A converged structure of **TS-2_{trans}** could not be located. The reported energy is from a structure close to the minimum, for which some bond distances have been frozen.

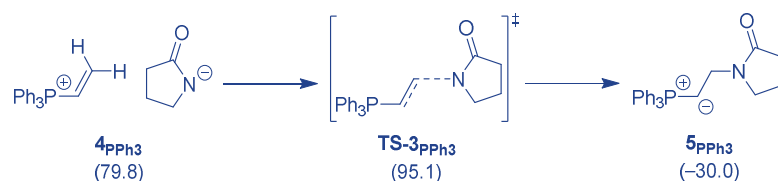
Although only the intermediates and transition states for $\mathbf{P}(n\mathbf{Bu})_3$ are shown in Scheme 5.8, it was also attempted to characterize the inversion and rotation transition states for the \mathbf{PPh}_3 system. However, this also remained unsuccessful and such *cis-trans* isomerization pathways were ruled out as highly unlikely.

The proposed catalytic cycle (as shown in Scheme 5.6) proceeds via the nucleophilic addition of the pyrrolidone anion to the phosphonium cation in ion pair **4**. The nucleophilic addition pathway as well as competing reaction steps were investigated and are shown in Scheme 5.9. The proposed reaction from **4** proceeds over a low activation barrier of 25.2 kJ mol^{-1} (via **TS-3**) and leads to the strongly exergonic formation of ylide **5** ($\Delta G^{413} = -57.3 \text{ kJ mol}^{-1}$). Apart from this pathway, two other potential transformations were calculated: Firstly, the nucleophilic addition of the pyrrolidone oxygen (instead of nitrogen in **TS-3**) to the cation of **4** was found to proceed over a significantly higher reaction barrier (**TS-4**: $\Delta G^\ddagger = 41.3 \text{ kJ mol}^{-1}$). The resulting endergonic intermediate **8** ($\Delta G^{413} = 19.4 \text{ kJ mol}^{-1}$) could react on to exergonically form the O-vinylated product **9** ($\Delta G^{413} = -22.2 \text{ kJ mol}^{-1}$), both of which are significantly less stable than the ylide species **5**, which is formed in the N-addition. Alternatively, the nucleophilic addition of the pyrrolidone nitrogen can also occur in α position (instead of the β position as in **TS-3**) with respect to the phosphine unit. This results in **TS-5** ($\Delta G^\ddagger = 72.2 \text{ kJ mol}^{-1}$), which leads to intermediate **10** ($\Delta G^{413} = 50.5 \text{ kJ mol}^{-1}$), with a significantly higher barrier than the two competing reactions. Consequently, both alternative pathways over **TS-4** and **TS-5** are regarded as of minor importance. In any case, even when populated, both pathways should not lead to interfering results as both are reversible with moderate activation barriers and intermediate **10** represents a precursor for the generation of the desired **NVP** product, which could be formed via $\mathbf{P}(n\mathbf{Bu})_3$ elimination.



Scheme 5.9: Pathways for nucleophilic addition of the pyrrolidone anion to the cation in intermediate **4**. Neither O-addition of the pyrrolidone anion (**TS-4**) nor addition to the α carbon atom of the activated acetylene (**TS-5**) can compete with the previously proposed **TS-3**. ΔG^{413} in kJ mol^{-1} ; referenced to **1**, **3** and $\text{P}(\text{nBu})_3$; RI-PBE0-D3(BJ)/def2-QZVPP//BP86/def2-SV(P); COSMO-RS (DMF).

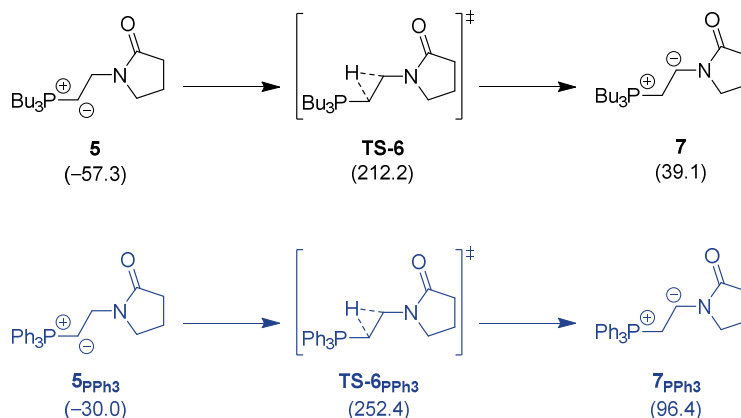
Once more, the nucleophilic N-addition of the pyrrolidone anion to the phosphonium cation, was also investigated for the use of PPh_3 instead of $\text{P}(\text{nBu})_3$ (see Scheme 5.10). From $\mathbf{4}_{\text{PPh}_3}$, only a small barrier of 15.3 kJ mol^{-1} (**TS-3_{PPh3}**) is found to exergonically convert the ion pair to the significantly more stable ylide $\mathbf{5}_{\text{PPh}_3}$ ($\Delta G^{413} = -30.0 \text{ kJ mol}^{-1}$). In comparison to $\text{P}(\text{nBu})_3$, where the barrier is 25.2 kJ mol^{-1} , this represents a slightly lower activation barrier, however, due to the over 80 kJ mol^{-1} less stable preceding intermediate, $\mathbf{4}_{\text{PPh}_3}$, **TS-3_{PPh3}** is still far closer to the acetylene activation barriers than **TS-3**.



Scheme 5.10: Reaction pathway for nucleophilic addition of the pyrrolidone anion to the cation in intermediate $\mathbf{4}_{\text{PPh}_3}$ to form $\mathbf{5}_{\text{PPh}_3}$. ΔG^{413} in kJ mol^{-1} ; referenced to **1**, **3** and PPh_3 ; RI-PBE0-D3(BJ)/def2-QZVPP//BP86/def2-SV(P); COSMO-RS (DMF).

After the ylide generation, a hydrogen transfer step was the logical next step to yield intermediate **7** (see Scheme 5.11), which represents the ideal precursor for $\text{P}(\text{nBu})_3$, elimination leading to catalyst regeneration and product formation. The investigation of this H-shift transition state for $\text{P}(\text{nBu})_3$, **TS-6**, and PPh_3 , **TS-6_{PPh3}**, quickly revealed a far too high energy barrier for this reaction to be feasible at the experimental conditions. With effective

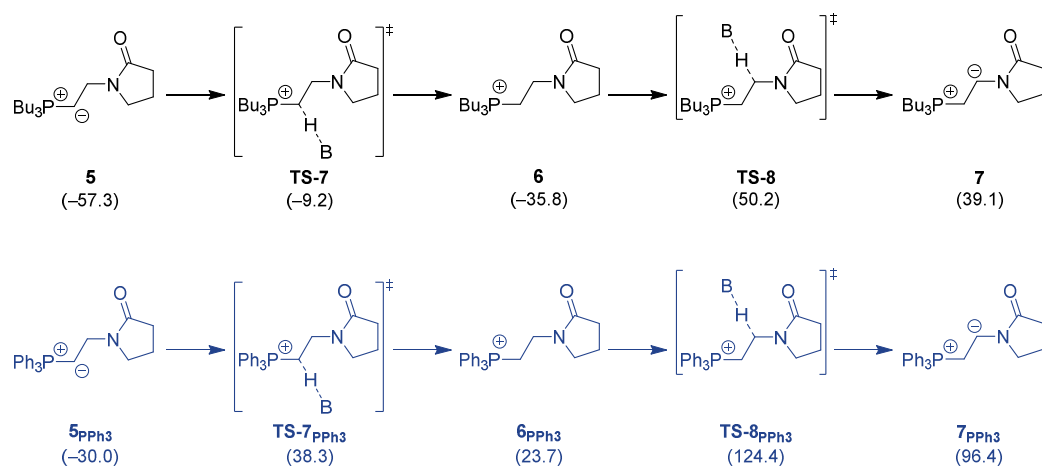
barriers of around 250 kJ mol^{-1} (**TS-6**: $\Delta G^\ddagger = 212.2 \text{ kJ mol}^{-1}$; **TS-6_{PPh₃}**: $\Delta G^\ddagger = 252.4 \text{ kJ mol}^{-1}$), it is clear that an alternative pathway needs to be responsible for the formation of **7** ($\Delta G^{413} = 39.1 \text{ kJ mol}^{-1}$) and **7_{PPh₃}** ($\Delta G^{413} = 96.4 \text{ kJ mol}^{-1}$).



Scheme 5.11: Reaction pathways for the unassisted H-shift from **4** to **7** and **4_{PPh₃}** to **7_{PPh₃}**. The unassisted H-shift transition states **TS-6** and **TS-6_{PPh₃}** are significantly too high in energy to be feasible at the given reaction conditions. ΔG^{413} in kJ mol^{-1} ; referenced to **1**, **3**, and **P(*n*Bu)₃** or **PPh₃**; RI-PBE0-D3(BJ)/def2-QZVPP//BP86/def2-SV(P); COSMO-RS (DMF).

Therefore, an alternative base-assisted pathway was investigated to connect intermediates **5** and **7** (see Scheme 5.12). Due to the high availability of substrate molecules compared to these intermediary species, the involvement of a second equivalent of pyrrolidone (**3**) to facilitate this isomerization seemed plausible. The protonation/deprotonation sequence starts with the transfer of the NH proton of **3** (like **TS-2_{cis}** and **TS-2_{trans}**; cf. Scheme 5.7) to the negatively charged carbon atom in intermediate **5**. This transfer proceeds over a moderate barrier of 48.1 kJ mol^{-1} (**TS-7**: $\Delta G^\ddagger = -9.2 \text{ kJ mol}^{-1}$) to cationic intermediate **6** with the corresponding pyrrolidone anion ($\Delta G^{413} = -35.8 \text{ kJ mol}^{-1}$). The deprotonation of **6** takes place via transition state **TS-8** ($\Delta G^\ddagger = 50.2 \text{ kJ mol}^{-1}$) and leads to the desired intermediate **7** ($\Delta G^{413} = 39.1 \text{ kJ mol}^{-1}$), which could not be accessed via the unassisted H-shift presented before (**TS-6**; see Scheme 5.11). Considering the high stability of ylide **5**, this step is associated with an activation barrier of $107.5 \text{ kJ mol}^{-1}$, which is higher than the previously highest transition state barrier along this reaction pathway (see **TS-1_{cis}**: $\Delta G^\ddagger = 99.2 \text{ kJ mol}^{-1}$). However, compared to the reaction barrier of **TS-6**, which was above 250 kJ mol^{-1} , the activation energy for **TS-8** is feasible at the given experimental conditions ($140 \text{ }^\circ\text{C}$; see Figure 2.1) and fits to the observed activity. In accordance with the previous reaction steps, an investigation of this protonation/deprotonation cascade was also carried out for the second considered phosphine, **PPh₃** (see Scheme 5.12 blue, bottom). The protonation of **5_{PPh₃}** takes place via **TS-7_{PPh₃}** with a barrier of 68.3 kJ mol^{-1} and generates ion pair **6_{PPh₃}** (with a phosphonium cation and pyrrolidone anion; $\Delta G^{413} = 23.7 \text{ kJ mol}^{-1}$). Subsequent reprotonation proceeds over **TS-8_{PPh₃}** ($\Delta G^\ddagger = 154.4 \text{ kJ mol}^{-1}$) leading to **7_{PPh₃}**

($\Delta G^{413} = 96.4 \text{ kJ mol}^{-1}$). In good agreement with the experimental observations, this barrier is significantly higher than the barrier for the $\text{P}(n\text{Bu})_3$ system.



Scheme 5.12: Reaction pathways for the base-assisted H-shift from **4** to **7** and $\mathbf{4}_{\text{PPh}_3}$ to $\mathbf{7}_{\text{PPh}_3}$. The use of a second equivalent of pyrrolidone (**3**) significantly reduces the activation barrier for the H-shift. ΔG^{413} in kJ mol^{-1} ; referenced to **1**, **3**, and $\text{P}(n\text{Bu})_3$ or PPh_3 ; RI-PBE0-D3(BJ)/def2-QZVPP//BP86/def2-SV(P); COSMO-RS (DMF).

Interestingly, this step, in combination with the unavailability of the unassisted hydrogen shift and the generation of the nucleophile, sets important limitations for the substrate scope that can be considered for this catalytic methodology. Firstly, the pK_a of an employed substrate cannot be too high as this will prevent initial deprotonation (TS-2_{cis}), which leads to nucleophile generation. Secondly, the pK_a of the substrate cannot be too low because this will prevent the protonation/deprotonation cascade (TS-7 and TS-8) from taking place. This results in a range of suitable pK_a values for substrates, which could also be confirmed by experiments (see experimental section in the publication). An alternative pathway, in which **5** or $\mathbf{5}_{\text{PPh}_3}$ are deprotonated, which leads to an anionic intermediate that could subsequently be reprotonated to yield **7**, was also investigated. However, neither the anionic intermediates nor the proton transfer transition states could be located, and thus, this reaction pathway was quickly ruled out. After zwitterionic intermediate **7** has been formed via the protonation/deprotonation cascade, only elimination of the phosphine catalyst is required to form the desired product, **NVP**. Due to the zwitterionic structure, in which a dative bond is formed from the phosphorus center to the carbon atom, a barrierless dissociation of $\text{P}(n\text{Bu})_3$ was assumed. This hypothesis was probed by performing a scan of the P–C bond length, over the course of which the catalyst is regenerated and the product is formed (see Figure 5.1). The plot of the electronic energies along this bond dissociation scan does not exhibit any sign of a reaction barrier, which leads to the assumption that this step proceeds barrierless. The small discontinuity between the 9th and 10th point of the potential energy scan

can be assigned to an insignificant alkane chain rearrangement in the phosphine unit and does not represent a reaction barrier.

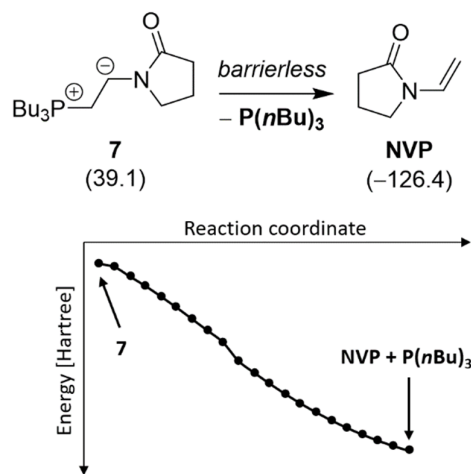


Figure 5.1: Scan of the P–C bond length to investigate the dissociation of **P(nBu)₃** from **7** leading to generation of the desired product (**NVP**) and regeneration of the phosphine catalyst. ΔG^{413} in kJ mol^{-1} (**7** and **NVP**; top section) and ΔE in Hartree (bond length scan); referenced to **1**, **3** and **P(nBu)₃**; RI-PBE0-D3(BJ)/def2-QZVPP//BP86/def2-SV(P); COSMO-RS (DMF).

For better comparability, the individual steps for the vinylation of pyrrolidone (**3**) to **NVP** are combined in Figure 5.2, both for **P(nBu)₃** (black, bottom) and **PPh₃** (blue, top). Already at a quick glance it is possible to identify that the reaction pathway for **P(nBu)₃** is consistently more feasible throughout all molecular transformation steps. While the rate-determining barrier for the use of tri-*n*-butylphosphine (**5**→**TS-8**) is $107.5 \text{ kJ mol}^{-1}$, even the initial acetylene activation energy barrier is significantly less feasible for **PPh₃** (**1** + **PPh₃**→**TS-1_{cis}/PPh₃**: $\Delta G^\ddagger = 122.8 \text{ kJ mol}^{-1}$). Therefore, pyrrolidone can be selectively vinyolated with **P(nBu)₃** at temperatures, where no activity or conversion is observed for **PPh₃** at all. The rate-determining reaction barrier for the vinylation of pyrrolidone with **PPh₃** is $154.4 \text{ kJ mol}^{-1}$ and the reaction could be facilitated by significantly increasing the reaction temperatures. It is assumed that the difference in activation barrier is caused by the electronic properties of the two phosphines. The positive inductive effect of the butyl group in **P(nBu)₃** leads to a significantly more electron rich phosphine, which should be more capable of stabilizing the cationic intermediates. Further analysis of the experimentally tested catalysts led to the same observation and to the assumption that steric effects do not play a significant role in determining activity.

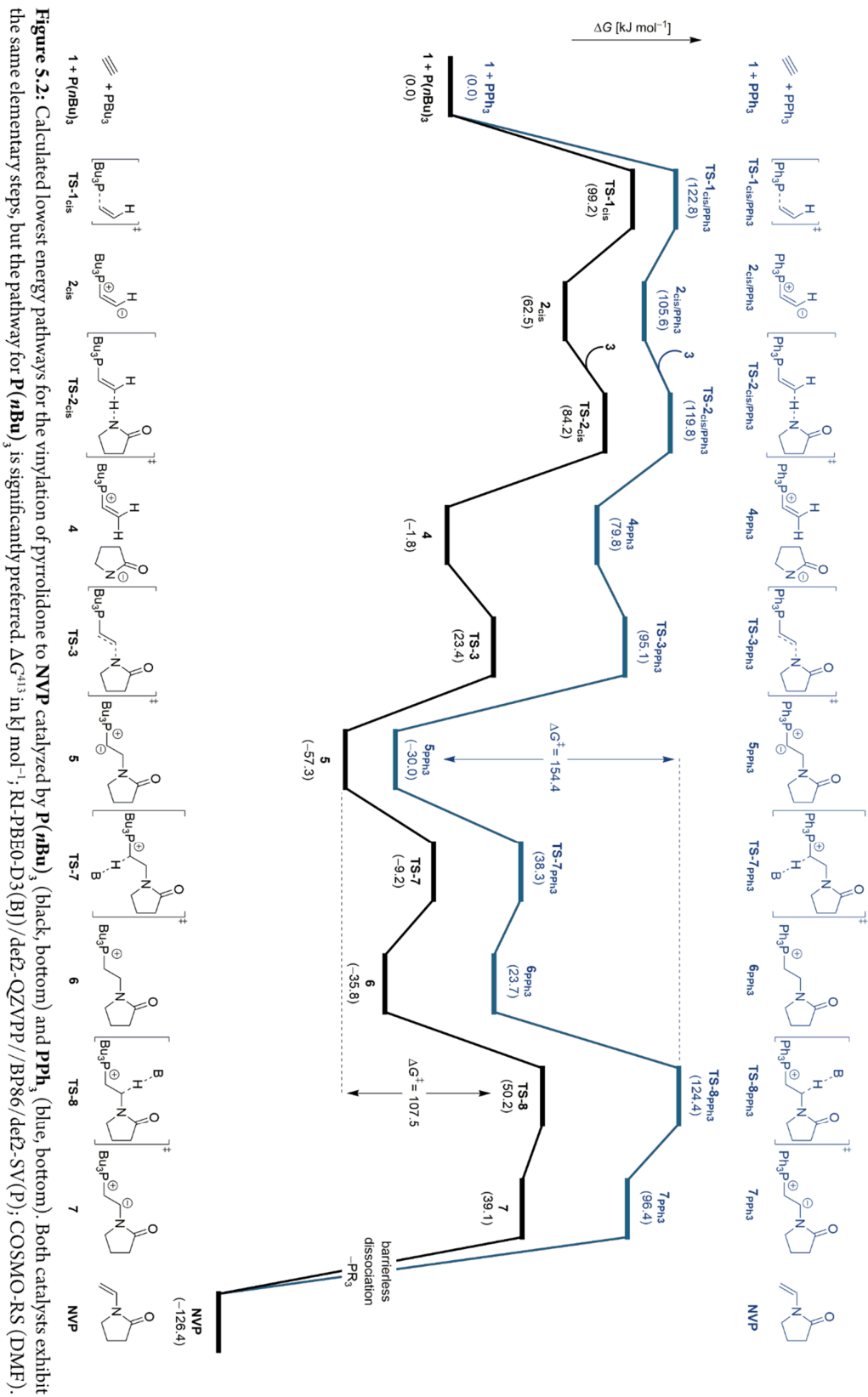
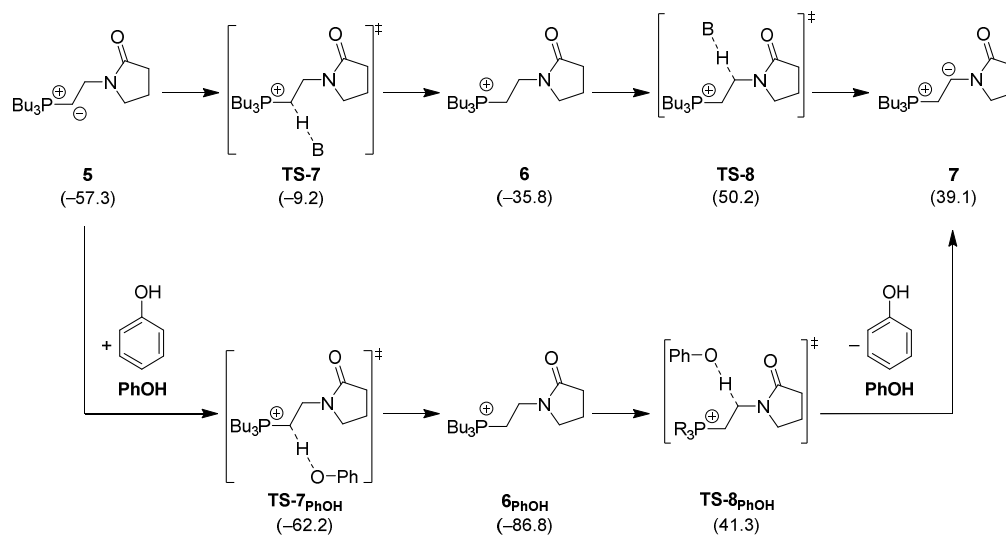


Figure S.2: Calculated lowest energy pathways for the vinylation of pyrrolidone to NVP catalyzed by P(nBu)₃ (black, bottom) and PPh₃ (blue, bottom). Both catalysts exhibit the same elementary steps, but the pathway for P(nBu)₃ is significantly preferred. ΔG^\ddagger in kJ mol⁻¹; RL-PBE0-D3(BJ)/def2-QZVPP//BP86/def2-SV(P); COSMO-RS (DMF).

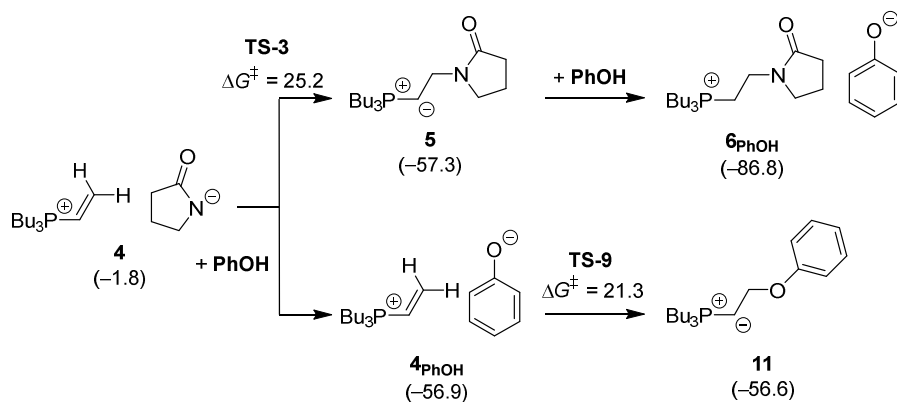
After the pathways for the nucleophilic reaction mechanism have been characterized and revealed that the rate-determining step is part of the protonation/deprotonation cascade, the possibility to tune this energy barrier by employing an additive was intriguing to the team. The addition of compounds, which might be more prone to reclaim a proton from the β position (after protonation at the α position), could lead to further improvement of the reaction methodology. For this reason, the protonation and deprotonation steps were recalculated for the use of phenol (**PhOH**) and are shown in Scheme 5.13. Protonation of **5** with **PhOH** takes place via **TS-7_{PhOH}** ($\Delta G^\ddagger = -62.2 \text{ kJ mol}^{-1}$) and leads to the highly stabilized intermediate **6_{PhOH}**, which is 29.5 kJ mol^{-1} more stable than ylide **5** (**6_{PhOH}**: $\Delta G^{413} = -86.8 \text{ kJ mol}^{-1}$). Subsequent transfer of the proton on the β carbon atom to the phenolate anion takes place in form of **TS-8_{PhOH}** ($\Delta G^\ddagger = 41.3 \text{ kJ mol}^{-1}$) and is – as intended – lower in energy than the pyrrolidone equivalent **TS-8** ($\Delta\Delta G^\ddagger = 8.9 \text{ kJ mol}^{-1}$). However, due to the highly stable nature of **6_{PhOH}**, the involvement of **PhOH** leads to an increase of the activation barrier from $107.5 \text{ kJ mol}^{-1}$ (**5**→**TS-8**) to $128.1 \text{ kJ mol}^{-1}$ (**6_{PhOH}**→**TS-8_{PhOH}**). Thus, the desired improvements by addition of **PhOH** are not expected to be observed in experiments.



Scheme 5.13: Investigation of the effect of phenol (**PhOH**) on the protonation-deprotonation cascade, which represents the rate-determining step of the catalytic cycle. The phenolate anion does lower the energy of transition state **TS-8** (to **TS-8_{PhOH}**) but leads to a significantly higher stabilization of intermediate **6** (to **6_{PhOH}**) leading to an overall increase in reaction barrier. ΔG^{413} in kJ mol^{-1} ; referenced to **1**, **3** and **P(*n*Bu)₃**; RI-PBE0-D3(BJ)/def2-QZVPP//BP86/def2-SV(P); COSMO-RS (DMF).

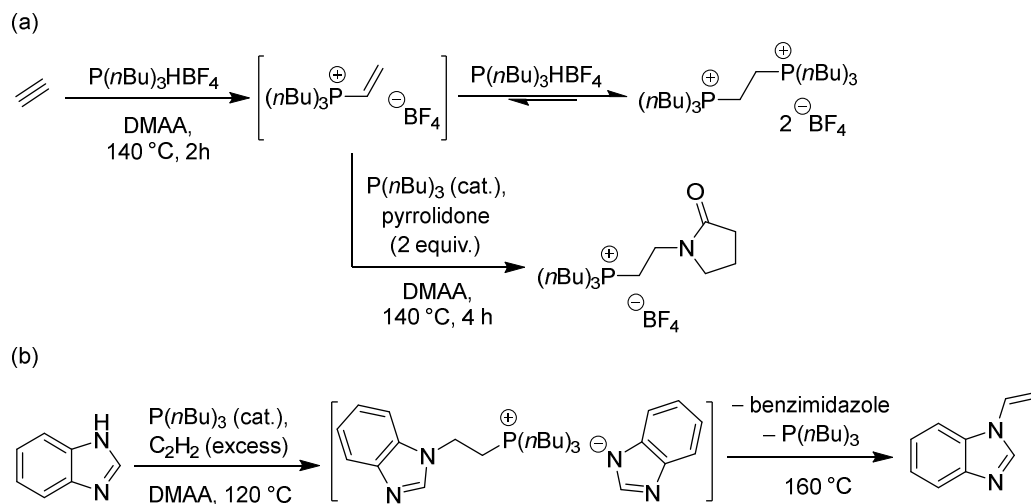
Because of the high stabilization of **6** by **PhOH**, an investigation into other phenol-based structures was carried out (see Scheme 5.14). Apart from the previously investigated pathway towards **6_{PhOH}** (readily accessible over **5**; see upper pathway), the anion exchange in **4** was of interest. The pyrrolidone anion is substituted by phenolate to form **4_{PhOH}**

($\Delta G^{413} = -56.9 \text{ kJ mol}^{-1}$), which is significantly more stable than the pyrrolidone system **4** ($\Delta\Delta G^{413} = -55.1 \text{ kJ mol}^{-1}$) and (within in the margin of error of DFT calculations) equally as stable as the ylide **5** ($\Delta G^{413} = -57.3 \text{ kJ mol}^{-1}$). Similar to the N- and O-addition of pyrrolidone in ion pair **4** (**TS-3** and **TS-4**, respectively), nucleophilic O-addition of the phenolate can take place with a barrier of 21.3 kJ mol^{-1} (**TS-9**) to form the alternative ylide species **11** ($\Delta G^{413} = -56.6 \text{ kJ mol}^{-1}$). Due to the reversible nature of all the reaction steps, an equilibrium formation of **6_{PhOH}**, which is significantly more stable than the other three species, is expected and potential follow-up reactions of ylide **11** were not investigated. This is also due to results that were obtained in the mechanistic experiments (see next paragraph), which indicated the formation of an entirely different phenol species, as well as the inherent limitation of the **PhOH** approach. While our attempts to employ **PhOH** solely focused on achieving a reduction of the rate-determining barrier (**5**→**TS-8**: $107.5 \text{ kJ mol}^{-1}$), the possible feasibility gain of this approach is also limited by the energy barrier of the activation of acetylene (**TS-1_{cis}**: $\Delta G^\ddagger = 99.2 \text{ kJ mol}^{-1}$), which is only 8.3 kJ mol^{-1} below the rate-determining step. As this activation is not necessarily affected by the addition of phenol, only small activity improvements could be achieved in an ideal scenario. However, the addition of another component to the system is also accompanied by various disadvantages: Firstly, apart from interacting with the components in the intended way, the additive can also interfere with any of the other reaction pathways and, thus, lead to the formation of unwanted side products and waste. Moreover, with such a small range for the possible activity gain, this improvement could most likely also be achieved by an adjustment of the reaction conditions. In contrast to the use of an additive, this is far less likely to require reconsideration of work-up procedures, component recycling strategies, and waste economy and therefore might present an easier, more economical, and more sustainable approach to process improvement.



Scheme 5.14: Overview of different intermediates and reaction pathways that were calculated to understand the effect of the addition of **PhOH** to the catalytic system. The previously investigated intermediate **6_{PhOH}** is the most stable species among the four intermediates. ΔG^{413} in kJ mol^{-1} ; referenced to **1**, **3** and **P(*n*Bu)₃**; RI-PBE0-D3(BJ)/def2-QZVPP//BP86/def2-SV(P); COSMO-RS (DMF).

After these extensive calculations on the nucleophilic reaction mechanism had been performed, the postdoctoral researcher carrying out all experimental aspects of this investigation, Nikolai Sitte, had attempted to characterize some of the proposed intermediates or potential follow-up products (see Scheme 5.15a). Initially, the generation of the vinyl phosphonium species (cf. computed structure **4**) was attempted by applying acetylene to a solution of the Brønsted acid-base adduct tri-*n*-butylphosphonium tetrafluoroborate ($P(nBu)_3HBF_4$). However, instead of the desired species, a dicationic bisphosphonium species could be characterized by NMR spectroscopy, mass spectrometry and X-ray crystallography (see Figure 5.3 and [CCDC 2090396](#)). Some examples of such species have been previously reported.²⁶⁷⁻²⁶⁸ This might occur when no suitable nucleophile is present to capture the highly reactive vinyl phosphonium species leading to the phosphine itself acting as nucleophile to generate the bisphosphonium species. Moreover, this indicates that the initial activation of acetylene by tri-*n*-butylphosphine does indeed take place as proposed by the quantum-chemical calculations. A similar behavior was observed for phenol, which also represents a Brønsted acidic but weakly nucleophilic species,²⁶⁹ although no crystal structure could be isolated in this case and the structural assignment is based on the similarity of the NMR spectra. The addition of catalytic amounts of phosphine and pyrrolidone to the dicationic species leads to formation of a tetraalkyl phosphonium compound (cf. computed intermediate **6**), which indicates that the dication represents an off-cycle species and can be reactivated when a suitable nucleophile is provided. Furthermore, this observation is well in line with the proposed mechanism, which proceeds over such an intermediate. In order to further investigate the completion of the catalytic cycle this transformation was tried again by employing benzimidazole, a nucleophile exhibiting a weaker basicity (see Scheme 5.15b).²⁷⁰ This procedure allowed the characterization of another tetraalkylphosphonium intermediate (cf. Scheme 5.15a and intermediate **6**) and the observation of the vinylation product after heating to 160 °C, which further supports the calculated catalytic pathways.



Scheme 5.15: (a) Mechanistic experiments with the use of $P(n\text{Bu})_3\text{HBF}_4$ to probe the initial activation steps of the nucleophilic reaction pathway and (b) experiments with benzimidazole to probe the last reaction step of the proposed catalytic cycle. All experiments were carried out by Nikolai Sitte at CaRLa.

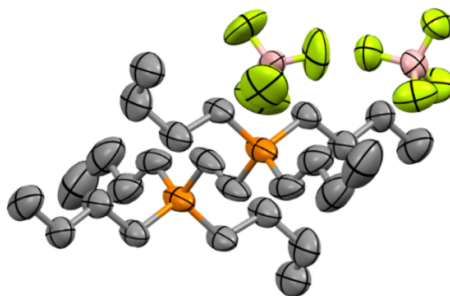
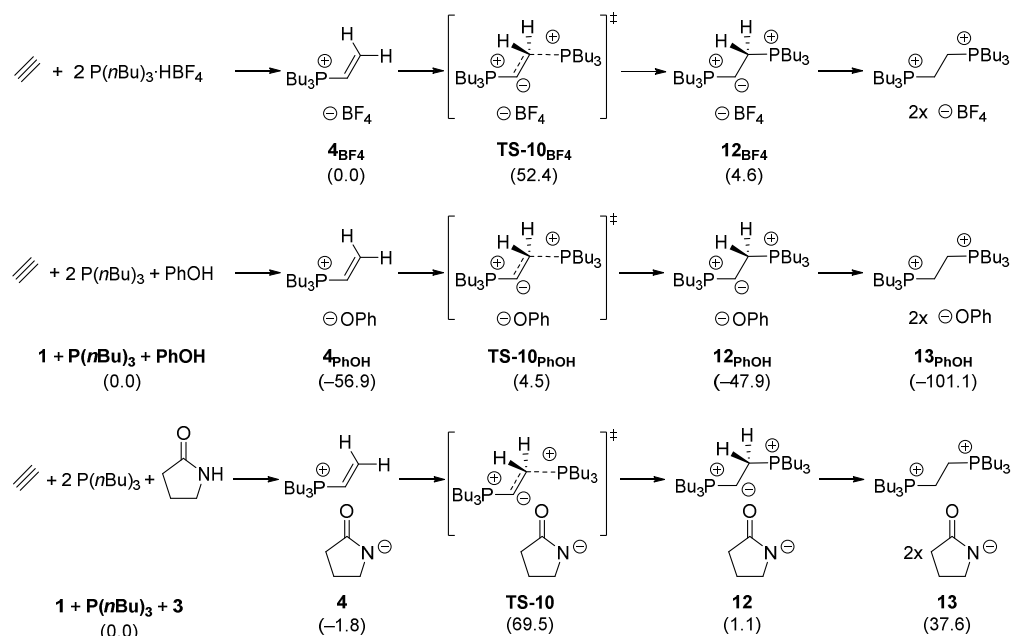


Figure 5.3: Crystal structure of the dicationic trialkyl ethylene bisphosphonium species (CCDC 2090396). Experiments and characterization were carried out by Nikolai Sitte and Frank Rominger.

In order to gain more insight into the generation of the dicationic bisphosphonium species (see Scheme 5.15a and Figure 5.3), the formation of this species was investigated for $P(n\text{Bu})_3\text{HBF}_4$, phenol (**PhOH**) and pyrrolidone (**3**) and is shown in Scheme 5.16. It should be noted that due to the complex way that would be required to (accurately) model the tetrafluoroborate adduct and the formation of the BF_4^- anion, the computational investigation was limited to the three intermediates that include a single anion. These calculations show that the addition of a second phosphine to $\mathbf{4}_{\text{BF}_4}$ can take place with a barrier of 52.4 kJ mol^{-1} (**TS-10** $_{\text{BF}_4}$). This leads to the formation of $\mathbf{12}_{\text{BF}_4}$ ($\Delta G^{413} = 4.6 \text{ kJ mol}^{-1}$), which requires protonation from the HBF_4 unit to yield the dicationic product. For **PhOH**, the whole reaction cascade was computed starting from acetylene (**1**), $P(n\text{Bu})_3$ and **PhOH**. Formation of the vinylphosphonium species is strongly exergonic as previously discussed in Scheme 5.14 ($\mathbf{4}_{\text{PhOH}}$: $\Delta G^{413} = -56.9 \text{ kJ mol}^{-1}$). The addition of a second equivalent of

P(*n*Bu)₃ is associated with a larger barrier of 61.4 kJ mol⁻¹ compared to the use of HBF₄ (**TS-10**_{PhOH}: $\Delta G^\ddagger = 4.5$ kJ mol⁻¹) but can still readily proceed at reaction conditions. From **12**_{PhOH} ($\Delta G^{413} = -47.9$ kJ mol⁻¹), which is formed by **TS-10**_{PhOH}, protonation from a second equivalent of **PhOH** leads to the formation of the dicationic bisphosphonium compound **13**_{PhOH} ($\Delta G^{413} = -101.1$ kJ mol⁻¹), which is significantly more stable than all previously computed phenol-based structures (cf. Scheme 5.14). This also is in good agreement with the experimental observation of this structure and with the low activity when **PhOH** is added to the catalytic system. Interestingly, while the dicationic species was characterized for the use of P(*n*Bu)₃HBF₄ and **PhOH**, no signs of this intermediate have been observed during countless experiments employing **3** or other suitable vinylation substrates, which could be easily assessed by recalculating the intermediates **12** and **13** as well as transition state **TS-10** for the use of **3**. Formation of **4** ($\Delta G^{413} = -1.8$ kJ mol⁻¹), which was discussed extensively in the previous sections, is slightly exergonic and sets the foundation for addition of the second phosphine unit via **TS-10** ($\Delta G^\ddagger = 69.5$ kJ mol⁻¹). Subsequent protonation of **12** ($\Delta G^{413} = 1.1$ kJ mol⁻¹) leads to the dicationic species **13** ($\Delta G^{413} = 37.6$ kJ mol⁻¹), which in contrast to its highly stable **PhOH** equivalent is significantly less stable than the reactants, than **4** or than the even more stable ylide intermediate (**5**: $\Delta G^{413} = -57.3$ kJ mol⁻¹; see Scheme 5.9 and Figure 5.2). This large difference between pyrrolidone anion and phenolate has also been observed in the investigation of phenol-containing species (see Scheme 5.14). All in all, these calculations provide a rationale for the different behavior of pyrrolidone, **PhOH** and P(*n*Bu)₃HBF₄. This is also an excellent example for the common limitations of mechanistic experiments, which require the use of alternative compounds to trap or stabilize on-cycle species. These substitute systems can lead to significant deviations to the behavior of the original substrate, which need to be carefully considered.



Scheme 5.16: Investigation of the addition of a second equivalent of phosphine to the activated acetylene intermediate. The addition is significantly favored for **PhOH**, but less feasible than the previously reported pathway when employing pyrrolidone (**3**). ΔG^{413} in kJ mol^{-1} ; RI-PBE0-D3(BJ)/def2-QZVPP//BP86/def2-SV(P); COSMO-RS (DMF).

With the intention to investigate the correlation of experimentally observed conversion/reaction yields and calculated activation barriers, this reaction mechanism was recalculated for the use of trimethylphosphine (**PMe₃**; see Figure 5.4). The initial activation step (**TS-1_{cis/PMe₃}**) is associated with an energy barrier of $102.7 \text{ kJ mol}^{-1}$, which is just slightly larger than the barrier for **P**(*n*Bu)₃ (**TS-1_{cis}**: $\Delta G^\ddagger = 99.2 \text{ kJ mol}^{-1}$) and leads to formation of **2_{cis/PMe₃}** ($\Delta G^{413} = 75.8 \text{ kJ mol}^{-1}$). The ion pair **4_{PMe₃}** ($\Delta G^\ddagger = 20.9 \text{ kJ mol}^{-1}$) is formed via proton transfer **TS-2_{cis/PMe₃}** ($\Delta G^{413} = 103.9 \text{ kJ mol}^{-1}$) and can continue along the reaction pathway by nucleophilic addition of the pyrrolidone anion to the vinyl phosphonium cation (**TS-3_{PMe₃}**: $\Delta G^\ddagger = 49.9 \text{ kJ mol}^{-1}$). Interestingly, this is the only of the three phosphine catalysts where the proton transfer transition state is less feasible than the acetylene activation step. However, this difference is very small (within the error margin of DFT) and the *trans*-configured reaction pathway over **TS-1_{trans/PMe₃}**, **2_{trans/PMe₃}** and **TS-2_{trans/PMe₃}** – similar to **P**(*n*Bu)₃ and **PPh₃** – stays associated with a higher activation barrier than the *cis* pathway (**TS-1_{trans/PMe₃}**: $\Delta G^\ddagger = 131.1 \text{ kJ mol}^{-1}$; **2_{trans/PMe₃}**: $\Delta G^{413} = 62.5 \text{ kJ mol}^{-1}$; **TS-2_{trans/PMe₃}**: $\Delta G^\ddagger = 68.1 \text{ kJ mol}^{-1}$). The nucleophilic addition leads to ylide **5_{PMe₃}** ($\Delta G^{413} = -51.1 \text{ kJ mol}^{-1}$), which serves as precursor for the unassisted (**TS-6_{PMe₃}**) and pyrrolidone-assisted hydrogen shift (**TS-7_{PMe₃}**→**6_{PMe₃}**→**TS-8_{PMe₃}**). The assisted pathway is significantly more feasible with a barrier of $128.3 \text{ kJ mol}^{-1}$ (**5_{PMe₃}**→**TS-8_{PMe₃}**) compared to a barrier of over 200 kJ mol^{-1} for **TS-6_{PMe₃}** ($\Delta G^\ddagger = 226.9 \text{ kJ mol}^{-1}$). Both pathways culminate in species **7_{PMe₃}**

($\Delta G^{413} = 59.8 \text{ kJ mol}^{-1}$), from which barrierless dissociation of **PMe₃** leads to the formation of the desired product (**NVP**: $\Delta G^{413} = -126.4 \text{ kJ mol}^{-1}$). A comparison of the calculated reaction barriers of **P(*n*Bu)₃**, **PMe₃** and **PPh₃** ($\Delta G^\ddagger = 107.5, 128.3$ and $154.5 \text{ kJ mol}^{-1}$, respectively) correlates well with the experimentally observed reaction yields (**P(*n*Bu)₃**: 98% conversion, 79% yield; **PMe₃**: 95% conversion, 74% yield; **PPh₃**: 5% conversion, 4% yield; 10 mol% catalyst, DMAA 16 h, 140 °C; see the full publication for the experimental investigations).²⁶⁴ While the energetic differences between **P(*n*Bu)₃** and **PMe₃** might suggest a more drastic drop in activity, the overall trend is well reproduced. The similarity between the experimental results for **P(*n*Bu)₃** and **PMe₃** could be caused by the very similar energies for acetylene activation with the two catalysts (99.2 kJ mol^{-1} vs. $102.7 \text{ kJ mol}^{-1}$), after which the ylide **5** (or **S_{PMe₃}**) should be readily formed. From the ylide, reverse reaction to **1** and **3** is significantly less feasible than the completion of the catalytic cycle (for **PMe₃**: $153.8 \text{ kJ mol}^{-1}$ vs. $128.3 \text{ kJ mol}^{-1}$), which might lead to slow formation of **NVP**. This could be probed by comparing kinetic parameters for the two reactions.

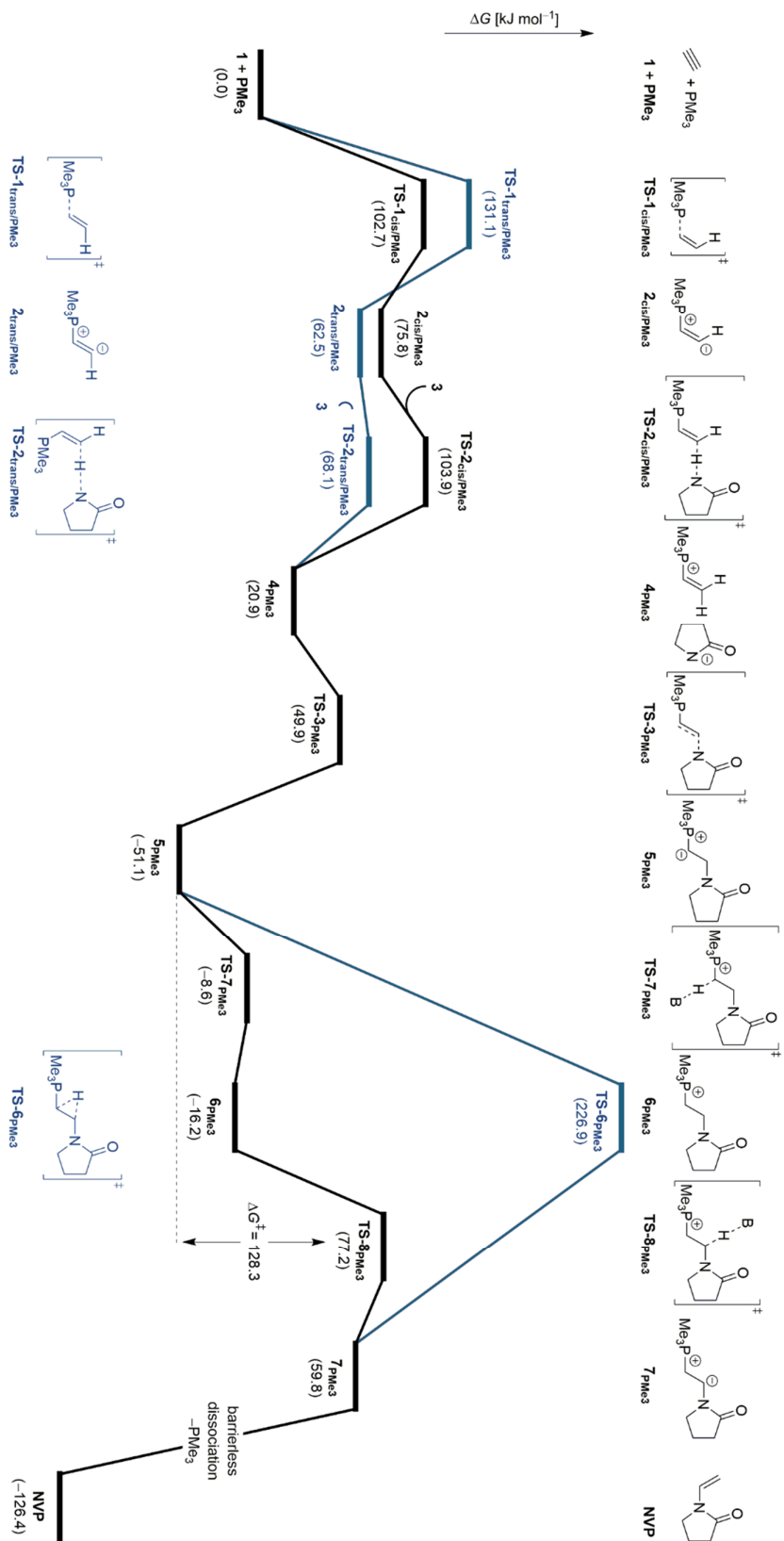
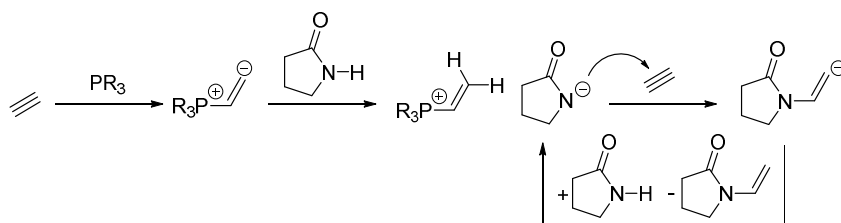


Figure 5.4: Calculated lowest energy pathway for the vinylation of pyrrolidone (3) to NVP catalyzed by PMe_3 (black). Alternative pathways that exhibit higher energies such as the *trans*-configured acetylene activation pathway and the unassisted H-shift are shown in blue. ΔG^{\ddagger} in kJ mol^{-1} ; RI-PBE0-D3(BJ)/def2-QZVP//BP86/def2-SV(P); COSMO-RS (DMF).

5.3.2 Investigation of the Reppe-type Mechanism

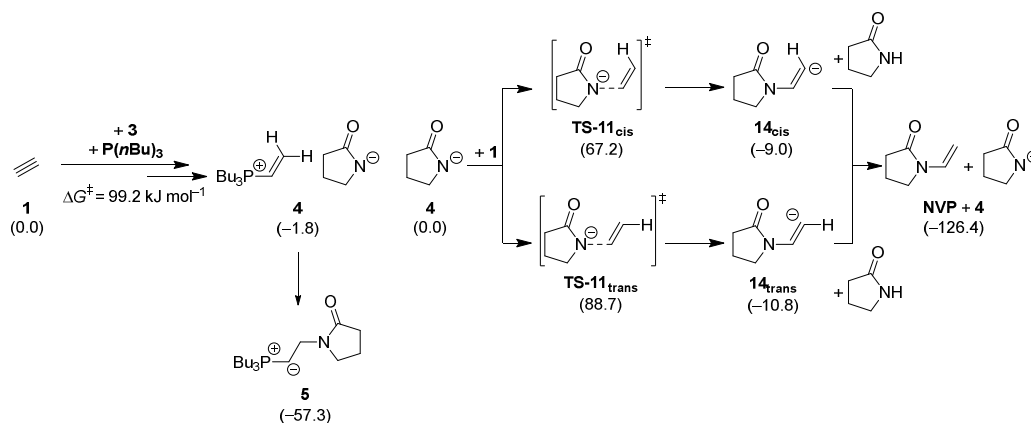
In addition to the calculations dealing with the nucleophilic reaction mechanism, a Reppe-type base-induced reaction pathway was also considered (see Scheme 5.17), which was designed based on previous suggestions.^{261,271} Similar to the nucleophilic pathway in Section 5.3.1, the Reppe-type pathway starts with the activation of acetylene by the employed phosphine and the NH proton transfer from pyrrolidone to the intermediate to form the vinyl phosphonium species. Instead of the nucleophilic addition of the pyrrolidone anion to vinyl phosphonium, the Reppe-type pathway further proceeds via the activation of a second unit of acetylene by the pyrrolidone anion. The formed NVP anion can be protonated by a second pyrrolidone molecule, which leads to simultaneous formation of the desired product, NVP, and regeneration of the active species, the pyrrolidone anion.



Scheme 5.17: General reaction scheme for the Reppe-type reaction pathway.

As the initial activation steps (**1**→**TS-1_{cis}**→**2_{cis}**→**TS-2_{cis}**→**4**) are identical to the acetylene activation pathways in the nucleophilic reaction mechanism, the feasibility and selectivity of these transformations have already been discussed extensively (see Schemes 5.7 and 5.8) and will only be briefly touched upon here. The activation proceeds over a *cis*-type pathway to ion pair **4** and is accessible via a reaction barrier of 99.2 kJ mol⁻¹ (see Scheme 5.18). The pyrrolidone anion in **4** sets the basis for the Reppe-type reaction pathway as it activates another equivalent of acetylene (**1**). One should note that in the subsequent calculations the cation was omitted and the approximative assumption was taken that the cation equally interacts/stabilizes all intermediates and transition states in this pathway. Considering the size of the ion pair, it would have been possible to compute the complete system, however, with no possibility to ensure that the most stabilizing interaction is found, this could also lead to an increase in error compared to the simple neglect of the cation. From **4**, activation of a second molecule of **1** can, similarly to the initial activation of **1**, occur in *cis* and *trans* configurations. Once more, the *cis*-configured reaction pathway, which takes place via **TS-11_{cis}** ($\Delta G^\ddagger = 67.2$ kJ mol⁻¹), is found to be more stable than its *trans*-configured counterpart (**TS-11_{trans}**: $\Delta G^\ddagger = 88.7$ kJ mol⁻¹; $\Delta\Delta G^\ddagger = 21.5$ kJ mol⁻¹). These transition states lead to **14_{cis}** and **14_{trans}** (-9.0 and -10.8 kJ mol⁻¹, respectively), of which **14_{trans}** once more represents the more stable intermediate following a less feasible transition state. Proton transfer from **3** to **14_{cis}** or **14_{trans}** leads to the formation of **NVP** and intermediate **4**, which

represents the on-cycle species of this catalytic cycle ($\Delta G^{413} = -126.4 \text{ kJ mol}^{-1}$). When evaluating the feasibility of this reaction, it is crucial to consider that the nucleophilic addition pathways are still available and strongly preferred over **TS-11_{cis}** and **TS-11_{trans}**. Therefore, the equilibrium between **4** and **5** would be expected to be (nearly) exclusively in favor of the ylide drastically increasing the barrier for the Reppe-type pathways.



Scheme 5.18: Investigation of the Reppe-type reaction pathways for the vinylation of pyrrolidone (**3**) to **NVP**. ΔG^{413} in kJ mol^{-1} ; RI-PBE0-D3(BJ)/def2-QZVPP//BP86/def2-SV(P); COSMO-RS (DMF).

For better comparability, the lowest energy pathways for the nucleophilic and Reppe-type reaction mechanisms are visualized in Figure 5.5. This allows a quick identification of the favored transition states and intermediates around intermediate **4**, where the reaction pathways split into the nucleophilic addition leading to **5** (black pathway) and the Reppe-type transformation leading to **14_{cis}** (blue pathway). It is also well suited for the comparison of the rate-determining steps of the two pathways, nucleophilic and Reppe-type mechanism ($\Delta G^\ddagger = 107.5$ and $126.3 \text{ kJ mol}^{-1}$, respectively), which shows that the nucleophilic reaction pathway is significantly more feasible and responsible for the observed product formation. This is also in good agreement with the observation that non-phosphine bases did not exhibit any catalytic activity, which indicates the importance of a phosphine-induced activation step.

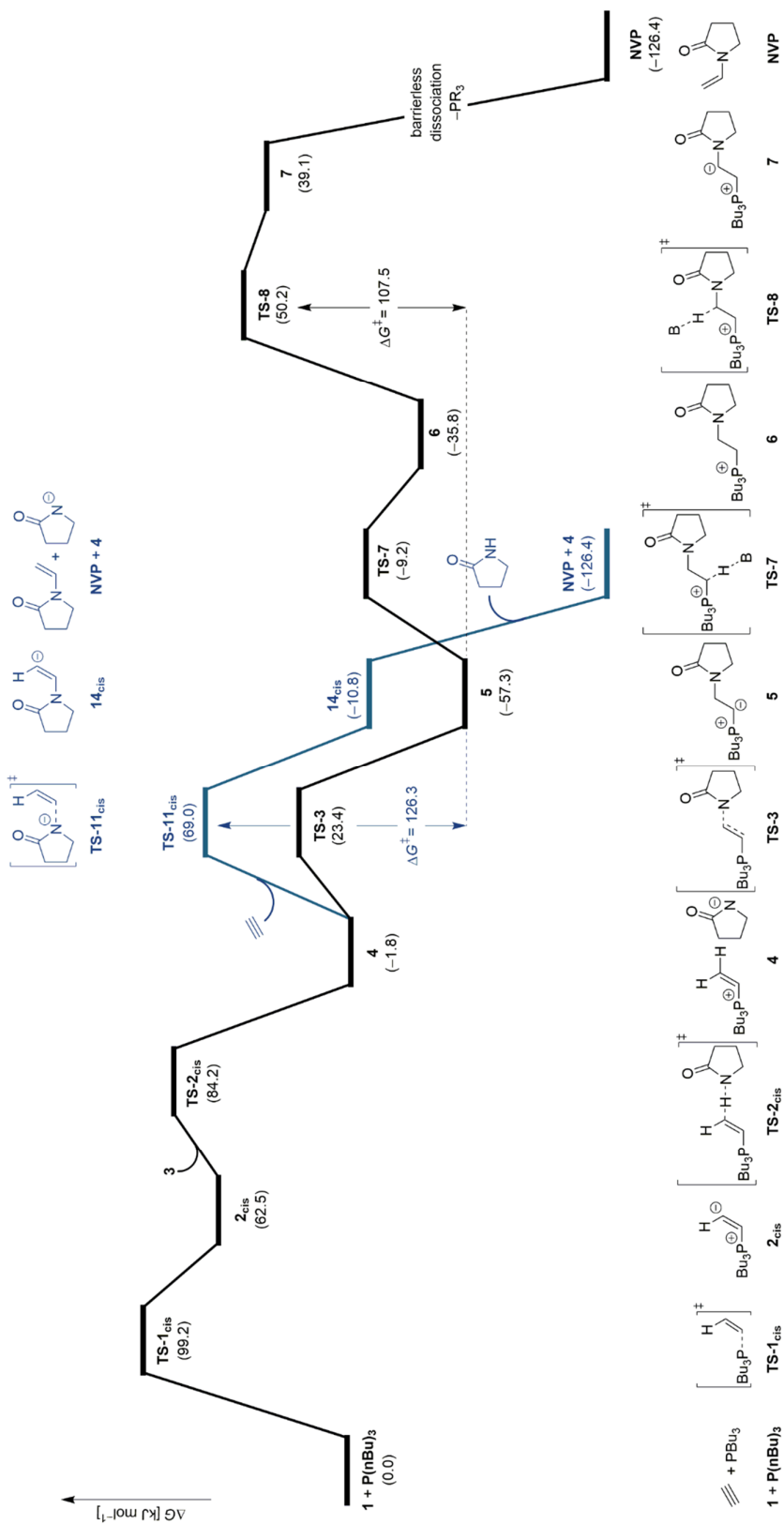
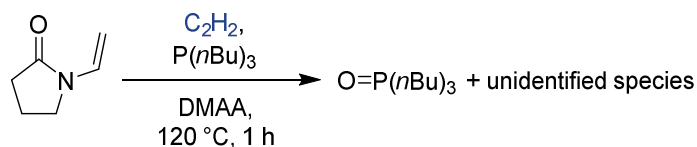


Figure S.5: Lowest energy pathways for the nucleophilic reaction mechanism (black) and the Repepe-type pathway (blue) in the vinylation of pyrrolidone (3) to NVP. ΔG^\ddagger in kJ mol^{-1} ; RI-PBE0-D3(BJ)/def2-QZVPP//BP86/def2-SV(P); COSMO-RS (DMF).

5.3.3 Wittig-type Extended Schweizer Reaction

Throughout the experimental investigations, the formation of phosphine oxide ($\text{OP}(n\text{Bu})_3$) was regularly observed. Initially, this was attributed to the identification of impurities in the acetylene gas such as acetone, however, subsequent purification did not resolve these problems. The assumption was made that this species is formed via Wittig-type reaction pathways during the nucleophilic reaction mechanism, which was discussed in detail above. To further counteract this unwanted formation, the formyl-containing solvent dimethylformamide (DMF), that had been employed in early screenings, was substituted with dimethylacetamide (DMAA), which is expected to be significantly less reactive towards Wittig-type transformations. Because the computational studies had already significantly advanced when this change of solvent was undertaken, the calculations continued to use DMF in the implicit solvent correction method COSMO-RS. Unfortunately, the change of solvent also did not fully suppress the formation of phosphine oxide. Thus, the involvement of the carbonyl groups in the substrate, in pyrrolidone, and in the product, NVP, had to be assumed. This culminated in a control experiment in which NVP, together with acetylene and the phosphine catalyst, was heated to reaction conditions for one hour (see Scheme 5.19). The experiment revealed the formation of phosphine oxide even when no substrate is present in the reaction mixture. Therefore, NVP itself must be reactive towards the mixture of acetylene and $\text{P}(n\text{Bu})_3$, which was shown to be responsible for the initial activation step of the nucleophilic reaction mechanism (see Section 5.3.1).



Scheme 5.19: Control experiment with NVP, acetylene, and $\text{P}(n\text{Bu})_3$. Heating the mixture to reaction conditions leads to the formation of phosphine oxide and further unidentified species. All experiments were carried out by Nikolai Sitte at CaRLa.

To understand the underlying processes, especially as it was not possible to identify any species besides phosphine oxide experimentally, and to evaluate whether reducing phosphine oxide formation is possible, the Wittig-type reaction pathways were investigated with DFT (see Figure 5.6). In this investigation, the reaction pathways were calculated for pyrrolidone (**3**; black, top pathway) and **NVP** (blue, bottom pathway) to understand whether the formation of phosphine oxide will only occur after conversion to **NVP** is completed or whether it can be directly formed from the substrate. As with previously studied pathways the activation of acetylene (**1**) by $\text{P}(n\text{Bu})_3$ represents the initial reaction step (**TS-1_{cis}**: $\Delta G^\ddagger = 99.2$ and -27.2 kJ mol^{-1} for **3** and **NVP**, respectively) and leads to **2_{cis}** ($\Delta G^{413} = 62.5$ and -63.9 kJ mol^{-1} for **3** and **NVP**, respectively). As this reaction does also occur without the

presence of **3** (*vide supra*), the possible proton transfer from **3** to **2_{cis}** (via **TS-2_{cis}**; see Scheme 5.7) was neglected initially and alternative pathways were explored. A similar proton transfer to **TS-2_{cis}** is also possible with **1** leading to **TS-12** ($\Delta G^\ddagger = 73.7$ and -52.7 kJ mol⁻¹ for **3** and **NVP**, respectively). This generates ion pair **15** ($\Delta G^{413} = 16.3$ and -110.1 kJ mol⁻¹ for **3** and **NVP**, respectively), which, similar to the previous protonation/deprotonation cascade (see Scheme 5.12), can be deprotonated in *a* position to generate ylide species **16** ($\Delta G^{413} = 9.5$ and -116.9 kJ mol⁻¹ for **3** and **NVP**, respectively) via **TS-13** ($\Delta G^\ddagger = 38.3$ and -88.1 kJ mol⁻¹ for **3** and **NVP**, respectively). At this point, the addition of **3** or **NVP** to the reaction intermediate will take place and the pathways will stop running in parallel. Addition of **3** to **16** proceeds over **TS-14** with an activation barrier (relative to **1**, **P(*n*Bu)₃**, and **3**) of 114.5 kJ mol⁻¹. This leads to **17** ($\Delta G^{413} = 29.0$ kJ mol⁻¹), which already exhibits a significant P–O interaction and can eliminate phosphine oxide (**OP(*n*Bu)₃**) via **TS-15** ($\Delta G^\ddagger = 101.9$ kJ mol⁻¹) to form the strongly exergonic allene product **18** ($\Delta G^{413} = -93.4$ kJ mol⁻¹). This pathway is less feasible than the nucleophilic vinylation pathway ($\Delta G^{413} = 107.5$ kJ mol⁻¹; see Figure 5.2), which is in good agreement with only small amounts of phosphine oxide being formed compared to quantitative formation that would be expected if this reaction pathway would be more stable than the vinylation. For **NVP**, the reaction proceeds via addition transition state **TS-14_{NVP}** ($\Delta G^\ddagger = -38.8$ kJ mol⁻¹) to **17_{NVP}** ($\Delta G^{413} = -112.3$ kJ mol⁻¹). Finally, rate-determining phosphine oxide elimination takes place with a barrier of 103.1 kJ mol⁻¹ to yield **18_{NVP}** (**TS-16_{NVP}**: $\Delta G^\ddagger = -23.3$ kJ mol⁻¹; **18_{NVP}**: $\Delta G^{413} = -235.3$ kJ mol⁻¹). This suggests that this degradation pathway is slightly more feasible than the vinylation and occurs in more significant amounts than observed experimentally. However, as with the Reppe-type pathway, one has to consider that formation of ylide **5**, which is part of the nucleophilic pathway, from **1**, **P(*n*Bu)₃**, and **3** is possible as long as **3** is available in the reaction mixture. The formation of **5** is associated with only a small barrier (see Figure 5.2) and significantly reduces the formation of **18** and **18_{NVP}** (and phosphine oxide). The interwoven nature of these mechanisms makes it difficult to precisely correlate the activation barriers to the observed amounts of side product. Moreover, drawing this correlation is inhibited by the fact that experimental characterization of the highly reactive allene species was not possible as follow-up reactions are expected. The only species that could be observed is phosphine oxide, which could be formed via a combination of multiple pathways. In any case, the Wittig-type reaction pathways provide an important rationale for the formation of phosphine oxide and suggest that a high concentration of substrate could be helpful to reduce side product formation by pushing the equilibrium towards **5** and the vinylation steps. Furthermore, the calculations indicate that stopping the reaction in time is crucial to reduce degradation. It also becomes clear that the potential for adjustments by adapting acetylene and phosphine concentrations is rather low as all pathways proceed over the same activation step and are similarly affected by these changes.

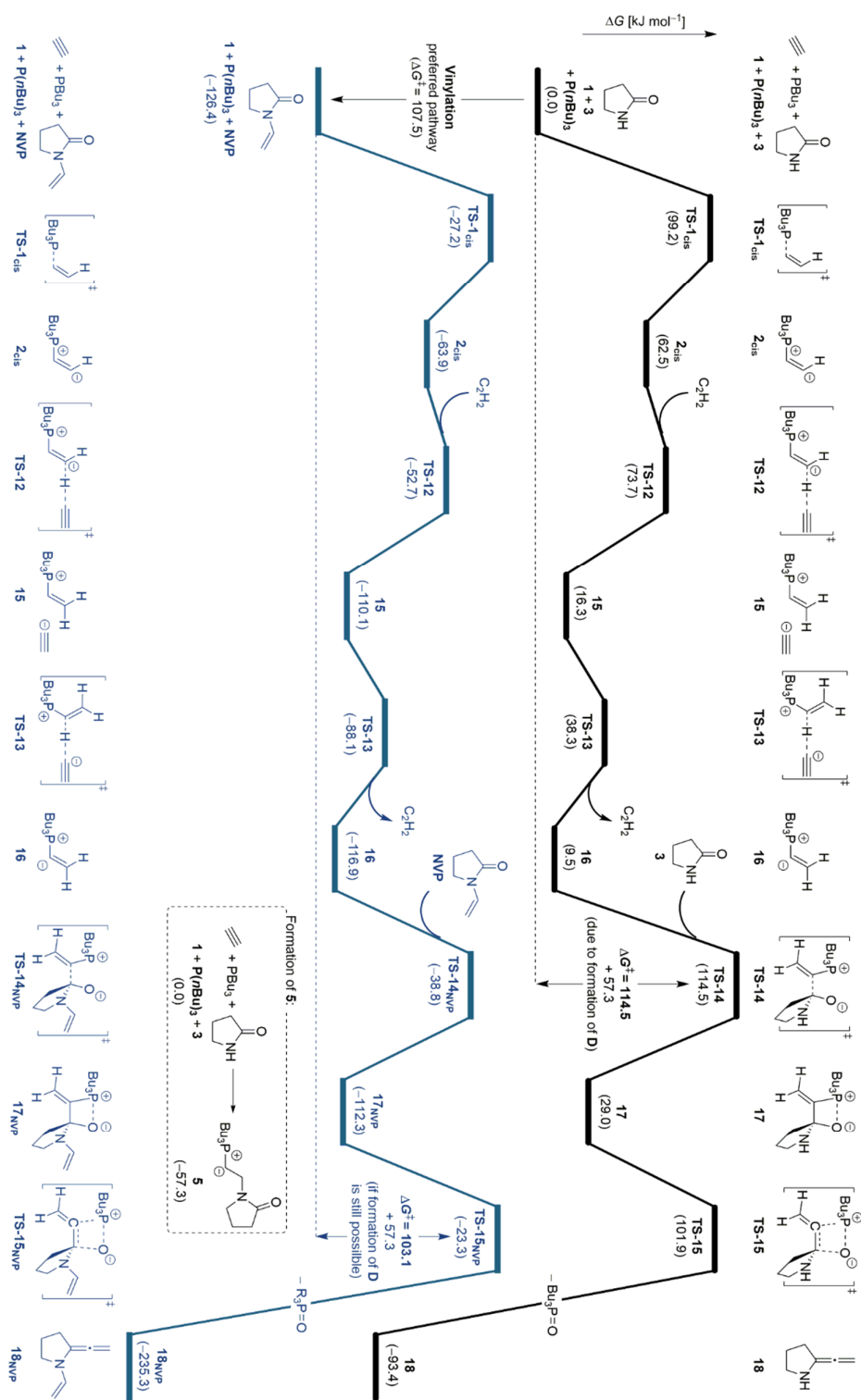
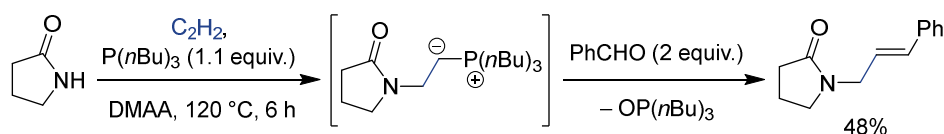


Figure 5.6: Calculated lowest energy pathway for the Wittig-type reaction of **3** (black, top) and the vinylation product **NVP** (blue, bottom) leading to allene products. ΔG^\ddagger in kJ mol^{-1} ; RI-PBEO-D3(BJ)/def2-QZVP//BP86/def2-SV(P); COSMO-RS (DMF).

To further test the hypothesis of Wittig pathways, the addition of benzaldehyde to the catalytic system was tested experimentally (see Scheme 5.20). For this, an excess of benzaldehyde was added to an equimolar mixture of pyrrolidone and $P(nBu)_3$ with acetylene and heating of this reaction mixture led to the formation of the Wittig product *N*-cinnamylpyrrolidone, which is proposed to be formed via the calculated ylide intermediate. The addition of nucleophiles to vinyl phosphonium salts to generate ylides was first reported by Edward E. Schweizer *et al.*²⁷² in 1966 and has subsequently been used synthetically.²⁷³⁻²⁷⁴ However, the approach presented here allows for the *in-situ* formation of the vinyl phosphonium species, which should significantly broaden the scope of the reaction (e.g., to unstable phosphonium species where salt formation/isolation cannot be achieved) and does not require two separate reaction steps.



Scheme 5.20: Reaction scheme for the addition of benzaldehyde to the catalytic system in order to form the Wittig product *N*-cinnamylpyrrolidone via the ylide intermediate. All experiments were carried out by Nikolai Sitte at CaRLa.

This alternative methodology employing Wittig-type/Schweizer-type concepts was also computationally studied to compare this functionalization approach to the undesired side reaction discussed before (see Figure 5.6). For this, the addition of benzaldehyde to ylide **5** was studied, which is the expected intermediate in the observed formation of *N*-cinnamylpyrrolidone (see Figure 5.7). The formation of ylide **5**, which was extensively discussed before, is associated with an energy barrier of 99.2 kJ mol^{-1} (**TS-1**_{cis}; see Schemes 5.7 and 5.9). Addition of benzaldehyde (**19**) can occur in two configurations leading either to the *cis* or *trans* configured double bond in final product **22**_{cis}/**22**_{trans}. The naming of the calculated intermediates and transition states is based on the configuration of the product that is afforded on the reaction pathway. Furthermore, addition can take place either with an *eclipse* or *gauche* conformation of the phosphorus and oxygen atoms, which will need to be able to form an interaction for the subsequent phosphine oxide elimination. Addition to the *trans*-configured reaction product take place via **TS-16**_{trans} in an *eclipse* conformation ($\Delta G^\ddagger = -11.9\text{ kJ mol}^{-1}$; black pathway) leading to **21**_{trans}, which exhibits a phosphorus-oxygen interaction in accordance with the *eclipse* conformation ($\Delta G^{413} = -61.7\text{ kJ mol}^{-1}$). Product formation takes place via phosphine oxide elimination transition state **TS-17**_{trans} with an effective barrier of 87.7 kJ mol^{-1} (**22**_{trans}: $\Delta G^{413} = -256.9\text{ kJ mol}^{-1}$). Alternatively, the pathway forming the *cis* product proceeds over the *gauche* addition of **19** (**TS-16**_{cis}: $\Delta G^\ddagger = -20.0\text{ kJ mol}^{-1}$; blue pathway) to the intermediate **20**_{cis} ($\Delta G^{413} = -47.4\text{ kJ mol}^{-1}$). The *trans-gauche* and *cis-eclipse* configuration could not be located and equally led to the reported

transition states. The rotation from *gauche* intermediate **20**_{cis} to *eclipse* intermediate **21**_{cis} was shown to be barrierless by a torsion angle scan. Subsequently, **21**_{cis} ($\Delta G^{413} = -66.7 \text{ kJ mol}^{-1}$) can eliminate **OP**(*n*Bu)₃ with a barrier of 98.4 kJ mol^{-1} (**TS-17**_{cis}) to form the *cis* product (**22**_{cis}; $\Delta G^{413} = -241.5 \text{ kJ mol}^{-1}$). With a barrier of 87.7 kJ mol^{-1} for **TS-17**_{trans}, this Wittig pathway is favored over the vinylation pathway (**TS-8**: $\Delta G^\ddagger = 107.5 \text{ kJ mol}^{-1}$), which is in good agreement with the significant amount of observed *N*-cinnamylpyrrolidone when benzaldehyde is added to the reaction mixture. The quantum-chemical calculations show that the formation of the *trans* product (**22**_{trans}) is kinetically and thermodynamically favored of the *cis* product (**22**_{cis}).

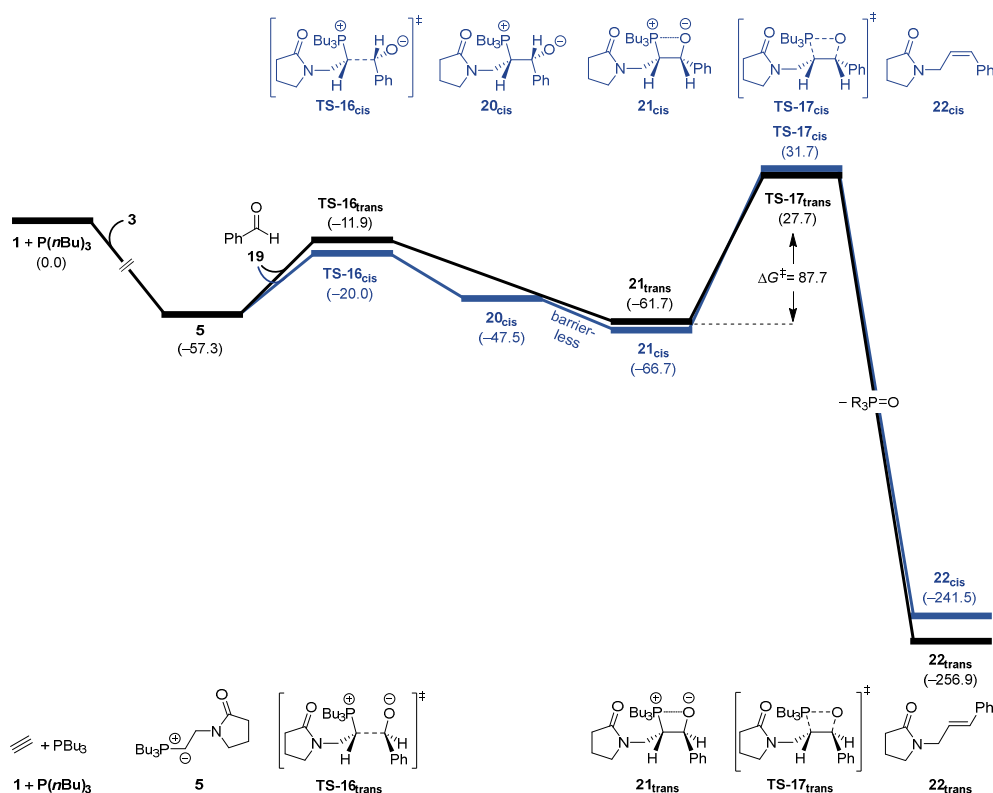
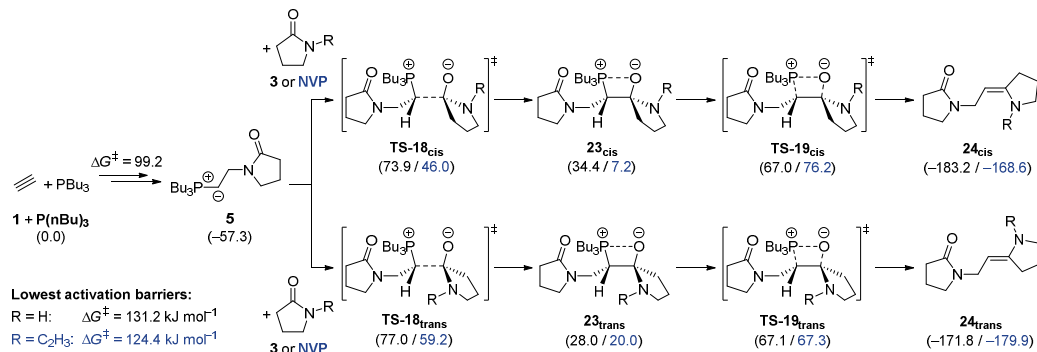


Figure 5.7. Reaction pathways for the formation of **21**_{cis}/**21**_{trans} via the Wittig-type addition of benzaldehyde to ylide **5**, which is an important intermediate in the nucleophilic vinylation pathway to **NVP**. ΔG^{413} in kJ mol^{-1} ; RI-PBE0-D3(BJ)/def2-QZVPP//BP86/def2-SV(P); COSMO-RS (DMF).

The combined results of the ylide **5** (with benzaldehyde **19**; see Figure 5.7) and **3**/**NVP** (with ylide **16**, see Figure 5.6) being able to react in these Wittig-type pathways raised the question whether similar reaction steps involving **5** and **3**/**NVP** could serve as an additional degradation/dimer formation pathway (see Scheme 5.21). Formation of ylide **5** will take place via the same pathway as for all previous pathways (**TS-1**_{cis}: $\Delta G^\ddagger = 99.2 \text{ kJ mol}^{-1}$; see Schemes 5.7 and 5.9). Subsequent reaction pathways can again either lead to the *cis* or *trans* product (**24**_{cis}/**24**_{trans}) and can proceed via *eclipse* and *gauche* conformation. However, only

eclipse-type intermediates could be located, and optimization attempts for *gauche* structures led to the more stable *eclipse* conformations. Addition to **5** takes place via **TS-18**_{cis} ($\Delta G^\ddagger = 73.9$ and 46.0 kJ mol⁻¹ for **3** and **NVP**, respectively) or **TS-18**_{trans} ($\Delta G^\ddagger = 77.0$ and 59.2 kJ mol⁻¹ for **3** and **NVP**, respectively). The formed *eclipse*-type structures (with an incorporated P–O contact) **23**_{cis} ($\Delta G^{413} = 34.4$ and 7.2 kJ mol⁻¹ for **3** and **NVP**, respectively) and **23**_{trans} ($\Delta G^{413} = 28.0$ and 20.0 kJ mol⁻¹ for **3** and **NVP**, respectively) can eliminate **OP**(*n***Bu**)₃ via **TS-19**_{cis} ($\Delta G^\ddagger = 67.0$ and 76.2 kJ mol⁻¹ for **3** and **NVP**, respectively) and **TS-19**_{trans} ($\Delta G^\ddagger = 67.1$ and 67.3 kJ mol⁻¹ for **3** and **NVP**, respectively). These lead to the formation of **24**_{cis} ($\Delta G^{413} = -183.2$ and -168.6 kJ mol⁻¹ for **3** and **NVP**, respectively) and **24**_{trans} ($\Delta G^{413} = -171.8$ and -179.9 kJ mol⁻¹ for **3** and **NVP**, respectively). Like the previous comparison of Wittig-type reactivity of **3** and **NVP** (see Figure 5.6), the activation barrier for **NVP** is once more significantly lower than the barrier for **3**. However, both, the lowest energy barriers for the Wittig reaction of **5** with **3** or **NVP**, are significantly less feasible than the nucleophilic vinylation pathway or the degradation pathway to allene products shown in Figure 5.6. Therefore, these reaction pathways are not expected to be populated in this catalytic system. One should note that this reaction pathway could also under no circumstances be responsible for the formation of phosphine oxide observed in the control experiment with **NVP**, acetylene (**1**) and **P**(*n***Bu**)₃ (see Scheme 5.19) as the generation of ylide **5** requires the presence of pyrrolidone (**3**).



Scheme 5.21: Reaction pathway for the Wittig-type dimerization based on ylide **5** and pyrrolidone (**3**) (R=H; black) or **NVP** (R=C₂H₅; blue). ΔG^{413} in kJ mol⁻¹; RI-PBE0-D3(BJ)/def2-QZVPP//BP86/def2-SV(P); COSMO-RS (DMF).

Kinetic investigations were performed in order to validate the above presented calculated mechanisms for the phosphine oxide formation pathways. Initially, the amounts of substrate and product, pyrrolidone and NVP, respectively, were measured over the course of five hours (see Figure 5.8a; solid lines). The experiments revealed a steady conversion of pyrrolidone to NVP, which is accompanied by a (significantly smaller) decrease in the sum of both components (dashed line) indicating the formation of other species. This is in good agreement with the proposed minor formation of allene products (*vide supra*). However,

more interestingly, these experiments also revealed that the amount of $P(nBu)_3$ significantly dropped over the course of the reaction while only small amounts of $OP(nBu)_3$ are formed (see Figure 5.8b; solid lines, circled data points). This was repeated in an experiment where only acetylene and phosphine catalyst $P(nBu)_3$ were employed, which showed the same overall loss of phosphine (squared data points). In contrast to the previous experiment with all components, the control experiment did not show any buildup of $OP(nBu)_3$, which is in accordance with the proposed degradation pathways that required the presence of pyrrolidone or NVP and led to the conclusion that another degradation mechanism must be at play here. To explain this significant loss of phosphorus in solution (dashed lines), the reaction mixture was analyzed. Experimental attempts to characterize the formed species were not successful, but small amounts of a brown residue in combination with the reaction components were interpreted as a possible formation of cuprene, an undefined acetylene polymer,²⁷⁵ which could be formed by phosphine-induced polymerization.

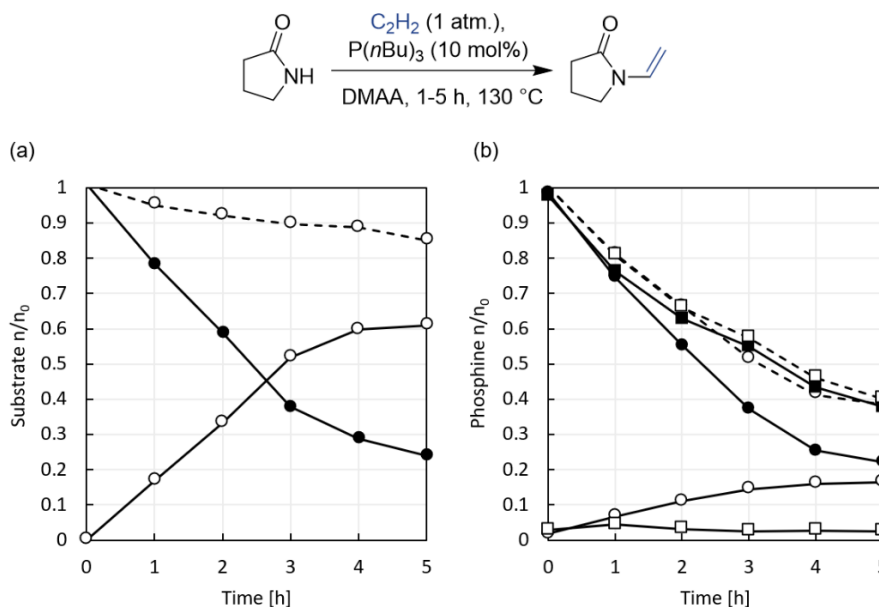
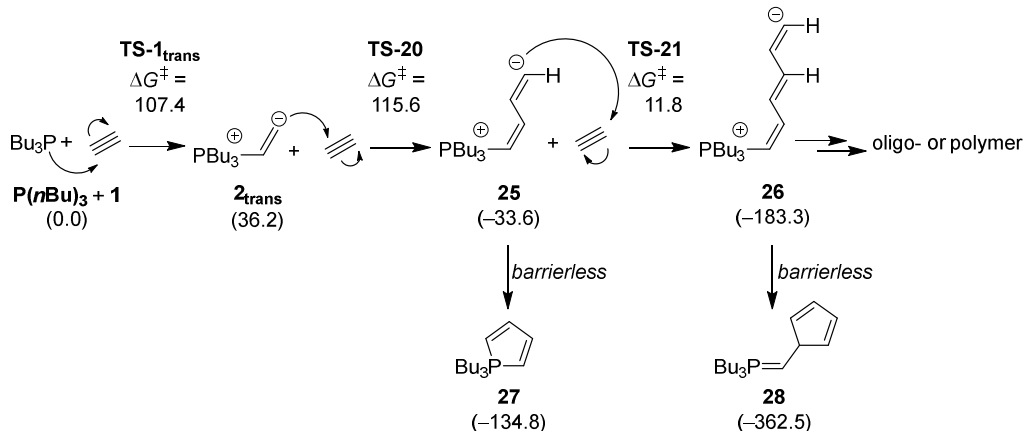


Figure 5.8. Kinetic investigation of the phosphine-catalyzed vinylation of pyrrolidone. (a) Plot of substrate amount versus time for pyrrolidone (●), NVP (○), and the sum of both components (○, dashed). (b) Plot of catalyst amount versus time for $P(nBu)_3$ (●), $OP(nBu)_3$ (○) and the sum of both components (○, dashed). A control reaction without substrate, pyrrolidone, was carried out and is shown with squared data points. $P(nBu)_3$ (▪), $OP(nBu)_3$ (□) and the sum of both components (□, dashed). All experiments were carried out by Nikolai Sitte at CaRLa.

The pathways for phosphine-induced formation of acetylene oligomers were also investigated with quantum-chemical methods (see Scheme 5.22). In contrast to the previously investigated reaction pathways **TS-1_{trans}** ($\Delta G^\ddagger = 107.4 \text{ kJ mol}^{-1}$) is specifically given instead of the more feasible **TS-1_{cis}** ($\Delta G^\ddagger = 99.2 \text{ kJ mol}^{-1}$), because subsequent **TS-20** ($\Delta G^\ddagger = 115.6 \text{ kJ mol}^{-1}$) from **2_{trans}** ($\Delta G^{413} = 36.2 \text{ kJ mol}^{-1}$) is lower in energy than the

equivalent transition state coming from $\mathbf{2}_{\text{cis}}$ ($\Delta G^{413} = 62.5 \text{ kJ mol}^{-1}$). After the addition of the second molecule of acetylene via **TS-20**, intermediate **25** is exergonically formed ($\Delta G^{413} = -33.6 \text{ kJ mol}^{-1}$), for which the addition of the next acetylene unit is significantly more feasible with a barrier of only 45.4 kJ mol^{-1} (**TS-21**). This leads to formation of intermediate **26**, which is significantly more stable to the point where reverse reactions should not be possible any longer ($\Delta G^{413} = -183.3 \text{ kJ mol}^{-1}$). Alternatively, formation of five-membered rings is possible from **25** and **26**, which leads to *P*-heterocycle **27** ($\Delta G^{413} = -134.8 \text{ kJ mol}^{-1}$) and intermediate **28** ($\Delta G^{413} = -362.5 \text{ kJ mol}^{-1}$). Both ring formations proceed without a reaction (see P–C bond length scan in Figure 5.9a for **27** and C–C bond length scan in Figure 5.9b for **28**) and are highly exergonic. It should also be noted that the formation of ylide **5**, which represents the most stable species along the previous reaction pathways and had to be specifically considered in some of the other mechanisms (*vide supra*), does not play a role here as reactivity was observed in reaction mixtures containing only $\text{P}(n\text{Bu})_3$ and pyrrolidone (**1**). However, the high stability of **5**, and therefore lower feasibility of this pathway, might be the reason why formation of the brownish residue was never observed during catalytic experiments, but only in the absence of **1**. All in all, the phosphine-induced polymerization of acetylene might provide a rationale for the observed loss of phosphine (see Figure 5.8b), which could only be provided by quantum chemistry. However, due to the scarce experimental indications, it is not possible to confidently identify the exact products.



Scheme 5.22: Reaction pathway for the phosphine-induced polymerization of acetylene (**1**) and cyclization pathways as a potential explanation for diminishing phosphine amounts. ΔG^{413} in kJ mol^{-1} ; RI-PBE0-D3(BJ)/def2-QZVPP//BP86/def2-SV(P); COSMO-RS (DMF).

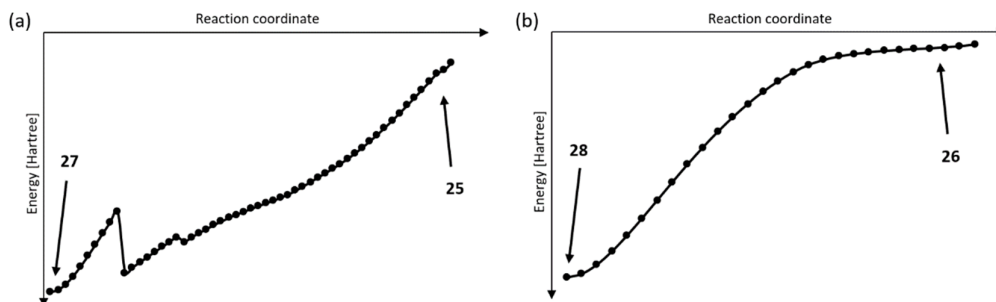
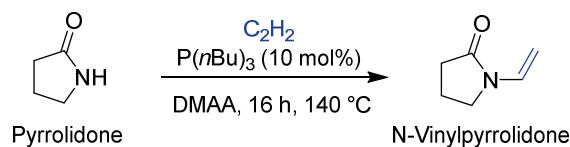


Figure 5.9: Bond lengths scans showing the barrierless formation/dissociation of (a) **27** and (b) **28** from **25** and **26**, respectively. The discontinuity in the left plot is caused by a conformational change of the alkyl substituents of **P(*n*Bu)₃**, and does not represent a reaction barrier. ΔE^{413} in kJ mol^{-1} ; RI-PBE0-D3(BJ)/def2-QZVPP//BP86/def2-SV(P); COSMO-RS (DMF).

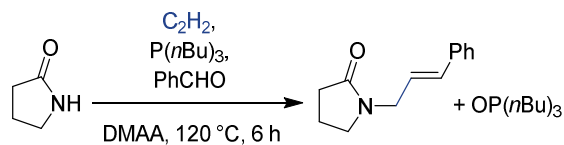
5.4 Summary and Outlook

The vinylation of pyrrolidone to *N*-vinylpyrrolidone with simple phosphine organocatalysts has been studied and an efficient protocol for low acetylene pressures has been developed.



Scheme 5.23: Organocatalytic vinylation of pyrrolidone to *N*-vinylpyrrolidone.

The results indicate that a nucleophilic reaction mechanism (see Figure 5.2) is more feasible than all other reaction pathways (see Schemes 5.9 and 5.21, Figures 5.5 and 5.6) and is responsible for the observed product formation. The proposed acetylene activation step through the phosphine is in good agreement with the experimental observation that amine bases are no competent catalysts for this reaction and the calculated reaction pathways for $\text{P}(\text{nBu})_3$, PPh_3 and PMe_3 correlate well with the experimentally observed conversions, which was attributed to the electronic properties of the organocatalyst. The calculated reaction mechanism suggests that only substrates within a specific range of $\text{p}K_a$ values are suitable to be used within the methodology, which was confirmed by the experimental substrate scope. Furthermore, the use of phenol as additive was evaluated and revealed various alternative reaction pathways that hinder the intended positive effect (see Schemes 5.13 and 5.14). Mechanistic experiments that supported the computed proposals revealed the unexpected formation of a dicationic trialkyl ethylene bisphosphonium species. The formation of this could be rationalized by the computational investigations and was found to be irrelevant in the case of the employed catalytic system (see Scheme 5.16). An alternative Wittig-type methodology could be developed that harnesses the in-situ formation of vinyl phosphonium and ylide species to introduce more complex moieties in the *N* position of the pyrrolidone substrate (see Figure 5.7)



Scheme 5.24: Wittig-type functionalization of pyrrolidone with acetylene, phosphine, and benzaldehyde.

Similar Wittig-type pathways are expected to be responsible for the formation of phosphine oxide during the reaction and subtle differences between the dedicated synthesis and the degradation pathway could be elaborated to explain the behavior (see Scheme 5.21, Figures 5.6 and 5.7). With this the DFT investigation also provided several insights and suggestions into how this degradation could be reduced experimentally. Lastly, another phosphine

degradation pathway was observed, which evaded identification by experimental means. Quantum-chemical methods provided a potential degradation pathway that might explain the observations (see Scheme 5.22).

The vinylolation methodology was further explored by extending and more precisely defining the substrate scope within the concept of the pK_a dependence that was introduced. It must be noted that this should be primarily focused on further base-sensitive reagents, which cannot be vinylated by classical and more economical procedures. Similarly, the scope for the Wittig-type modification could be investigated, for which only a principal proof of concept was developed in the boundaries of this project. This allows for the formation of complex *N*-substituted molecules by *in-situ* formation of vinyl phosphonium and ylide species from simple precursors. An approach aimed at improving the reaction yields would be a thorough optimization of the reaction conditions. While the use of substituted alkynes is economically less desired, the adaption of the vinylolation methodology to these reagents was successful and offers further possibilities for the generation of complex structural motifs. Lastly, the combination of employing substituted alkynes and achieving the Wittig-type modification has not yet been tested and could afford even more complex building blocks.

6

Summary and Outlook

In this thesis, detailed mechanistic investigations were performed with the means of density functional theory to gain insights into homogeneously catalyzed reactions of industrial relevance. Three reactions were studied: the Ru-catalyzed dehydrogenative coupling of alcohols to esters (Chapter 3), the Ni-catalyzed carbonylation of alcohols to carboxylic acids (Chapter 4) and the organocatalyzed vinylation of nucleophiles to *N*-vinyl compounds (Chapter 5). All projects were carried out in close collaboration with experimental colleagues to allow for mutual validation in an agile and supportive environment.

Dehydrogenative Coupling of Alcohols:

The investigations on the dehydrogenative coupling of alcohols to esters were motivated by the high instability of commonly employed (de-)hydrogenation catalysts (e.g., Ru-MACHO), which were shown to undergo base-induced decomposition at catalytic reaction conditions. The efforts to stabilize the activated on-cycle ruthenium species with phosphines were successful and led to two differing structural motifs, which were both competent catalysts in the base-free dehydrogenative coupling of alcohols as well as the reverse hydrogenation reaction. The quantum-chemical calculations were able to rationalize the formation of the two complexes, an octahedral Ru^{II} species, which resembles the coordination environment of the catalyst precursor and a trigonal-bipyramidal Ru⁰ species.

Moreover, the calculations provided an explanation for the varying results of the two complexes in stoichiometric reactions with alcohols, which were carried to gain first insights into the reactivity of the catalysts towards the employed substrates. At a later stage, when solid-state structures had been obtained from isolated crystals, the close collaboration of experiments and quantum chemistry enabled an evaluation of the employed DFT methodology, which showed a remarkable accuracy for structural parameters, configurational isomerism and metallacycle conformations. Subsequently, two possible catalytic cycles for dehydrogenation, which have been previously reported in the scientific literature, were adapted to the employed catalytic species and compared. The investigations revealed that the commonly proposed Noyori-type catalytic cycle, which incorporates metal-ligand cooperation to achieve the desired reaction, is less feasible than the recently developed Dub-type catalytic cycle. The latter is based on the concept of metal-ligand assistance, in which the NH functionality that is incorporated into the backbone of the tridentate PNP ligand is, contrary to the processes in metal-ligand cooperation, not cleaved but kept intact throughout the catalytic cycle. Importantly, a combination of both mechanisms is accessible and responsible for product formation. The initial generation of the Dub-type on-cycle species can proceed via two pathways that are very close in energy. While one of the two pathways required NH cleavage, the second set of molecular transformation steps circumvents this necessity and enables completely new approaches for the design of Ru (de-)hydrogenation catalysts, which incorporate suitable functional groups to build up a stabilizing hydrogen bonding network. The two catalytic pathways were compared against a number of other possible catalytic cycles, which were investigated to rule out interfering influences and to understand if the additional phosphine ligand or the different oxidation states (Ru^{II} and Ru^0) would enable specific reactivity for one of the two complexes. Moreover, the dissociation of various ligands in both the octahedral Ru^{II} complex and the trigonal-bipyramidal Ru^0 complex was computed to understand if the additional phosphine ligand could lead to other (unwanted) catalyst degradation or (desired) substrate conversion pathways. Additionally, the mechanism for alcohol-aldehyde coupling, which occurs after the initial dehydrogenation of alcohol to the corresponding aldehyde and leads to the formation of the desired esters, was investigated. A comparison with the reaction pathways for the formation of a hemiacetal, which subsequently would need to undergo dehydrogenation to the ester, demonstrated that ester formation directly takes place on the metal center without any formation of the intermediary hemiacetal. All results combined, the DFT investigations show that both isolated structural motifs represent different resting states for the on-cycle species, proceed via the same reaction mechanisms, and will not be hindered by alternative reaction pathways or a resting state, which is too stable for reaction to take place. Finally, this might be utilized in catalyst recycling experiments, which demonstrated the superior performance of the base-free stabilized catalytic system over the commercial Ru-MACHO system and represents the starting point for further stability optimization studies.

Carbonylation of Alcohols:

The carbonylation of alcohols represents a straightforward and atom-efficient methodology for the synthesis of carboxylic acids and is applied in multiple large-scale processes in the chemical industry such as the production of ibuprofen, which includes a late-stage Pd-catalyzed carbonylation step. In this context, phenyl ethyl alcohol was used as a model substrate and a procedure for the carbonylation with cheaper earth-abundant Ni complexes as well as lower pressures and corrosivity was developed. A thorough quantum-chemical investigation was performed to understand the nature of involved key species and to build an understanding of the role of the reaction components. The calculations enabled the comparison of a mono- and diphosphine-coordinated reaction system as well as of a phosphine-free Ni carbonyl complex. Together with the close interaction of the experiments and computational approaches, this enabled insights into the required equivalents of phosphine ligand, which could be validated by the use of non-coordinating bases such as Hünig's base. Furthermore, the calculations were able to explain the drastic influence of the LiI additive, which, contrary to prior expectations, does not (solely) influence the initial Ni^{II} to Ni⁰ reduction step but enables the generation of anionic Ni iodide complexes. These species can facilitate the same catalytic conversion via similar transformation steps on an anionic potential energy surface parallel to the neutral pathways of the phosphine-coordinated complexes. Interestingly, the catalytic cycle was shown to proceed via a stepwise oxidative addition pathway, which is based on two one-electron transformations as opposed to the classical two-electron oxidative addition steps suggested in previous publications. This transformation, which proceeds over a tetrahedral Ni^I complex and the benzylic phenyl ethyl radical, could be further supported by mechanistic experiments and EPR spectroscopy. The mechanistic investigations could be extended to other employed phosphines such as Buchwald-type ligands and bidentate phosphines and remained an excellent tool for gaining insights into the underlying processes, which were found to be influenced by additional factors. Moreover, a broad range of possible side reactions, which could interfere with the desired carbonylation reactivity, were studied and ruled out. Overall, the methodology was shown to be an efficient way of synthesizing carboxylic acids from alcohol with the possibility to tune the catalytic activity with specific phosphines and additives. These capabilities were demonstrated by employing a broad range of benzylic and aliphatic substrates including the synthesis of the active pharmaceutical ingredients ibuprofen and naproxene.

In the second part of the investigations into the Ni-catalyzed carbonylation of alcohols to carboxylic acids, the methodology was adapted to *tert*-butyl alcohol. This was driven by the observed radical-based oxidative addition pathway as well as by the S_N1-type generation of alkyl iodides from the employed alcohols, which should favor the formation of tertiary Koch-type carbonylation products. Apart from the Koch-type carbonylation process, most processes and procedures reported in the literature lead to *n*- or *iso*-acids. An efficient and

economic method, which would avoid the problems of the Koch reaction, would be highly desirable. Surprisingly, the initial tests with *tert*-butyl alcohol led to the formation of a mixture of 2,2-dimethylpropanoic acid (pivalic acid) and 3-methylbutanoic acid (isovaleric acid) and thus indicated the isomerization of the *tert*-butyl group to an *iso*-butyl group. Due to these unexpected results, a second set of quantum-chemical calculations was employed to gather insights into the underlying mechanistic processes. The recalculation of the neutral and anionic catalytic cycles that had been developed in the first part, the carbonylation of phenyl ethyl alcohol, revealed that the pathways should be feasible at the employed reaction conditions and should exhibit the same influence of the LiI additive (i.e., enabling access to the anionic regime, which is associated with lower activation barriers). Furthermore, the calculations showed that isomerization pathways leading from the *t*Bu moiety to the observed *i*Bu product should not be accessible and thus did not rationalize the observed product ratios. Subsequent control experiments with *tert*-butyl iodide and *iso*-butyl iodide revealed the degradation of the alkyl halides at reaction conditions and provided indications for a reaction mechanism, which, contrary to the carbonylation of phenyl ethyl alcohol, is not based on the formation of alkyl iodides. Instead, experiments supported the formation of the corresponding olefin, isobutene. Further calculations were employed to investigate a new catalytic cycle based on the isobutene substrate, which can lead to the formation of pivalic acid and isovaleric acid. Once more, the catalytic cycle was investigated in neutral phosphine-coordinated and phosphine-free environments to gather insights into the competing underlying processes. This demonstrated that the olefin-based reaction pathways also are accessible at the given reaction conditions and that the predicted product ratios are in good agreement with the experimentally observed selectivities for the formation of pivalic acid and isovaleric acid. A wide range of HI and isobutene coordination schemes was investigated to understand the key steps that enable the observed reactivity. Moreover, the calculations were extended to the anionic Ni halide complexes, which were found to have the same effect as in the carbonylation of the phenyl ethyl alcohol and enable access to a more feasible anionic catalytic cycle. These results could be validated by experiments, which were able to show the conversion of isobutene as well as the beneficial effect of LiI. Overall, the project also serves as an excellent example for the importance of detailed and tightly integrated computational investigations and to pay close attention even when only small changes to the catalytic system are made. The results enable the consideration of other alcohols and olefins to be carbonylated with the developed Ni-based catalytic methodology. Additionally, based on the different regimes or even coordination schemes suggesting different isomer ratios, other phosphine and additives could be extensively tested to specifically tune the obtained product mixture.

Vinylation of Pyrrolidone:

The vinylation of nucleophiles to *N*-vinyl compounds by the means of organocatalysis and directly employing acetylene at low pressure was developed. The conditions, contrary to the industrially used Reppe process with strong bases and higher pressures, enable the conversion of sensitive substrate. The reactivity was further investigated with the model substrate, pyrrolidone, which is converted to *N*-vinylpyrrolidone and represents an important monomer in the chemical industry. The use of quantum-chemical methods enabled a detailed investigation of the underlying nucleophilic reaction mechanism and possible side reactions. Furthermore, the use of phenol as a potential additive, based on the observed protonation/deprotonation cascade, was investigated and predicted to not lead to the desired benefit due to interfering reactivity. In the context of the collaboration between experiments and computations, the reaction mechanism and the role of phenol were validated by mechanistic experiments. The use of a BF₄ anion led to the isolation of a novel diphosphonium species, which could subsequently be explained by the DFT calculations, which also ruled out the involvement of this motif under catalytic conditions (i.e., deprotonated pyrrolidone acting as the anion). Additionally, the investigations enabled the comparison of different phosphine catalysts (i.e., the demonstration of the good catalytic performance of tri-*n*-butylphosphine vs. the absence of conversion when employing triphenylphosphine). Alternative Reppe-type pathways were studied and compared to the nucleophilic reaction mechanism. The applicability of the vinylation methodology is limited to a set of substrates in a specific pK_a range by the requirements of the underlying reaction steps of the nucleophilic reaction mechanism, and this could be demonstrated for a range of cyclic and non-cyclic nucleophiles. Due to the regular observation of phosphine oxide as side product, quantum-chemical investigations into possible Wittig-type pathways leading to the formation of these species were undertaken and identified as feasible at reaction conditions. The results were compared with kinetic investigations, which surprisingly had also revealed the constant consumption of the phosphine catalyst, even when no substrate or product were present in the reaction mixture. The calculations were used to evaluate a phosphine-induced acetylene polymerization pathway, which was suggested after the experimental observation and provided a rationale for the observed reactivity. Lastly, a Wittig-type modification of the reaction, that takes advantage of the developed substrate/product degradation pathways, was predicted with quantum chemistry and experimentally applied. The reaction enables the *in-situ* formation of vinyl phosphonium intermediates, which have been applied in this type of transformations by Schweizer *et al.* but were severely limited due to the required isolation of the instable species. After compelling evidence has been provided for the accessibility of the calculated Wittig-type pathways, a thorough investigation of possible reagents would be interesting and could offer an easy methodology to introduce complex substituents at the *N* positions.

7

Appendix

7.1 Dehydrogenative Coupling of Alcohols

7.1.1 Geometries of Computed Species

Due to the large number of calculated species, the XYZ coordinates of the species cannot be included directly in this appendix. Therefore, two supplemental files have been provided with this thesis:

coordinates-dehydrogenation.xyz

coordinates-dehydrogenation.txt

These supplemental files contain the computed Cartesian coordinates of all intermediates and transition states reported in this study. The *.txt* file may be opened to read the coordinates, while the *.xyz* file can directly be opened in molecular modeling/viewing programs such as Mercury (<http://www.ccdc.cam.ac.uk/pages/Home.aspx>) for visualization and analysis.

The XYZ coordinates are given in the following format:

Number of atoms in the species

Compound - Total energy [Hartree] at the level of geometry optimization

XYZ coordinates

7.1.2 Energies

Table 7.1: Total Gibbs free energies $G(\text{Total})$ [kJ mol^{-1}], electronic energies at the level of geometry optimization $E(\text{Opt})$ (BP86/def2-SV(P)) [Hartree], electronic energies at the level of the single-point energy calculations $E(\text{SP})$ (PBE0-D3(BJ)/def2-QZVPP) [Hartree], thermodynamic corrections $\Delta G(\text{Therm})$ [kJ mol^{-1}], and solvent corrections $\Delta G(\text{Solv})$ [kJ mol^{-1}] for the dehydrogenative coupling of alcohols to esters.

Structure	$G(\text{Total})$ PBE0-D3(BJ)/ def2-QZVPP [kJ mol^{-1}]	$E(\text{Opt})$ BP86/ def2-SV(P) [Hartree]	$E(\text{SP})$ PBE0-D3(BJ)/ def2-QZVPP [Hartree]	$\Delta G(\text{Therm})$ [kJ mol^{-1}]	$\Delta G(\text{Solv})$ [kJ mol^{-1}]
1	-6536578.3	-2490.27915	-2490.11065	1277.9	-71.6
2	-6536569.4	-2490.26899	-2490.10667	1283.6	-78.9
3	-8045317.6	-3065.07280	-3064.88645	1639.1	-98.5
4	-8045347.7	-3065.07661	-3064.89629	1643.4	-107.0
5	-6939745.8	-2643.87730	-2643.73988	1487.5	-95.2
6	-7343161.1	-2797.56221	-2797.40415	1513.1	-90.7
7	-8851880.4	-3372.34085	-3372.16908	1867.0	-118.8
8	-5624024.3	-2142.60367	-2142.44091	1022.9	-69.5
9	-5624048.2	-2142.60691	-2142.45211	1038.7	-79.7
10	-5326617.5	-2029.32895	-2029.16024	1014.1	-72.1
11	-5733262.0	-2184.25031	-2184.10829	1190.9	-77.4
12	-5733261.5	-2184.24789	-2184.09993	1175.2	-83.1
13	-5736390.1	-2185.45423	-2185.31907	1243.0	-78.8
14	-5736334.4	-2185.43522	-2185.29693	1234.8	-72.9
15	-6549659.4	-2495.29963	-2495.21052	1595.7	-80.8
16	-6546558.9	-2494.10721	-2494.01209	1553.4	-84.5
17	-6139971.7	-2339.20935	-2339.09161	1388.3	-75.9
18	-6537790.5	-2490.72760	-2490.56808	1320.8	-125.7
19	-8046526.5	-3065.51747	-3065.34318	1677.3	-146.4
20	-6941277.4	-2644.43961	-2644.30334	1469.7	-129.7
21	-8449974.9	-3219.22413	-3219.06914	1835.8	-145.9
22	-6941209.6	-2644.40642	-2644.26430	1448.0	-142.7
23	-8449913.9	-3219.19551	-3219.03759	1816.7	-148.7
24	-6536555.4	-2490.26914	-2490.10314	1277.9	-68.4
25	-8045291.2	-3065.06161	-3064.87579	1637.8	-98.8
26	-5326549.1	-2029.29826	-2029.13354	1012.8	-72.6
27	-5730092.5	-2183.03546	-2182.89104	1161.0	-74.0
28	-5730076.9	-2183.03119	-2182.88431	1153.8	-68.8

Section 7.1 – Dehydrogenative Coupling of Alcohols

29	-5730134.8	-2183.05149	-2182.89435	1130.8	-77.3
30	-5326580.3	-2029.30873	-2029.14282	1018.2	-84.8
31	-5733285.5	-2184.26784	-2184.12332	1206.7	-77.3
32	-6133082.2	-2336.56806	-2336.40326	1235.5	-91.8
33	-6536428.8	-2490.22190	-2490.03818	1248.2	-82.7
34	-6536456.8	-2490.23019	-2490.04676	1254.4	-94.4
35	-6537639.7	-2490.66509	-2490.49534	1292.7	-137.9
36	-5733201.1	-2184.23482	-2184.08148	1186.9	-82.9
37	-8045172.3	-3065.02098	-3064.81659	1612.5	-110.1
38	-8045230.3	-3065.04102	-3064.83960	1616.9	-112.0
39	-8046403.2	-3065.47318	-3065.28687	1653.6	-147.3
40	-6133091.5	-2336.57154	-2336.40703	1239.8	-95.6
41	-6239114.3	-2376.98321	-2376.80918	1262.5	-65.2
42	-6239046.8	-2376.95325	-2376.78423	1267.4	-68.2
43	-6240300.8	-2377.41665	-2377.25375	1294.8	-116.7
44	-5435762.2	-2070.94469	-2070.79605	1190.0	-77.9
45	-7747873.1	-2951.77853	-2951.59096	1623.2	-95.4
46	-7747808.5	-2951.75393	-2951.56908	1631.5	-96.5
47	-7749052.8	-2952.21255	-2952.03596	1656.8	-140.3
48	-5835674.3	-2223.28217	-2223.12802	1239.4	-91.9
49	-6950138.6	-2647.86388	-2647.79037	1711.0	-77.0
51	-810221.5	-308.64546	-308.68495	230.3	0.4
52	-6136797.9	-2337.97974	-2337.84948	1300.6	-75.5
53	-6136845.9	-2338.00707	-2337.87913	1338.7	-83.8
54	-6136835.6	-2337.99988	-2337.87362	1333.9	-83.2
55	-6136799.3	-2337.98952	-2337.85952	1333.3	-83.4
56	-5329724.5	-2030.52089	-2030.36076	1068.0	-81.0
57	-6953211.0	-2649.03658	-2648.96314	1728.5	-87.7
58	-6543449.8	-2492.91116	-2492.80879	1504.6	-85.9
14_unstabilized	-5329659.1	-2030.49951	-2030.33541	1055.9	-70.2
Acetaldehyde	-403556.9	-153.71472	-153.72381	37.9	7.0
CO	-297371.1	-113.22996	-113.23639	-69.0	0.0
Ethylacetate	-807171.0	-307.47783	-307.50049	169.2	2.2
EtOH	-406660.1	-154.90739	-154.93484	116.1	5.1
H2	-3101.5	-1.17000	-1.16877	-32.9	0.0
PhOH	-806550.7	-307.24439	-307.25381	149.3	-5.3
PMe3	-1209915.0	-460.92298	-460.89772	166.1	5.7
PPh3	-2718687.4	-1035.73251	-1035.67490	512.6	-35.9
TS-1	-5733257.8	-2184.25290	-2184.10825	1192.8	-75.2
TS-10	-6136782.1	-2337.98512	-2337.85929	1340.1	-73.5
TS-11	-6950122.9	-2647.84486	-2647.77185	1684.2	-83.1
TS-14	-1216768.0	-463.54362	-463.58943	392.8	-7.0
TS-15	-6136804.6	-2337.99108	-2337.86499	1334.4	-75.3
TS-16	-6543452.3	-2492.92061	-2492.81536	1515.1	-81.7

Chapter 7 – Appendix

TS-17	-6546525.2	-2494.09946	-2493.99859	1548.8	-81.6
TS-2	-6139908.8	-2339.17817	-2339.05980	1370.5	-78.6
TS-2_unassisted	-5733246.6	-2184.24947	-2184.10474	1195.4	-75.8
TS-3	-5736316.3	-2185.43216	-2185.28824	1231.1	-73.9
TS-3_unassisted	-5329614.8	-2030.48090	-2030.31511	1048.0	-71.3
TS-4	-6142993.5	-2340.36540	-2340.24805	1406.8	-79.9
TS-4_twice-stabilized	-6549643.3	-2495.30081	-2495.20792	1601.7	-77.6
TS-5	-6546563.4	-2494.10887	-2494.01770	1557.5	-78.4
TS-7	-5733121.0	-2184.20934	-2184.05228	1182.3	-74.9
TS-8	-6943052.5	-2645.13614	-2644.98828	1451.0	-87.8
TS-8_stabilized	-7349722.6	-2800.06493	-2799.94441	1617.7	-87.3
TS-9	-8451798.5	-3219.93131	-3219.76719	1813.0	-114.0

7.2 Carbonylation of Alcohols

7.2.1 Geometries of Computed Species

Due to the large number of calculated species, the XYZ coordinates of the species cannot be included directly in this appendix. Therefore, two supplemental files have been provided with this thesis:

coordinates-carbonylation.xyz
coordinates-carbonylation.txt

These supplemental files contain the computed Cartesian coordinates of all intermediates and transition states reported in this study. The *.txt* file may be opened to read the coordinates, while the *.xyz* file can directly be opened in molecular modeling/viewing programs such as Mercury (<http://www.ccdc.cam.ac.uk/pages/Home.aspx>) for visualization and analysis.

The XYZ coordinates are given in the following format:

Number of atoms in the species

Compound - Total energy [Hartree] at the level of geometry optimization

XYZ coordinates

7.2.2 Energies

Table 7.2: Total Gibbs free energies $G(\text{Total})$ [kJ mol^{-1}], electronic energies at the level of geometry optimization $E(\text{Opt})$ (BP86/def2-SV(P)) [Hartree], electronic energies at the level of the single-point energy calculations $E(\text{SP})$ (PBE0-D3(BJ)/def2-QZVPP) [Hartree], thermodynamic corrections $\Delta G(\text{Therm})$ [kJ mol^{-1}], and solvent corrections $\Delta G(\text{Solv})$ [kJ mol^{-1}] for the carbonylation of alcohols to carboxylic acids.

Structure	$G(\text{Total})$ PBE0-D3(BJ)/ def2-QZVPP [kJ mol^{-1}]	$E(\text{Opt})$ BP86/ def2-SV(P) [Hartree]	$E(\text{SP})$ PBE0-D3(BJ)/ def2-QZVPP [Hartree]	$\Delta G(\text{Therm})$ [kJ mol^{-1}]	$\Delta G(\text{Solv})$ [kJ mol^{-1}]
1	-8829842.2	-3363.93152	-3363.66762	1500.1	-34.2
2	-10670017.7	-4065.10219	-4064.85688	2309.3	-46.8
3	-6989598.5	-2662.73619	-2662.45674	694.5	-13.9
4	-12510174.5	-4766.25820	-4766.04399	3129.1	-56.9
5	-5149312.5	-1961.52148	-1961.23730	-100.6	15.9
6	-4554459.2	-1734.93593	-1734.66744	-106.2	15.7
7	-6394692.3	-2436.12283	-2435.86461	687.2	-18.0
8	-8234859.5	-3137.29194	-3137.04434	1486.6	-37.4
9	-8532357.4	-3250.61624	-3250.35164	1482.1	-42.6
10	-6692153.6	-2549.43415	-2549.16090	684.8	-17.4

Chapter 7 – Appendix

11	-8287619.9	-3157.34612	-3156.94658	980.5	-38.4
12	-7474001.9	-2847.32761	-2846.94040	666.5	-27.5
13	-8287620.7	-3157.35035	-3156.95263	999.6	-42.4
14	-8287662.0	-3157.36453	-3156.96894	1001.8	-43.1
15	-8585005.2	-3270.61908	-3270.22055	1002.7	-45.1
16	-8584989.6	-3270.60688	-3270.21105	987.3	-39.0
17	-10127825.7	-3858.52791	-3858.14304	1781.7	-54.3
18	-9314276.2	-3548.53093	-3548.16448	1473.3	-45.1
19	-10127860.4	-3858.53426	-3858.16254	1806.8	-62.9
20	-10127931.9	-3858.56650	-3858.19261	1811.0	-59.7
21	-10425240.1	-3971.81267	-3971.43684	1824.3	-58.5
22	-10425184.3	-3971.78654	-3971.40586	1799.1	-58.9
23	-6447383.5	-2456.14980	-2455.74351	182.9	-12.7
24	-5633682.0	-2146.10522	-2145.70796	-132.8	6.3
25	-6447314.1	-2456.13166	-2455.72057	194.1	-14.8
26	-6447379.4	-2456.14896	-2455.74676	196.1	-13.3
27	-6744710.2	-2569.40424	-2568.99585	201.5	-14.0
28	-6744746.4	-2569.40954	-2569.00581	189.3	-12.0
29	-5634043.8	-2146.22244	-2145.81907	-129.5	-67.1
30	-6932086.3	-2640.84374	-2640.30838	158.4	-116.0
31	-6118490.5	-2330.83430	-2330.32447	-155.8	-68.7
32	-6932119.9	-2640.85484	-2640.33012	167.4	-101.6
33	-6932178.9	-2640.87186	-2640.35218	169.8	-105.1
34	-7229508.2	-2754.12310	-2753.60013	176.2	-108.3
35	-7229478.0	-2754.10588	-2753.58471	164.9	-107.2
36	-7474285.1	-2847.40750	-2847.01316	670.3	-123.5
37	-8772317.0	-3342.02908	-3341.50401	942.8	-142.3
38	-7958767.9	-3032.02469	-3031.53253	645.3	-125.7
39	-8772378.3	-3342.04809	-3341.54098	971.3	-134.9
40	-8772429.0	-3342.06366	-3341.55949	979.8	-145.6
41	-9069776.0	-3455.32704	-3454.81539	980.8	-140.3
42	-9069682.8	-3455.28387	-3454.77598	968.0	-137.8
43	-8546689.5	-3255.96875	-3255.68829	1161.1	-42.3
44	-9844757.1	-3750.58851	-3750.18981	1431.3	-66.5
45	-9031103.4	-3440.56358	-3440.17588	1133.4	-56.3
46	-9844716.4	-3750.58209	-3750.18710	1467.6	-69.2
47	-9844762.9	-3750.59651	-3750.20317	1464.9	-70.8
48	-10142089.9	-3863.85070	-3863.45141	1470.7	-70.4
49	-10142110.0	-3863.84954	-3863.45414	1453.7	-66.3
50	-7383626.5	-2812.80104	-2812.49300	591.3	-18.5
51	-8681634.1	-3307.40608	-3306.97902	873.7	-35.6
52	-7868054.7	-2997.39774	-2996.98610	566.5	-35.3
53	-8681695.2	-3307.42776	-3307.00654	895.4	-46.2
54	-8681744.1	-3307.43866	-3307.02800	904.8	-48.2

Section 7.2 – Carbonylation of Alcohols

55	-8979085.1	-3420.69519	-3420.27984	902.8	-44.4
56	-8978999.3	-3420.66921	-3420.24713	894.8	-36.5
57	-9798687.8	-3733.14179	-3732.66002	1462.0	-52.3
58	-9798657.2	-3733.13077	-3732.64569	1470.1	-67.4
59	-8352522.9	-3182.02876	-3181.50181	557.8	-48.9
60	-9142051.8	-3482.91963	-3482.66368	1728.2	-47.8
61	-9142052.3	-3482.92471	-3482.67207	1743.5	-41.6
62	-7301870.4	-2781.74204	-2781.47619	922.7	-28.4
63	-7301844.1	-2781.74100	-2781.47271	933.3	-21.9
64	-4851908.7	-1848.23543	-1847.95854	-111.2	16.9
65	-5461639.0	-2080.54539	-2080.27350	120.1	-1.9
66	-5461617.9	-2080.53644	-2080.26749	120.5	3.1
67	-8083694.7	-3079.60835	-3079.24399	904.0	-44.8
68	-8083669.1	-3079.60700	-3079.23908	908.1	-36.2
69	-8083697.8	-3079.60831	-3079.24423	901.5	-44.7
70	-8083682.0	-3079.60521	-3079.24047	901.2	-38.5
71	-5336629.6	-2032.93849	-2032.54088	-131.7	-62.6
72	-5946346.7	-2265.23206	-2264.84308	101.1	-103.2
73	-5946319.9	-2265.23056	-2264.83886	101.9	-88.2
74	-6728202.8	-2563.12431	-2562.62892	73.0	-94.5
75	-9830377.1	-3745.23010	-3744.84393	1770.3	-61.0
76	-7990189.2	-3044.05469	-3043.65762	974.1	-41.4
77	-6149977.2	-2342.86817	-2342.46513	177.6	-13.4
78	-9346018.7	-3560.64256	-3560.38145	1813.1	-51.6
79	-7505794.3	-2859.45965	-2859.17947	1008.2	-27.9
80	-5665540.5	-2158.25800	-2157.96679	202.4	-2.0
81	-6150302.7	-2342.96207	-2342.55692	173.9	-94.3
90	-7590354.9	-2891.74289	-2891.35893	939.4	-32.5
97	-6234832.3	-2375.24302	-2374.72608	102.4	-92.3
100	-7475476.2	-2847.90775	-2847.51159	691.6	-27.3
101	-7178130.8	-2734.63790	-2734.25853	692.3	-28.4
102	-412299.7	-157.09246	-157.09562	138.3	16.5
103	-8830847.3	-3364.29932	-3364.03279	1522.9	-103.4
104	-6693153.8	-2549.78909	-2549.52725	718.3	-89.3
105	-7475453.6	-2847.89573	-2847.49801	676.5	-25.2
106	-7475443.3	-2847.88659	-2847.49433	676.1	-24.1
107	-7104421.0	-2706.55446	-2706.28113	940.2	-21.1
108	-6807040.9	-2593.27989	-2593.01247	932.3	-19.9
109	-7590348.8	-2891.74298	-2891.35118	922.6	-29.9
110	-7105431.5	-2706.90922	-2706.64651	955.3	-87.4
111	-6808064.3	-2593.63801	-2593.38327	950.0	-87.5
112	-9315755.1	-3549.11191	-3548.73407	1500.6	-55.7
113	-9018378.1	-3435.83599	-3435.47024	1499.4	-51.7
114	-9430592.0	-3592.92924	-3592.56682	1743.0	-52.2

Chapter 7 – Appendix

119	-8830847.3	-3364.29932	-3364.03279	1522.9	-103.4
120	-8533482.5	-3251.02827	-3250.77131	1519.6	-103.3
121	-9315694.5	-3549.08856	-3548.70055	1469.2	-51.8
122	-9315649.8	-3549.06933	-3548.68755	1474.1	-46.1
123	-8944621.3	-3407.73371	-3407.47562	1745.8	-41.2
124	-8647225.8	-3294.45316	-3294.20093	1735.1	-37.6
125	-9430569.0	-3592.92749	-3592.55236	1729.7	-53.9
126	-8945717.6	-3408.12958	-3407.87944	1769.7	-101.2
127	-8648332.5	-3294.85370	-3294.60923	1767.3	-104.5
128	-5635192.0	-2146.69541	-2146.29099	-114.3	8.4
129	-5337837.6	-2033.42212	-2033.03388	-112.7	4.7
130	-5750075.7	-2190.53414	-2190.13572	124.9	-0.2
135	-6990522.5	-2663.05992	-2662.78857	716.8	-89.0
136	-4852747.8	-1848.51571	-1848.25459	-86.7	-69.4
137	-5635187.5	-2146.68886	-2146.28579	-121.3	6.3
138	-5635204.4	-2146.69147	-2146.29141	-120.5	3.5
139	-5264189.3	-2005.35733	-2005.07778	133.9	7.8
140	-4966811.5	-1892.08617	-1891.81249	131.4	10.0
141	-5750097.9	-2190.53915	-2190.14037	116.0	-1.1
142	-5265064.9	-2005.65721	-2005.38919	154.6	-70.9
143	-4967710.5	-1892.38683	-1892.12977	145.2	-69.7
144	-6119952.1	-2331.40778	-2330.88683	-138.4	-71.2
145	-5822600.2	-2218.14155	-2217.63270	-135.1	-71.3
146	-6119951.6	-2331.41077	-2330.88371	-147.9	-69.4
147	-6119921.9	-2331.39074	-2330.86826	-149.0	-79.1
148	-5748829.2	-2190.04982	-2189.65460	108.2	-84.8
149	-5451520.1	-2076.77317	-2076.38314	105.3	-82.2
150	-6234835.8	-2375.24775	-2374.72643	97.5	-90.0
151	-5452721.1	-2077.26604	-2076.87720	119.7	-0.5
152	-7474285.1	-2847.40750	-2847.01316	670.3	-123.5
153	-7176846.5	-2734.10736	-2733.72117	664.9	-127.5
154	-7960241.1	-3032.60593	-3032.10069	669.3	-131.1
155	-7662855.9	-2919.31877	-2918.82807	670.6	-144.5
156	-8075088.8	-3076.43139	-3075.93351	910.2	-136.8
115_iBu	-9430648.5	-3592.94734	-3592.59029	1750.1	-54.1
115_tBu	-9430604.5	-3592.93304	-3592.57611	1754.7	-52.0
116_iBu	-9727998.7	-3706.20940	-3705.84343	1748.9	-57.1
116_tBu	-9727941.5	-3706.19135	-3705.82776	1762.8	-54.9
117_iBu	-9728060.4	-3706.23939	-3705.87575	1769.0	-54.0
117_tBu	-9728051.9	-3706.23220	-3705.87539	1773.6	-51.1
118_iBu	-10025420.3	-3819.49225	-3819.13229	1767.8	-57.8
118_tBu	-10025385.7	-3819.47897	-3819.12173	1775.9	-58.9
131_iBu	-5750114.8	-2190.54438	-2190.15644	141.2	-1.1
131_tBu	-5750084.4	-2190.53760	-2190.14641	148.2	-4.0

Section 7.2 – Carbonylation of Alcohols

132_iBu	-5750155.0	-2190.55641	-2190.16767	146.4	-17.0
132_tBu	-5750160.2	-2190.55657	-2190.17047	145.7	-14.1
133_iBu	-6047525.5	-2303.82634	-2303.43174	145.5	-11.9
133_tBu	-6047526.0	-2303.82606	-2303.43399	148.9	-9.8
134_iBu	-6344852.8	-2417.07990	-2416.68284	152.0	-4.9
134_tBu	-6344845.0	-2417.07545	-2416.68182	156.0	-3.8
157_iBu	-8075145.0	-3076.43710	-3075.95378	916.4	-145.9
157_tBu	-8075118.4	-3076.42793	-3075.94445	914.7	-142.1
158_iBu	-8372520.6	-3189.72256	-3189.22785	924.9	-129.0
158_tBu	-8372505.8	-3189.71921	-3189.22583	928.5	-123.0
159_iBu	-8372580.2	-3189.72730	-3189.24287	922.9	-147.2
159_tBu	-8372561.5	-3189.72872	-3189.24390	937.8	-140.6
160_iBu	-8669916.0	-3303.00147	-3302.50202	930.4	-128.5
160_tBu	-8669906.0	-3302.99725	-3302.50038	935.1	-127.6
82_iBu	-7887763.2	-3005.01711	-3004.63514	933.8	-28.5
82_tBu	-7887774.6	-3005.02138	-3004.63866	932.5	-29.4
83_iBu	-7887748.2	-3005.01827	-3004.63488	952.6	-33.1
83_tBu	-7887746.4	-3005.01848	-3004.63586	957.0	-33.0
84_iBu	-7590404.8	-2891.75823	-2891.38150	946.1	-29.8
84_tBu	-7590372.4	-2891.74835	-2891.36827	948.8	-35.0
85_iBu	-7590421.8	-2891.76249	-2891.38473	945.9	-38.2
85_tBu	-7590421.1	-2891.76084	-2891.38639	950.3	-37.5
86_iBu	-7887801.4	-3005.03948	-3004.65548	954.9	-34.5
86_tBu	-7887813.3	-3005.03458	-3004.66063	955.5	-33.4
87_iBu	-8185151.0	-3118.29723	-3117.91084	957.9	-35.2
87_tBu	-8185145.8	-3118.29143	-3117.90865	956.0	-33.8
88_iBu	-8185128.6	-3118.28270	-3117.90030	946.9	-29.4
88_tBu	-8185130.8	-3118.27965	-3117.90027	944.9	-29.7
89_iBu	-1493008.2	-568.83227	-568.71812	159.4	1.5
89_tBu	-1493007.1	-568.83029	-568.71886	161.4	2.7
91_iBu	-6532240.2	-2488.51211	-2487.99743	98.8	-102.7
91_tBu	-6532251.5	-2488.51470	-2487.99961	96.3	-105.7
92_iBu	-6532246.8	-2488.52473	-2488.01430	120.1	-86.3
92_tBu	-6532230.9	-2488.52102	-2488.01152	125.0	-82.6
93_iBu	-6532324.1	-2488.54557	-2488.04002	123.5	-99.5
93_tBu	-6532326.8	-2488.54440	-2488.04295	125.4	-96.4
94_iBu	-6829640.9	-2601.79664	-2601.28511	127.8	-95.6
94_tBu	-6829638.0	-2601.79277	-2601.28532	132.3	-96.7
95_iBu	-6829619.1	-2601.77985	-2601.27279	118.1	-96.4
95_tBu	-6829623.3	-2601.77847	-2601.27402	116.8	-96.2
96_iBu	-6234906.5	-2375.26343	-2374.75939	114.6	-91.3
96_tBu	-6234886.2	-2375.25656	-2374.75093	115.5	-94.0
98_iBu	-6234906.5	-2375.26343	-2374.75939	114.6	-91.3
98_tBu	-6234886.2	-2375.25656	-2374.75093	115.5	-94.0

Chapter 7 – Appendix

99_iBu	-6234941.0	-2375.26740	-2374.77403	121.1	-93.7
99_tBu	-6234914.7	-2375.25102	-2374.76097	122.2	-102.9
CO	-297355.5	-113.22996	-113.23639	-53.4	0.0
CO2	-494896.6	-188.46402	-188.47555	-54.1	0.0
DavePhos	-3694736.9	-1407.68643	-1407.67251	1148.1	-41.4
depe	-2828988.5	-1077.76227	-1077.72207	578.3	-7.9
H2O	-200582.5	-76.34503	-76.38579	-43.4	11.8
HI	-783308.1	-298.44387	-298.31962	-89.1	19.1
iBuI	-1195631.3	-455.56786	-455.45269	153.1	6.5
iBu-radical	-413750.9	-157.64779	-157.65531	156.4	16.7
MEK	-609764.1	-232.28836	-232.30170	135.7	8.2
PhEtCOI	-1892856.6	-721.15383	-721.02597	205.8	-9.0
PhEtCO-radical	-1110985.4	-423.23645	-423.23462	217.8	-0.9
PhEtI	-1595491.0	-607.89384	-607.76338	198.0	-6.5
PhEt-radical	-813667.0	-309.99954	-309.99022	208.0	4.2
PnBu3	-2137599.8	-814.44014	-814.43541	705.7	-5.7
tBuI	-1195639.6	-455.57042	-455.45565	153.6	5.4
tBu-radical	-413785.6	-157.66121	-157.66709	152.3	17.0
TS-1	-8287599.3	-3157.34435	-3156.94536	1002.5	-43.0
TS-10	-6447287.9	-2456.11253	-2455.69896	182.4	-33.6
TS-11	-6932107.8	-2640.84819	-2640.32480	169.2	-105.2
TS-12	-7229465.6	-2754.10364	-2753.58482	177.2	-107.0
TS-14	-8772353.6	-3342.03418	-3341.53135	975.4	-139.8
TS-15	-9069678.2	-3455.27285	-3454.77190	968.4	-144.3
TS-16	-9844693.2	-3750.57517	-3750.17706	1464.8	-69.6
TS-17	-10142080.5	-3863.84453	-3863.44785	1467.8	-67.4
TS-18	-9844639.2	-3750.55399	-3750.14861	1447.0	-72.5
TS-19	-8681679.9	-3307.42475	-3307.00338	900.0	-43.8
TS-2	-8584974.0	-3270.60271	-3270.20867	997.8	-40.2
TS-20	-8979014.4	-3420.67172	-3420.25432	893.4	-31.4
TS-21_iBu	-7590395.0	-2891.75259	-2891.37801	948.5	-31.7
TS-21_tBu	-7590361.4	-2891.74153	-2891.36576	949.8	-31.4
TS-22_iBu	-8185124.2	-3118.27786	-3117.89705	945.7	-32.3
TS-22_tBu	-8185111.0	-3118.27407	-3117.89476	952.6	-32.1
TS-23_iBu	-7590349.5	-2891.73556	-2891.35436	937.3	-37.0
TS-23_tBu	-7590351.8	-2891.73248	-2891.35158	932.9	-42.2
TS-24_iBu	-7887729.0	-3005.01290	-3004.62882	955.9	-33.1
TS-24_tBu	-7887709.4	-3005.00615	-3004.62221	958.0	-33.0
TS-25_iBu	-6532238.8	-2488.51762	-2488.00913	120.9	-92.7
TS-25_tBu	-6532211.9	-2488.50804	-2487.99906	120.8	-92.1
TS-26_iBu	-6829607.0	-2601.77711	-2601.27229	127.9	-95.5
TS-26_tBu	-6829589.8	-2601.76986	-2601.26363	125.7	-98.8
TS-27_iBu	-6234832.9	-2375.23198	-2374.72544	102.1	-94.3
TS-27_tBu	-6234828.1	-2375.23462	-2374.72437	101.0	-91.2

Section 7.2 – Carbonylation of Alcohols

TS-28_iBu	-6234885.3	-2375.24918	-2374.75065	116.2	-94.6
TS-28_tBu	-6234856.2	-2375.23856	-2374.73752	112.9	-96.7
TS-29_iBu	-9430578.7	-3592.92083	-3592.56243	1753.2	-60.6
TS-29_tBu	-9430560.8	-3592.91774	-3592.55567	1749.3	-56.5
TS-3	-8287520.1	-3157.31410	-3156.90901	985.6	-42.3
TS-30_iBu	-9727983.7	-3706.19967	-3705.84111	1762.0	-61.3
TS-30_tBu	-9727936.7	-3706.18514	-3705.82663	1767.8	-58.1
TS-31_iBu	-10025304.1	-3819.45271	-3819.08923	1764.0	-50.8
TS-31_tBu	-10025279.6	-3819.44399	-3819.08209	1770.2	-51.2
TS-32_iBu	-5750063.2	-2190.52582	-2190.12974	130.6	-9.0
TS-32_tBu	-5750070.7	-2190.52766	-2190.13201	129.3	-9.3
TS-33_iBu	-5750102.8	-2190.54016	-2190.15246	146.3	-4.7
TS-33_tBu	-5750073.0	-2190.52948	-2190.13920	143.8	-7.2
TS-34_iBu	-6344835.8	-2417.07664	-2416.67920	155.8	-1.3
TS-34_tBu	-6344831.0	-2417.07303	-2416.67854	158.5	-0.9
TS-35	-6119939.5	-2331.41055	-2330.88351	-135.6	-70.0
TS-37_iBu	-8372520.1	-3189.71665	-3189.22599	924.9	-133.3
TS-37_tBu	-8372488.1	-3189.70785	-3189.21786	931.6	-129.4
TS-38_iBu	-8669815.3	-3302.94575	-3302.45704	918.8	-134.4
TS-38_tBu	-8669810.5	-3302.94384	-3302.45709	923.4	-134.1
TS-5	-1110954.8	-423.22285	-423.21941	206.6	1.0
TS-6	-10127851.4	-3858.52984	-3858.15837	1810.2	-68.3
TS-7	-10425176.9	-3971.78423	-3971.40544	1806.4	-59.7
TS-8	-6447299.9	-2456.12729	-2455.71456	195.3	-17.5
TS-9	-6744689.5	-2569.39998	-2568.98988	204.5	-12.1

7.3 Vinylation of Pyrrolidone

7.3.1 Geometries of Computed Species

Due to the large number of calculated species, the XYZ coordinates of the species cannot be included directly in this appendix. Therefore, two supplemental files have been provided with this thesis:

coordinates-vinylation.xyz
coordinates-vinylation.txt

These supplemental files contain the computed Cartesian coordinates of all intermediates and transition states reported in this study. The *.txt* file may be opened to read the coordinates, while the *.xyz* file can directly be opened in molecular modeling/viewing programs such as Mercury (<http://www.ccdc.cam.ac.uk/pages/Home.aspx>) for visualization and analysis.

The XYZ coordinates are given in the following format:

Number of atoms in the species

Compound - Total energy [Hartree] at the level of geometry optimization

XYZ coordinates

7.3.2 Energies

Table 7.3: Total Gibbs free energies $G(\text{Total})$ [kJ mol^{-1}], electronic energies at the level of geometry optimization $E(\text{Opt})$ (BP86/def2-SV(P)) [Hartree], electronic energies at the level of the single-point energy calculations $E(\text{SP})$ (PBE0-D3(BJ)/def2-QZVPP) [Hartree], thermodynamic corrections $\Delta G(\text{Therm})$ [kJ mol^{-1}], and solvent corrections $\Delta G(\text{Solv})$ [kJ mol^{-1}] for the vinylation of pyrrolidone to NVP.

Structure	$G(\text{Total})$ [kJ mol^{-1}]	$E(\text{Opt})$ BP86/ def2-SV(P) [Hartree]	$E(\text{SP})$ PBE0-D3(BJ)/ def2-QZVPP [Hartree]	$\Delta G(\text{therm})$ [kJ mol^{-1}]	$\Delta G(\text{solv})$ [kJ mol^{-1}]
1	-202853.5	-77.26481	-77.26103	-22.9	18.2
3	-751900.3	-286.42510	-286.44014	155.4	-7.2
4	-3092323.9	-1178.16047	-1178.18211	1036.3	-43.5
5	-3092379.4	-1178.18626	-1178.21127	1047.9	-34.1
6	-3844258.1	-1464.62955	-1464.67065	1288.5	-54.4
7	-3092283.0	-1178.14875	-1178.16868	1038.1	-39.7
8	-3092302.7	-1178.15412	-1178.17736	1042.3	-40.8
9	-954775.9	-363.72933	-363.73800	219.8	-1.7
10	-3092271.5	-1178.14409	-1178.16636	1039.4	-35.6
11	-3147014.2	-1198.99368	-1199.00985	1024.2	-38.5

Section 7.3 – Vinylation of Pyrrolidone

12	-5229889.3	-1992.60189	-1992.64115	1851.6	-62.3
13	-5981753.1	-2279.04392	-2279.10075	2097.6	-72.5
15	-2543259.0	-968.96828	-968.97484	830.1	-46.0
16	-2543265.8	-968.98106	-968.98236	830.1	-33.1
17	-3092293.1	-1178.14953	-1178.18146	1050.9	-29.0
18	-757306.1	-288.52431	-288.52407	214.1	-0.4
19	-906501.2	-345.32797	-345.32200	145.6	-4.0
25	-2543308.9	-968.99936	-969.00271	859.7	-52.4
26	-2746312.1	-1046.34297	-1046.33947	928.5	-76.7
27	-2543410.1	-969.05494	-969.06121	874.5	-14.7
28	-2746491.3	-1046.42341	-1046.43013	943.4	-32.8
12_BF4	-5593632.2	-2130.95927	-2131.10934	1659.3	-64.7
12_PhOH	-5284595.5	-2013.44051	-2013.46804	1834.6	-70.5
13_PhOH	-6091206.2	-2320.73048	-2320.77158	2060.3	-81.6
14_cis	-953328.5	-363.11553	-363.12783	185.9	-122.4
14_trans	-953330.2	-363.12301	-363.13458	187.6	-108.1
17_NVP	-3295287.9	-1255.49702	-1255.52300	1121.5	-34.3
18_NVP	-960301.5	-365.87200	-365.86482	280.1	-3.6
2_cis	-2340359.3	-891.67466	-891.67927	783.6	-39.3
2_cis-PMe3	-1412700.8	-538.15761	-538.14020	211.9	-25.7
2_cis-PPh3	-2921449.8	-1112.96751	-1112.91482	559.2	-51.6
2_trans	-2340385.6	-891.68841	-891.69307	785.6	-31.4
2_trans-PMe3	-1412714.1	-538.16658	-538.15036	215.5	-16.0
2_trans-PPh3	-2921460.4	-1112.97003	-1112.92017	558.5	-47.4
20_cis	-3998870.8	-1523.52392	-1523.55742	1290.5	-61.9
21_cis	-3998890.0	-1523.53894	-1523.57297	1301.3	-51.1
21_trans	-3998885.0	-1523.54078	-1523.57277	1305.1	-50.5
22_cis	-1663955.4	-633.93302	-633.93350	461.8	-25.1
22_trans	-1663970.9	-633.93957	-633.93841	459.7	-25.5
23_cis-C2H3	-4047195.1	-1541.95425	-1542.00233	1384.2	-52.7
23_cis-H	-3844187.9	-1464.60283	-1464.65749	1315.4	-45.6
23_trans-C2H3	-4047182.3	-1541.95191	-1542.00062	1388.0	-48.2
23_trans-H	-3844194.3	-1464.60585	-1464.66001	1315.6	-45.6
24_cis-C2H3	-1712261.5	-652.34538	-652.35837	533.3	-28.1
24_cis-H	-1509296.2	-575.01747	-575.03568	477.6	-17.8
24_trans-C2H3	-1712272.8	-652.35485	-652.36776	540.8	-22.3
24_trans-H	-1509284.8	-575.00959	-575.02847	472.8	-20.6
4_BF4	-3456068.5	-1316.51073	-1316.64475	830.7	-48.9
4_PhOH	-3147036.2	-1198.99776	-1199.00427	1003.8	-54.7
4_PMe3	-2164656.0	-824.63789	-824.63568	458.0	-33.3
4_PPh3	-3673376.0	-1399.42288	-1399.39472	798.7	-64.4
5_PMe3	-2164728.0	-824.67418	-824.67726	477.7	-15.9
5_PPh3	-3673485.7	-1399.47248	-1399.44539	811.8	-54.2
6_PhOH	-3898966.4	-1485.46705	-1485.49303	1259.7	-64.6

Chapter 7 – Appendix

6_PMe3	-2916593.3	-1111.11214	-1111.12939	719.9	-43.4
6_PPh3	-4425332.3	-1685.90285	-1685.89385	1060.0	-78.7
7_PMe3	-2164617.1	-824.63084	-824.62844	466.8	-22.2
7_PPh3	-3673359.4	-1399.43682	-1399.40008	816.5	-51.5
NVP	-954880.2	-363.77040	-363.77830	226.4	-6.8
OPnBu3	-2335109.4	-889.63760	-889.66908	737.1	-20.7
PhOH	-806557.5	-307.24439	-307.25379	138.7	-1.5
PMe3	-1209923.1	-460.92297	-460.89770	155.2	8.5
PnBu3	-2137568.3	-814.43463	-814.43069	730.7	-11.6
PPh3	-2718702.0	-1035.73249	-1035.67485	493.6	-31.6
TS-1_cis	-2340322.6	-891.67273	-891.66856	784.4	-31.5
TS-1_cis-PMe3	-1412673.9	-538.15679	-538.13265	211.8	-18.7
TS-1_cis-PPh3	-2921432.7	-1112.96648	-1112.90800	554.5	-47.6
TS-1_trans	-2340314.4	-891.67449	-891.66776	779.5	-20.6
TS-1_trans-PMe3	-1412645.5	-538.15374	-538.12619	209.9	-5.3
TS-1_trans-PPh3	-2921405.1	-1112.95746	-1112.89749	547.5	-40.6
TS-10	-5229820.9	-1992.58841	-1992.61970	1863.9	-62.6
TS-10_BF4	-5593584.4	-2130.95076	-2131.08932	1651.2	-61.4
TS-10_PhOH	-5284543.2	-2013.43162	-2013.45037	1835.2	-65.2
TS-11_cis	-953252.3	-363.09647	-363.10364	171.2	-95.0
TS-11_trans	-953230.8	-363.08924	-363.09685	173.1	-93.3
TS-12	-2543201.6	-968.93752	-968.94160	828.2	-74.0
TS-13	-2543237.0	-968.96522	-968.96835	830.9	-41.9
TS-14	-3092207.6	-1178.11787	-1178.14319	1044.5	-37.6
TS-14_NVP	-3295214.4	-1255.46739	-1255.48671	1109.1	-43.7
TS-15	-3092220.2	-1178.11809	-1178.15069	1045.1	-31.1
TS-15_NVP	-3295198.9	-1255.46133	-1255.48845	1119.0	-33.5
TS-16_cis	-3998843.4	-1523.52057	-1523.54867	1291.0	-57.9
TS-16_trans	-3998835.2	-1523.52190	-1523.54877	1294.8	-53.3
TS-17_cis	-3998791.7	-1523.50354	-1523.53383	1293.7	-47.9
TS-17_trans	-3998795.6	-1523.50401	-1523.53408	1290.7	-48.1
TS-18_cis-C2H3	-4047156.3	-1541.94126	-1541.98285	1376.8	-57.7
TS-18_cis-H	-3844148.4	-1464.59292	-1464.63866	1307.4	-47.6
TS-18_trans-C2H3	-4047143.0	-1541.93570	-1541.97942	1379.8	-56.4
TS-18_trans-H	-3844145.3	-1464.58728	-1464.63561	1306.4	-51.5
TS-19_cis-C2H3	-4047126.1	-1541.92884	-1541.97639	1381.2	-48.8
TS-19_cis-H	-3844155.3	-1464.58986	-1464.64319	1308.7	-43.9
TS-19_trans-C2H3	-4047135.0	-1541.93074	-1541.97999	1379.4	-46.5
TS-19_trans-H	-3844155.3	-1464.58732	-1464.64187	1306.5	-45.0
TS-2_cis	-3092237.9	-1178.12691	-1178.14279	1022.1	-46.5
TS-2_cis-PMe3	-2164573.0	-824.60792	-824.60254	450.3	-29.7
TS-2_cis-PPh3	-3673336.0	-1399.41350	-1399.37549	789.9	-66.1
TS-2_trans	-3092271.9	-1178.14258	-1178.16225	1030.0	-37.4
TS-2_trans-PMe3	-2164608.8	-824.62176	-824.61892	452.5	-24.6

Section 7.3 – Vinylolation of Pyrrolidone

TS-2_trans-PPh3	-3673349.9	-1399.41555	-1399.38371	790.1	-58.6
TS-20	-2543159.7	-968.94160	-968.94250	833.6	-35.2
TS-21	-2746117.0	-1046.26461	-1046.26452	902.6	-52.5
TS-3	-3092298.7	-1178.15775	-1178.17908	1047.8	-37.7
TS-3_PMe3	-2164627.0	-824.63781	-824.63575	474.3	-20.4
TS-3_PPh3	-3673360.7	-1399.43172	-1399.40121	818.4	-51.7
TS-4	-3092280.8	-1178.14163	-1178.16232	1036.3	-52.3
TS-5	-3092249.9	-1178.14144	-1178.16026	1046.1	-36.6
TS-6	-3092109.9	-1178.08008	-1178.09801	1030.8	-44.7
TS-6_PMe3	-2164450.0	-824.56305	-824.55892	455.5	-26.4
TS-6_PPh3	-3673203.4	-1399.37211	-1399.33203	799.7	-57.3
TS-7	-3844231.6	-1464.61788	-1464.65679	1280.8	-56.5
TS-7_PhOH	-3898941.8	-1485.45982	-1485.48986	1266.5	-55.2
TS-7_PMe3	-2916585.7	-1111.11127	-1111.12599	713.3	-38.1
TS-7_PPh3	-4425317.7	-1685.90197	-1685.89014	1060.6	-74.4
TS-8	-3844172.2	-1464.59563	-1464.62831	1274.5	-65.7
TS-8_PhOH	-3898838.2	-1485.42991	-1485.44784	1259.4	-54.9
TS-8_PMe3	-2916500.0	-1111.07778	-1111.08650	703.9	-46.7
TS-8_PPh3	-4425231.6	-1685.87475	-1685.85332	1049.4	-73.8
TS-9	-3147014.9	-1198.99163	-1199.00707	1028.9	-51.2

8

References

- (1) American Chemical Society (ACS), *12 Principles of Green Chemistry*. <https://www.acs.org/content/acs/en/greenchemistry/principles/12-principles-of-green-chemistry.html> (accessed on July 22nd, 2021)
- (2) Schaub, T., Efficient Industrial Organic Synthesis and the Principles of Green Chemistry. *Chem. Eur. J.* **2021**, *27*, 1865-1869.
- (3) Schrödinger, E., An Undulatory Theory of the Mechanics of Atoms and Molecules. *Phys. Rev.* **1926**, *28*, 1049-1070.
- (4) Hartree, D. R., The Wave Mechanics of an Atom with a Non-Coulomb Central Field. Part I. Theory and Methods. *Math. Proc. Cambridge* **1928**, *24*, 89-110.
- (5) Fock, V., Näherungsmethode zur Lösung des quantenmechanischen Mehrkörperproblems. *Z. Phys.* **1930**, *61*, 126-148.
- (6) Roothaan, C. C. J., New Developments in Molecular Orbital Theory. *Rev. Mod. Phys.* **1951**, *23*, 69-89.
- (7) Hall, G. G., The molecular orbital theory of chemical valency VIII. A method of calculating ionization potentials. *P. Roy. Soc. Lond. A Mat.* **1951**, *205*, 541-552.

- (8) Frisch, M. J.; Trucks, G. W.; Schlegel, H. B.; Scuseria, G. E.; Robb, M. A.; Cheeseman, J. R.; Scalmani, G.; Barone, V.; Petersson, G. A.; Nakatsuji, H.; Li, X.; Caricato, M.; Marenich, A. V.; Bloino, J.; Janesko, B. G.; Gomperts, R.; Mennucci, B.; Hratchian, H. P.; Ortiz, J. V.; Izmaylov, A. F.; Sonnenberg, J. L.; Williams; Ding, F.; Lipparini, F.; Egidi, F.; Goings, J.; Peng, B.; Petrone, A.; Henderson, T.; Ranasinghe, D.; Zakrzewski, V. G.; Gao, J.; Rega, N.; Zheng, G.; Liang, W.; Hada, M.; Ehara, M.; Toyota, K.; Fukuda, R.; Hasegawa, J.; Ishida, M.; Nakajima, T.; Honda, Y.; Kitao, O.; Nakai, H.; Vreven, T.; Throssell, K.; Montgomery Jr., J. A.; Peralta, J. E.; Ogliaro, F.; Bearpark, M. J.; Heyd, J. J.; Brothers, E. N.; Kudin, K. N.; Staroverov, V. N.; Keith, T. A.; Kobayashi, R.; Normand, J.; Raghavachari, K.; Rendell, A. P.; Burant, J. C.; Iyengar, S. S.; Tomasi, J.; Cossi, M.; Millam, J. M.; Klene, M.; Adamo, C.; Cammi, R.; Ochterski, J. W.; Martin, R. L.; Morokuma, K.; Farkas, O.; Foresman, J. B.; Fox, D. J., *Gaussian 16 Rev. C.01*, **2016**.
- (9) Becke, A. D., Density-functional exchange-energy approximation with correct asymptotic behavior. *Physical Review A* **1988**, *38*, 3098-3100.
- (10) Lee, C.; Yang, W.; Parr, R. G., Development of the Colle-Salvetti correlation-energy formula into a functional of the electron density. *Phys. Rev. B* **1988**, *37*, 785-789.
- (11) Becke, A. D., Density-functional thermochemistry. III. The role of exact exchange. *J. Chem. Phys.* **1993**, *98*, 5648-5652.
- (12) Moore, G. E., Cramping more components onto integrated circuits. *Electronics* **1965**, *38*, 114-117.
- (13) Quantum Technology and Application Consortium (QUTAC), Quantum Computing: Leading German corporations agree on large-scale application. *Press Release* **2021**.
- (14) Prometheus GmbH, *Top500 Supercomputer List - System: Curiosity*. <https://www.top500.org/system/179110/> (accessed on July 14th, 2021)
- (15) Szabo, A.; Ostlund, N. S., *Modern Quantum Chemistry*. McGraw-Hill, Inc.: New York, **1989**.
- (16) Koch, W.; Holthausen, M. C., *A Chemist's Guide to Density Functional Theory*. Wiley-VCH: Weinheim, **2001**.
- (17) Jensen, F., *Introduction to Computational Chemistry*. Wiley-VCH: Weinheim, **2017**.
- (18) Harvey, J., *Computational Chemistry*. Oxford University Press: Oxford, **2018**.
- (19) Born, M.; Oppenheimer, R., Zur Quantentheorie der Molekeln. *Ann. Phys.* **1927**, *389*, 457-484.
- (20) Pauli, W., Über den Zusammenhang des Abschlusses der Elektronengruppen im Atom mit der Komplexstruktur der Spektren. *Z. Phys.* **1925**, *31*, 765-783.

-
- (21) Slater, J. C., The Theory of Complex Spectra. *Phys. Rev.* **1929**, *34*, 1293-1322.
- (22) Slater, J. C., Atomic Shielding Constants. *Phys. Rev.* **1930**, *36*, 57-64.
- (23) Boys, S. F., Electronic wave functions - I. A general method of calculation for the stationary states of any molecular system. *P. Roy. Soc. Lond. A Mat.* **1950**, *200*, 542 - 554.
- (24) Kato, T., On the eigenfunctions of many-particle systems in quantum mechanics. *Commun. Pur. Appl. Math.* **1957**, *10*, 151-177.
- (25) March, N. H., Spatially dependent generalization of Kato's theorem for atomic closed shells in a bare Coulomb field. *Phys. Rev. A* **1986**, *33*, 88-89.
- (26) Hehre, W. J.; Stewart, R. F.; Pople, J. A., Self-Consistent Molecular-Orbital Methods. I. Use of Gaussian Expansions of Slater-Type Atomic Orbitals. *J. Chem. Phys.* **1969**, *51*, 2657-2664.
- (27) Ditchfield, R.; Hehre, W. J.; Pople, J. A., Self-Consistent Molecular-Orbital Methods. IX. An Extended Gaussian-Type Basis for Molecular-Orbital Studies of Organic Molecules. *J. Chem. Phys.* **1971**, *54*, 724-728.
- (28) Hehre, W. J.; Ditchfield, R.; Pople, J. A., Self-Consistent Molecular Orbital Methods. XII. Further Extensions of Gaussian—Type Basis Sets for Use in Molecular Orbital Studies of Organic Molecules. *J. Chem. Phys.* **1972**, *56*, 2257-2261.
- (29) Hariharan, P. C.; Pople, J. A., The influence of polarization functions on molecular orbital hydrogenation energies. *Theor. Chim. Acta* **1973**, *28*, 213-222.
- (30) Binkley, J. S.; Pople, J. A.; Hehre, W. J., Self-consistent molecular orbital methods. 21. Small split-valence basis sets for first-row elements. *J. Am. Chem. Soc.* **1980**, *102*, 939-947.
- (31) Francl, M. M.; Pietro, W. J.; Hehre, W. J.; Binkley, J. S.; Gordon, M. S.; DeFrees, D. J.; Pople, J. A., Self-consistent molecular orbital methods. XXIII. A polarization-type basis set for second-row elements. *J. Chem. Phys.* **1982**, *77*, 3654-3665.
- (32) Gordon, M. S.; Binkley, J. S.; Pople, J. A.; Pietro, W. J.; Hehre, W. J., Self-consistent molecular-orbital methods. 22. Small split-valence basis sets for second-row elements. *J. Am. Chem. Soc.* **1982**, *104*, 2797-2803.
- (33) Pietro, W. J.; Francl, M. M.; Hehre, W. J.; DeFrees, D. J.; Pople, J. A.; Binkley, J. S., Self-consistent molecular orbital methods. 24. Supplemented small split-valence basis sets for second-row elements. *J. Am. Chem. Soc.* **1982**, *104*, 5039-5048.
- (34) Dunning, T. H., Gaussian basis sets for use in correlated molecular calculations. I. The atoms boron through neon and hydrogen. *J. Chem. Phys.* **1989**, *90*, 1007-1023.
-

- (35) Kendall, R. A.; Dunning, T. H.; Harrison, R. J., Electron affinities of the first-row atoms revisited. Systematic basis sets and wave functions. *J. Chem. Phys.* **1992**, *96*, 6796-6806.
- (36) Schäfer, A.; Horn, H.; Ahlrichs, R., Fully optimized contracted Gaussian basis sets for atoms Li to Kr. *J. Chem. Phys.* **1992**, *97*, 2571-2577.
- (37) Schäfer, A.; Huber, C.; Ahlrichs, R., Fully optimized contracted Gaussian basis sets of triple zeta valence quality for atoms Li to Kr. *J. Chem. Phys.* **1994**, *100*, 5829-5835.
- (38) Weigend, F.; Furche, F.; Ahlrichs, R., Gaussian basis sets of quadruple zeta valence quality for atoms H–Kr. *J. Chem. Phys.* **2003**, *119*, 12753-12762.
- (39) Weigend, F.; Ahlrichs, R., Balanced basis sets of split valence, triple zeta valence and quadruple zeta valence quality for H to Rn: Design and assessment of accuracy. *Physical Chemistry Chemical Physics* **2005**, *7*, 3297-3305.
- (40) Weigend, F., Accurate Coulomb-fitting basis sets for H to Rn. *Physical Chemistry Chemical Physics* **2006**, *8*, 1057-1065.
- (41) Hohenberg, P.; Kohn, W., Inhomogeneous Electron Gas. *Phys. Rev.* **1964**, *136*, B864-B871.
- (42) Kohn, W.; Sham, L. J., Self-Consistent Equations Including Exchange and Correlation Effects. *Phys. Rev.* **1965**, *140*, A1133-A1138.
- (43) Perdew, J. P.; Schmidt, K., Jacob's ladder of density functional approximations for the exchange-correlation energy. *AIP Conf. Proc.* **2001**, *577*, 1-20.
- (44) Perdew, J. P.; Ruzsinszky, A.; Tao, J.; Staroverov, V. N.; Scuseria, G. E.; Csonka, G. I., Prescription for the design and selection of density functional approximations: More constraint satisfaction with fewer fits. *J. Chem. Phys.* **2005**, *123*, 062201.
- (45) Hermsen, M., Quantum Chemical Investigations in Homogeneous Catalysis: Dehydroperoxidation and Asymmetric Reductive Amination (PhD Thesis). Ruprecht-Karls-Universität Heidelberg, **2018**.
- (46) Vosko, S. H.; Wilk, L.; Nusair, M., Accurate spin-dependent electron liquid correlation energies for local spin density calculations: a critical analysis. *Can. J. Phys.* **1980**, *58*, 1200-1211.
- (47) Perdew, J. P.; Wang, Y., Accurate and simple analytic representation of the electron-gas correlation energy. *Phys. Rev. B* **1992**, *45*, 13244-13249.
- (48) Perdew, J. P., Accurate Density Functional for the Energy: Real-Space Cutoff of the Gradient Expansion for the Exchange Hole. *Phys. Rev. Lett.* **1985**, *55*, 1665-1668.

-
- (49) Perdew, J. P.; Chevary, J. A.; Vosko, S. H.; Jackson, K. A.; Pederson, M. R.; Singh, D. J.; Fiolhais, C., Atoms, molecules, solids, and surfaces: Applications of the generalized gradient approximation for exchange and correlation. *Phys. Rev. B* **1992**, *46*, 6671-6687.
- (50) Burke, K.; Perdew, J. P.; Ernzerhof, M., Why the generalized gradient approximation works and how to go beyond it. *Int. J. Quantum Chem.* **1997**, *61*, 287-293.
- (51) Perdew, J. P., Density-functional approximation for the correlation energy of the inhomogeneous electron gas. *Physical Review B* **1986**, *33*, 8822-8824.
- (52) Perdew, J. P.; Burke, K.; Ernzerhof, M., Generalized Gradient Approximation Made Simple. *Phys. Rev. Lett.* **1996**, *77*, 3865-3868.
- (53) Tao, J.; Perdew, J. P.; Staroverov, V. N.; Scuseria, G. E., Climbing the Density Functional Ladder: Nonempirical Meta-Generalized Gradient Approximation Designed for Molecules and Solids. *Phys. Rev. Lett.* **2003**, *91*, 146401.
- (54) Zhao, Y.; Truhlar, D. G., The M06 suite of density functionals for main group thermochemistry, thermochemical kinetics, noncovalent interactions, excited states, and transition elements: two new functionals and systematic testing of four M06-class functionals and 12 other functionals. *Theor. Chem. Acc.* **2008**, *120*, 215-241.
- (55) Zhao, Y.; Truhlar, D. G., Density Functionals with Broad Applicability in Chemistry. *Acc. Chem. Res.* **2008**, *41*, 157-167.
- (56) Peverati, R.; Truhlar, D. G., Improving the Accuracy of Hybrid Meta-GGA Density Functionals by Range Separation. *J. Phys. Chem. Lett.* **2011**, *2*, 2810-2817.
- (57) Salomon, O.; Reiher, M.; Hess, B. A., Assertion and validation of the performance of the B3LYP* functional for the first transition metal row and the G2 test set. *J. Chem. Phys.* **2002**, *117*, 4729-4737.
- (58) Mardirossian, N.; Head-Gordon, M., Thirty years of density functional theory in computational chemistry: an overview and extensive assessment of 200 density functionals. *Mol. Phys.* **2017**, *115*, 2315-2372.
- (59) Grimme, S., Semiempirical hybrid density functional with perturbative second-order correlation. *J. Chem. Phys.* **2006**, *124*, 034108.
- (60) Eichkorn, K.; Treutler, O.; Öhm, H.; Häser, M.; Ahlrichs, R., Auxiliary basis sets to approximate Coulomb potentials. *Chem. Phys. Lett.* **1995**, *240*, 283-290.
- (61) Whitten, J. L., Coulombic potential energy integrals and approximations. *J. Chem. Phys.* **1973**, *58*, 4496-4501.
- (62) Vahtras, O.; Almlöf, J.; Feyereisen, M. W., Integral approximations for LCAO-SCF calculations. *Chemical Physics Letters* **1993**, *213*, 514-518.
-

- (63) Deglmann, P.; May, K.; Furche, F.; Ahlrichs, R., Nuclear second analytical derivative calculations using auxiliary basis set expansions. *Chem. Phys. Lett.* **2004**, 384, 103-107.
- (64) Weigend, F., A fully direct RI-HF algorithm: Implementation, optimised auxiliary basis sets, demonstration of accuracy and efficiency. *Phys. Chem. Chem. Phys.* **2002**, 4, 4285-4291.
- (65) Eisenschitz, R.; London, F., Über das Verhältnis der van der Waalsschen Kräfte zu den homöopolaren Bindungskräften. *Z. Phys.* **1930**, 60, 491-527.
- (66) London, F., Zur Theorie und Systematik der Molekularkräfte. *Z. Phys.* **1930**, 63, 245-279.
- (67) London, F., The general theory of molecular forces. *T. Faraday Soc.* **1937**, 33, 8b-26.
- (68) Grimme, S., Semiempirical GGA-type density functional constructed with a long-range dispersion correction. *J. Comput. Chem.* **2006**, 27, 1787-1799.
- (69) Grimme, S.; Antony, J.; Ehrlich, S.; Krieg, H., A consistent and accurate ab initio parametrization of density functional dispersion correction (DFT-D) for the 94 elements H-Pu. *The Journal of Chemical Physics* **2010**, 132, 154104-154119.
- (70) Goerigk, L.; Grimme, S., A thorough benchmark of density functional methods for general main group thermochemistry, kinetics, and noncovalent interactions. *Phys. Chem. Chem. Phys.* **2011**, 13, 6670-6688.
- (71) Grimme, S., Density functional theory with London dispersion corrections. *WIREs Comput. Mol. Sci.* **2011**, 1, 211-228.
- (72) Caldeweyher, E.; Bannwarth, C.; Grimme, S., Extension of the D3 dispersion coefficient model. *J. Chem. Phys.* **2017**, 147, 034112.
- (73) Caldeweyher, E.; Ehlert, S.; Hansen, A.; Neugebauer, H.; Spicher, S.; Bannwarth, C.; Grimme, S., A generally applicable atomic-charge dependent London dispersion correction. *J. Chem. Phys.* **2019**, 150, 154122.
- (74) Grimme, S.; Ehrlich, S.; Goerigk, L., Effect of the damping function in dispersion corrected density functional theory. *Journal of Computational Chemistry* **2011**, 32, 1456-1465.
- (75) Klamt, A., Conductor-like Screening Model for Real Solvents: A New Approach to the Quantitative Calculation of Solvation Phenomena. *The Journal of Physical Chemistry* **1995**, 99, 2224-2235.
- (76) Klamt, A.; Jonas, V.; Bürger, T.; Lohrenz, J. C. W., Refinement and Parametrization of COSMO-RS. *J. Phys. Chem. A* **1998**, 102, 5074-5085.

-
- (77) Eckert, F.; Klamt, A., Fast solvent screening via quantum chemistry: COSMO-RS approach. *AIChE J.* **2002**, *48*, 369-385.
- (78) Miertuš, S.; Scrocco, E.; Tomasi, J., Electrostatic interaction of a solute with a continuum. A direct utilization of AB initio molecular potentials for the prevision of solvent effects. *Chem. Phys.* **1981**, *55*, 117-129.
- (79) Miertuš, S.; Tomasi, J., Approximate evaluations of the electrostatic free energy and internal energy changes in solution processes. *Chem. Phys.* **1982**, *65*, 239-245.
- (80) Klamt, A.; Schüürmann, G., COSMO: a new approach to dielectric screening in solvents with explicit expressions for the screening energy and its gradient. *J. Chem. Soc. Perk. T. 2* **1993**, 799-805.
- (81) Ferrarini, F.; Flôres, G. B.; Muniz, A. R.; de Soares, R. P., An open and extensible sigma-profile database for COSMO-based models. *AIChE J.* **2018**, *64*, 3443-3455.
- (82) Pyykko, P., Relativistic effects in structural chemistry. *Chem. Rev.* **1988**, *88*, 563-594.
- (83) Dolg, M.; Cao, X., Relativistic Pseudopotentials: Their Development and Scope of Applications. *Chem. Rev.* **2012**, *112*, 403-480.
- (84) Andrae, D.; Häußermann, U.; Dolg, M.; Stoll, H.; Preuß, H., Energy-adjusted ab initio pseudopotentials for the second and third row transition elements. *Theoretica chimica acta* **1990**, *77*, 123-141.
- (85) Ahlrichs, R.; Bär, M.; Häser, M.; Horn, H.; Kölmel, C., Electronic structure calculations on workstation computers: The program system turbomole. *Chem. Phys. Lett.* **1989**, *162*, 165-169.
- (86) Treutler, O.; Ahlrichs, R., Efficient molecular numerical integration schemes. *J. Chem. Phys.* **1995**, *102*, 346-354.
- (87) Balasubramani, S. G.; Chen, G. P.; Coriani, S.; Diedenhofen, M.; Frank, M. S.; Franzke, Y. J.; Furche, F.; Grotjahn, R.; Harding, M. E.; Hättig, C.; Hellweg, A.; Helmich-Paris, B.; Holzer, C.; Huniar, U.; Kaupp, M.; Marefat Khah, A.; Karbalaei Khani, S.; Müller, T.; Mack, F.; Nguyen, B. D.; Parker, S. M.; Perlt, E.; Rappoport, D.; Reiter, K.; Roy, S.; Rückert, M.; Schmitz, G.; Sierka, M.; Tapavicza, E.; Tew, D. P.; van Wüllen, C.; Voora, V. K.; Weigend, F.; Wodyński, A.; Yu, J. M., TURBOMOLE: Modular program suite for ab initio quantum-chemical and condensed-matter simulations. *J. Chem. Phys.* **2020**, *152*, 184107.
- (88) TURBOMOLE V7.3 2018, a development of University of Karlsruhe and Forschungszentrum Karlsruhe GmbH, TURBOMOLE GmbH, available from <http://www.turbomole.org>.
- (89) COSMOtherm, Version 18.0.0 (Revision 4360), COSMOlogic GmbH & Co KG, available from <http://www.cosmologic.de>.
-

- (90) Feng, X.; Gu, J.; Xie, Y.; King, R. B.; Schaefer, H. F., Homoleptic Carbonyls of the Second-Row Transition Metals: Evaluation of Hartree–Fock and Density Functional Theory Methods. *J. Chem. Theory Comput.* **2007**, *3*, 1580-1587.
- (91) Minenkov, Y.; Singstad, Å.; Occhipinti, G.; Jensen, V. R., The accuracy of DFT-optimized geometries of functional transition metal compounds: a validation study of catalysts for olefin metathesis and other reactions in the homogeneous phase. *Dalton Trans.* **2012**, *41*, 5526-5541.
- (92) Plessow, P. N., New Insights into Homogeneously Catalyzed Reactions: Theoretical Investigations (PhD Thesis). Ruprecht-Karls-Universität Heidelberg, **2014**.
- (93) Ernzerhof, M.; Scuseria, G. E., Assessment of the Perdew–Burke–Ernzerhof exchange-correlation functional. *The Journal of Chemical Physics* **1999**, *110*, 5029-5036.
- (94) Pople, J. A.; Head-Gordon, M.; Fox, D. J.; Raghavachari, K.; Curtiss, L. A., Gaussian-1 theory: A general procedure for prediction of molecular energies. *J. Chem. Phys.* **1989**, *90*, 5622-5629.
- (95) Ryu, H.; Park, J.; Kim, H. K.; Park, J. Y.; Kim, S.-T.; Baik, M.-H., Pitfalls in Computational Modeling of Chemical Reactions and How To Avoid Them. *Organometallics* **2018**, *37*, 3228-3239.
- (96) Yang, M.; Zou, J.; Wang, G.; Li, S., Automatic Reaction Pathway Search via Combined Molecular Dynamics and Coordinate Driving Method. *J. Phys. Chem. A* **2017**, *121*, 1351-1361.
- (97) Grimme, S., Exploration of Chemical Compound, Conformer, and Reaction Space with Meta-Dynamics Simulations Based on Tight-Binding Quantum Chemical Calculations. *J. Chem. Theory Comput.* **2019**, *15*, 2847-2862.
- (98) Kopecký, S.; Martínez-Núñez, E.; Soto, J.; Peláez, D., vdW-TSSCDS—An automated and global procedure for the computation of stationary points on intermolecular potential energy surfaces. *Int. J. Quantum Chem.* **2019**, *0*, e26008.
- (99) Maeda, S.; Harabuchi, Y., On Benchmarking of Automated Methods for Performing Exhaustive Reaction Path Search. *J. Chem. Theory Comput.* **2019**, *15*, 2111-2115.
- (100) Robertson, C.; Habershon, S., Fast screening of homogeneous catalysis mechanisms using graph-driven searches and approximate quantum chemistry. *Catal. Sci. Technol.* **2019**.
- (101) Zimmerman, P., Reliable Transition State Searches Integrated with the Growing String Method. *J. Chem. Theory Comput.* **2013**, *9*, 3043-3050.
- (102) Zimmerman, P. M., Navigating molecular space for reaction mechanisms: an efficient, automated procedure. *Mol. Simulat.* **2015**, *41*, 43-54.

-
- (103) Fukui, K., The path of chemical reactions - the IRC approach. *Accounts of Chemical Research* **1981**, *14*, 363-368.
- (104) Evans, M. G.; Polanyi, M., Some applications of the transition state method to the calculation of reaction velocities, especially in solution. *T. Faraday Soc.* **1935**, *31*, 875-894.
- (105) Besora, M.; Maseras, F., Microkinetic modeling in homogeneous catalysis. *WIREs Comput. Mol. Sci.* **2018**, *8*, e1372.
- (106) Harvey, J. N.; Himo, F.; Maseras, F.; Perrin, L., Scope and Challenge of Computational Methods for Studying Mechanism and Reactivity in Homogeneous Catalysis. *ACS Catal.* **2019**, *9*, 6803-6813.
- (107) Jaraíz, M.; Rubio, J. E.; Enríquez, L.; Pinacho, R.; López-Pérez, J. L.; Lesarri, A., An Efficient Microkinetic Modeling Protocol: Start with Only the Dominant Mechanisms, Adjust All Parameters, and Build the Complete Model Incrementally. *ACS Catal.* **2019**, *9*, 4804-4809.
- (108) Ager, D. J.; de Vries, A. H. M.; de Vries, J. G., Asymmetric homogeneous hydrogenations at scale. *Chem. Soc. Rev.* **2012**, *41*, 3340-3380.
- (109) de Vries, J. G., *The Handbook of Homogeneous Hydrogenation*. Wiley-VCH: Weinheim, **2007**.
- (110) Pritchard, J.; Filonenko, G. A.; van Putten, R.; Hensen, E. J. M.; Pidko, E. A., Heterogeneous and homogeneous catalysis for the hydrogenation of carboxylic acid derivatives: history, advances and future directions. *Chem. Soc. Rev.* **2015**, *44*, 3808-3833.
- (111) Zhang, J.; Leitus, G.; Ben-David, Y.; Milstein, D., Facile Conversion of Alcohols into Esters and Dihydrogen Catalyzed by New Ruthenium Complexes. *J. Am. Chem. Soc.* **2005**, *127*, 10840-10841.
- (112) Zhang, J.; Leitus, G.; Ben-David, Y.; Milstein, D., Efficient Homogeneous Catalytic Hydrogenation of Esters to Alcohols. *Angew. Chem. Int. Ed.* **2006**, *45*, 1113-1115.
- (113) Spasyuk, D.; Gusev, D. G., Acceptorless Dehydrogenative Coupling of Ethanol and Hydrogenation of Esters and Imines. *Organometallics* **2012**, *31*, 5239-5242.
- (114) Filonenko, G. A.; Aguila, M. J. B.; Schulpen, E. N.; van Putten, R.; Wiecko, J.; Müller, C.; Lefort, L.; Hensen, E. J. M.; Pidko, E. A., Bis-N-heterocyclic Carbene Aminopincer Ligands Enable High Activity in Ru-Catalyzed Ester Hydrogenation. *J. Am. Chem. Soc.* **2015**, *137*, 7620-7623.
- (115) Spasyuk, D.; Vicent, C.; Gusev, D. G., Chemoselective Hydrogenation of Carbonyl Compounds and Acceptorless Dehydrogenative Coupling of Alcohols. *J. Am. Chem. Soc.* **2015**, *137*, 3743-3746.
-

- (116) Spasyuk, D.; Smith, S.; Gusev, D. G., Replacing Phosphorus with Sulfur for the Efficient Hydrogenation of Esters. *Angew. Chem. Int. Ed.* **2013**, *52*, 2538-2542.
- (117) Zhang, L.; Raffa, G.; Nguyen, D. H.; Swesi, Y.; Corbel-Demilly, L.; Capet, F.; Trivelli, X.; Desset, S.; Paul, S.; Paul, J.-F.; Fongarland, P.; Dumeignil, F.; Gauvin, R. M., Acceptorless dehydrogenative coupling of alcohols catalysed by ruthenium PNP complexes: Influence of catalyst structure and of hydrogen mass transfer. *J. Catal.* **2016**, *340*, 331-343.
- (118) Nielsen, M.; Kammer, A.; Cozzula, D.; Junge, H.; Gladiali, S.; Beller, M., Efficient Hydrogen Production from Alcohols under Mild Reaction Conditions. *Angew. Chem. Int. Ed.* **2011**, *50*, 9593-9597.
- (119) Nielsen, M.; Junge, H.; Kammer, A.; Beller, M., Towards a Green Process for Bulk-Scale Synthesis of Ethyl Acetate: Efficient Acceptorless Dehydrogenation of Ethanol. *Angew. Chem. Int. Ed.* **2012**, *51*, 5711-5713.
- (120) Oldenhuis, N. J.; Dong, V. M.; Guan, Z., Catalytic acceptorless dehydrogenations: Ru-Macho catalyzed construction of amides and imines. *Tetrahedron* **2014**, *70*, 4213-4218.
- (121) Kuriyama, W.; Matsumoto, T.; Ogata, O.; Ino, Y.; Aoki, K.; Tanaka, S.; Ishida, K.; Kobayashi, T.; Sayo, N.; Saito, T., Catalytic Hydrogenation of Esters. Development of an Efficient Catalyst and Processes for Synthesising (R)-1,2-Propanediol and 2-(1-Menthoxy)ethanol. *Org. Process Res. Dev.* **2012**, *16*, 166-171.
- (122) Fairweather, N. T.; Gibson, M. S.; Guan, H., Homogeneous Hydrogenation of Fatty Acid Methyl Esters and Natural Oils under Neat Conditions. *Organometallics* **2015**, *34*, 335-339.
- (123) Wei, Q.; Zhang, F.; Zhao, X.; Wang, C.; Xiao, J.; Tang, W., Ru-Catalyzed highly diastereoselective hydrogenation of N-tert-butylsulfinyl ketimines for the synthesis of aryl glycine derivatives. *Org. Biomol. Chem.* **2017**, *15*, 5468-5471.
- (124) Han, Z.; Rong, L.; Wu, J.; Zhang, L.; Wang, Z.; Ding, K., Catalytic Hydrogenation of Cyclic Carbonates: A Practical Approach from CO₂ and Epoxides to Methanol and Diols. *Angew. Chem. Int. Ed.* **2012**, *51*, 13041-13045.
- (125) Kothandaraman, J.; Goepfert, A.; Czaun, M.; Olah, G. A.; Prakash, G. K. S., Conversion of CO₂ from Air into Methanol Using a Polyamine and a Homogeneous Ruthenium Catalyst. *J. Am. Chem. Soc.* **2016**, *138*, 778-781.
- (126) A registered trademark of Takasago International Corporation. Kuriyama, W.; Matsumoto, T.; Ino, Y.; Ogata, O. Novel ruthenium carbonyl complex having a tridentate ligand and manufacturing method and usage therefor. WO2011048727A, **2010**.

-
- (127) Bertoli, M.; Choualeb, A.; Lough, A. J.; Moore, B.; Spasyuk, D.; Gusev, D. G., Osmium and Ruthenium Catalysts for Dehydrogenation of Alcohols. *Organometallics* **2011**, *30*, 3479-3482.
- (128) Ding, K.; Han, Z. Novel ruthenium complex and method for preparing methanol and diol. WO2014059757A1, **2013**.
- (129) Alberico, E.; Lennox, A. J. J.; Vogt, L. K.; Jiao, H.; Baumann, W.; Drexler, H.-J.; Nielsen, M.; Spannenberg, A.; Checinski, M. P.; Junge, H.; Beller, M., Unravelling the Mechanism of Basic Aqueous Methanol Dehydrogenation Catalyzed by Ru-PNP Pincer Complexes. *J. Am. Chem. Soc.* **2016**, *138*, 14890-14904.
- (130) Zhang, L.; Nguyen, D. H.; Raffa, G.; Trivelli, X.; Capet, F.; Desset, S.; Paul, S.; Dumeignil, F.; Gauvin, R. M., Catalytic Conversion of Alcohols into Carboxylic Acid Salts in Water: Scope, Recycling, and Mechanistic Insights. *ChemSusChem* **2016**, *9*, 1413-1423.
- (131) Bruch, Q. J.; Lindley, B. M.; Askevold, B.; Schneider, S.; Miller, A. J. M., A Ruthenium Hydrido Dinitrogen Core Conserved across Multielectron/Multiproton Changes to the Pincer Ligand Backbone. *Inorg. Chem.* **2018**, *57*, 1964-1975.
- (132) Choi, J.-H.; Heim, L. E.; Ahrens, M.; Pechtl, M. H. G., Selective conversion of alcohols in water to carboxylic acids by in situ generated ruthenium trans dihydrido carbonyl PNP complexes. *Dalton Trans.* **2014**, *43*, 17248-17254.
- (133) Krishnakumar, V.; Chatterjee, B.; Gunanathan, C., Ruthenium-Catalyzed Urea Synthesis by N-H Activation of Amines. *Inorg. Chem.* **2017**, *56*, 7278-7284.
- (134) Anaby, A.; Schelwies, M.; Schwaben, J.; Rominger, F.; Hashmi, A. S. K.; Schaub, T., Study of Precatalyst Degradation Leading to the Discovery of a New Ru⁰ Precatalyst for Hydrogenation and Dehydrogenation. *Organometallics* **2018**, *37*, 2193-2201.
- (135) Muthaiah, S.; Hong, S. H., Acceptorless and Base-Free Dehydrogenation of Alcohols and Amines using Ruthenium-Hydride Complexes. *Adv. Synth. Catal.* **2012**, *354*, 3045-3053.
- (136) Tseng, K.-N. T.; Kampf, J. W.; Szymczak, N. K., Base-Free, Acceptorless, and Chemoselective Alcohol Dehydrogenation Catalyzed by an Amide-Derived NNN-Ruthenium(II) Hydride Complex. *Organometallics* **2013**, *32*, 2046-2049.
- (137) Le, L.; Liu, J.; He, T.; Malek, J. C.; Cervarich, T. N.; Buttner, J. C.; Pham, J.; Keith, J. M.; Chianese, A. R., Unexpected CNN-to-CC Ligand Rearrangement in Pincer-Ruthenium Precatalysts Leads to a Base-Free Catalyst for Ester Hydrogenation. *Organometallics* **2019**.
- (138) Belkova, N. V.; Bakhmutova-Albert, E. V.; Gutsul, E. I.; Bakhmutov, V. I.; Golub, I. E.; Filippov, O. A.; Epstein, L. M.; Peruzzini, M.; Rossin, A.; Zanobini, F.; Shubina, E. S., Dihydrogen Bonding in Complex (PP3)RuH(η^1 -BH4) Featuring Two Proton-Accepting Hydride Sites: Experimental and Theoretical Studies. *Inorg. Chem.* **2014**, *53*, 1080-1090.
-

- (139) Golub, I. E.; Filippov, O. A.; Belkova, N. V.; Gutsul, E. I.; Epstein, L. M.; Rossin, A.; Peruzzini, M.; Shubina, E. S., Competition between the Hydride Ligands of Two Types in Proton Transfer to [κ^3 -P-CH₃C(CH₂CH₂PPh₂)₃RuH(η^2 -BH₄)]. *Eur. J. Inorg. Chem.* **2017**, 2017, 4673-4682.
- (140) He, T.; Buttner, J. C.; Reynolds, E. F.; Pham, J.; Malek, J. C.; Keith, J. M.; Chianese, A. R., Dehydroalkylative Activation of CNN- and PNN-Pincer Ruthenium Catalysts for Ester Hydrogenation. *J. Am. Chem. Soc.* **2019**.
- (141) Rodríguez-Lugo, R. E.; Trincado, M.; Vogt, M.; Tewes, F.; Santiso-Quinones, G.; Grützmacher, H., A homogeneous transition metal complex for clean hydrogen production from methanol–water mixtures. *Nat. Chem.* **2013**, 5, 342.
- (142) Ogata, O.; Nakayama, Y.; Nara, H.; Fujiwhara, M.; Kayaki, Y., Atmospheric Hydrogenation of Esters Catalyzed by PNP-Ruthenium Complexes with an N-Heterocyclic Carbene Ligand. *Org. Lett.* **2016**, 18, 3894-3897.
- (143) Kar, S.; Sen, R.; Kothandaraman, J.; Goeppert, A.; Chowdhury, R.; Munoz, S. B.; Haiges, R.; Prakash, G. K. S., Mechanistic Insights into Ruthenium-Pincer-Catalyzed Amine-Assisted Homogeneous Hydrogenation of CO₂ to Methanol. *J. Am. Chem. Soc.* **2019**, 141, 3160-3170.
- (144) Nguyen, D. H.; Trivelli, X.; Capet, F.; Swesi, Y.; Favre-Réguillon, A.; Vanoye, L.; Dumeignil, F.; Gauvin, R. M., Deeper Mechanistic Insight into Ru Pincer-Mediated Acceptorless Dehydrogenative Coupling of Alcohols: Exchanges, Intermediates, and Deactivation Species. *ACS Catal.* **2018**, 8, 4719-4734.
- (145) Weigend, F.; Häser, M.; Patzelt, H.; Ahlrichs, R., RI-MP2: optimized auxiliary basis sets and demonstration of efficiency. *Chemical Physics Letters* **1998**, 294, 143-152.
- (146) Hellweg, A.; Hättig, C.; Höfener, S.; Klopper, W., Optimized accurate auxiliary basis sets for RI-MP2 and RI-CC2 calculations for the atoms Rb to Rn. *Theor. Chem. Acc.* **2007**, 117, 587-597.
- (147) Legault, C. Y., *Cylview 1.0b*, Université de Sherbrooke, available from <http://www.cylview.org>, **2009**.
- (148) Tolman, C. A., Steric effects of phosphorus ligands in organometallic chemistry and homogeneous catalysis. *Chem. Rev.* **1977**, 77, 313-348.
- (149) Cooper, R. I.; Thompson, A. L.; Watkin, D. J., CRYSTALS enhancements: dealing with hydrogen atoms in refinement. *J. Appl. Crystallogr.* **2010**, 43, 1100-1107.
- (150) Chen, X.; Jing, Y.; Yang, X., Unexpected Direct Hydride Transfer Mechanism for the Hydrogenation of Ethyl Acetate to Ethanol Catalyzed by SNS Pincer Ruthenium Complexes. *Chem. Eur. J.* **2016**, 22, 1950-1957.

-
- (151) Dub, P. A.; Gordon, J. C., Metal–Ligand Bifunctional Catalysis: The “Accepted” Mechanism, the Issue of Concertedness, and the Function of the Ligand in Catalytic Cycles Involving Hydrogen Atoms. *ACS Catal.* **2017**, *7*, 6635-6655.
- (152) Gunanathan, C.; Milstein, D., Metal–Ligand Cooperation by Aromatization–Dearomatization: A New Paradigm in Bond Activation and “Green” Catalysis. *Acc. Chem. Res.* **2011**, *44*, 588-602.
- (153) Gusev, D. G., Dehydrogenative Coupling of Ethanol and Ester Hydrogenation Catalyzed by Pincer-Type YNP Complexes. *ACS Catal.* **2016**, *6*, 6967-6981.
- (154) Dub, P. A.; Scott, B. L.; Gordon, J. C., Why Does Alkylation of the N–H Functionality within M/NH Bifunctional Noyori-Type Catalysts Lead to Turnover? *J. Am. Chem. Soc.* **2017**, *139*, 1245-1260.
- (155) Jiang, Y.-Y.; Xu, Z.-Y.; Yu, H.-Z.; Fu, Y., A self-catalytic role of methanol in PNP-Ru pincer complex catalysed dehydrogenation. *Sci. China Chem.* **2016**, *59*, 724-729.
- (156) Pinggen, D.; Choi, J.-H.; Allen, H.; Murray, G.; Ganji, P.; van Leeuwen, P. W. N. M.; Prechtel, M. H. G.; Vogt, D., Amide versus amine ligand paradigm in the direct amination of alcohols with Ru-PNP complexes. *Catal. Sci. Technol.* **2018**, *8*, 3969-3976.
- (157) Agapova, A.; Alberico, E.; Kammer, A.; Junge, H.; Beller, M., Catalytic Dehydrogenation of Formic Acid with Ruthenium-PNP-Pincer Complexes: Comparing N-Methylated and NH-Ligands. *ChemCatChem* **2019**, *11*, 1910-1914.
- (158) Lu, Y.; Liu, Z.; Guo, J.; Qu, S.; Zhao, R.; Wang, Z.-X., A DFT study unveils the secret of how H₂ is activated in the N-formylation of amines with CO₂ and H₂ catalyzed by Ru(II) pincer complexes in the absence of exogenous additives. *Chem. Commun.* **2017**, *53*, 12148-12151.
- (159) Zhang, L.; Han, Z.; Zhao, X.; Wang, Z.; Ding, K., Highly Efficient Ruthenium-Catalyzed N-Formylation of Amines with H₂ and CO₂. *Angew. Chem. Int. Ed.* **2015**, *54*, 6186-6189.
- (160) Kaithal, A.; Schmitz, M.; Hölscher, M.; Leitner, W., On the Mechanism of the Ruthenium-catalyzed β -methylation of Alcohols with Methanol. *ChemCatChem* **2020**, *12*, 781-787.
- (161) Noyori, R.; Yamakawa, M.; Hashiguchi, S., Metal–Ligand Bifunctional Catalysis: A Nonclassical Mechanism for Asymmetric Hydrogen Transfer between Alcohols and Carbonyl Compounds. *J. Org. Chem.* **2001**, *66*, 7931-7944.
- (162) Noyori, R.; Ohkuma, T., Asymmetric Catalysis by Architectural and Functional Molecular Engineering: Practical Chemo- and Stereoselective Hydrogenation of Ketones. *Angew. Chem. Int. Ed.* **2001**, *40*, 40-73.
-

- (163) Abdur-Rashid, K.; Clapham, S. E.; Hadzovic, A.; Harvey, J. N.; Lough, A. J.; Morris, R. H., Mechanism of the Hydrogenation of Ketones Catalyzed by trans-Dihydrido(diamine)ruthenium(II) Complexes. *J. Am. Chem. Soc.* **2002**, *124*, 15104-15118.
- (164) Noyori, R., Asymmetric Catalysis: Science and Opportunities (Nobel Lecture). *Angew. Chem. Int. Ed.* **2002**, *41*, 2008-2022.
- (165) Dub, P. A.; Gordon, J. C., The role of the metal-bound N–H functionality in Noyori-type molecular catalysts. *Nat. Rev. Chem.* **2018**, *2*, 396-408.
- (166) Liu, C.; van Putten, R.; Kulyaev, P. O.; Filonenko, G. A.; Pidko, E. A., Computational insights into the catalytic role of the base promoters in ester hydrogenation with homogeneous non-pincer-based Mn-P,N catalyst. *J. Catal.* **2018**, *363*, 136-143.
- (167) Shu, S.; Huang, M.; Jiang, J.; Qu, L.-B.; Liu, Y.; Ke, Z., Catalyzed or non-catalyzed: chemoselectivity of Ru-catalyzed acceptorless dehydrogenative coupling of alcohols and amines via metal–ligand bond cooperation and (de)aromatization. *Catal. Sci. Technol.* **2019**, *9*, 2305-2314.
- (168) Dub, P. A.; Henson, N. J.; Martin, R. L.; Gordon, J. C., Unravelling the Mechanism of the Asymmetric Hydrogenation of Acetophenone by [RuX₂(diphosphine)(1,2-diamine)] Catalysts. *J. Am. Chem. Soc.* **2014**, *136*, 3505-3521.
- (169) Dub, P. A.; Gordon, J. C., The mechanism of enantioselective ketone reduction with Noyori and Noyori–Ikariya bifunctional catalysts. *Dalton Trans.* **2016**, *45*, 6756-6781.
- (170) Hasanayn, F.; Baroudi, A.; Bengali, A. A.; Goldman, A. S., Hydrogenation of Dimethyl Carbonate to Methanol by trans-[Ru(H)₂(PNN)(CO)] Catalysts: DFT Evidence for Ion-Pair-Mediated Metathesis Paths for C–OMe Bond Cleavage. *Organometallics* **2013**, *32*, 6969-6985.
- (171) Tindall, D. J.; Menche, M.; Schelwies, M.; Paciello, R. A.; Schäfer, A.; Comba, P.; Rominger, F.; Hashmi, A. S. K.; Schaub, T., Ru⁰ or Ru^{II}: A Study on Stabilizing the “Activated” Form of Ru-PNP Complexes with Additional Phosphine Ligands in Alcohol Dehydrogenation and Ester Hydrogenation. *Inorg. Chem.* **2020**, *59*, 5099-5115.
- (172) Rauch, M.; Luo, J.; Avram, L.; Ben-David, Y.; Milstein, D., Mechanistic Investigations of Ruthenium Catalyzed Dehydrogenative Thioester Synthesis and Thioester Hydrogenation. *ACS Catal.* **2021**, *11*, 2795-2807.
- (173) Pham, J.; Jarczyk, C. E.; Reynolds, E. F.; Kelly, S. E.; Kim, T.; He, T.; Keith, J. M.; Chianese, A. R., The key role of the latent N–H group in Milstein's catalyst for ester hydrogenation. *Chem. Sci.* **2021**, *12*, 8477-8492.
- (174) Shaalan, Y.; Boulton, L.; Jamieson, C., Ruthenium-Catalyzed Ester Reductions Applied to Pharmaceutical Intermediates. *Org. Process Res. Dev.* **2020**, *24*, 2745-2751.

-
- (175) Dub, P. A.; Batrice, R. J.; Gordon, J. C.; Scott, B. L.; Minko, Y.; Schmidt, J. G.; Williams, R. F., Engineering Catalysts for Selective Ester Hydrogenation. *Org. Process Res. Dev.* **2020**.
- (176) Dub, P. A.; Tkachenko, N. V., Mechanism of Potassium tert-Butoxide-Catalyzed Ketones Hydrogenation in the Solution Phase. *J. Phys. Chem. A* **2021**, *125*, 5726-5737.
- (177) Bertleff, W., Roeper, M. and Sava, X., Carbonylation. In *Ullmann's Encyclopedia of Industrial Chemistry*, Wiley-VCH: Weinheim, **2012**.
- (178) Kubitschke, J., Lange, H. and Strutz, H., Carboxylic Acids Aliphatic. In *Ullmann's Encyclopedia of Industrial Chemistry*, Wiley-VCH: Weinheim, **2014**.
- (179) Wu, X. F.; Fang, X. J.; Wu, L. P.; Jackstell, R.; Neumann, H.; Beller, M., Transition-Metal-Catalyzed Carbonylation Reactions of Olefins and Alkynes: A Personal Account. *Acc. Chem. Res.* **2014**, *47*, 1041-1053.
- (180) Brennfuhrer, A.; Neumann, H.; Beller, M., Palladium-Catalyzed Carbonylation Reactions of Alkenes and Alkynes. *ChemCatChem* **2009**, *1*, 28-41.
- (181) Brennfuhrer, A.; Neumann, H.; Beller, M., Palladium-Catalyzed Carbonylation Reactions of Aryl Halides and Related Compounds. *Angew. Chem. Int. Ed.* **2009**, *48*, 4114-4133.
- (182) Barnard, C. F. J., Palladium-Catalyzed Carbonylation-A Reaction Come of Age. *Organometallics* **2008**, *27*, 5402-5422.
- (183) Paulik, F. E.; Roth, J. F., Novel Catalysts For Low-Pressure Carbonylation Of Methanol To Acetic Acid. *Chem. Commun.* **1968**, 1578.
- (184) Zoeller, J. R.; Cloyd, J. D.; Lafferty, N. L.; Nicely, V. A.; Polichnowski, S. W.; Cook, S. L., Rhodium-catalyzed carbonylation of methyl acetate. *Adv. Chem. Ser.* **1992**, 377-394.
- (185) Haynes, A., Catalytic Methanol Carbonylation. In *Advances in Catalysis*, Gates, B. C.; Knozinger, H.; Jentoft, F. C., Eds. **2010**; Vol. 53, pp 1-45.
- (186) Garland, C. S., Giles, M. F. , Sunley, J. G. Process and catalyst for the production of acetic acid. EP0643034B1, **1997**.
- (187) Le Berre, C., Serp, P. , Kalck, P. and Torrence, G. P., Acetic Acid. In *Ullmann's Encyclopedia of Industrial Chemistry*, Wiley-VCH: Weinheim, **2014**.
- (188) Eastham, G. R., Richards, P. I. A process for the carbonylation of ethylenically unsaturated compound and a catalytic system. WO 2009/010782 A1, **2008**.
- (189) Samel, U., Kohler, W. , Gamer, A. O., Keuser, U. , Yang, S. , Jin, Y. , Lin, M. and Wang, Z., Propionic Acid and Derivatives. In *Ullmann's Encyclopedia of Industrial chemistry*; Wiley-VCH, Ed.: Weinheim, 2014.
-

- (190) Elango, V., Murphy, M. A., Smith, B. L. Mott, G. N., Moss, G. L. Process for producing ibuprofen. EP0284310A1, **1988**.
- (191) Nicholson, J. S.; Adams, S. S. Phenyl propionic acids. US3385886A, **1963**.
- (192) Qu, R., Evaluation and Improvement of Synthesis Method for Ibuprofen. *IOP C. Ser. Earth Env.* **2019**, *242*, 052001.
- (193) BASF SE Catalysts Division, *Daily Metal Prices History Chart for Palladium (August 5th, 2010 to August 5th, 2021)*. <https://apps.catalysts.basf.com/apps/eibprices/mp/DPCharts.aspx> (accessed on August 5th, 2021)
- (194) Rizkalla, N., Acetic Acid Production via Low-Pressure, Nickel-Catalyzed Methanol Carbonylation. In *Industrial Chemicals via C1 Processes*, American Chemical Society: Washington, D.C., **1987**; Vol. 328, pp 61-76.
- (195) Ubale, R. S.; Kelkar, A. A.; Chaudhari, R. V., Carbonylation of ethanol using Ni-isoquinoline complex catalyst: Activity and selectivity studies. *J. Mol. Catal. A: Chem.* **1997**, *118*, 9-19.
- (196) Kelkar, A. A.; Ubale, R. S.; Deshpande, R. M.; Chaudhari, R. V., Carbonylation Of Methanol Using Nickel-Complex Catalyst - A Kinetic-Study. *J. Catal.* **1995**, *156*, 290-294.
- (197) Kelkar, A. A.; Ubale, R. S.; Chaudhari, R. V., Promoting effects of metal iodides in Ni(Isoq)₄Cl₂-catalyzed carbonylation of ethanol and n-propanol. *J. Catal.* **1992**, *136*, 605-608.
- (198) Tanaka, K., Shima, Y. Process for production of alpha-(4-isobutylphenyl)propionic acid. EP0361021A1, **1989**.
- (199) Chaudhari, R. V., Seayad, J., Seayad, A. Process for the preparation of 2-aryl propionic acids. US 6660883 B1, **2000**.
- (200) Fell, B., Hydrocarboxylation Reaction Of Unsaturated-Compounds With Nickel Carbonyl-Complex And Cobalt Carbonyl-Complex Catalysts. *Fett. Wiss. Technol.* **1974**, *76*, 193-196.
- (201) Sanz, R.; Miguel, D.; Martinez, A.; Alvarez-Gutierrez, J. M.; Rodriguez, F., Bronsted acid-catalyzed benzylolation of 1,3-dicarbonyl derivatives. *Org. Lett.* **2007**, *9*, 2027-2030.
- (202) Sabater, S.; Menche, M.; Ghosh, T.; Krieg, S.; Rück, K. S. L.; Paciello, R.; Schäfer, A.; Comba, P.; Hashmi, A. S. K.; Schaub, T., Mechanistic Investigation of the Nickel-Catalyzed Carbonylation of Alcohols. *Organometallics* **2020**, *39*, 870-880.

-
- (203) Matsumoto, S.; Naito, M.; Oseki, T.; Akazome, M.; Otani, Y., Selective reaction of benzyl alcohols with HI gas: Iodination, reduction, and indane ring formations. *Tetrahedron* **2017**, *73*, 7254-7259.
- (204) Andersen, T. L.; Donslund, A. S.; Neumann, K. T.; Skrydstrup, T., Carbonylative Coupling of Alkyl Zinc Reagents with Benzyl Bromides Catalyzed by a Nickel/NN2 Pincer Ligand Complex. *Angew. Chem. Int. Ed.* **2018**, *57*, 800-804.
- (205) Bottoni, A.; Miscione, G. P.; Carvajal, M. A.; Novoa, J. J., The mechanism of transition metal catalyzed carbonylation of allyl halides: A theoretical investigation. *J. Organomet. Chem.* **2006**, *691*, 4498-4507.
- (206) Bottoni, A.; Miscione, G. P.; Novoa, J. J.; Prat-Resina, X., DFT Computational Study of the Mechanism of Allyl Halides Carbonylation Catalyzed by Nickel Tetracarbonyl. *J. Am. Chem. Soc.* **2003**, *125*, 10412-10419.
- (207) Breitenfeld, J.; Ruiz, J.; Wodrich, M. D.; Hu, X. L., Bimetallic Oxidative Addition Involving Radical Intermediates in Nickel-Catalyzed Alkyl-Alkyl Kumada Coupling Reactions. *J. Am. Chem. Soc.* **2013**, *135*, 12004-12012.
- (208) Breitenfeld, J.; Wodrich, M. D.; Hu, X., Bimetallic Oxidative Addition in Nickel-Catalyzed Alkyl-Aryl Kumada Coupling Reactions. *Organometallics* **2014**, *33*, 5708-5715.
- (209) Donslund, A. S.; Neumann, K. T.; Corneliussen, N. P.; Grove, E. K.; Herbstritt, D.; Daasbjerg, K.; Skrydstrup, T., Access to β -Ketonitriles through Nickel-Catalyzed Carbonylative Coupling of α -Bromonitriles with Alkylzinc Reagents. *Chem. Eur. J.* **2019**, *25*, 9856-9860.
- (210) Liu, Y.; Cornella, J.; Martin, R., Ni-Catalyzed Carboxylation of Unactivated Primary Alkyl Bromides and Sulfonates with CO₂. *J. Am. Chem. Soc.* **2014**, *136*, 11212-11215.
- (211) Shi, R.; Hu, X., From Alkyl Halides to Ketones: Nickel-Catalyzed Reductive Carbonylation Utilizing Ethyl Chloroformate as the Carbonyl Source. *Angew. Chem. Int. Ed.* **2019**, *58*, 7454-7458.
- (212) Weix, D. J., Methods and Mechanisms for Cross-Electrophile Coupling of Csp² Halides with Alkyl Electrophiles. *Acc. Chem. Res.* **2015**, *48*, 1767-1775.
- (213) Wotal, A. C.; Ribson, R. D.; Weix, D. J., Stoichiometric Reactions of Acylnickel(II) Complexes with Electrophiles and the Catalytic Synthesis of Ketones. *Organometallics* **2014**, *33*, 5874-5881.
- (214) Zhao, C.; Jia, X.; Wang, X.; Gong, H., Ni-Catalyzed Reductive Coupling of Alkyl Acids with Unactivated Tertiary Alkyl and Glycosyl Halides. *J. Am. Chem. Soc.* **2014**, *136*, 17645-17651.
-

- (215) Zhao, S.; Mankad, N. P., Metal-catalysed radical carbonylation reactions. *Catal. Sci. Technol.* **2019**, *9*, 3603-3613.
- (216) Fukuyama, T.; Nishitani, S.; Inouye, T.; Morimoto, K.; Ryu, I., Effective acceleration of atom transfer carbonylation of alkyl iodides by metal complexes. Application to the synthesis of the hinokinin precursor and dihydrocapsaicin. *Org. Lett.* **2006**, *8*, 1383-6.
- (217) Fusano, A.; Sumino, S.; Nishitani, S.; Inouye, T.; Morimoto, K.; Fukuyama, T.; Ryu, I., Pd/Light-Accelerated Atom-Transfer Carbonylation of Alkyl Iodides: Applications in Multicomponent Coupling Processes Leading to Functionalized Carboxylic Acid Derivatives. *Chem. Eur. J.* **2012**, *18*, 9415-9422.
- (218) Stille, J. K.; Cowell, A. B., Oxidative addition of benzyl halides to tetrakis(triphenylphosphine)nickel(0). *J. Organomet. Chem.* **1977**, *124*, 253-261.
- (219) Goossen, L. J.; Koley, D.; Hermann, H. L.; Thiel, W., Mechanistic Pathways for Oxidative Addition of Aryl Halides to Palladium(0) Complexes: A DFT Study. *Organometallics* **2005**, *24*, 2398-2410.
- (220) Manzoor, A.; Wienefeld, P.; Baird, M. C.; Budzelaar, P. H. M., Catalysis of Cross-Coupling and Homocoupling Reactions of Aryl Halides Utilizing Ni(0), Ni(I), and Ni(II) Precursors; Ni(0) Compounds as the Probable Catalytic Species but Ni(I) Compounds as Intermediates and Products. *Organometallics* **2017**, *36*, 3508-3519.
- (221) Nilges, M. J.; Barefield, E. K.; Belford, R. L.; Davis, P. H., Electronic-structure of 3-coordinate Nickel (I) - electron-paramagnetic resonance of Nickel-doped halobis(triphenylphosphine)Copper(I). *J. Am. Chem. Soc.* **1977**, *99*, 755-760.
- (222) Cassar, L.; Foà, M., Halogenotricarbonylnickel anions. *Inorg. Nucl. Chem. Lett.* **1970**, *6*, 291-294.
- (223) Reppe, W.; Kröper, H., Carbonylierung II. Carbonsäuren und ihre Derivate aus olefinischen Verbindungen und Kohlenoxyd. *Liebigs Ann. Chem.* **1953**, *582*, 38-71.
- (224) Reppe, W.; Kröper, H.; v. Kutepow, N.; Pistor, H. J., Carbonylierung III. Umsetzung von Alkoholen und offenen Äthern mit Kohlenoxyd zu Carbonsäuren. *Liebigs Ann. Chem.* **1953**, *582*, 72-86.
- (225) Koch, H.; Haaf, W., Über die Synthese verzweigter Carbonsäuren nach der Ameisensäure-Methode. *Liebigs Ann. Chem.* **1958**, *618*, 251-266.
- (226) Koch, H.; Huisken, W.; Möller, K.-E.; Lohbeck, K. Verfahren zur Herstellung von Carbonsäuren aus Olefinen, Kohlenoxyd und Wasser. DE972315, **1956**.
- (227) Fadini, L.; Frasca, G.; Mongbanziama, Y.; Allemann, C. A process for producing carboxylic acids from tertiary alcohols under continuous flow. EP3381886A1, **2017**.

-
- (228) Tsumori, N.; Xu, Q.; Souma, Y.; Mori, H., Carbonylation of alcohols over Nafion-H, a solid perfluoroalkanesulfonic acid resin catalyst. *J. Mol. Catal. A: Chem.* **2002**, *179*, 271-277.
- (229) Qiao, K.; Yokoyama, C., Koch carbonylation of tertiary alcohols in the presence of acidic ionic liquids. *Catal. Commun.* **2006**, *7*, 450-453.
- (230) Souma, Y.; Sano, H.; Iyoda, J., Synthesis of tert-carboxylic acids from olefins and carbon monoxide by copper(I) carbonyl catalyst. *J. Org. Chem.* **1973**, *38*, 2016-2020.
- (231) Xu, Q.; Imamura, Y.; Fujiwara, M.; Souma, Y., A New Gold Catalyst: Formation of Gold(I) Carbonyl, $[\text{Au}(\text{CO})_n]^+$ ($n = 1, 2$), in Sulfuric Acid and Its Application to Carbonylation of Olefins. *J. Org. Chem.* **1997**, *62*, 1594-1598.
- (232) Jayasree, S.; Seayad, A.; Chaudhari, R. V., Novel Palladium(II) Complex Containing a Chelating Anionic N–O Ligand: Efficient Carbonylation Catalyst. *Org. Lett.* **2000**, *2*, 203-206.
- (233) Dong, K.; Sang, R.; Liu, J.; Razzaq, R.; Franke, R.; Jackstell, R.; Beller, M., Palladium-Catalyzed Carbonylation of sec- and tert-Alcohols. *Angew. Chem. Int. Ed.* **2017**, *56*, 6203-6207.
- (234) Rupp, C.; Corbiere, P. Continuous process for the preparation of pivaloyl chloride and of aroyl chloride. US6605743B1, **1998**.
- (235) Weissemel, K.; Arpe, H.-J., Syntheses involving Carbon Monoxide. In *Industrial Organic Chemistry*, Wiley-VCH: Weinheim, **2003**; pp 127-144.
- (236) Zhou, H.; Lu, S.; Li, H.; Chen, J.; Fu, H.; Wang, H., Palladium-catalyzed carbonylation of tert-butyl alcohol to esters of iso-valeric acid. *J. Mol. Catal. A: Chem.* **1997**, *116*, 329-333.
- (237) Lichtenberger, N.; Menche, M.; Rück, K. S. L.; Paciello, R.; Schäfer, A.; Comba, P.; Hashmi, A. S. K.; Schaub, T., Revisiting Nickel-Catalyzed Carbonylations: Unexpected Observation of Substrate-dependent Mechanistic Differences. *manuscript in preparation* **2021**.
- (238) Haaf, F.; Sanner, A.; Straub, F., Polymers of N-Vinylpyrrolidone: Synthesis, Characterization and Uses. *Polym. J.* **1985**, *17*, 143-152.
- (239) Reppe, W., Polyvinylpyrrolidon. *Angew. Chem.* **1953**, *65*, 577-578.
- (240) Harreus, A. L.; Backes, R.; Eichler, J.-O.; Feuerhake, R.; Jäkel, C.; Mahn, U.; Pinkos, R.; Vogelsang, R., 2-Pyrrolidone. In *Ullmann's Encyclopedia of Industrial Chemistry*, **2011**.
- (241) Tsutsumi, N., Molecular design of photorefractive polymers. *Polym. J.* **2016**, *48*, 571-588.
-

- (242) Cortez-Lemus, N. A.; Licea-Claverie, A., Poly(N-vinylcaprolactam), a comprehensive review on a thermoresponsive polymer becoming popular. *Prog. Polym. Sci.* **2016**, *53*, 1-51.
- (243) Shubo, F.; Shuyuan, L.; Cunfeng, H.; Erli, Z.; Xinliang, T., Synthesis of N-vinyl caprolactam. *Catal. Today* **2009**, *140*, 169-173.
- (244) Asami, T.; Hiraoka, T. N., D. Curable composition, curable ink, storing container, two-dimensional or three-dimensional image forming device, two-dimensional or three-dimensional image forming method, cured product, printed matter, and adhesive label. US20190284416A1, **2019**.
- (245) Borg, K.; Slater, S. A printing ink. GB2573207A, **2019**.
- (246) Osborne, G.; Slater, S. A printing ink. WO2019193359A1, **2019**.
- (247) Reppe, W., Vinylierung. *Liebigs Ann. Chem.* **1956**, *601*, 81-138.
- (248) Werner, G.; Rodygin, K. S.; Kostin, A. A.; Gordeev, E. G.; Kashin, A. S.; Ananikov, V. P., A solid acetylene reagent with enhanced reactivity: fluoride-mediated functionalization of alcohols and phenols. *Green Chem.* **2017**, *19*, 3032-3041.
- (249) Rodygin, K. S.; Bogachenkov, A. S.; Ananikov, V. P., Vinylation of a Secondary Amine Core with Calcium Carbide for Efficient Post-Modification and Access to Polymeric Materials. *Molecules* **2018**, *23*.
- (250) Ciapetti, P.; Taddei, M., A simple preparation of N-vinyl derivatives of DNA nucleobases. *Tetrahedron* **1998**, *54*, 11305-11310.
- (251) Pässler, P.; Hefner, W.; Buckl, K.; Meinass, H.; Meiswinkel, A.; Wernicke, H.-J.; Ebersberg, G.; Müller, R.; Bässler, J.; Behringer, H.; Mayer, D., Acetylene. In *Ullmann's Encyclopedia of Industrial Chemistry*, **2011**.
- (252) Bienewald, F.; Tužina, P.; Vogelsang, R.; Berger, F. I.; Peter, S., Vinyl Ethers. In *Ullmann's Encyclopedia of Industrial Chemistry*, **2021**; pp 1-12.
- (253) Trotuş, I.-T.; Zimmermann, T.; Schüth, F., Catalytic Reactions of Acetylene: A Feedstock for the Chemical Industry Revisited. *Chem. Rev.* **2014**, *114*, 1761-1782.
- (254) Reppe, E. H. W., Chemie und Technik der Acetylen-Druck-Reaktionen. *Chem. Ing. Tech.* **1950**, *22*, 273-283.
- (255) Huang, L.; Arndt, M.; Gooßen, K.; Heydt, H.; Gooßen, L. J., Late Transition Metal-Catalyzed Hydroamination and Hydroamidation. *Chem. Rev.* **2015**, *115*, 2596-2697.
- (256) Cheung, H. W.; So, C. M.; Pun, K. H.; Zhou, Z.; Lau, C. P., Hydro(trispyrazolyl)borato-Ruthenium(II) Diphosphinoamino Complex-Catalyzed

Addition of β -Diketones to 1-Alkynes and Anti-Markovnikov Addition of Secondary Amines to Aromatic 1-Alkynes. *Adv. Synth. Catal.* **2011**, 353, 411-425.

(257) Gooßen, L. J.; Arndt, M.; Blanchot, M.; Rudolphi, F.; Menges, F.; Niedner-Schatteburg, G., A Practical and Effective Ruthenium Trichloride-Based Protocol for the Regio- and Stereoselective Catalytic Hydroamidation of Terminal Alkynes. *Adv. Synth. Catal.* **2008**, 350, 2701-2707.

(258) Gooßen, L. J.; Rauhaus, J. E.; Deng, G., Ru-Catalyzed Anti-Markovnikov Addition of Amides to Alkynes: A Regio- and Stereoselective Synthesis of Enamides. *Angew. Chem. Int. Ed.* **2005**, 44, 4042-4045.

(259) Buba, A. E.; Arndt, M.; Gooßen, L. J., Z-Selective hydroamidation of terminal alkynes with secondary amides and imides catalyzed by a Ru/Yb-system. *J. Organomet. Chem.* **2011**, 696, 170-178.

(260) Semina, E.; Tuzina, P.; Bienewald, F.; Hashmi, A. S. K.; Schaub, T., Ruthenium-catalyzed synthesis of vinylamides at low acetylene pressure. *Chem. Commun.* **2020**, 56, 5977-5980.

(261) Fan, Y. C.; Kwon, O., Advances in nucleophilic phosphine catalysis of alkenes, allenes, alkynes, and MBHADs. *Chem. Commun.* **2013**, 49, 11588-11619.

(262) Methot, J. L.; Roush, W. R., Nucleophilic Phosphine Organocatalysis. *Adv. Synth. Catal.* **2004**, 346, 1035-1050.

(263) Trost, B. M.; Dake, G. R., Nucleophilic α -Addition to Alkynoates. A Synthesis of Dehydroamino Acids. *J. Am. Chem. Soc.* **1997**, 119, 7595-7596.

(264) Sitte, N.; Menche, M.; Tužina, P.; Bienewald, F.; Schäfer, A.; Comba, P.; Rominger, F.; Hashmi, A. S. K.; Schaub, T., Phosphine-catalyzed Vinylation at Low Acetylene Pressure. *J. Org. Chem.* **2021**, manuscript accepted.

(265) Chen, V. Y.; Kwon, O., Unified Approach to Furan Natural Products via Phosphine-Palladium Catalysis. *Angew. Chem. Int. Ed.* **2021**, 60, 8874-8881.

(266) Ziegenbalg, N.; Lohwasser, R.; D'Andola, G.; Adermann, T.; Brendel, J. C., Oxa-Michael polyaddition of vinylsulfonylethanol for aliphatic polyethersulfones. *Polym. Chem.* **2021**.

(267) Schweizer, E. E.; Bach, R. D., Phosphonium Salts. II. 2-Bromophenetole and Triphenylphosphorus as Novel Phosphonioethylation Precursors. *J. Org. Chem.* **1964**, 29, 1746-1751.

(268) Ovakimyan, M. Z.; Barsegyan, S. K.; Kikoyan, N. M.; Indzhikyan, M. G., Properties of Onium Salts of Phosphorus and Nitrogen. *Russ. J. Gen. Chem.* **2005**, 75, 1074-1076.

- (269) Bordwell, F. G.; McCallum, R. J.; Olmstead, W. N., Acidities and hydrogen bonding of phenols in dimethyl sulfoxide. *J. Org. Chem.* **1984**, *49*, 1424-1427.
- (270) Bordwell, F. G., Equilibrium acidities in dimethyl sulfoxide solution. *Acc. Chem. Res.* **1988**, *21*, 456-463.
- (271) Guo, H.; Fan, Y. C.; Sun, Z.; Wu, Y.; Kwon, O., Phosphine Organocatalysis. *Chem. Rev.* **2018**, *118*, 10049-10293.
- (272) Schweizer, E. E.; Smucker, L. D.; Votral, R. J., Reactions of Phosphorus Compounds. VII. A General Chain-Extension Reaction. *J. Org. Chem.* **1966**, *31*, 467-471.
- (273) Meyers, A. I.; Lawson, J. P.; Carver, D. R., Highly stereoselective route to (E)-allyl amines via vinyltri-n-butylphosphonium salts (Schweizer reaction). *J. Org. Chem.* **1981**, *46*, 3119-3123.
- (274) Lee, M.-J.; Kim, S. C.; Kim, J. N., Synthesis of 3,4-Disubstituted Pyridines Starting from Baylis-Hillman Adducts Using Schweizer Reaction. *B. Korean Chem. Soc.* **2006**, *27*, 439-442.
- (275) Fredericks, R. J.; Lynch, D. G.; Daniels, W. E., Thermal properties of poly(acetylene): On the origin of cuprene in reppe's cyclooctatetraene synthesis. *J. Polym. Sci. Pol. Lett.* **1964**, *2*, 803-808.

**Eidesstattliche Versicherung gemäß § 8 der Promotionsordnung für die
Naturwissenschaftlich-Mathematische Gesamtfakultät der Universität Heidelberg**

1. Bei der eingereichten Dissertation zu dem Thema

*„Quantum Chemical Investigations in Homogeneous Catalysis:
Dehydrogenation, Carbonylation and Vinylation”*

handelt es sich um meine eigenständig erbrachte Leistung.

2. Ich habe nur die angegebenen Quellen und Hilfsmittel benutzt und mich keiner unzulässigen Hilfe Dritter bedient. Insbesondere habe ich wörtlich oder sinngemäß aus anderen Werken übernommene Inhalte als solche kenntlich gemacht.
3. Die Arbeit oder Teile davon habe ich bislang nicht an einer Hochschule des In- oder Auslands als Bestandteil einer Prüfungs- oder Qualifikationsleistung vorgelegt.
4. Die Richtigkeit der vorstehenden Erklärungen bestätige ich.
5. Die Bedeutung der eidesstattlichen Versicherung und die strafrechtlichen Folgen einer unrichtigen oder unvollständigen eidesstattlichen Versicherung sind mir bekannt.

Ich versichere an Eides statt, dass ich nach bestem Wissen die reine Wahrheit erklärt und nichts verschwiegen habe.

.....
Ort und Datum

.....
Unterschrift